Out of equilibrium dynamics in a paraxial fluid of light

Murad Abuzarli

THÈSE DE DOCTORAT
DE SORBONNE UNIVERSITÉ

Spécialité : Physique

École doctorale nº564: Physique en Île-de-France

réalisée sous la direction de Dr. Quentin Glorieux

au Laboratoire Kastler Brossel

présentée par

Murad Abuzarli

Sujet de la thèse :

Dynamique hors équilibre dans un fluide de lumière paraxial

soutenue le 21 4 2022

devant le jury composé de :

Mme	Pruvost Laurence,	DR,	Université / ENS Paris-Saclay,	Rapporteur
M.	Mussot Arnaud,	Full Prof.,	Université de Lille,	Rapporteur
M.	Bellec Matthieu,	MCF,	Université de Sophia Antipolis, Nice,	Examinateur
M.	Defienne Hugo,	MCF,	University of Glasgow,	Membre Invité
M.	Dubessy Romain,	MCF,	Université Paris-Nord, Villetaneuse,	Examinateur
Mme	Schwob Catherine,	Full Prof.,	Sorbonne Université,	Examinateur
M.	Glorieux Quentin,	MCF,	Sorbonne Université,	Directeur de thèse

Contents

Acknowledgements

I would like to thank all people who encouraged and were around me during this work. First of all, thanks to the jury members for evaluatig this work and for the constructive remarks for its improvement. I am grateful to the permanent members of our group, Quentin Glorieux, Alberto Bramati, Elisabeth Giacobino, for accepting me to the group. Special thanks to my supervisor, Quentin for critical remarks, suggestions for the experiment, for the improvement of posters and figures, and of course for the mountain hikes in les Houches and in Vercors. Thanks to my mentors within the lab, Pierre-Jean Nacher and Saïda Guellati-Khélifa for making sure my PhD advances well. I would also like to thank Jeff Steinhauer, with whom I collaborated on the daily basis for the quench experiment and from whom I learned much. Special thanks also to Nicolas Cherroret for the fruitful collaboration around the prethermalization experiment and for countless very interesting discussions. Special thanks to the PhD student who preceded me in this work, Quentin Fontaine, from whom I learned a lot. I would also like to thank all other PhDs, interns and postdocs from the group, with whom I had pleasure to interact: Anne, Ferdinand, Kevin, Malo, Chengjie, Huiqin, Guillaume, Clara and Bojana, Laurita and Aurelien, Sagnik, Esther, Tom Bienaimé. Special thanks to my office mates, Tom Bienaimé, Jérémy, Tridib, Alexandra, Ferdinand, Tangui, Myrann, Wei and Guillaume for the usual positive mood during the work. Special thanks to the members of other groups: the whole quantum network group, and especially Tom Darras and Alexandra Sheremet. Special thanks to Louisiane Devaud from the Optical Imaging in biogical and complex media team for countless very interesting and stimulating discussions. Thanks to the members of the optomechanics team: Michael Croquette, Ferhat Loubar, Olga Kozlova and especially Samuel Deleglise for interesting discussions and for helping me setting up the pyrpl lockbox. I would like to thank all my teachers and previous supervisors who contributed to my scientific and general development, special thanks to Elshad Muellim from Baku for having taught me to have fun while learning math and physics. This work would not have been possible without my friends and immense efforts by my family members, for what I am deeply grateful. Finally I would like to thank Elena for valuable time and support.

Chapter 1

Introduction and context of this work

During my PhD thesis I had the pleasure to explore several aspects of the out of equilibrium evolution of paraxial fluids of light inside the hot atomic vapor cells. Before going into the core of the explored topics I would first like to give the general context of this work by defining the terms used in the title and giving a non-exhaustive small review of important results preceding this work.

1.1 From single particles to quantum fluids

1.1.1 Introduction: why study quantum many-body systems?

Single-particle quantum physics: In order to understand the interest of studying correlated many-body systems, it may be useful to first shortly review the main achievements of the exploration of the so called single-particle quantum physics. At the beginning of 20-th century the discovery of energy quantization by Max Planck for explaining thermal radiation by matter [88], gave birth to a new field of physics, called "quantum physics", which appeared to be a necessary toolbox to understand the World at microscopic scale where the particles composing matter appear to behave as waves and waves such as light, behave, under certain circumstances, as particles of energy, called photons. In particular, further exploration of this field had tremendous implications for the atomic theory, revealing the energy quantification of the electrons surrounding the atomic core. Even more fascinating phenomena like wave-particle duality [162, 46], matter-wave interference [52] could be predicted (and observed) based on the theory developed for single particles (like atoms) and considering systems containing many of such particles in the regime where they all behave independently of each other.

More particles: quantum correlations: However, the "single particle" picture of quantum physics is clearly not enough to explain phenomena in systems consisting of many linked or correlated particles, for example a gaz of interacting quantum particles. This observation comes along with the seminal article: "More is different" by P. W. Anderson [5], explaining among others, that changing the observation scale of a physical system can lead to significant changes in its behavior arising from the interactions among particles composing it. Primary results of

exploration of many-particle quantum systems revealed novel effects like non-classical correlations or entanglement among quantum particles, leading to phenomena which are impossible to explain with classical physics. Multiple examples range from two particle systems like pairs of entangled photons [8] to macroscopic quantum systems like superfluids (macroscopic quantum systems with interactions among particles, that behave as fluids but with strictly absent dissipation) and superconductors.

Quantum simulation: While the complexity of theoretical description of such systems increases exponentially with particle number, it seems at first glance hopeless to solve the models describing the physics of macroscopic quantum systems. To face this challenge, R. Feynmann proposed to study the theoretically intractable many-body quantum models with analogue experimental setups with well controllable parameters which are described by the same theoretical description [149]. In this way, the analogue experimental platforms play the role of calculators letting the nature solve the studied model and provide the result in form of of a measurable parameter (called observable). Fine control over experimental parameters allows to infer their influence on the solution of the studied model, which may not be easily feasible for the originally simulated system. This idea has gained momentum in scientific community over last decades establishing the research field of quantum simulation. Probably a most intuitive example of quantum simulation is a whole series of experiments worldwide, consisting in trapping cold atomic gases in optically created periodic potentials (called optical lattices) [68, 136], reproducing a well controlled experimental analogue of system described by a mathematical model called Fermi-Hubbard model that can hardly be numerically simulated at specific conditions. In fact, the exploration of the so called "underdoped region" of the Fermi–Hubbard model could explain the origin of the high-critical temperature superconductivity in cuprates [136].

Interacting quantum systems: new states of matter? Besides the exploration of the models which could explain the already observed phenomena such as superconductivity, quantum simulation already allowed to predict and observe new exotic states of matter. Probably the most celebrated result in this series is the superfluid to Mott insulator transition which is a quantum phase transition due to the fact that it is driven by quantum rather than thermal fluctuations of the system. This transition was predicted in [79] and observed shortly after in [63], in a gas of ultracold atoms in an optical lattice by varying the optical potential's depth, which controls the inter-site tunneling rate at fixed on-site interaction. In the superfluid phase, each atom wavefunction extends over the entire lattice, with long-range phase coherence, while in the insulating phase, exact numbers of atoms are localized at individual lattice sites, with no phase coherence among the different lattice sites. Since then the investigation has been extended to the influence of the system's dimensionality as well as the lattice geometry with reported results for the realization of triangular [15], cagomé [81] and even quasi-crystal [152] lattice geometries.

Alternatively, the quest for the influence of dissipation and disorder in the lattice potential on the Mott insulator-superfluid transition revealed the phenomenon of the many-body localization (MBL) [1, 134]. In difference to the Mott insulator state, MBL states appear as stationary but out of equilibrium localized (and therefore insulating) states which persist even at nonzero

temperature, preventing the system from thermalization. Summarizing the discussion one can conclude that quantum simulation is also a possible research strategy to explore new phenomena in quantum systems with large number of particles.

1.1.2 Quantum fluids

From superfluid helium to diluted cold-atomic Bose-Einstein Condensates: As mentioned in the previous section, superfluids and superconductors are examples of systems explored by means of quantum simulation with their "simplified" and better controlled analogues. The two features uniting these systems are their macroscopic quantum coherence and interactions among the particles, and allow for their common classification as "quantum fluids". The macroscopic coherence consists in the fact that a significant fraction of particles in these systems occupy the same quantum state (in case of bosonic particles, i.e. having an integer spin) and most importantly, are described by a common wave-function, behaving as a collective wave with extended spatial coherence (a well defined phase relationship of the common wave function between various points of the system). These systems are commonly observed in cold and low-energy systems, where the thermal fluctuations are negligibly small and do not have enough energy to destroy the macroscopic coherence. In fact, for a system at thermal equilibrium, the temperature T imposes the coherence range for each particle's wave function, known as the De Broglie length $\lambda_{dB} = h/u$ with h-the Planck's constant and u-the particle's temperature dependent average velocity magnitude $u \sim \sqrt{T}$. As the system's temperature drops, the de Broglie wavelength increases. As soon as it becomes much larger than the average inter-particle distance, the system acquires macroscopic coherence. Although macroscopic coherence is necessary requirement for superfluidity, it is not enough. The important ingredient transforming a quantum gas into a quantum fluid is the interaction among the particles. Indeed it is the key ingredient significantly complexifying the description of the system and motivating the quantum simulation approach to study it.

While some examples of quantum fluids are known from early days of quantum mechanics, they are still objects of intense research due to the rich physics stemming from strong interactions among the particles and due to the new details they might provide to shed light on better understanding of the many-body quantum physics.

More recently, thanks to the pioneering works on manipulation of atoms with lasers, impressive progress has been achieved in trapping the dilute ensembles of atomic alkali metal gases and cooling them down to to ultra-cold temperatures. At such small temperatures, the cold atomic gases become degenerate and acquire macroscopic coherence undergoing a phase transition, called Bose-Einstein condensation [118].

1.1.3 Quantum fluids of light

1.1.3.1 Requirements

Coherent and interacting photons: While cold atomic gases are commonly considered as a standard experimental platform for quantum simulation experiments, various alternative platforms emerge demonstrating promising results in this direction. Some of these platforms use light quanta, photons, as constituents of a macroscopic quantum system to perform quantum simulation. In fact, much larger experience of manipulating light as well as development of laser technology allows unprecedented experimental control, outperforming the cold atom systems. Firstly, being composed of photons which are quantum particles, the exploration of quantum-many body effects stemming from the presence of quantum fluctuations and correlations is possible. Secondly, having macroscopic coherence in case of laser illumination makes from light a well suited instrument for sumulation of quantum models which is more immune to decoherence than massive systems. Nevertheless, two problems arise for photons as particles in this way: the are mass-less and do not interact in free space until very high (currently exprerimentally unreachable) intensity threshold, known as the Schwinger limit [26]. Luckily, this is not the end of the story and thanks to recent advances in non-linear optical and micro-fabrication technology, there are solutions for both problems. Concerning the photon-photon interactions, it is known since the emergence of non-linear optics that photons can interact with each other indirectly, via the matter they polarize via its non-linear response. For example, second harmonic generation process inside a non-linear crystal can be interpreted as the interaction of two photons of an intense pump beam which get annihilated and give birth to a photon having the double frequency (in agreement with the energy conservation) of the pump photons.

Contact interactions-Kerr effect: However, as will be evidenced mathematically and physically interpreted in the next section, the analogy between quantum fluids (for instance cold atomic gases) having contact type interactions with light (photons) is only possible with a special type of optical non-linearity: the Kerr-effect. A medium with Kerr effect is a medium which has a light's intensity (photon density) dependent refractive index: $n = n^{(1)} + n_2 I$, with $n^{(1)}$ the medium's linear refractive index and n_2 the Kerr index, quantifying the strength of the non-linearity.

In fact, depending on the considered system and configuration, the efficiency (cross-section in a certain sense) of this interaction may be enhanced by multiple orders of magnitude with respect to the case of photons interacting in vacuum [29], making it possible to produce states of light with interacting photons in table-top laboratory experiments.

Several theoretical studies highlighted the possibility for light propagating in a Kerr medium to show analogue superfluid hydrodynamic effects [41, 58] back in the 90's. This idea was then developed by means of the quantization of the light field in a medium with Kerr type interactions, leading to its interpretation as a quantum fluid [32, 31].

Multiple experimental platforms aiming to produce strong and controllable photon interactions have been developed since then. The general strategy to enhance the optical non-linearity consists in either working with very high light intensities or increasing the light-matter interaction

strength. In fact, the stronger is the light-matter interaction, the lower laser intensities are required to induce the optical non-linearity.

Increasing light-matter cooperativity: Before listing the experimental platforms involved in production of quantum fluids of light, it is useful to discuss the general ideas involved in their engineering. Coupling between light and matter can first be enhanced by increasing the interaction time between the photons and the medium. This can be achieved either with media of large refractive index for cw illumination, or "slow light" media where an optical pulse is drastically slowed down due to steep spectral refractive index gradients or finally by putting the interacting medium inside an optical cavity: trapping the photons inside the cavity increases the effective time during which the photons "see" the medium, increasing therefore the interaction efficiency. Alternatively, the coupling between light and atoms can also be optimized by increasing the medium's optical depth via medium's density and using its optical resonances, which is the strategy used in this work.

1.1.3.2 Cavity configuration: exciton-polaritons

Strong coupling: Probably the most prominent example for an experimental platform using the cavity configuration to enhance coupling with light, is exciton-polariton in a microcavity. In semiconductor materials, as for example GaAs, bound states of electron-hole pairs, called excitons, are involved in the interaction with light. It is possible to fabricate a hybrid layered planar structure consisting of a central layer (of size of several microns or equivalently of the order of several optical wavelengths) of GaAs and surrounded from both sides by periodically arranged dielectric layers forming two Bragg mirrors around the central semiconductor layer [44]. Matching the cavity's and exciton's resonance frequencies (this condition is called the quasi-resonance in the polariton community), the resonant light entering the cavity interacts with semiconductor's excitons and during its multiple round trips between the dielectric mirrors gets absorbed and emitted many times due to this interaction, before leaving the medium typically after a period of time called the cavity lifetime. If the cavity lifetime is much larger than the typical interaction time estimated from the light-matter coupling rate, the so-called strong coupling regime is reached. Of course, this is a rather simplified picture of what happens, and more precise description is obtained by solving this system to find its eigenstates, corresponding to the stationary states of the system in the strong coupling regime. The result of this calculation was reported for the first time in [73] giving rise to a new mixed quasi-particle, called polariton. It can be written as a coherent superposition of a cavity photon and exciton. Thanks to its hybrid nature, polariton can still be seen as a quasi-particle of light due to its photonic component, but now it inherits the interactions and mass due to its excitonic component. These relatively strong interactions between the matter components (excitons) of polaritons induce indeed the polariton-polariton interactions which can also be interpreted as the optical Kerr nonlinearity between their photon components. Note that the strong coupling regime can be achieved not only in semi-conductors but also in a number of other material systems ranging from atomic gases to superconducting Josephson junctions (see [29], p.3), which will not be discussed here.

The state of the system can be probed with photons leaking out of the cavity. This also implies that unless being able to image the cavity plane with very high temporal resolution ($\sim$ ps), the imaged state of the system is rather its stationary state, obtained by the dynamic equilibrium between the pumping rate by laser and the cavity loss rate.

Polariton quantum fluids: Exciton-polaritons is the first hybrid photonic and solid-state platform in which Bose Einstein condensation was observed [83, 40]. It is however important to note that due to the driven-dissipative nature of polariton fluids, the observed BE condensation is not equivalent to the one reported in equilibrium systems and can rather be described as a phase transition in driven dissipative systems. The interactions within polariton condensates confer to this system the superfluidity, which has been observed in this system in [4] by studying the flow of a polariton fluid around a structural defect inside the cavity. Thanks to the progress in microfabrication of polariton cavities in form of pillars, it is possible to produce the polariton fluids in specific symmertries in the 2D geometry. This feature can be seen as an alternative to an optical lattice acting on ultracold atoms as an external potential, and is nowadays actively used to perform quantum simulation with polariton fluids. For example, simulation of periodic chains of atoms described by several quantum-mechanical Hamiltonians, is reported in [10, 78, 148]. More recently, polariton fluids have been also used to perform quantum simulation of a quasi-periodic lattice [61]. A very recent result demonstrates that the evolution of the phase in a driven-dissipative one-dimensional polariton condensate, being described by the Kardar-Parisi-Zhang model, follows a universal dynamics emerging in various fields of physics and observable via specific scaling laws in the phase correlation function. The latter was directly measured in [57] in a 1D polariton fluid.

Although massively used for quantum simulation experiments, exploration and characterisation of excitations emerging in polariton fluids in specific configurations is an important milestone in this platform. A very recent result reported significant progress in this direction, presenting an original angle-resolved coherent probe spectroscopy technique to study the dispersion of the excitation modes in a fluid of polaritons under resonant pumping [34].

Note that many very interesting and not less important results obtained with polariton fluids and other cavity based interactionless photon condensate platforms [87] were not be included in this short review. Interested reader is invited to consult more specialized literature for more details. The most extensive review including most existing experimental platforms is [29].

1.1.3.3 Cavityless propagating configuration

Despite tremendous success of the cavity based fluid of light platforms, one of their main drawbacks consists in the difficulty to probe system's evolution at various times. It is therefore sensible to consider alternative cavityless platforms in which the propagation direction z plays the role of time and the system's state at various times can be probed by simply imaging the various z positions. The simplicity of this approach consists in the fact that this configuration could be realized by shining light in any bulk $\chi^{(3)}$ medium. Moreover, in difference to the cavity based platforms which are by construction driven-dissipative (photons leaking the cavity are necessary to probe the system's state), the cavity-less platforms are "conservative", i.e. have

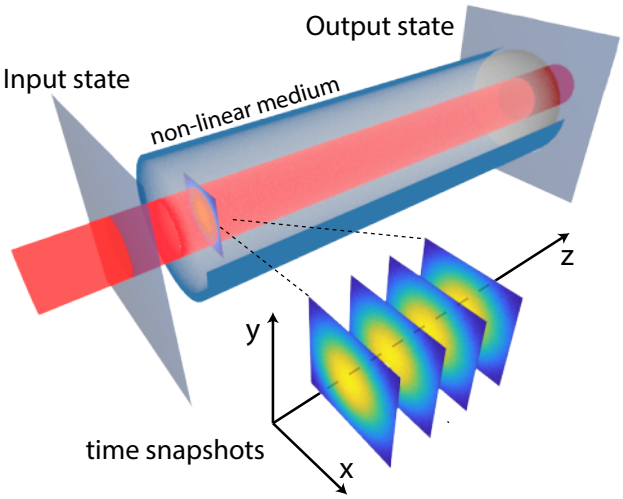

Figure 1.1: Schematic visualization of a fluid of light in the propagating geometry: A laser beam enters a non-linear Kerr medium and propagates inside it until reaching the exit plane. The propagation coordinate playing the role of time, the medium's input/exit plane corresponds to the the fluid's initial/final state in presence of the photonic Kerr interactions. Image adapted from [56].

conserved number of particles (in the absence of losses) and do not require additional pumping to compensate the medium losses. Taking the example of a Gaussian beam, the Kerr effect can be interpreted as the photon density dependent photon-photon (repulsion) attraction force in a plane perpendicular to the optical axis, resulting in its self-(de)focusing, depending on the sign of the Kerr index.

However in this regard two questions arise: how to enhance the interactions and how to give to photons the mass? While the response to the second question will be given in the next section during the derivation of the propagation equation, let's focus on the problematic of optimizing the photon interactions in cavityless propagating geometries and review the possible strategies as well as the recent progress in this direction.

Increase interaction time: Similarly to the cavity based platforms, the idea of increasing the light-matter coupling strength by increasing the interaction time can be exploited in the propagating geometry as well. This can be achieved with the "Slow light" strategy, consisting in slowing down the light inside the non-linear medium be means of refractive index engineering. For instance, for the cw illumination, the speed of light inside a medium is reduced by a factor equal to the medium's refractive index and therefore increasing the latter would help to increase the interaction time. However, this seemingly simple idea is hard to realize because producing a transparent material with large refractive index (say, $n^{(1)} = 10$) is currently a long standing and unsolved issue. In contrast to the cw case, the group velocity of a pulse depends strongly on the spectral variation of the refractive index via the so called group index: $v_g = c/n_g$ with $n_g(\omega) = n^{(1)} + \omega.dn^{(1)}/d\omega$. The latter can be engineered, for example, by means of the electromagnetically induced transparency (EIT) in three-level media [70], slowing the light by multiple orders of magnitude inside the medium.

The idea of using the EIT effect to increase the efficiency of the photon-photon interactions has attracted much attention over the last decades and is explored by multiple groups across the World in the Rydberg excitation regime [85], i.e. in atomic media excited to states with high principal numbers. The advantage of working with Rydberg atoms resides in strong dipole-dipole interactions [166] in these systems. Many of these works focus on this platform's possible application for quantum simulation [157] but not yet much on the possible superfluid and hydrodynamic behavior of light.

Well known Kerr media: photorefractive crystals and thermo-optic liquids: On the contrary, the hydrodynamic and superfluid-like behavior of light in cavity-less configuration has been experimentally investigated in well known materials presenting the Kerr non-linearity: photorefractive crystals [155, 80, 147, 103, 48], thermo-optic media [14, 163, 24]. In these media additional effects, such as the space-charge separation in case of the photorefractive crystals [22] and the enhanced absorption via added graphene particles in case of thermo-optic media are involved which should in presence of high light intensity modify the local refractive index of the considered host medium.

Atomic optical resonance for optical non-linearity: Another more recent approach successfully employed for the study of the fluids of light is dense atomic Rubidium vapor [54, 165, 56, 9, 119, 18]. The idea in using this type of media resides in exploiting the strong light-matter interaction arising from the optical resonances of the valence electron's transitions. The photon-photon interactions at relatively low intensities due to the saturation of the medium, and various atomic and laser parameters can be used as powerful knobs to tune and control these interactions, as will be described in details in the following chapters.

1.1.3.4 State of the art: fluid of light experiments in Kerr media

Optical hydrodynamics: For instance, in [155, 14, 9, 18], the nonlinear hydrodynamical behavior in a locally disturbed fluid of light was evidenced with the observation of dispersive and dissipationless shock waves. More quantitative analysis of the shock behavior in hot atomic vapor based fluids of light is reported in [18]. Still in link with hydrodynamics, the Rayleigh-Taylor Instability was observed in a photorefractive crystal based fluid of light [80].

Superfluidity and dispersion measurement: Despite the significance of these results, the observation of non-linear hydrodynamics with light is not enough to prove the superfluidity of light. In fact, the superfluidity can primarily be evidenced by observing the dispersion of small density perturbations, respecting the Landau criterion for superfluidity. Alternatively, most convincing demonstration of superfluidity is the observation of the fluid's loss-less flow around an obstacle. Several recent experiments succeeded in measuring the Bogoliubov dispersion relation, well known in cold atomic superfluids, for light in hot Rubidium vapors [54, 56, 119] Three different measurement methods were developed in these experiments. In [54] the dispersion was calculated from the group velocity measurement, in [56] via the phase velocity measurement of the small perturbations added on top of a background fluid, and finally in [119] an analogue of the Bragg spectroscopy technique [144, 138] was realized, well known in the cold atomic Bose-Einstein Condensate community.

Superfluid flow observation: Superfluid to normal fluid transition in light propagating inside photorefractive crystals, was studied in [103], demonstrating the onset of superfluidity with the suppression of scattered fraction of fluid flowing past an optically imprinted obstacle. More recently [48], the influence of the obstacle size on the fluid's resulting phase diagram was studied identifying turbulent structures in form of optical vortices at the wake of the defect.

Pre-condensation of light: Finally the question of pre-condensation or kinetic condensation for light was addressed in a photorefractive crystal based fluid of light [147] and more recently in a hot atomic vapor based fluid of light [165]: the interaction driven emergence of the non-zero average field for a spatially incoherent input state (fully developed speckle) was retrieved from the momentum distribution measurement in [147] and from the measured speckle intensity statistics in [165], where it was interpreted as the "condensed" fraction of light.

Conclusion: In this discussion various existing experimental platforms for creation and study of the fluids of light were reviewed along with the explanation of general ideas behind their engineering and citation of recent experimental results. In particular cavity based platforms were compared with the propagating geometry platforms. This work was performed with hot atomic vapor mediated fluids of light, therefore in the following section I describe in more details the formal analogy between propagating light and a superfluid with short-range contact interactions evolving in time.

1.2 Fluid of light in the propagating geometry

In this section the propagation equation for the electric field envelope in a Kerr medium is derived for cw and pulsed illuminations. The results are compared with the 2D and 3D Gross-Pitaevskii equation, which is the mean-field evolution equation of superfluids with contact interactions. It is then explained how optical quantities can be mapped to the corresponding quantum fluid parameters elucidating the concept of quantum fluids of light in propagating geometries. The second subsection explains why a fluid of light propagating in a Kerr medium generally undergoes a nonequilibrium evolution and why the propagating geometry is a well-suited configuration for the exploration of nonequilibrium physics of quantum fluids. The nonequilibrium aspects of the phenomena studied in this work are briefly described. Finally, several recent works on the exploration of nonequilibrium evolution in closed quantum systems is reviewed, drawing the reader's attention on main motivations and challenges of this field.

1.2.1 Propagation equation

1.2.1.1 CW laser: 2D fluid of light

In this section I derive the propagation equation for continuous wave light's transverse electric field's complex envelope in a Kerr medium and link it with the Gross-Pitaevskii equation describing a quantum fluid with contact interactions among the particles. Starting with the

Maxwell's equations for the total electric field $\mathbf{E}(\mathbf{r},\omega)$, we have:

$$\nabla \times \nabla \times \mathbf{E}(\mathbf{r},\omega) = \frac{\omega^2}{c^2}(1+\chi(\mathbf{r},\omega))\mathbf{E}(\mathbf{r},\omega) \tag{1.1}$$

where $\times$ stands for the cross product, the medium's total susceptibility $\chi(\mathbf{r},\omega) = \chi^{(1)}(\mathbf{r},\omega) + \chi^{(3)}(\omega)|\mathbf{E}(\mathbf{r},\omega)|^2$ is supposed real for simplicity and represents the sum of its linear $\chi^{(1)}(\mathbf{r},\omega)$ and non-linear (intensity dependent) $\chi^{(3)}(\omega)|\mathbf{E}(\mathbf{r},\omega)|^2$ parts. The former is generally allowed to depend on space due to a possible additional spatial inhomogeneity: $\chi^{(1)}(\mathbf{r},\omega) = \chi^{(1)} + \delta\chi^{(1)}(\mathbf{r},\omega)$ of (intensity independent) refractive index representing an external potential, which may, for example, confine the light within a given region of space as in case of guided light inside optical fibers. Assuming propagation in an isotropic medium the susceptibility is supposed scalar and the field's polarization unchanged. Working within the weak guidance and the paraxial approximations the double curl may be simplified to a laplacian: $\nabla \times \nabla \times \simeq -\nabla^2$, resulting in:

$$\nabla^2\mathbf{E}(\mathbf{r},\omega) = -\frac{\omega^2}{c^2}(1+\chi(\mathbf{r},\omega))\mathbf{E}(\mathbf{r},\omega) \tag{1.2}$$

The field consists of the laser's angular frequency ω_L centered carrier plane wave modulated by its envelope. Within the considered polarization mode, the field reads:

$$E(\mathbf{r}) = \frac{1}{2}\mathcal{E}(x,y,z)\mathrm{e}^{ik_L z} + \text{c.c.} \tag{1.3}$$

where $k_L = n^{(1)}\omega_L/c = 2\pi/\lambda$, with λ the laser's central wavelength inside the considered medium and $n^{(1)} = (1+\chi^{(1)}(\omega_L))^{1/2}$ the mediums linear refractive index. Inserting the product (eqn. 1.3) into eqn. 1.2 the evolution equation for the field's envelope is derived. Decomposing the Laplacian into its transverse and longitudinal parts $\nabla^2 = \nabla_\perp^2 + \partial_z^2$, let's first compute the longitudinal derivative:

$$\frac{\partial^2 E}{\partial z^2} = \left(\frac{\partial^2\mathcal{E}}{\partial z^2} + 2ik_L\frac{\partial\mathcal{E}}{\partial z} - k_L^2\mathcal{E}\right)\mathrm{e}^{ik_L z} \simeq \left(2ik_L\frac{\partial\mathcal{E}}{\partial z} - k_L^2\mathcal{E}\right)\mathrm{e}^{ik_L z}. \tag{1.4}$$

Field envelope's second derivative in z can be neglected with the slowly varying envelope approximation. One can now use the dispersion relation: $k^2 = [1+\chi^{(1)}(\omega)]\omega^2/c^2$ to simply rewrite the eqn. 1.2 for the field envelope:

$$i\frac{\partial\mathcal{E}}{\partial z} + \frac{1}{2k_L}\nabla_\perp^2\mathcal{E} = -k_0\frac{\delta\chi^{(1)}(\mathbf{r},\omega)}{2[1+\chi^{(1)}(\omega)]}\mathcal{E} - k_0\frac{\chi^{(3)}(\omega)}{2[1+\chi^{(1)}(\omega)]}|\mathcal{E}|^2\mathcal{E} \tag{1.5}$$

With $k_0 = \omega_L/c$. The paraxial propagation regime is valid as long as both left hand side terms are small with respect to one [28]. The eqn. 1.5 is called the Non-Linear Schrödinger Equation (NLSE) and is indeed formally analogous to a Schrödinger equation with an extra non-linear term, written for a macroscopic quantum wave-function (i.e. the wavefunction of the state

massively occupied in a system with large particle number):

$$i\hbar\frac{\partial\psi}{\partial t} + \frac{\hbar^2}{2m}\nabla_\perp^2\psi = V(\mathbf{r})\psi + g|\psi|^2\psi \tag{1.6}$$

In this equation V is a potential acting, for example, as a trap, confining the system at a given location, or as an obstacle on the system's trajectory. The non-linear term accounts for the two-body contact interactions within the mean-field approximation. This description is valid for Bose Einstein Condensates of dilute ultra-cold atomic gases with moderate interactions behaving as superfluids and is commonly called the Gross-Pitaevskii Equation (GPE) [121]. Indeed, the NLSE (eqn. 1.5) is mathematically analogous to the GPE (eqn. 1.6) and several aspects of this analogy require special attention:

- **Time:** the time coordinate of the eqn. 1.6 is replaced by the light's propagation direction z. This fact has deep consequence in the interpretation of light as an analog quantum fluid: the former is analogous to a 2D quantum fluid, living in the plane transverse to the propagation direction, whose various evolution steps in time are simply accessible at different values of the propagation coordinate inside the non-linear medium. Therefore the z coordinate of a fluid of light plays the role of an effective time and the system's state at various times can be accessed by imaging the field's map at the medium's various z planes. In particular, the system's final state is the one corresponding to the cell's exit plane.

- **Mass:** one can also remark the absence of the Planck's constant in the NLSE and the mass in the kinetic energy term replaced by a quantity proportional to the laser wavevector k. While strict analogy is obtained by defining a photon mass as: $m_{Ph} = \hbar k_L/c$, its interpretation from an optician's perspective is also straightforward: the laplacian term in the NLSE, which plays the role of the "kinetic energy" of a quantum fluid, stems from diffraction and expresses the Heisenberg's uncertainty principle, which links the wave function's widths in spatial and momentum domains:

  $$\Delta x\Delta p \geq \frac{1}{2} \quad \text{with: } p = k_L\Delta\theta \tag{1.7}$$

  where $\Delta\theta$ is the typical width of beam's angular dispersion. According to this principle, the more one increases the spatial resolution of photons in a system, the larger becomes the uncertainty on their momenta, meaning that for a fixed typical length scale within a beam, the typical momenta of the photons will drop as the photon mass k increases or, in other words, a beam diffracts more as its laser wavelength increases.

- **Potential:** as discussed with an intuitive picture of guided light inside optical fibers, the spatial refractive index inhomogeneity acts as an external potential, such that its gradient is proportional to a force acting on the beam of light. Comparing the NLSE (eqn. 1.5)

with the GPE (eqn. 1.6), one can give the potential's mathematical expression:

$$V(\mathbf{r}) = -k_0 \frac{\delta\chi^{(1)}(\mathbf{r},\omega)}{2[1+\chi^{(1)}(\omega)]} = -k_0\delta n(\omega) \tag{1.8}$$

with the last equality defining the spatially dependent part of the linear refractive index. To get an expression for a potential having dimension of energy one needs to multiply the eqn. 1.8 by $\hbar c$. While none of the experiments performed in this work contained an external potential, it may be useful to estimate its order of magnitude currently attainable in our experiments: for $k = 2\pi/0,78.10^{-6}$ m^{-1}, $\delta n \simeq 10^{-4}$, one gets: $V \simeq 2.10^{-4}$ eV.

- **Interactions:** Finally the last term of the NLSE is probably the most important one, since it transforms a gas of independent photons into a fluid of light. Again, comparing the NLSE and the GPE one can express the photonic contact interaction constant as function of the non-linear part of the susceptibility:

$$g = -k_0 \frac{\chi^{(3)}(\omega)}{2[1+\chi^{(1)}(\omega)]} \tag{1.9}$$

As for the external potential, to get the interaction energy this quantity needs to be multiplied by $\hbar c$. While the magnitude of g determines the interaction strength, its sign reveals whether the interactions are repulsive or attractive. If g is positive, the interactions are repulsive while negative g results in attractive interactions. Recalling that the squared amplitude of the field is proportional to the light's intensity, one can get a comprehensive interpretation of the interaction term: with $g > 0$, taking an example of a Gaussian beam, the interaction energy has large values at the regions with high laser intensity and low values where there is no light. This results in a force pushing photons towards the low energy regions, i.e. away from the beam centre. This phenomenon can be easily realized in any medium with $\mathrm{Re}\{\chi^{(3)}\} < 0$ and is called self de-focusing. The opposite situation happens if $g < 0$ ($\mathrm{Re}\{\chi^{(3)}\} > 0$) and is called self-focusing. Note that all experiments in this work were performed in the self-defocusing regime, in order to avoid the modulational instability effect arising in the self-focusing case [96].

It is important to note that the derivation performed in this section is valid for cw illumination and reveals that in this case the fluid of light is bi-dimensional with the propagation direction playing the role of time.

1.2.1.2 Pulsed laser: a 3D fluid of light

While the model presented in the previous section is valid for the cw illumination, switching to the pulsed illumination requires taking into account some additional effects. Before going into details let's recall that the electric field envelope now depends on time:

$$E(\mathbf{r},t) = \frac{1}{2}\mathcal{E}(\mathbf{r},t)\mathrm{e}^{ik(\omega_L)z - i\omega_L t} + \text{c.c.} \tag{1.10}$$

The corresponding Fourier transform in time reads:

$$E(\mathbf{r},\omega) = \frac{1}{2}\mathcal{E}(\mathbf{r},\omega-\omega_L)\mathrm{e}^{ik(\omega_L)z} + \text{c.c.} \tag{1.11}$$

In difference to the previous case where the electric field envelope contained a single frequency component at $\omega = \omega_L$, now various spectral components present in $\mathcal{E}$ may be affected by dispersion, i.e. dependence of the refractive index $n^{(1)}$ on frequency. This means that starting from the eqn. 1.2 and using the eqn. 1.4, one gets now (supposing no external potential for simplicity and neglecting as in section 1.2.1.1 the field envelope's second derivative in z with the slowly varying envelope approximation):

$$i\frac{\partial\mathcal{E}}{\partial z} + \frac{1}{2k_L}\nabla_\perp^2\mathcal{E} + \frac{1}{2k_L}\left[k^2(\omega) - k_L^2\right]\mathcal{E} + g|\mathcal{E}|^2\mathcal{E} = 0. \tag{1.12}$$

Note that for this derivation we suppose the linear refractive index $n^{(1)}(\omega)$ contained in $k(\omega)$ frequency dependent and that g does not depend on frequency, (the last assumption can be reformulated as: the spectrum of g is much "flatter" than $n^{(1)}$'s spectrum, this can obviously be wrong for some non-linear media). To obtain the propagation equation in time domain this equation has to be back Fourier transformed, resulting in the most general case in a complicated convolution product of the field envelope with the medium's linear response function. Nevertheless a considerable simplification can be achieved, noticing that for optical pulses the bandwidth $\Delta\omega$, defined as the width of $\mathcal{E}(\omega-\omega_L)$, is usually much smaller than the central wavelength ω_L. This suggests that only the refractive index behavior in close vicinity of the ω_L carrier frequency will affect the propagation. One can assume this spectral variation of the refractive index sufficiently small within $\Delta\omega$ or equivalently, $[k(\omega)-k_L)]/k_L \ll 1$, to write: $[k^2(\omega)-k_L^2] \simeq 2k_L[k(\omega)-k_L)]$ (see [23], p.379). This is why dispersion effects on optical pulses are usually considered by expanding the wavevector $k(\omega)$ around ω_L. Performing the expansion up to the second order in $\delta\omega/\omega_L = (\omega-\omega_L)/\omega_L$, one gets:

$$\frac{1}{2k_L}\left[k^2(\omega) - k_L^2\right] \simeq \frac{\partial k}{\partial\omega}\delta\omega + \frac{1}{2}\frac{\partial^2 k}{\partial\omega^2}\delta\omega^2 \tag{1.13}$$

Defining the group velocity of the pulse $v_g(\omega_L) = (dk/d\omega)^{-1}$ and the group velocity dispersion (GVD) $D_0(\omega_L) = d^2k/d\omega^2$ (both evaluated at ω_L), one gets:

$$i\frac{\partial\mathcal{E}}{\partial z} + \frac{1}{2k_L}\nabla_\perp^2\mathcal{E} + \frac{1}{v_g}\delta\omega\mathcal{E} + \frac{1}{2}D_0\delta\omega^2\mathcal{E} + g|\mathcal{E}|^2\mathcal{E} = 0 \tag{1.14}$$

One can now go back to the time-domain by noting that upon the inverse Fourier transform "$\times\delta\omega$" becomes $-i\mathrm{e}^{i\omega_L t}\partial_t$:

$$i\frac{\partial\mathcal{E}}{\partial z} - i\frac{1}{v_g}\frac{\partial\mathcal{E}}{\partial t} + \frac{1}{2k_L}\nabla_\perp^2\mathcal{E} - \frac{D_0}{2}\frac{\partial^2\mathcal{E}}{\partial t^2} + g|\mathcal{E}|^2\mathcal{E} = 0 \tag{1.15}$$

Note that the non-linear term stays unchanged after the inverse Fourier transform. This is obviously an approximation but can be justified by the fact that being given the pulse bandwidth $\Delta\omega$ of $\mathcal{E}(\delta\omega)$, the former becomes narrower for $|\mathcal{E}(\delta\omega)|^2$ and can therefore be approximated by its spectral value at ω_L. This approximation amounts to a physical interpretation that the non-linear response of the medium is much faster than the intensity variation due to the pulse bandwidth, or in other words, the medium's non-linear response is instantaneous.

Interpretation of the new terms: As the result of including the effect of dispersion via the second order expansion of the wave vector with respect to frequency, two new terms with first and second time derivatives have appeared in the propagation equation of the electric field envelope. The term proportional to the first derivative in time shifts the pulse in time at speed v_g. In fact in the lab frame the wave packet of the pulse moves at the speed v_g. The term proportional to the second derivative in time acts similarly as the transverse laplacian but in time dimension, i.e. it induces the broadening of the pulse during propagation due to dispersion, or induces the beam's diffraction in time with an "effective mass" given by the inverse of the spectral curvature of the refractive index. In fact from this point of view, the time can be regarded as a third spatial dimension, this idea will be elaborated later in the discussion.

Comoving frame: The eqn. 1.15 can be simplified by switching to the so-called "comoving" frame, i.e. a reference frame in which the pulse is immobile. Here I choose to "follow" the pulse in time by defining a variable substitution: $z' = v_g t + z$ and $\tau = z/v_g$. Then the first order derivatives become:

$$\frac{\partial}{\partial z} = \frac{1}{v_g}\frac{\partial}{\partial \tau} + \frac{\partial}{\partial z'} \quad \text{and:} \quad \frac{\partial}{\partial t} = v_g \frac{\partial}{\partial z'} \tag{1.16}$$

Resulting in the following propagation equation in the comoving frame:

$$\frac{i}{v_g}\frac{\partial \mathcal{E}}{\partial \tau} + \frac{1}{2k_L}\nabla_\perp^2 \mathcal{E} - \frac{v_g^2 D_0}{2}\frac{\partial^2 \mathcal{E}}{\partial z'^2} + g|\mathcal{E}|^2\mathcal{E} = 0 \tag{1.17}$$

This is the evolution equation for an optical pulse in a comoving frame with respect to the effective time, defined as the ratio between the propagation direction and the group velocity of the pulse, evolving in a three dimensional space described by the (x, y, z') coordinates. However, in this three dimensional case, the fluid's mass in its third dimension $m_{z'} = -1/(v_g^2 D_0)$ generally differs in magnitude (sometimes even in sign) from its mass m in other directions. Nevertheless, it is possible to "correct" this anisotropy via contraction/extension of the third dimension by a factor: $\sqrt{m/m_{z'}} = \sqrt{k_L v_g^2 D_0}$. In this case one gets an equation analogous to a 3D Gross Pitaevskii Equation:

$$\frac{i}{v_g}\frac{\partial \mathcal{E}}{\partial \tau} + \frac{1}{2k_L}\nabla^2 \mathcal{E} + g|\mathcal{E}|^2\mathcal{E} = 0 \tag{1.18}$$

with this time a three-dimensional laplacian. Note that the performed rescaling makes physical sense only in the $D_0 < 0$ case, giving a positive mass, because otherwise $\sqrt{m/m_{z'}}$ becomes imaginary complex, which is much more complicated to interpret. In conclusion, an important aspect of the derivation revealed the dimensionality of the system: working with cw illumination

one gets a 2D fluid of light while with pulsed illumination and in a medium with appropriate optical characteristics the fluid of light becomes three-dimensional.

1.2.2 Out of equilibrium evolution

Propagating geometry is naturally out-of equilibrium: In the previous section formal analogy has been established between the propagation of light in Kerr media and Bose-Einstein condensates with contact interactions in 2 and 3 dimensions. A very important conclusion from the derivation highlights that the propagation coordinate plays the role of time. This implies that in the propagating geometry a perturbed system's evolution at various times can be probed by measuring its state at various propagation distances z, making it possible to study the fluid of light's out-of-equilibrium dynamics. This leads us to a very important aspect explored in most experiments of this work, if the nonequilibrium evolution is regarded from a general perspective of quantum many-body systems.

From equilibrium to nonequilibrium descriptions: The description of macroscopic classical systems usually relies on a small set of macroscopic variables, defining the system's state. While it is possible to link the system's microscopic details to its macroscopic state with statistical physics tools, an important assumption commonly employed in various treatments consists in supposing the system in thermal equilibrium, allowing to establish the system's equation of state, i.e. the relation linking the system's macroscopic parameters. Moreover, statistical methods also allowed to reach significant progress in understanding various mechanisms for nonequilibrium systems to evolve towards equilibrium. These methods may also involve an external reservoir with which the system can exchange particles or energy to reach a state of thermal equilibrium, while the latter is implicitly assumed in thermal equilibrium. If one avoids invoking an even larger reservoir to thermalize the system under study, a fundamental question naturally arises on whether a single, isolated many-body system can evolve in such a way that it reaches an (apparent) thermal equilibrium state [94].

Understanding the nonequilibrium many-body quantum systems: In fact, despite the progress made in the past for classical systems, there are no rigorously justified generalizations of any of these approaches to generic quantum nonequilibrium systems [122]. It is thus not obvious that the theoretical study of the dynamics of simplified models would accurately describe experiments of more complex systems [122]. In addition there are fewer available tools for analyzing dynamics of even simple interacting models [122]. For the moment, in this respect cold atomic gases and nanostructures make possible what would be arduous otherwise: a fruitful comparison between nonequilibrium theories based on simple models and carefully designed experiments with tunable system parameters [122].

Finding systematic ways to understand the nonequilibrium physics of interacting systems is not only of fundamental importance, but could also be crucial for future technologies [122]. A quantum computer, for example, will definitely require the capability of performing real time manipulations of interacting quantum systems [122].

How to access the nonequilibrium regime? While ultra-cold atomic gases emerge as a possible

testbed for investigating nonequilibrium behavior of many-body quantum systems, it is useful to describe how this system can be driven out-of-equilibrium. The general idea is the following: the system's initial state is prepared, and then the Hamiltonian of the system is rapidly changed such that the initial state is not anymore the new Hamiltonian's eigenmode. If these changes or perturbations of the system are performed very quickly with respect to the other relevant timescales, it is referred to as a quench [136]. Since two important control knobs of the Hamiltonian are the external potential and its inter-particle interactions, a rapid variation of any of these terms results in a nonequilibrium state of the system, whose evolution can then be studied. It is an open question whether a steady state emerges and if so, what the properties of this state are [94].

Away from equilibrium with interaction quench: If we assume that some isolated quantum systems can appear (for all practical purposes) thermalized, the next important question is how the thermalization proceeds. For example, there might be partial relaxation only, where instead of a complete loss of memory of the initial state, the system only partially forgets the initial conditions [94]. First experimental results in this avenue have recently been reported in [92, 93] in an interacting 1D ultracold quantum gas. The nonequilibrium aspect of the system consists in preparing the it at finite small temperature and turning on the interactions. The prepared state evolves under the effect of the new Hamiltonian showing that the relaxation towards equilibrium follows a local scenario, with phase correlations approaching the equilibrium case result within the dynamically evolving light-cone of the system's elementary excitations.

In another experiment, [75], a 2D atomic superfluid was prepared by loading a quantum degenerate sample of bosonic ^{133}Cs atoms into a highly oblate trap. The system was then taken out of equilibrium by suddenly changing (or quenching) the interaction strength. The subsequent evolution of the nonequilibrium state showed two aspects: at long timescales, the system adjusted its overall density profile to the new interaction energy [94], while at shorter timescales, density fluctuations in the cloud, stemming from the interaction quench, behave as synchronized spectrally multi-component sound waves. giving rise, as the result of their interference, to a multi-peak structure in the system's spatial density spectrum. The authors also linked their observation to the Sakharov oscillations, known in the context of cosmology as the consequence of the quantum fluctuations during the inflation of the early Universe [75]. These fluctuations give rise to similar peak in the angular power spectrum of the cosmic microwave background, also called "acoustic peaks". This experiment shows that nonequilibrium quantum fluids can also be used as lab-scale analogues to reproduce cosmologic [75] or analogue gravity [145] models.

Finally, one can note that the non-linear hydrodynamic behavior of superfluids can be studied by preparing an initial state with strongly perturbed density, for example, before switching on the interactions. Strong density perturbations were reported [72] to result in shock waves in an atomic BEC.

Away from equilibrium with external potential quench: As mentioned above, a second control knob commonly used for driving a many-body quantum system out-of-equilibrium is the external potential. In case of ultracold atoms trapped in optical lattices the control of the ex-

ternal potential is straightforward. For example, the lattice depth can be changed either nearly instantaneously or by a continuous, but still fast, sweep across a phase transition [136]. In fact, changing the lattice depth from the deep Mott-insulator regime to the shallow superfluid gives access to the phase coherence dynamics of the system [136, 64].
Alternatively, it is also possible to drive the system Hamiltonian periodically in time. Inspiring from the classical case, where such modulation gives rise to new equilibrium states, typically inaccessible in the equilibrium systems, as for example the Kapitza-Dirac pendulum [158], new phenomena, arising from such periodic modulation are being investigated for quantum systems, resulting over the last decade in a new field of research: "Floquet engineering" [158].

1.2.3 Parallel with fluids of light: outline of this work

After the short review of recent progress in exploration of nonequilibrium systems in atomic superfluids, it now makes sense to come back to the fluids of light in propagating geometry and highlight how some nonequilibrium aspects of of its evolution can readily be investigated, making the link with the experiments presented in this work.
First of all, the fluid of light's initial state is prepared by shaping the laser beam at the medium's entrance plane. This can be achieved by conventional optical beam shaping elements (collimation lenses, beam-splitters, mirrors and single mode optical fibers), as well as with Spatial Light Modulators (SLMs) or Digital Micromirror Devices (DMDs).

Experimental platform details: control knobs

In the next chapter 2 I present the details of hot Rubidium vapors which is the non-linear medium used in all the experiments, as well as the laser excitation and detection tools used throughout the work. The photon-photon interactions are instantaneously switched on as soon as the beam enters the non-linear medium, acting as an interaction quench.

Measurement of interactions

Further on the fluid of light evolves in presence of the Kerr-effect mediated photon-photon interactions. The chapter 3 is devoted to investigation and measurement of the Kerr effect in hot (dense) Rubidium cells. Main experimental discussion focuses on the spatially inhomogeneous non-linear phase acquired by a Gaussian beam after propagation in hot Rubidium vapor. Two methods, based on off-axis interferometry, to measure it are presented. The experimental results of the non-linear refractive index variation measurement in hot Rubidium vapors are then presented, revealing the strong beam size and time dependence of the non-linearity, providing additional information for its accurate modeling.

Blast waves

Preparation of an initial state with strong density gradients favors the emergence of non-linear hydrodynamic behavior of the fluid of light. Such behavior is studied in chapter 4 of this work within a broad context of shock waves in order to observe and investigate a special type of waves called blast waves in two different dimensional geometries.

Response of quantum fluctuations to interaction quenches

The final state of the system is usually probed at the medium's exit plane. But recalling the

analogy between the propagation direction z and the fluid's time, this interface can also be interpreted as the point in time at which the photon-photon interactions are quenched to zero. Therefore a fluid of light, propagating in a slab of non-linear medium inevitably undergoes two interaction quenches [96] and analyzing the optical fluid's state in a plane after the second quench should give access to the fluid's corresponding short time response. This response was measured for the fluid of light's quantum fluctuations stemming from the laser shot noise, and the corresponding experiment is described in details in chapter 5.

Pre-thermalization

Finally, the question of the possible relaxation towards equilibrium of weakly nonequilibrium states prepared by superimposing of a coherent background with weak speckle (mimicking thermal fluctuations in an atomic superfluid) is addressed in chapter 6. The evoulution of such states in presence of photonic interactions was investigated and characterized via its spatial coherence, demonstrating the pre-thermalization. The corresponding experiment is presented in details in chapter 6.

Chapter 2

Presentation of the system

In all experiments presented in this thesis, hot Rubidium vapor cells were used to produce fluids of light. This chapter is devoted to the description of this experimental platform, discussion of its available control knobs, as well as to listing the lasers and the photodiodes/ cameras used for production of a fluid of light and its detection, respectively.

2.1 Why hot Rubidium cells?

A bit of history and context: Alkali metal vapors are used for decades in quantum optics experiments. Although they are also among first media intensely investigated for spectroscopic studies, the relative simplicity in their manipulation, as well as the wide range of tunable parameters in these systems still makes them commonly used media for research in quantum/nonlinear optics. Typical optical response of an alkali atom appears as a series of relatively narrow (up to several Gigahertz large) compared to solid state materials (with typical linewidths of multiple nanometers or thousands of GHz) absorption lines which can be attributed to various transitions of the (single) valence electron and can be easily addressed by a laser with stable and well resolved (typically up to the MHz range) frequency. Narrow spectral variation of extinction coefficient is accompanied by a strong index variation in agreement with the Kramers-Kronig relations.

Saturation induced Kerr effect in atomic vapors: global picture: The strategy used in this work to produce the Kerr-type photon-photon interaction consisted in using the line saturation, i.e. depletion of the medium's susceptibility under the effect of large light intensity (photon density). The optical saturation is usually presented as the laser intensity dependent reduction of absorption, corresponding to the reduction of the imaginary part of medium's susceptibility. However, same holds for the susceptibility's real part, responsible for the medium's refractive index. As will be shown in the next chapter, for the near resonant light in dense atomic vapors, the intensity dependence of the refractive index is noticeable over a broader spectral range than that of the absorption coefficient. The refractive index variation with laser intensity is linear for moderate intensities (below the saturation intensity), corresponding well to the the Kerr effect, but ends up saturating as in the limit of infinite laser intensity the medium becomes

transparent or equivalently, the medium's susceptibility drops to zero.

Want to increase interactions? Increase the linear refractive index! The maximal photon interaction strength which is given by the maximal possible refractive index variation, corresponds hence to half the real part of the linear susceptibility. This means that in order to increase the former one needs to increase the real part of the linear susceptibility. For this one can first use its frequency dependence due to the atomic resonance. Indeed, approaching the *laser frequency* to the transition frequency, the vapor's refractive index difference with respect to vacuum, $n^{(1)} - 1$, increases. This obviously happens at the expense of increasing the absorption rate, which does not allow to approach too close to the resonance frequency, preventing the light from being transmitted. More generally, a key parameter quantifying the strength of light-matter interaction, is the optical depth OD, defined as the on-resonant $OD = -\log(\mathcal{T})$ with $\mathcal{T}$ power transmission through the medium. For hot atomic vapors the on-resonant OD can reach the value above 10^3. It can be well increased by means of a second experimentally largely tunable parameter: the *atomic density* controlled via the vapor temperature, as will be shown later in this chapter. But in order to better understand the effect of the control parameters, the linear susceptibility in hot Rb vapor needs first to be derived, and this is the goal of the next section.

Linear susceptibility: practical utility: Before the derivation, it is important to remark, that from the practical point of view, the knowledge of the linear susceptibility, with its easily measurable imaginary part, is used to determine the vapor density (or equivalently the vapor temperature) and calibrate the laser frequency, as will be explained in details later. These are, in turn, the relevant parameters, controlling the photon-photon interaction strength, as will be shown in the next chapter 3, therefore their most precise determination is necessary for the optimal control of the photonic interactions.

2.2 Linear susceptibility of hot Rubidium vapors

In this section the linear susceptibility of hot Rb vapor at the D2 line (780.24 nm) is derived based on a two-level system model. The model is then generalized to take into account all the Doppler effect broadened hyperfine transitions of the D2 line as in [140] and the resonant collisional broadening [160], which becomes relevant in the dense vapor regime typical above the experimental temperatures of around 150 °C.

2.2.1 Two level system

Atomic density matrix: Probably the most simple quantum mechanical model, known as a two-level system driven by/coupled to an external field is the major building block for deriving the linear optical susceptibility. Calling the ground state $|g\rangle$ of zero energy and the excited state $|e\rangle$ with energy $\hbar\omega_{eg}$ (with $\omega_{eg} > 0$), we can first construct an atomic density matrix

$\hat{\rho}_A = |\psi_A\rangle\langle\psi_A|$, corresponding to the atomic state $|\psi_A\rangle$ in the $\{|g\rangle,|e\rangle\}$ basis:

$$\hat{\rho}_A = \begin{pmatrix} |\langle g|\psi_A\rangle|^2 & \langle g|\psi_A\rangle\langle\psi_A|e\rangle \\ \langle e|\psi_A\rangle\langle\psi_A|g\rangle & |\langle e|\psi_A\rangle|^2 \end{pmatrix} := \begin{pmatrix} \rho_{gg} & \rho_{ge} \\ \rho_{eg} & \rho_{ee} \end{pmatrix} \tag{2.1}$$

Atomic optical susceptibility: The knowledge of the atomic density matrix is not only useful for the evaluation of the atomic state but also for the calculation of the quantum average values of any observable linked with the atomic state, in particular the atomic electric dipole **d**. The average of the latter is linked with the optical susceptibility χ via:

$$\mathbf{P} = N\langle\mathbf{d}\rangle = \mathrm{Tr}[\hat{\rho}_A.\ \mathbf{d}] = \epsilon_0\chi\mathbf{E} \tag{2.2}$$

where **P** is the medium's average polarization per unit volume and N the atomic number density. In the absence of an electric field $\langle\mathbf{d}\rangle = 0$ for neutral Rb atoms. Therefore this quantity needs first to be calculated in presence of a laser field in order to deduce then the atomic optical susceptibility.

Light-matter coupling: electric dipole of a transition: Rubidium atom interacts with an external electric field via its valence electron's electric dipole. Since the dipole is induced (not permanent), the dipole operator's only non-zero components are those which couple states of opposite parity under the effect of local electric field, i.e. $\hat{d} = d_{ge}|g\rangle\langle e| + d_{eg}|e\rangle\langle g|$. Although it is in general a vectorial operator, the interaction is supposed via the spatial component corresponding to the projection on the electric field's direction, therefore the light-matter interaction Hamiltonian becomes: $\hat{H}_I = d_j.E_j$, with j standing for the polarization mode of the electric field. Note that this formulation, with a local coupling in the electric field, is an approximation, called "dipolar approximation", which is valid as long as the typical electric dipole moment length scale is much smaller than the light's wavelength, or in other words the field variations at the dipole's length scale are negligible. This is true for the Rb D2 transition addressed in this work.

The Hamiltonian: Writing the electric field as: $E = \mathcal{E}.(\mathrm{e}^{-i\omega_L t}+\mathrm{e}^{i\omega_L t})/2$ the system's Hamiltonian becomes:

$$\hat{H} = \hat{H}_0 + \hat{V} = \hbar\omega_{eg}|e\rangle\langle e| + \begin{pmatrix} 0 & \frac{1}{2}d_{ge}\mathcal{E} \\ \frac{1}{2}d_{eg}\mathcal{E} & 0 \end{pmatrix}\left(\mathrm{e}^{-i\omega_L t} + \mathrm{e}^{i\omega_L t}\right) \tag{2.3}$$

where $\hat{H}_0 = \hbar\omega_{eg}|e\rangle\langle e|$ represents the bare atomic state energies and V represents the interaction with light. The light-matter coupling strength is quantified for each transition with the Rabi frequency: $\Omega_{eg} = d_{eg}\mathcal{E}/\hbar$. In the following I assume without loss of generality that $d_{eg} = d_{ge}$ and that $\mathcal{E}$ is real.

Evolution: the Lindblad master equation: The evolution of the atomic density matrix is governed by the Liouville Von-Neumann equation, also called the Lindblad master equation:

$$\frac{\mathrm{d}\hat{\rho}_A}{\mathrm{d}t} = -\frac{i}{\hbar}[\hat{H}, \hat{\rho_A}] + \Gamma_0\sum_{\nu\neq 0}\left(\hat{L}_\nu\hat{\rho_A}\hat{L}_\nu^\dagger - \frac{1}{2}\left\{\hat{L}_\nu^\dagger\hat{L}_\nu, \hat{\rho_A}\right\}\right) \tag{2.4}$$

In this equation the first rhs term accounts for the unitary (with conserved energy) evolution while the second term represents the dissipation due to coupling with electromagnetic modes, or more simply, the spontaneous emission. It is quantified with the excited state's total decay rate Γ_0. $[\hat{a},\hat{b}] = \hat{a}.\hat{b} - \hat{b}.\hat{a}$, the index ν runs over all possible decay channels of the excited state(s), $L_\nu^\dagger/L_\nu$ are the corresponding "up"/"down" jump operators, coupling the states involved in the decay channel and $\{\hat{a},\hat{b}\} = \hat{a}.\hat{b} + \hat{b}.\hat{a}$. In case of a two level system there is only one decay channel: $\hat{L} = |g\rangle\langle e|$.

Rotating Wave Approximation and interaction representation: In order to get rid of the time independent part of the Hamiltonian one can define an operator $\hat{U}_0 = \exp(-i\hat{H}_0 t/\hbar)$ accounting for the "free" atomic evolution. In particular, this allows to switch to the interaction representation by applying the transformation:

$$\hat{H}_I = \hat{U}_0^\dagger.\hat{H}.\hat{U}_0 = \hbar \begin{pmatrix} 0 & \frac{1}{2}\Omega_{ge}\mathrm{e}^{i\Delta t} \\ \frac{1}{2}\Omega_{eg}\mathrm{e}^{-i\Delta t} & \omega_{eg} \end{pmatrix} \tag{2.5}$$

$$\hat{\rho}_{AI} = \hat{U}_0^\dagger.\hat{\rho}_A.\hat{U}_0 = \begin{pmatrix} \rho_{gg} & \rho_{ge}\mathrm{e}^{-i\omega_{eg}t} \\ \rho_{eg}\mathrm{e}^{i\omega_{eg}t} & \rho_{ee} \end{pmatrix} \tag{2.6}$$

In eq. 2.5 the laser detuning $\Delta = \omega_L - \omega_{eg}$ is introduced and all terms with frequency above ω_L were neglected using the Rotating Wave Approximation, which roughly amounts to saying that the fast oscillating terms give upon temporal averaging negligible contribution. With this transformation (or change of basis), one can verify that the master equation of the atomic density matrix, 2.4, becomes:

$$\frac{\mathrm{d}\hat{\rho}_{AI}}{\mathrm{d}t} = -\frac{i}{\hbar}[\hat{V}_I, \hat{\rho}_{AI}] - \Gamma_0 \begin{pmatrix} -\rho_{ee} & \frac{1}{2}\rho_{ge}\mathrm{e}^{-i\omega_{eg}t} \\ \frac{1}{2}\rho_{eg}\mathrm{e}^{i\omega_{eg}t} & \rho_{ee} \end{pmatrix} \tag{2.7}$$

where: $V_I = H_I - H_0$ is the time dependent part of the interaction Hamiltonian.

Optical Bloch equations (simplest case): Combining the eqns. 2.5, 2.6, 2.7 and defining the atomic coherence σ_{ge} as: $\rho_{ge} = \sigma_{ge}\mathrm{e}^{i\omega_L t}$ (and: $\rho_{eg} = \sigma_{eg}\mathrm{e}^{-i\omega_L t}$) one can write final evolution equations for the density matrix elements:

$$\frac{\mathrm{d}\rho_{gg}}{\mathrm{d}t} = -\mathrm{Im}\left\{\sigma_{eg}\Omega_{ge}\right\} + \Gamma_0\rho_{ee} \tag{2.8}$$

$$\frac{\mathrm{d}\rho_{ee}}{\mathrm{d}t} = \mathrm{Im}\left\{\sigma_{eg}\Omega_{ge}\right\} - \Gamma_0\rho_{ee} \tag{2.9}$$

$$\frac{\mathrm{d}\sigma_{eg}}{\mathrm{d}t} = -\frac{i\Omega_{ge}}{2}(\rho_{ee} - \rho_{gg}) - \left(\frac{\Gamma_0}{2} - i\Delta\right)\sigma_{eg} \tag{2.10}$$

Where I used that: $\frac{\mathrm{d}}{\mathrm{d}t}\left(\rho_{eg}\mathrm{e}^{i\omega_{eg}t}\right) = \left(\frac{\mathrm{d}\sigma_{eg}}{\mathrm{d}t} - i\Delta\sigma_{eg}\right)\mathrm{e}^{-i\Delta t}$. The set of eqns. 2.8, 2.9 and 2.10 is called the Optical Bloch equations. One can search for the steady-state solution of the density matrix in order to evaluate the medium's susceptibility in the cw illumination case. The corresponding solutions can be written in a compact form by defining the intensity dependent

saturation parameter s:

$$s = \frac{\Omega_{ge}^2}{\gamma_0\Gamma_0}\frac{1}{1+\frac{\Delta^2}{\gamma_0^2}} := \frac{I}{I_s(\Delta)} \tag{2.11}$$

where $\gamma_0 = \Gamma_0/2$. The last equality also defines a saturation intensity $I_s(\Delta)$. With this new quantity s, the steady state solutions for the density matrix elements read:

$$\rho_{gg} = \left(1+\frac{\Delta^2}{\gamma_0^2}+\frac{\Omega_{ge}^2}{2\gamma_0\Gamma_0}\right)\frac{1}{1+\frac{\Delta^2}{\gamma_0^2}+\frac{\Omega_{ge}^2}{\gamma_0\Gamma_0}} = \frac{1+s/2}{1+s} \tag{2.12}$$

$$\rho_{ee} = \frac{\Omega_{ge}^2}{2\gamma_0\Gamma_0}\frac{1}{1+\frac{\Delta^2}{\gamma_0^2}+\frac{\Omega_{ge}^2}{\gamma_0\Gamma_0}} = \frac{s/2}{1+s} \tag{2.13}$$

$$\sigma_{eg} = \frac{\Omega_{ge}}{2\gamma_0}\frac{i-\Delta/\gamma_0}{1+\frac{\Delta^2}{\gamma_0^2}+\frac{\Omega_{ge}^2}{\gamma_0\Gamma_0}} = \frac{\Omega_{ge}}{2\gamma_0}\frac{i-\Delta/\gamma_0}{1+\frac{\Delta^2}{\gamma_0^2}}\frac{1}{1+s} \tag{2.14}$$

The saturation parameter depends on light's intensity and contains therefore the information on the model's non-linear behavior. For better understanding of the non-linear optical response of the medium, one can use the eqn. 2.2 and readily calculate the medium's susceptibility with the formula: $\chi = 2Nd_{ge}\sigma_{eg}/(\epsilon_0\mathcal{E})$ giving:

$$\chi(\Delta,\Omega) = \frac{Nd_{ge}^2}{\hbar\epsilon_0\gamma_0}\frac{i-\Delta/\gamma_0}{1+\frac{\Delta^2}{\gamma_0^2}+\frac{\Omega^2}{\gamma_0\Gamma_0}} = \chi^{(1)}(N,\Delta)\frac{1}{1+s} \tag{2.15}$$

$$\chi^{(1)}(N,\Delta) = \frac{Nd_{ge}^2}{\hbar\epsilon_0\gamma_0}\frac{i-\Delta/\gamma_0}{1+\frac{\Delta^2}{\gamma_0^2}} \tag{2.16}$$

Population inversion and the linear regime: Note that the saturation parameter dependent factor in the eqn.: 2.14 is equal to the difference between the ground and the excited state populations (commonly called population inversion in laser physics):

$$\chi(\Delta,\Omega) = \chi^{(1)}(N,\Delta)\frac{\Delta N_{ge}(\Delta,\Omega)}{N} \tag{2.17}$$

where $\Delta N_{ge}/N = \rho_{gg} - \rho_{ee}$. This remark is very important for the following chapter, where the the non-linear optical response will be modeled with more details. As the intensity increases the excited level population ρ_{ee} increases more and more until reaching its asymptotic value of 1/2. The opposite happens with the ground state's population while the atomic coherence tends to zero. This regime corresponds to a completely saturated medium which becomes transparent to light. On the contrary, when s is negligibly small, the excited state is not populated at all and the total population remains undisturbed in the ground state. This is when the susceptibility tends to its linear value: $\chi(\Delta,\Omega) \underset{s\to 0}{\to} \chi^{(1)}(N,\Delta)$. As will be explained further, this weak intensity regime is the regime of validity of the two-level model, because only in this regime the atomic populations are unaffected by the laser beam and each atomic transition can be considered as independent from the possible neighboring transitions.

Refraction and absorption: A monochromatic laser beam propagating in a medium with the susceptibility χ becomes:

$$E(z,t) = \mathcal{E}(z=0)\mathrm{e}^{i\tilde{k}z - i\omega_L t} \tag{2.18}$$

$$\tilde{k} = \frac{\omega_L}{c}(1+\chi)^{1/2} \simeq \frac{\omega_L}{c}\left(\left[1 + \frac{\mathrm{Re}\{\chi\}}{2}\right] + i\frac{\mathrm{Im}\{\chi\}}{2}\right) \tag{2.19}$$

The linearization of the square root is a safe approximation since the refractive index and the imaginary part of the susceptibility of dense Rb vapors within the temperature range explored in this work, does not exceed 0.05 in magnitude. This result shows that a laser field crossing a medium of independent two-level atoms with number density N experiences on average a phase shift, stemming from the medium's refractive index due to the real part of the susceptibility, and exponential extinction due to its imaginary part.

Dependence parameters: Considering the spectral shape of the linear susceptibility $\chi^{(1)}(N,\Delta)$, one can observe that its imaginary part is a Lorentzian function decaying as $1/\Delta^2$, and its real part is an antisymmetric function, decaying as $1/\Delta$ in magnitude for large detunings. It's also important to note that the susceptibility (both real and imaginary parts) linearly increases with the atomic density within the considered model. This is a result coming along with the assumption of medium composed of independent atoms. It is valid in dilute gases when $N\lambda^3 \ll 1$, it clearly needs to be revisited in the regime where $N\lambda^3 \simeq 1$ [160]. While several issues will be taken into account (slightly generalized) in the next section in order to apply the two-level atomic susceptibility to accurately model the linear susceptibility in hot Rb vapor, the result presented in this section already allows to conclude that in media with resonant light-matter coupling such as hot Rb vapors, the enhanced light-matter interaction in terms of refractive index always comes along with the increased absorption rate (unless additional coherent atomic interference effects such as the EIT, briefly described in section 1.1.3.3, are employed). The derived model also allows to identify the two key control parameters used in this work to tune light-matter interactions: the atomic density N and the laser detuning Δ.

2.2.2 Real energy level structure

Isotopes: Rubidium atoms exist in form of two stable isotopes: ^{85}Rb (72.2 % of natural abundance) and ^{87}Rb (27.8 % of natural abundance). Depending on the used cell, either natural isotopic mix cells or isotopically purified cells (above 99 % of isotopic fraction) are available for the experiments. A useful reference for the physical and optical properties of ^{85}Rb and ^{87}Rb that are relevant to various quantum optics experiments are given in [37, 38]. The two Rb isotopes slightly differ by the atomic mass, have different nuclear spins and the transition frequencies. The atomic level structure of both isotopes is shown on fig. 2.1 b).

Hyperfine structure: The shown level skim is called the hyperfine structure of the Rb $5S_{1/2}$ and $5P_{3/2}$ states, arising with all relevant effects (in the energetic scale) up to the coupling between the total electron angular momentum **J** and the nuclear spin angular momentum **I**. Then the quantum number F corresponding to the atomic angular momentum $\mathbf{F} = \mathbf{J} + \mathbf{I}$, can

take the integer values between $|J-I|$ and $|J+I|$. The corresponding values of F are marked next to each shown state. As can be appreciated from the scheme, each $5S_{1/2}$ state splits into 2, and each $5P_{3/2}$ state is split into 4 hyperfine states.

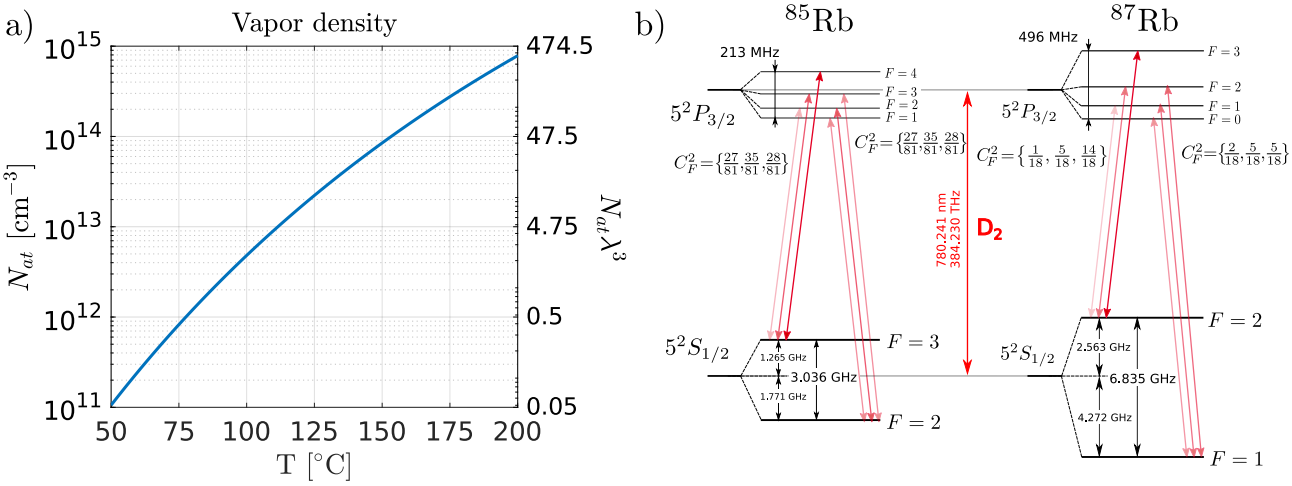

Figure 2.1: Relevant physical characteristics of hot Rubidium vapors: a) vapor density at vapor's saturation pressure as function of its temperature also expressed as number of atoms within a cube of laser wavelength volume at $\lambda = 780$ nm [140]. b) Hyperfine structure of Rubidium's D2 line for both isotopes. Red arrows show all possible (allowed by the selection rules) transitions with color brightness qualitatively reflecting the corresponding transition strengths C_{ge}^2, reported nearby. Adapted from [55].

Why Zeeman magnetic sublevels not considered separately? Note that each hyperfine state is composed by $2F+1$ sublevels usually labeled with their m_F value and referred to as magnetic Zeeman sublevels [55]. While Zeeman sublevels and their unequal populations play an important role in the light-matter interactions in cold atoms, being largely involved in the optical pumping and inducing vectorial (polarization direction dependent) effects for light, they are usually considered as irrelevant in thermal Rubidium vapor cells [71, 140]. In fact, the thermal energy of atomic vapor at the temperature of around 130 °C is of the order of k_BT, corresponds to the typical energy dispersion within the atoms in the vapor. If one converts this energy into angular frequency via $\delta\nu \simeq k_BT/h$, one gets a value of the order of 10 THz, which is orders of magnitude above the $5S_{1/2}$ ground state's hyperfine splitting, which is around 5 GHz, but at the same time much below the transition frequencies of the D2 line, which lie around 384 THz. This means that in thermal equilibrium the atomic populations are distributed equally among all the magnetic sublevels of the $5S_{1/2}$ manifold, while all the sub-levels of the $5P_{3/2}$ state are completely unoccupied. Therefore within this work the energy levels are resolved up to the hyperfine structure.

Possible optical transitions: Multiple transitions can be optically addressed within this structure and are shown on fig. 2.1 b) with red double sided arrows, with the color brightness qualitatively representing their relative strengths. Note that due to the selection rules the transitions within the same manifold are forbidden and transitions among different manifolds

are only possible for neighboring atomic angular momenta of the involved states: $|F_e - F_g| \leq 1$, with F_g/F_e corresponding to the ground/excited state.

Implications for the linear susceptibility model: The real energy level structure of Rb can easily be taken into account within the 2-level atomic model to describe the linear optical suseptibility in Rb vapors by adding the contributions of various involved transitions [140]:

$$\chi^{(1)}(\Delta) = \sum_{i,g,e} \frac{n_i C_{ge}^2}{2(2\mathcal{I}_i + 1)} \chi^{(1)}(\Delta_{ige}) \tag{2.20}$$

In this equation i stands for the considered isotope (^{85}Rb or ^{87}Rb), n_i is hence the molar isotopic fraction, g/e is the considered ground/excited hyperfine state, $\mathcal{I}$ is the nuclear spin (5/2 for ^{85}Rb and 3/2 for ^{87}Rb) giving in total 12/8 ground state sublevels for ^{85}Rb/ ^{87}Rb, sharing equally the total atomic population. The coefficients C_{ge}^2 are the strengths of each considered transition [140, 71, 55] and are reported on fig. 2.1 b) as C_F^2. The linear susceptibility $\chi^{(1)}$ of various involved transitions is the one given in the eqn. 2.16. The detuning $\Delta = \omega_L - \omega_{ref}$ is taken with respect to a reference frequency (the lowest D2 transition frequency of the considered isotope was taken in this work) and therefore in order to account for different line center frequencies ω_{ige} of considered transitions, their detuning is calculated as: $\Delta_{ige} = \omega_L - \omega_{ige}$.

Independent transitions: The eqn. 2.20 shows that the total linear susceptibility is the superposition of contributions from all involved transitions. There are two key reasons for the validity of this assumption: the fact that the medium is sufficiently dilute to neglect the atomic collisional effects, dipole-dipole interactions and local field effects [160, 159, 142] on the one hand, and the fact that in the linear regime the ground state populations are unchanged on the other hand, i.e. all the involved transitions, sharing the common hyperfine ground state, do not "see" each other because none of the transitions affects the common ground state's population. While accurate in the linear regime, this assumption becomes obviously wrong for strong laser intensities, as will be discussed in the next chapter 3.

2.2.3 Effect of temperature and high density

2.2.3.1 The temperature dependence of density

In all vapor cells used in this work, the Rb vapor is in thermal equilibrium with some liquid Rubidium droplets, condensed at the side walls of the cell, typically at the vicinity of the so called "cold finger": short extension of the cell serving as the cell's coldest point to trap liquid Rubidium [55]. The liquid-vapor equilibrium implies that the vapor's pressure equals to the saturated vapor pressure p_V which strongly increases with the vapor temperature, according to the following law (same for both isotopes) [140]:

$$\log_{10} p_V = 15.88253 - \frac{4529.635}{T} + 0.00058663 \times T - 2.99138 \times \log_{10} T \tag{2.21}$$

Knowing the vapor pressure one can calculate with the ideal gas law the number density of Rb vapor:

$$N = \frac{133.323 \times p_V}{k_B T} \tag{2.22}$$

The factor of 133.323 converts the vapour pressure from Torr to Pa. The dependence of the atomic vapor density on the vapor temperature, calculated with the eqns. 2.21 and 2.22 is shown on fig. 2.1 a). It can be seen that increasing the vapor temperature from 50 °C to 200 °C the vapor density is increased by 4 orders of magnitude. This is a very efficient tools to control atomic vapor density and consequently the light-matter coupling, mediating the photon-photon interactions.

2.2.3.2 Moving atoms: the Doppler effect

Another important feature arising with temperature in atomic vapors is the so-called Doppler broadening. In fact the vapor is composed of atoms moving in random directions and with random velocities inside the cell. Their root mean squared velocity is $u_{3D} = \sqrt{3k_B T/M}$ in 3D with M the atomic mass and is around 350 m.s^{-1} at T=150 °C. The atomic motion significantly modifies the line shape around the resonance due to the Doppler effect: depending on the atomic velocity in the laser's propagation direction v_z, the laser frequency appears shifted by an amount $k.v_z$ in the atomic referential and therefore its response is not anymore $\chi(\Delta)$ but $\chi(\Delta - k.v_z)$. One can remark that the atoms respond differently depending on their velocity class (giving rise to inhomogeneous broadening) and that for given laser frequency the total atomic response is the sum over the contributions of all involved velocity classes:

$$\chi_D(\Delta) = \int_{-\infty}^{+\infty} \mathrm{d}v_z \chi(\Delta - k.v_z) P(v_z) \tag{2.23}$$

The thermal atomic velocity along the propagation axis is given by the Maxwell–Boltzmann distribution, characterized by a Gaussian function, with a 1/e width of $u = \sqrt{2k_B T/M}$. With this consideration the eqn. 2.23 can be rewritten in terms of angular frequency $\omega' = k.v_z$:

$$\chi_D(\Delta) = \frac{1}{\sigma_D \sqrt{\pi}} \int_{-\infty}^{+\infty} \mathrm{d}\omega' \chi(\Delta - \omega').\exp\left(-\frac{\omega'^2}{\sigma_D^2}\right) \tag{2.24}$$

with $\sigma_D = ku$ the width of the Doppler shift's distribution. Note that for Rb vapors $\sigma_D/(2\pi) \sim 100$ MHz $\gg \Gamma_0/(2\pi) \simeq 6$ MHz. The equation 2.24 is a convolution product of the static atomic response with a Gaussian function accounting for the Doppler shift experienced by different atomic velocity classes. This convolution integral can be solved analytically [142, 140, 55]

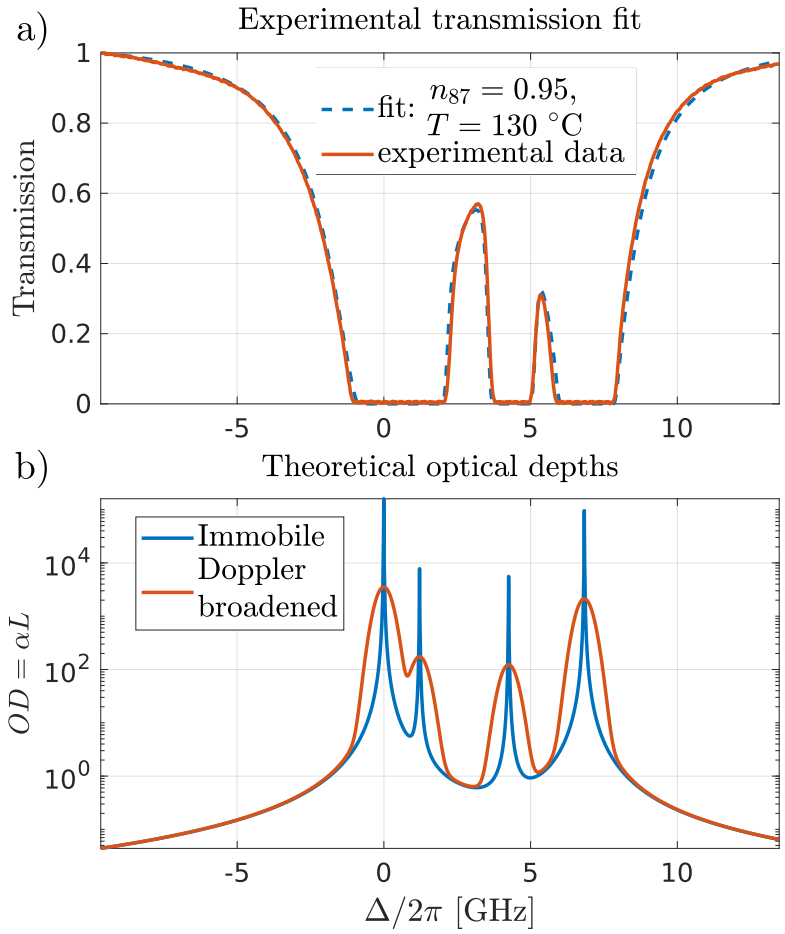

Figure 2.2: Visualization of the Doppler broadening: a) Measured and fitted (with the model developped in [140] and including the collisional self-broadening [160]) transmission spectrum of a weak probe propagating in a L=75 mm long cell. b) the corresponding theoretical optical depths, defined as $OD = -\ln(T)$, with and without the Doppler broadening taken into account.

involving the Voigt function V (also known as the plasma dispersion or the Faddeeva function):

$$\chi_D^{(1)}(\Delta) = \frac{Nd^2\sqrt{\pi}}{\hbar\epsilon_0\sigma_D} \cdot V\left(\frac{\gamma_0}{\sigma_D} - i\frac{\Delta}{\sigma_D}\right) \tag{2.25}$$

$$\chi_D(\Delta) = \frac{Nd^2\sqrt{\pi}}{\hbar\epsilon_0\sigma_D}\left[\mathrm{Re}\left\{V\left(\frac{\gamma_0\sqrt{1+s_0}}{\sigma_D} - i\frac{\Delta}{\sigma_D}\right)\right\} + \frac{i}{\sqrt{1+s_0}}\mathrm{Im}\left\{V\left(\frac{\gamma_0\sqrt{1+s_0}}{\sigma_D} - i\frac{\Delta}{\sigma_D}\right)\right\}\right] \tag{2.26}$$

Its expression is: $\forall z \in \mathbb{C}$, $V(z) = i.\mathrm{e}^{z^2}.\mathrm{erfc}(z)$, with: $\mathrm{erfc}(z) = 1-\mathrm{erf}(z)$ and erf is the error function. This function has been efficiently numerically implemented, for example on Matlab via the `fadf` function [132]. The introduced on resonant saturation parameter s_0 in the eqn. 2.26 is the one given in 2.11 at resonance: $s_0 = s(\Delta = 0)$. From the eqn. 2.24 one can understand that the Doppler broadening results in smoothing the susceptibility spectrum of static atoms by a Gaussian function of width σ_D. In order to better visualize the result, the Figure 2.2a)

shows an experimentally measured transmission spectrum $\mathcal{T}$ of a weak probe in a 75 mm long ^{87}Rb vapor cell (orange line). The data is fitted (blue dashed line) by a theoretically calculated [140] transmission $\mathcal{T} = \exp(-k_0.\mathrm{Im}(\chi^{(1)})L)$ including the Doppler broadened linear susceptibility (eqn. 2.25) and taking into account the real hyperfine structure of Rb (eqn. 2.20). The vapor temperature and molar fraction of ^{87}Rb were used as free parameters. The details of the measurement procedure will be detailed in section 2.3. Figure 2.2b) shows the theoretically calculated optical depth $OD = -\ln(\mathcal{T})$, corresponding to the experimental parameters retrieved from the fit in Figure 2.2a) both including (orange line) and neglecting (blue line) the Doppler broadening. The blue line shows the result $OD = \mathrm{Im}(\chi^{(1)})k_0L$ as a sum (eqn. 2.20) of all transition contributions given by the bare 2-level atomic model, eqn. 2.16 (Lorentzian profile), while the orange line shows the same result but now with each transition's contribution given by the Doppler broadened 2-level atomic model, eqn. 2.25 (Voigt profiles). From figure 2.2b) it can be concluded that both curves only differ in the vicinity of the resonance frequencies, where the OD spectrum changes its behavior from a Lorentzian and becomes dominated by the Gaussian velocity distribution of the atoms. This result is in agreement with a more detailed study presented in [141], showing that the susceptibility spectrum is affected by the Doppler effect within the detuning range below $|\Delta| < 2\sigma_D$. Importantly, for detunings larger than $|\Delta| < 2\sigma_D$ the Doppler effect can be safely neglected. Note that $\sigma_D \simeq 0.36$ GHz for Rb vapors at temperatures around 150 °C.

2.2.3.3 Resonant collisional broadening: step into the high density regime

The right y-axis of the fig. 2.1 a) shows the average number of atoms per cubic volume of size of laser wavelength. Increasing the temperature from 100 °C to 150 °C one increases the number of atoms from several to several tens per wavelength cube, which makes the vapor dense enough such that the picture of a "dilute medium with independent atoms" may not hold anymore. In fact thanks to the vapor's saturation pressure which increases almost exponentially with temperature, the atomic vapor density can be tuned from very dilute $N\lambda^3 \ll 1$ to very dense regimes $N\lambda^3 \gg 1$. As the atomic density increases, the atomic collisions [160, 159], as well as the coherent multiple scattering effects [91] become more pronounced. This can result in considerable changes in light-matter interaction [159]. In fact, from the expression 2.16 for the linear susceptibility derived above, which depends linearly on the atomic density, one could conclude that increasing the atomic vapor density to very high values one could increase arbitrarily the medium's refractive index and hence enhance drastically the light-matter coupling. This conclusion obviously wrong and is, for example, in contradiction with the observation, that the refractive index of solid state materials, with atomic density much larger $> 10^{20}$ cm^{-3} than that of Rb vapors $\sim 10^{14}$ cm^{-3} at 150 °C, hardly surpasses the value of 2.5. It turns out that inter-atomic dipole-dipole interactions, which become important in the dense regime, strongly affect the optical susceptibility avoiding its divergence in the limit of infinite density [6, 84].

Indeed, it was shown in [160] that the linear susceptibility model developed in [140] and demonstrated as extremely accurate for vapor temperatures up to 40 °C becomes inaccurate already

at temperatures above 120 °C. It was however found that the model [140] can be simply generalized by rescaling the homogeneous line-width in the susceptibility, given by the excited state decay rate Γ, by the one including the density dependent contribution stemming the interaction among the atoms:

$$\Gamma = \Gamma_0 + \beta N \tag{2.27}$$

where $\beta = 2\pi \times 1.03 \times 10^{-7}$ Hz.cm^3 is called the self-broadening coefficient. The value of the self-broadening correction equals the value of Γ_0 at approximately 150 °C for the Rb D2 line. The dominant effect arises from the dipole-dipole interaction between two identical atoms, in superpositions of the ground and excited states, within the binary dipole-diplole approximation [160]. This is an important detail because it means that it is enough for a laser beam to simply induce the atomic coherence (the off-diagonal density matrix term) without affecting the atomic populations, which is exactly what happens in the linear propagation regime, in order to cause this dipole-dipole interaction. This result also suggests that additional effects of dipole-dipole interactions could be expected in the non-linear regime where the atomic populations are affected by the laser intensity, such as the 2-body interactions between the atoms in ground-excited or excited-excited states.

Finally, note that including the self-broadening correction (eqn. 2.27) in the on resonant linear susceptibility, eqn. 2.16, one gets:

$$\chi_N^{(1)}(N, \Delta = 0) = \frac{d_{ge}^2}{\hbar \epsilon_0} \frac{iN}{\gamma_0 + \beta N/2} \tag{2.28}$$

a result which does not diverge anymore as N tends to infinity but rather saturates as $\sim N/(\gamma_0 + \beta N/2)$. This shows that inter-atomic interactions play crucial role in the light-matter interaction in the high density regime.

Conclusion: Taking into account all the generalization points developed in this section, the linear susceptibility is accurately described by a modified two-level susceptibility:

$$\chi^{(1)}(\Delta) = \sum_{i,g,e} \frac{n_i C_{ge}^2}{2(2\mathcal{I}_i + 1)} \chi_D^{(1)}(\Delta_{ige}) \tag{2.29}$$

where i is the considered isotope (^{85}Rb or ^{87}Rb), n_i: the molar isotopic fraction, g/e: the considered ground/excited state, C_{ge}^2: the corresponding transition strength (see fig. 2.1 b)), $\mathcal{I}_i$: the nuclear spin (5/2 for ^{85}Rb and 3/2 for ^{87}Rb) and $\chi_D^{(1)}$ given by the equation 2.25 with the natural linewidth Γ_0 replaced by the modified expression given in the eqn. 2.27. Various physical parameters in $\chi_D^{(1)}$ are: N the atomic vapor density (which can be related to the vapor temperature via the eqns. 2.22 and 2.21), the electric dipole value of the Rb D2 line $d = 5.177 e a_0$ with $e = 1.602 \times 10^{-19}$ C the elementary electric charge and $a_0 = 0.529 \times 10^{-10}$ m the Bohr radius and $\Gamma = 2\pi \times 6.06$ MHz for the D2 line [140]. All detunings Δ and Δ_{ige} are calculated with respect to a common reference frequency ω_{ref}.

2.3 System characterization

The discussion of the previous section allowed to review the currently most accurate model [140, 160] to describe the linear optical susceptibility under cw illumination in hot Rb vapors, starting from the simplest 2-level atomic description and complexifying it step by step to take into account the additional eefects encountered in real life, such as the atomic hyperfine structure, the Doppler effect and self broadening. Most importantly for this work, this description allowed to identify Rb vapor's key two parameters allowing to finely tune the light-vapor interactions: vapor density controlled via its temperature and the laser detuning. This section focuses on the experimental details of the vapor density measurement as well as the laser frequency control.

2.3.1 Laser control

All experiments of this work were performed with two diode lasers: a fibered μQuans SML780 (unformally named in the lab after the mount Kapaz 3066 m) and a Toptica TA pro laser system (unformally named after the mount Kilimandjaro 5895 m).

2.3.1.1 Kilimandjaro

The Toptica TA pro is composed of an External Cavity Diode Laser (ECDL) followed by a Tapered Amplifier, all controlled with a DLC pro module. It produces a highly coherent (linewidth below 1 MHz) and stable (in frequency and power) light with tunable wavelength from 775 nm to 800 nm. The laser frequency can be tuned by four means depending on the desired scan range and scan rate:

- Adjusting manually the angle of a diffraction grating inside the cavity. In fact the radiative emission of a diode is broadband, and a frequency mode which oscillates inside the external cavity can be selected with the diffraction grating placed inside the cavity. By tuning the grating angle, the cavity mode's wavelength can be changed. This method is thought for a gross variation of the laser wavelength, allowing for example switch the wavelength from 780 nm to 795 nm to excite the Rb D1 line.

- The diode current modulation (current control). One of the main characteristics of diode lasers is that the laser wavelength depends on the electric current of the diode. Therefore the current modulation of a diode allows for a relatively fast modulation of the laser frequency but within a relatively small frequency exploration range (up to 50 GHz typically). However, the dependence of the laser frequency on the modulation current is not necessarily linear.

- Changing the external cavity length with a piezoelectric drive (piezo control). This method also allows for a relatively fast (up to kHz range typically) modulation of the laser frequency but within a relatively small frequency exploration range (up to 50 GHz typically). In difference to the current modulation, the piezo control voltage can be linearly converted to the resulting laser frequency. This method is used to perform a laser

frequency scan within a typical range up to 20 GHz around an atomic line at a rate of several Hz, for example, in order to measure the weak probe transmission spectrum.

- Controlling the diode temperature (temperature control). Most diode lasers can be tuned over a few nanometers by varying the junction temperature [113]. In case of the Kilimandjaro laser, the diode temperature was typically around 20 °C and was sometimes slightly changed by a value below one degree in order to avoid mode hops, i.e. discontinuous frequency jumps during laser frequency scan. Temperature control cannot be used for laser frequency scan due to the relatively long $\sim$ 10 s time scales it involves to reach the target temperature value.

The laser's output power can be controlled with the TA current. Typically set to 4.5 A the amplification in a TA results in a azimuthally asymmetric transverse mode with linear polarization and total power above 3 W. The further usage the beam is then usually mode cleaned by being transported through a single mode fiber. In fact there the TA pro laser system also provides a second output beam of power around 10 mW, called "seed", which comes directly from the ECDL without being amplified by the TA. This seed beam is used for spectroscopy and frequency control/measurement purposes. The laser frequency can be calibrated with a frequency scan using the Saturable Absorption Spectroscopy (SAS) setup, as will be explained later in this section. In order to avoid the laser frequency drift, the laser frequency can be actively controled with a Pound-Drewer-Hall technique [20]. The DLC pro control box allows to allows to lock the laser frequency by simply using the only input in form of a SAS signal. Note that it is also possible to lock with DLC pro the laser power of a TA pro by using a reference photodiode signal as input error signal. By acting on the TA current this lock compensates possible laser power drifts.

2.3.1.2 Kapaz

The μQuans SML is laser system dedicated to Rb laser cooling experiments. It is composed of a seeder diode operating at the wavelength of 1560 nm, followed by a phase shifter, then amplified with an Erbium Doped Fiber Amplifier (EDFA). The amplified beam is then frequency doubled in a PPLN waveguide to get a 780 nm beam which is then delivered with a FC/APC connectorized fiber (fiber output surface sightly tilted with respect to the plane perpendicular to the propagation axis).

Kapaz characterization: Kapaz delivers a highly coherent laser illumination (with bandwidth of the order of 100 kHz) in the TEM_{00} mode with maximal power of 1.2 W. The results of the μQuans SML laser characterization are shown on fig. 2.3. In order to assess the frequency stability in the unlocked case, the laser frequency was measured with a lambdameter and is plotted on fig. 2.3 a) as function of the measurement time. The result shows laser frequency fluctuation of around 150 MHz within 12 min. Taking into account the Rb vapor response "smoothed" by the Doppler effect and working sufficiently far from resonance, the measured laser fluctuation can be considered as acceptable for the experiments. During the experiments shown in this thesis the Kapaz laser was not frequency locked.

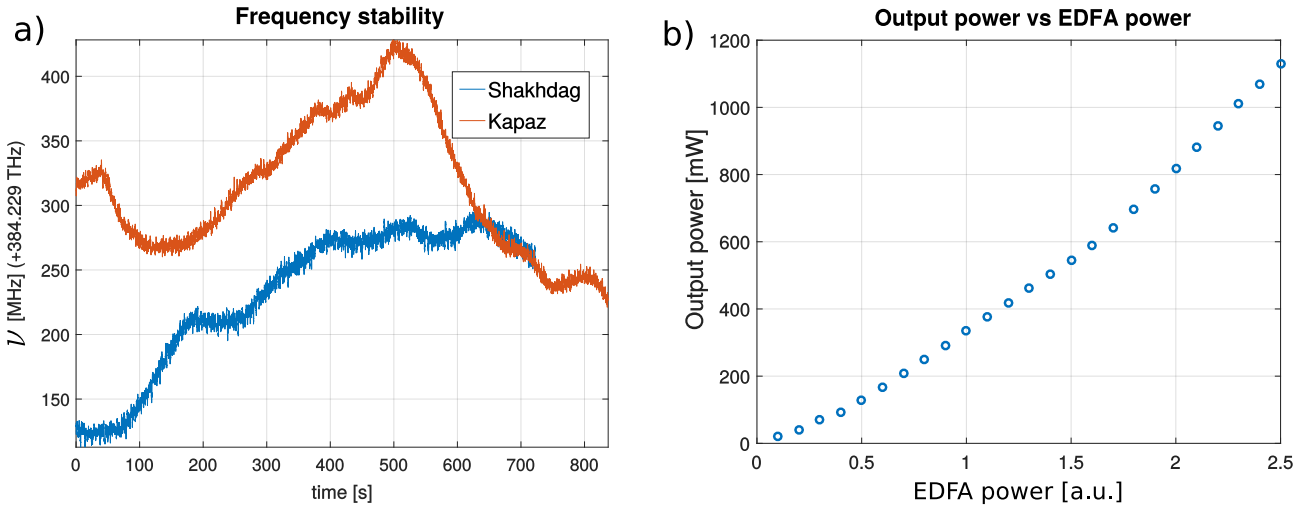

Figure 2.3: μQuans SML characterization. a) Frequency stability measurement: laser frequency measured with a lambdameter Spectra Resolver, as function of time, for two different μQuans SML lasers. b) Laser output power measured with a bolometer based powermeter, as function of the input parameter value controlling the Erbium Doped Fiber Amplifier (EDFA).

Frequency control:
In difference to Kilimandjaro, the frequency of Kapaz can only be tuned within a small range of 50 GHz around 780 nm. The frequency can be controlled by the diode temperature and current modulation. The temperature is controlled with a Peltier module and can be typically varied between 18 °C and 36 °C and is used to move the scan range window, while the diode current modulation is used for laser frequency scan. The current modulation is performed by applying a signal generated with an Arbitrary Waveform Generator (AWG) on the slow current modulation input of the diode. Importantly, the dependence of the laser frequency on the modulation current is not linear, which needs to be accounted for during frequency calibration.

2.3.1.3 Laser frequency measurement

Two methods were used in this work to measure the laser frequency: the first one consists in sending via an optical fiber a small portion of light to the lambdameter device, and the second technique is the saturated absorption spectroscopy in a Rb vapor cell at room temperature.
Lambdameter: MogWave MWM wavemeter was used for laser frequency measurements. While the device shows the frequency up to the 10 MHz range, its accuracy reported in the datasheet is only "below 1 GHz". For the performed experiments, the device has to be calibrated by comparing its output value with the known Rb transition frequency of the corresponding on resonant beam. This allows to access the absolute offset of the measurement error. The relative error was verified to be not significant by tuning the laser to two "distant" Rb resonances, calculating the difference of the corresponding output values of the lambdameter and comparing it with the known transition frequency difference. Lambdameter is a useful to measure the

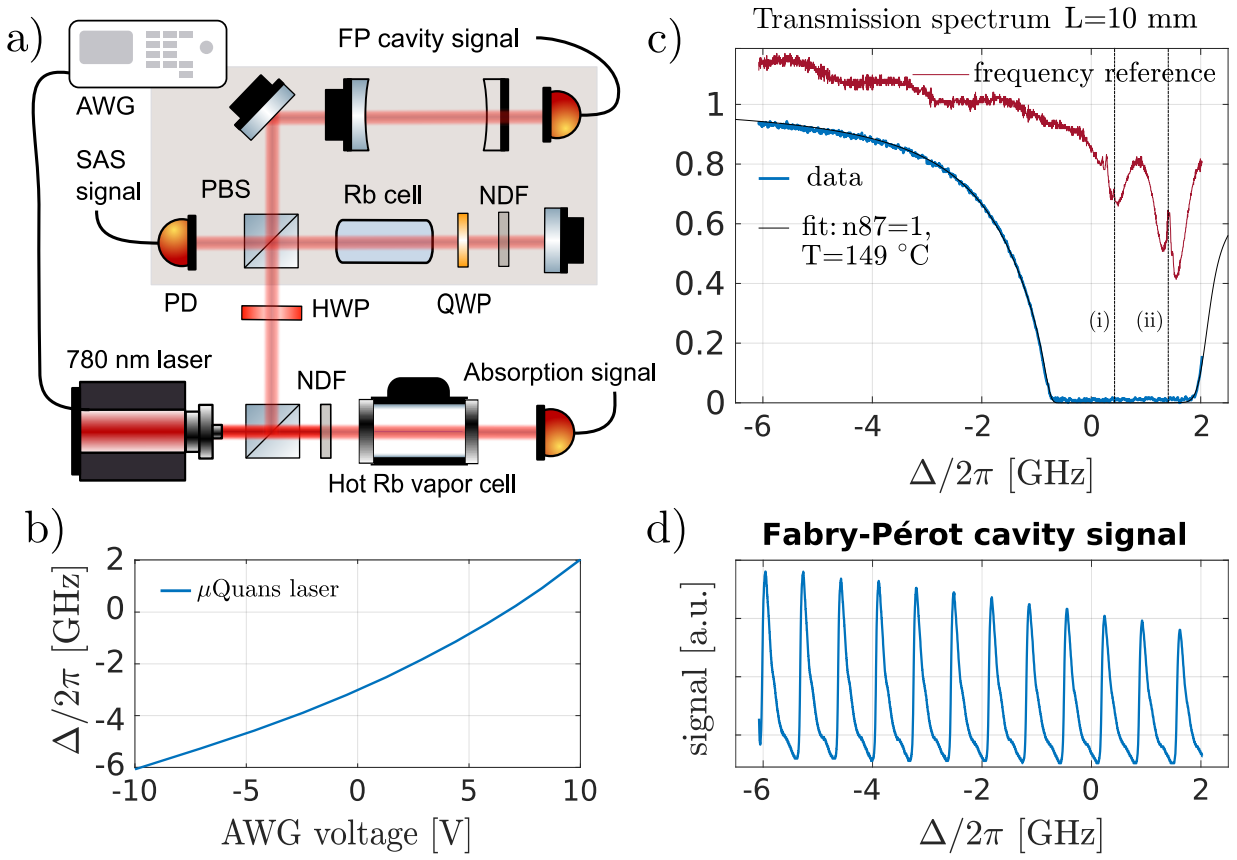

Figure 2.4: Laser frequency measurement and vapor cell characterization. a) Schematic experimental setup to measure the transmission spectrum around the Rb D2 line. List of abbreviations: SAS-saturated absorption spectroscopy, NDF-neutral density filter, PD-photodiode, PBS-polarizing beam splitter, HWP-half wave plate, QWP-quarter wave plate, AWG-arbitrary wavefront generator, FPC-Fabry-Pérot cavity. b) the measured (with the FPC and SAS signals) laser frequency during a current modulated laser frequency scan as function of the AWG signal fed into the diode. c) blue: weak probe absorption spectrum, black: fit based on the model: 2.31, dark red: SAS signal with two peaks which were used for frequency calibration and identified as: (i) ^{87}Rb $F_g = 2 \rightarrow F_e = 3$, with $\Delta_{(i)}/(2\pi) = 0.42$ GHz and (ii) ^{85}Rb $F_g = 3 \rightarrow F'_e$, with $\Delta_{(ii)}/(2\pi) = 1.41$ GHz.

frequency drift or fluctuation during an experiment where the laser frequency needs to be ideally constant.

Saturated absorption spectroscopy (SAS): The key technique used to calibrate the frequency of the transmission spectra, is the saturated absorption spectroscopy (SAS). It is based on probing the atomic velocity selective sub-Doppler line saturation in the contra-propagating geometry. The experimental setup to perform the SAS is shown in the clear brown box of the figure 2.4 a). A collimated pump laser beam of the several mW in power and up to several millimeters in size crosses a room temperature Rb vapor cell with isotopic fraction corresponding to Rb's natural abundance. The beam is then back-reflected by a mirror and attenuated with a neutral density filter to follow exactly its incident path. The back-reflected beam plays the role of a

probe, which measures the atomic saturation degree via transmission recorded on a photodiode. Recalling that the probe's extinction coefficient reads: $\alpha_p = k_0 \mathrm{Im}\{\chi_p\}$, one can qualitatively describe the behavior of the probe's susceptibility for a given atomic velocity class v_z:

$$\mathrm{Im}\{\chi(\Delta, s_0, v_z)\} \propto \frac{1}{1+\left(\frac{\Delta}{\gamma}+\frac{k.v_z}{\gamma}\right)^2} \frac{1}{1+s_0/\left[1+\left(\frac{\Delta}{\gamma}-\frac{k.v_z}{\gamma}\right)^2\right]} \tag{2.30}$$

At room temperature the Doppler width dominates the natural linewidth: $\sigma_D \gg \Gamma$, therefore one can imagine a simplified picture where the two level atoms only absorb the on resonant incident photons in their rest frame. This leads to a Gaussian Doppler broadened lineshape after averaging of the first rhs factor over different velocity classes. However, the probe beam actually encounters the the atoms which may have absorbed the incident pump beam photons. This is taken into account by the second factor of the rhs in eqn. 2.30. For a given detuning Δ the pump saturates the atoms corresponding to the $v_{z,pump} = \Delta/k_0$ velocity, while the probe beam addresses the atomic fraction moving at $v_{z,probe} = -\Delta/k_0$. As long as the probe and the pump address different atoms, or $v_{z,probe} \neq v_{z,pump}$, the second factor equals to 1 and the probe's transmission is a Gaussian Doppler broadened profile. Nevertheless, for $\Delta = 0$ one has $v_{z,probe} = v_{z,pump}$ and the probe addresses exactly the atoms which have absorbed pump photons. For these atoms the second factor in the rhs of the eqn. 2.30 is drastically reduced since these atoms are saturated and are now forced by the probe beam to emit the absorbed photons by stimulated emission. This results to a transparency peak resulting from the reduced susceptibility exactly at the line centre. The width of the transparency window is given by the pump power broadened natural linewidth $\Gamma\sqrt{1+s_0} \ll \sigma_D$, which is still much smaller than the Doppler width of the probe's absorption profile, allowing for the identification of the line centre frequencies of various transitions, as can be seen on the dark red plot of the figure 2.4 b), and the consequent calibration of the frequency axis. Note that in case of several transitions placed within the same Doppler broadened profile, additional peaks, called cross-over peaks, appear exactly at the spectral half way between the considered transition pairs. In the cross-over peaks the probe and pump address the same atoms which are however resonant with two different transitions. The model based on a two-level system being valid for the qualitative picture, note that the quantitative calculation of the SAS peaks requires taking into account some more effects [71].

Fabry-Pérot cavity (FPC): SAS signal is enough to calubrate the Kilimandjaro laser's frequency scan, performed by applying linear voltage ramp on a piezo, inducing the linear frequency variation. However, this is not anymore the case for the Kapaz laser, which is frequency scanned by means of the diode current modulation. In order to measure the instantaneous frequency variation rate during a linear current modulation ramp, a tiny fraction of laser beam was sent into a Fabry-Pérot cavity with its transmission measured on a photodiode, as shown on figure 2.4 a). Acquiring a FPC transmission signal and a SAS signal during a frequency scan one gets a series of unequally spaced peaks. An important feature of the FPC used here is that the FPC transmission spectrum shows equally spaced peaks, with the frequency period called

"free spectral range" (FSR). This allows to access the "local" frequency scan rate during a scan, which is simply proportional to the measured local peak spacing. With the obtained result one can get a quantity proportional to the frequency as function of the input AWG signal. This quantity can now be calibrated using the SAS peaks with known detunings to give access to the "true" laser detuning. The laser detuning (with respect to the ^{87}Rb $F_g = 2 \rightarrow F_e = 1$ transition) as function of the AWG voltage is shown on figure 2.4 b) and the FPC transmission is plotted as function of the calibrated frequency in figure 2.4 d). The latter plot shows now a series of equally spaces peaks, confirming a successful frequency calibration.

2.3.1.4 Laser power measurement

Accurate description of the non-linear optics experiments as the ones performed in this work require the knowledge of the laser power and the resulting laser intensity. In fact the laser power is used in this work as a tool to control the photon-photon interactions. Depending on the laser power it was either measured with a bolometer based powermeter for high powers (above 20 mW) and with a photodiode based powermeter for low powers (below 20 mW).

2.3.2 Medium control: vapor temperature measurement

Experiment: In Rb vapors the vapor temperature is the key knob to control the atomic density. In the experiment, the temperature of the vapor cell is controlled with flexible heaters from "Omega" which were wound around the cells. The heaters consist of electric resistances which are constructed in the configuration minimizing the magnetic field stemming from the total electric current. By doing so it is possible to heat the vapor to the temperatures up to 200 °C. The experimental scheme of the transmission measurement is shown in figure 2.4 a). The transmitted laser power is measured with a photodiode.

Fit model: Using cw illumination with a large beam and weak power, the total beam transmission $\mathcal{T}$ obeys the Beer-Lambert's law:

$$\mathcal{T} = \frac{P}{P_0} = \exp\left(-\alpha z\right) \quad \text{with:} \quad \alpha = k_0 \mathrm{Im}\left\{\chi^{(1)}(N, \Delta)\right\} \tag{2.31}$$

where P_0 / P is the power at the entrance / exit of the medium. The susceptibility model is the one presented in the eqn. 2.29 taking into account the Doppler broadening, self broadening (eqn. 2.27) and the dependence of the atomic density on the temperature (eqns. 2.22 and 2.21). This model is used to infer the atomic density (and hence the vapor temperature) as well as the isotopic fraction inside the vapor cell, by fitting the transmission spectrum of a weak probe with a typical power $P_0 \simeq 1$ μW.

Result: The blue curve in figure 2.4 c) shows a measured transmission spectrum in a $L = 10$ mm long ^{87}Rb cell. The black line shows the corresponding least square fit result with the obtained parameters: $T = 150$ °C and $n_{87} = 1$. The agreement between the fit and the experimental is impressive.

2.3.3 Imaging

All fluid of light experiments require the cell output imaging in order to probe the fluid dynamics. In all experiments of this work, the 4f imaging configuration is used for imaging the cell output plane. The Hamamatsu ORCA Flash 4.0 camera is used for all experiments. It has the quantum efficiency of 55 %, the frame rate up to 30 Hz if the full-size images are acquired (2048×2048 pixels of 6.5 μm pitch). Note that the frame rate can be increased if reduced sized images are acquired. Depending on the imaging magnification, the spatial resolution of 2-3 µm was reached in the images.

2.4 Limitations

This chapter presented the details of the hot Rb vapors as a platform for exploration of the fluids of light. In the first part, the derivation of the to date most realistic linear susceptibility identified two efficient knobs to control the light-matter interaction in this platform: the atomic density and the the laser detuning from resonance. The second part focused on the experimental control of these parameters. Together with the laser intensity, one gets at least three experimentally well controllable parameters to tune the light-matter interaction and hence the photon-photon interactions. Before describing in details the link between the two, (this is the object of the next chapter), several remarks need to be made on the experimental platform:

Absorption: The resonant interaction used in this platform, inevitably adds photon losses via absorption (or more precisely scattering) controlled by the imaginary part of the susceptibility. Nevertheless one can note that the linear refractive index variation $n^{(1)} - 1$ controlled by the real part of the susceptibility (eqn. 2.16) decays slower with the detuning $\sim 1/\Delta$ than the absorption rate $\sim 1/\Delta^2$. Therefore for the fluid of light experiments the common strategy [54, 165] strategy consists in working with a laser detuned sufficiently far from resonance, to avoid significant absorption while keeping significant refractive index difference.

Finite cell length: Another limitation which rather concerns all the fluid of light platforms in the propagating geometry is the finite cell length. In fact, the fluid's evolution in presence of photon-photon interactions can therefore be studied only until the finite final "time". A possible so far not sufficiently explored strategy to overcome this issue could consist in reinjecting the fluid's measured output state into the non-linear medium and for accessing even longer times, reiterating this procedure [147, 105].

Impossibility to image inside: Finally, another obstacle for accessing the fluid's state continuously for different propagation times consists in the impossibility to image inside a non-linear medium. This results from the fact that if one tries to do so, the propagation between the imaged plane inside the cell and the exit plane affects the image in an intensity dependent way, which may affect the measured image in an uncontrolled way. Therefore in the fluid of light experiments "times" before the one corresponding the medium's exit plane, can be probed. A possible strategy to overcome this issue will be discussed in the chapter 4.

Chapter 3

Nonlinear refractive index measurement

3.1 Objective of the chapter

What did we know? This chapter is devoted to understanding the photon-photon interactions in hot Rb vapors. First, it is explained how in case of resonant light-matter interaction the saturation gives rise to the Kerr effect, based on the existing literature. As in the previous chapter, the discussion starts with the simplest 2-level atomic model, which is then upgraded step by step by adding some more relevant effects. This approach is in line with current research strategy on quantum optics and light-matter interaction in hot atomic vapors, which consists in starting with a simple model and generalizing it by including various additional effects existing in hot atomic vapors. In order to highlight (without going into details) the complexity and rich physics of possible non-linear optical effects in hot atomic vapors, the figure 3.1 a) shows a measured fluorescence spectrum [159] from a hot Rb vapor illuminated with a strong laser beam around the D2 resonance at 780 nm, and figure 3.1 b) shows the Rb atomic level structure with all observed transitions in the visible domain [159], where the only one, labeled with "q", was explored in this work.

How accurate do we model the Kerr effect? Indeed, to the best of my knowledge, to date, there is no theoretical model, predicting quantitatively the non-linear variation of the refractive index in hot Rubidium vapors. Nevertheless, the intensity dependent 2-level atomic susceptibility gives already a good qualitative picture of the optical behavior of Rubidium vapors, while completely failing the quantitative prediction.

Finally, in order to explain the observed results, the discussion focuses on the theoretical description of the Kerr interactions, focusing on the role of additional effects, such as the transit broadening and hyperfine optical pumping, which become relevant in the non-linear regime and are crucial for more accurate description of Kerr interactions in hot Rubidium vapor.

This work's contribution to its accurate measurement/control: Then the two off-axis interferometric experimental techniques, developed and used throughout the whole work in order to measure these interactions, are described. The results of application of both techniques for the Kerr index measurement in hot Rubidium vapor cells are shown, revealing in particular two medium specific features of the Kerr photon-photon interactions in Rb vapors, measured for

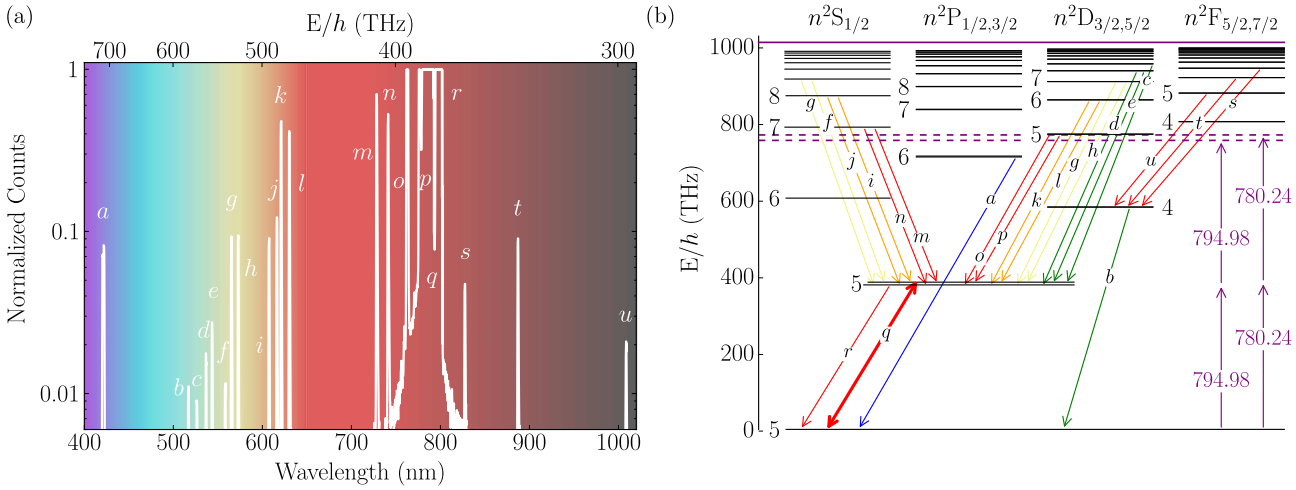

Figure 3.1: List of possible transitions in the visible range for Rubidium. a) Measured fluorescence spectrum of a hot Rb vapor cell ($T = 200$ °C) illuminated with a relatively intense D2 line resonant laser beam (780 nm). b) Energy levels involved in the possible optical transitions in Rb atom. In this work, only the line q (the Rb D2 line at around 780 nm) was addressed in all experiments. Adapted from [159].

the first time in this work. Firstly, strong dependence of the hot Rubidium's Kerr index on the laser beam size is reported. Secondly, preliminary experimental measurement of its transient evolution before reaching the steady-state value, are shown.

3.2 Photon interactions in dense Rubidium vapors: how it works?

3.2.1 Revisiting the 2-level model

Kerr effect and the susceptibility: As briefly mentioned in the previous chapter, this work's strategy to produce the Kerr effect induced photon-photon interactions exploits the line saturation. Reminding the definition from the introduction chapter 1, a medium with the Kerr effect has a refractive index which linearly depends on the light's intensity: $n = n^{(1)} + n_2.I$. In order to include a more general dependence of the refractive index on intensity, such as, for example, the saturable Kerr non-linearity ($n = n^{(1)} + n_2.I/(1 + I/I_s)$), it is more convenient to define the intensity dependent refractive index variation $\Delta n(I) = n(I) - n^{(1)}$. The refractive index, as well as the extinction coefficient α are linked to the susceptibility as:

$$n = (1 + \mathrm{Re}\{\chi\})^{1/2} \simeq 1 + \frac{\mathrm{Re}\{\chi(\Delta, I)\}}{2} \quad \text{and} \quad \alpha = k_0 \mathrm{Im}\left(\chi(\Delta, I)\right) \tag{3.1}$$

where I assume that $|\chi| \ll 1$, which is a safe assumption for hot Rb vapors at temperatures considered in this work.

Starting point: 2-level system: As a first step one can now recall the results (eqns. 2.16 and 2.15) derived in the previous chapter for a far detuned two level system and simply use their

intensity dependence:

$$\chi(\Delta, I) = \chi^{(1)}(\Delta)\frac{1}{1 + I/I_s(\Delta)} = \chi^{(1)}(\Delta) - \frac{\chi^{(1)}}{I_s(\Delta)}\frac{I}{1 + I/I_s(\Delta)} \tag{3.2}$$

$$\chi^{(1)}(N, \Delta) = \frac{N d_{ge}^2}{\hbar\epsilon_0\gamma}\frac{i - \Delta/\gamma}{1 + \Delta^2/\gamma^2} \tag{3.3}$$

From the eqn.: 3.2 one can see that at weak intensity ($I/I_s(\Delta) \to 0$), the susceptibility logically tends to its linear regime expression $\chi^{(1)}(\Delta)$. The intensity dependent factor is strictly equal to the population difference between the ground and the excited states, as shown in previous chapter (see eqn.: 2.17). Keeping only the first order term in laser intensity and recalling the definition of the light intensity $I = \epsilon_0 n^{(1)} c|\mathcal{E}|^2/2$, one gets the direct link with the third order non-linear optical susceptibility $\chi^{(3)}$:

$$\chi(\Delta, \mathcal{E}) \simeq \chi^{(1)}(\Delta) + \chi^{(3)}(\Delta)|\mathcal{E}|^2 = \chi^{(1)}(\Delta) + \frac{-\chi^{(1)}(\Delta)}{|\mathcal{E}_s(\Delta)|^2}|\mathcal{E}|^2 \tag{3.4}$$

where $\mathcal{E}_s$ is the electric field value, corresponding to the saturation intensity. Furthermore, with the following definition of the light intensity: $I = \epsilon_0 c n^{(1)}|\mathcal{E}|^2/2$, and using the eqn. 3.1, the Kerr index n_2 is linked to the third order susceptibility as follows:

$$n_2 = \frac{\mathrm{Re}\left\{\chi^{(3)}\right\}}{\epsilon_0 c n^{(1)}} \tag{3.5}$$

In fact, the Doppler broadening is neglected with the assumption $|\Delta| > 2\sigma_D \simeq 0.8$ GHz and one can imagine that multiple transitions of the Rb hyperfine structure somewhat add up to give a result described by an effective two level model [165]. While the validity of this interpretation will be investigated throughout the chapter, this result gives a good starting point allowing to understand some known characteristic features of hot Rb vapors. Recalling the definition of the saturation parameter, eqn. 2.11, but now including the self broadening:

$$s = \frac{\Omega^2}{\gamma\Gamma}\frac{1}{1 + \Delta^2/\gamma^2} = \frac{I}{I_s(\Delta)}, \tag{3.6}$$

one can assess the typical scalings for various quantities.

- **Non-linear Kerr coefficient**: from the eqn. 3.2 it follows that the refractive index variation can be written as: $\Delta n = n_2 I/(1+I/I_s)$. Then, using the eqn. 3.1, the Kerr index becomes:

$$n_2(\Delta) = -\frac{\mathrm{Re}\{\chi^{(1)}(N, \Delta)\}}{2I_s(\Delta)} \underset{\Delta \gg \gamma}{\simeq} \frac{N d_{ge}^2}{2\hbar\epsilon_0\gamma I_s(0)}\frac{1}{(\Delta/\gamma)^3} \tag{3.7}$$

  where I used that in the far-detuned regime $\Delta \gg \sigma_D$ we necessarily have $\Delta \gg \gamma$. Note that being an antisymmetric function of the detuning, the Kerr index changes sign as one changes the spectral side of the resonance. This is a very useful feature if one wants

to change the photon interaction nature from repulsive to attractive. If $\Delta < 0$, the interactions are repulsive, resulting in the beam's self de-focusing and for $\Delta > 0$ the interactions are attractive and result in the beam's self focusing. All experiments shown in this work were performed in the self-defocusing regime ($\Delta < 0$), which is dynamically more stable against the modulational instability, than the self-focusing case [55, 96].

- **Non-linear absorption coefficient**: Similarly the eqn. 3.2 also tells us that absorption rate changes with intensity as: $\Delta\alpha = \alpha_2 I/(1 + I/I_s)$.

$$\alpha_2(\Delta) = -\frac{Nd_{ge}^2}{\hbar\epsilon_0\gamma I_s(0)}\frac{1}{(1+\Delta^2/\gamma^2)^2} \underset{\Delta\gg\gamma}{\simeq} -\frac{Nd_{ge}^2}{\hbar\epsilon_0\gamma I_s(0)}\frac{1}{(\Delta/\gamma)^4} \tag{3.8}$$

  Note that in difference to the Kerr index, the non-linear absorption coefficient is a pair function of the detuning and is always negative, meaning that no matter the sign of detuning, under effect of the laser intensity the absorption will drop.

- **Saturation intensity**: Both non-linear refraction and absorption saturate at large laser intensity. This is logical within a two-level model which becomes transparent at the infinite intensity, resulting in: $\Delta n(\Delta, I) \underset{I\to\infty}{\to} \mathrm{Re}\{\chi^{(1)}(\Delta)\}/2$ for the refractive index variation and in $\Delta\alpha(\Delta, I) \underset{I\to\infty}{\to} -\mathrm{Im}\{\chi^{(1)}(\Delta)\}$ for the absorption. From the eqn. 3.6 it is known that:

$$I_s(\Delta) = I_s(0)(1 + \Delta^2/\gamma^2) \tag{3.9}$$

  At constant laser intensity, the saturation parameter reduces hence as $s \sim 1/\Delta^2$ with the laser detuning. This means that in order to have the non-linear refractive index variation most similar to the pure Kerr effect, $\Delta n \simeq n_2 I$, it is preferable to increase the detuning and in this way to move far away from resonance. However, this will reduce the Kerr index n_2, which decays as $\sim 1/\Delta^3$. Therefore at a given atomic density N, the laser needs to be tuned to an intermediate detuning value to have a sufficiently large Kerr index n_2 while having a sufficiently small saturation parameter. As will be seen in the following, the atomic density N plays a crucial role in this regard, because increasing N (by means of the vapor temperature) allows to increase the detuning (and therefore reduce the saturation parameter) while keeping the Kerr index n_2 sufficiently large.

  Value of the on-resonant saturation intensity: Another a priori fixed atomic parameter, controlling the Kerr index and the saturation parameter, is the on resonant saturation intensity $I_s(0)$. While in case of a two level system it has a well known simple expression:

$$I_{s,ge}(0) = \frac{\hbar^2\gamma^2\epsilon_0 c}{C_{ge}^2 d_0^2} \tag{3.10}$$

  as will be shown later, there are several reasons for this expression to be inaccurate for prediction of the real saturation behavior in hot Rb vapors. However, as a reference value for comparison, I give a value of the 2 level saturation intensity of the Rb D2 line:

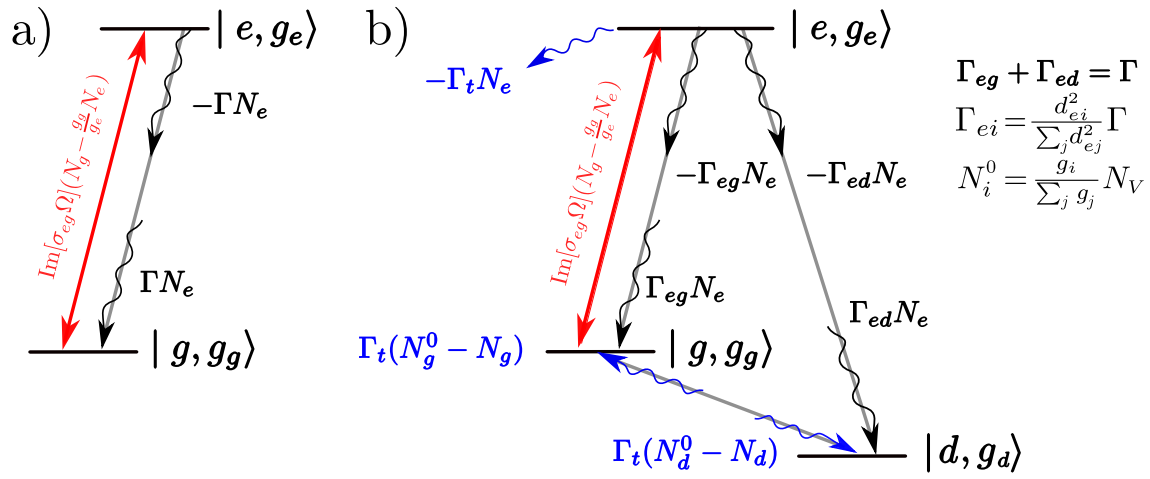

Figure 3.2: Optical pumping modelling within a 3-level approxiamtion. a) The rate equations describing a closed two-level system: no optical pumping. N_e stands for the excited state population. b) A three level system with two ground states via the decay rates Γ_{eg} and $\Gamma_e d$, distributed according to the corresponding fractional transition strengths: the excited state can now decay into both ground states, giving rise to the optical pumping. The arrows show the necessary the dynamical rates due to the laser (red), spontaneous emission (black) and the transit rate (blue), added via it's estimated value Γ_t (see eqn. 3.13) to be taken into account for states' population modelling. The atomic populations N_i^0 and N_i are respectively those at thermal equilibrium (no laser) and driven out-of equilibrium by the laser. The populations N_i^0 are calculated from the total vapor density N_V as being equally distributed in each sublevel of both g_i degenerate ground states.

$I_{s,2L}(0) = \hbar^2\gamma^2\epsilon_0 c/d_0^2 = 32.7$ W/m^2, with $d_0 = 5.177e.a_0$, $\gamma = (\Gamma_0 + \beta N)/2$ [160] and $N = 8.4 \times 10^{13}$ cm^{-3}, corresponding to $T = 150$ °C. Note, that if $\gamma = \Gamma_0/2$ is taken, one gets: $I_{s,2L}(0) = 5.6$ W/m^2. Note that here we suppose linear laser polarization.

Non-linear absorption can be neglected: From the eqns. 3.7 and 3.8 one can infer that the ratio between the Kerr index and the non-linear absorption coefficient increases with laser detuning as $n_2/\alpha_2 = \Delta/\gamma \gg 1$. In the far-detuned regime, typically used for the experiments in this work, α_2 becomes negligible with respect to n_2. For example, at $\Delta/(2\pi) = -2$ GHz $n_2/\alpha_2 \simeq 330$. This explains why in hot Rb vapors the intensity dependent phase variation may be observed without significant variation of transmission. Moreover, throughout this work, the non-linear absorption was checked to be negligible with respect to the linear absorption. Therefore the non-linear absorption will not be taken into account in the propagation equation to describe the fluid of light's evolution.

3.2.2 Optical pumping and transit rate

Non-linear case: superposition of the transition responses not valid anymore: As in the previous chapter's linear case, the non-linear optical susceptibility also includes contributions of various involved transitions. However, in difference to the linear case, in which the total

susceptibility is simply the sum of independent two-level susceptibility contributions of all possible transitions, the situation is more complicated in the non-linear case and in particular, the "superposition principle" approach is not anymore valid. There are at least two reasons for that, both in link with the modified atomic ground/excited states populations in presence of the laser field. On the one hand, the various transitions, sharing the common ground state, are not anymore independent, because the photon absorption through any of these transitions, affects the ground state population of the others. On the other hand, as soon as the atoms are promoted to the excited state, due to the hyperfine structure of the $5S_{1/2}$ state, they can decay into two possible ground states via spontaneous emission. Due to the sufficiently short lifetime of the excited state (typically below $\sim 1/\Gamma_0 \simeq 30$ ns), this results in the pumping of the atoms from the ground state to the second ground state, as shown on Fig.: 3.2 b). This effect is known as the hyperfine optical pumping [110, 131] and will be considered in more details in the following.

3.2.2.1 Optical pumping

The presence of an additional decay channel for the excited state implies that in order to consider the system as closed, it should now involve at least three levels: the two ground states and an excited state as shown on figure 3.2 b). The second ground state, initially not addressed by the laser, and corresponding to a further detuned transition, acts as a dark state, because the atoms decaying into this state, become almost "invisible" to the laser. This phenomenon is called hyperfine optical pumping. One can estimate the steady-state rate of the optical pumping as a conditional probability of decaying from the excited state (given by γ_{ed}) being given the probability for an atom to be at the excited state (given by the excited state population within the two level approximation):

$$R_{OP} = \gamma \times \rho_{ee} = \frac{\gamma_{ed} s}{2} \frac{1}{1+s} \underset{s \ll 1}{\propto} \frac{\Omega^2}{2\Gamma} \tag{3.11}$$

where γ_{ed} is the spontaneous emission rate to the dark state. Pure theoretically, if the density matrix is only governed by the laser "pump" (absorption and stimulated emission) and the spontaneous emission, then no matter the laser intensity, the steady state solution of the ground and excited states becomes zero while total atomic population appears "pumped" in the dark state, making the medium transparent.

3.2.2.2 Effects compensating the optical pumping

Obviously, this is not the full story of what can happen to the atomic populations in a hot Rb vapor cell. In fact, thanks to the atomic thermal motion, thermal energy and the dipole-dipole interactions, several new effects arise acting as compensation to the optical pumping. In the end, the system's steady state is a balance among all pumping and depumping rates.

- **Transit broadening**. First, it has to be mentioned that the laser beam has a finite size and the atoms are driven out of their thermal equilibrium populations only inside the beam.

Recalling, that at $T = 150$ °C the atoms move on average at $u_{3D} = \sqrt{3k_BT/m} \simeq 350$ m/s, this implies, that there are permanently the atoms entering and exiting the beam. This results in a small yet important mechanism acting on the atomic populations inside the beam. As a first order correction, this result can be modeled as a transit relaxation rate:

$$\left(\frac{\partial \rho_{ii}}{\partial t}\right)_{tr} = \Gamma_t(\rho_{ii}^{(0)} - \rho_{ii}) \tag{3.12}$$

with i is the considered state: ground, excited or the dark one. In these equations the first rhs term accounts for the atoms entering the beam and which are supposed at their equilibrium populations, while the second term accounts for the laser driven atoms leaving the beam. As for the value of of the transit rate Γ_t, several expressions have been reported in [65, 131, 71, 55], all of them have in common the scaling: $\Gamma_t \propto u/\omega_0$ with $u = \sqrt{2k_BT/m}$ and ω_0 the $1/e^2$ radius (in intensity) of a Gaussian beam. Taking the value reported in [131] as reference, one has:

$$\Gamma_t = \sqrt{\frac{2}{\pi \ln(2)}}\frac{u}{\omega_0} \tag{3.13}$$

To obtain this result, all possible transverse trajectories crossing the beam within its FWHM diameter, were averaged over the 2D Maxwell-Boltzmann probability distribution of the atomic velocities [131, 55]. Note that the choice of the beam size is somehow arbitrary: in fact, it is possible to go one step further and define an effective intensity dependent beam size, inside which the atoms "see" the intensity above the effective saturation intensity at the given detuning [71]:

$$\Gamma_{t,I}(I_0) = \left[\frac{1}{2}\ln\left(\frac{I_0}{I_s(\Delta)}\right)\right]^{-\frac{1}{2}}\Gamma_t \tag{3.14}$$

with I_0 the laser's central intensity. This correction was, however, not implemented in this work.

- **Collisions and dipole-dipole interactions** Another effect prone to affect the atomic populations in the high vapor density regime, stems from the atomic collisions. For example, in [151], the authors had to include the the hyperfine ground state changing collisions (beyond the optical pumping) into account, in order to reproduce theoretically the observed intensity dependent on-resonant absorption in hot Rb vapors. Moreover, as highlighted in [160], the interactions between two identical atoms in superposition of the ground and excited states, contribute significantly to the optical susceptibility via the self-broadening already in the linear regime, where the atomic populations aren't affected. Therefore a more complex situation in terms of possible interaction mechanisms is expected in the non-linear regime, where the atomic populations are affected by the laser. For example, an effect, well known to all experimentalists, working with hot Rubidium vapors, is the

emergence of blue fluorescence from the Rb cell, heated to temperatures above 130 °C, and illuminated with a near resonant cw laser around the D2 (or D1) lines. For temperatures below ≃160 °C, this effect stems from the so called "energy pooling", which arises when two optically-excited atoms collide inelastically, resulting in energy transfer to states with higher energy [159]. Indeed, as can be seen on fig. 3.1 b), the frequency sum of two photons at 780/795 nm is close, up to several THz, to the transition frequency between the 5S and 5D states. The difference being compensated by the atomic thermal energy, the inelastic collision promotes one of the atoms to the 5D which then rapidly decays to 6P and then back to the 5S ground states, emitting a photon at 422 nm. At the temperatures above ≃160 °C, the dipole-dipole interactions seem to drastically enhance the fluorescence from the even higher-lying states, as shown on fig. 3.1 a) (referring to the experiment performed in [159]), which cannot anymore be explained by the energy pooling mechanism [159]. These examples show the complexity of the light-matter interactions in hot Rb vapors emerging in the non-linear regime. Yet, the effect of collisions on the non-linear refraction in hot Rb vapor has not been investigated in this work.

Optical pumping and the non-linear refractive index: While numerous studies pointed out the drastic effect of hyperfine optical pumping on the intensity dependent absorption in alkali metal vapors [110, 131, 143, 98, 140, 71, 151], as well as the atomic ensembles trapped around nanofibers [82], its effect on the refractive effect of the hot alkali vapors has barely been discussed. In the experiments measuring the Kerr effect in atomic vapors: [7, 102] the authors report a value $n_2 \simeq 10^{-11}$ m^2/W for Rb vapor heated at 78 °C at 1 GHz detuning. Moving to higher temperatures, in [165] the authors measure the non-linear phase in a Rb vapor cell heated to $T_V \simeq 150$ °C and model the observed results with an effective two level system.

3.2.2.3 Modelling the optical pumping

To the best of my knowledge, the influence of the optical pumping compensated by the transit rate on the Kerr effect in hot atomic vapors was first theoretically explored in [55]. Following the approach developed in [55], it is useful to derive the optical susceptibility of a 3-level system shown on fig. 3.2 b) in order to quantify the the effect of the optical pumping on the Kerr effect in hot Rb. For this, we rewrite the OBEs for the density matrix elements of the three level system:

$$\frac{\mathrm{d}\rho_{gg}}{\mathrm{d}t} = -\mathrm{Im}\left\{\sigma_{eg}\Omega_{ge}\right\} + \Gamma_{eg}\rho_{ee} + \Gamma_t(\rho_{gg}^{(0)} - \rho_{gg}) \tag{3.15}$$

$$\frac{\mathrm{d}\rho_{ee}}{\mathrm{d}t} = \mathrm{Im}\left\{\sigma_{eg}\Omega_{ge}\right\} - (\Gamma + \Gamma_t)\rho_{ee} \tag{3.16}$$

$$\frac{\mathrm{d}\rho_{dd}}{\mathrm{d}t} = (\Gamma - \Gamma_{eg})\rho_{ee} + \Gamma_t(\rho_{dd}^{(0)} - \rho_{dd}) \tag{3.17}$$

$$\frac{\mathrm{d}\sigma_{eg}}{\mathrm{d}t} = -\frac{i\Omega_{ge}}{2}(\rho_{ee} - \rho_{gg}) - \left(\frac{\Gamma}{2} - i\Delta\right)\sigma_{eg} \tag{3.18}$$

In this approach we suppose that the laser couples only the $g-e$ transition, because the laser is

significantly more detuned from the $d-e$ transition. The equilibrium populations of the ground states $\rho_{gg}^{(0)}$ can already be explicited as the fractional degeneracies: $\rho_{ii}^{(0)} = g_i/(g_g + g_d) = G_i$. Again, one can search for the steady-state solution ($\mathrm{d}\rho/\mathrm{dt}$=0) of the density matrix in order to evaluate the medium's susceptibility in the cw illumination case. At steady state the eqn. 3.18 becomes:

$$\sigma_{eg} = \frac{\Omega}{2\gamma}\frac{i - \Delta/\gamma}{1 + (\Delta/\gamma)^2}(\rho_{gg} - \rho_{ee}) \tag{3.19}$$

From previous chapter (eqn. 2.15) we know that this quantity needs to be calculated in order to access the optical susceptibility. From the eqn. 3.19 one remarks that for the calculation one needs to solve the difference between the ground and excited state populations (also called the population inversion in laser physics classes). In case if the ground and the excited states have different degeneracies g_i, the population inversion factor $(\rho_{gg} - \rho_{ee})$ has to be replaced by: $\left(\rho_{gg} - \frac{g_g}{g_e}\rho_{ee}\right)$. For the simplicity of the main text the derivation of the steady-state solutions ($\mathrm{d}\rho_{ii}/\mathrm{dt}$=0, $i = \{g, e, d\}$) of the density matrix populations can be found in in the appendix section A. Interestingly, one ends up with the population inversion which is qualitatively governed by the same saturation law as in case of a 2-level system (eqn. 3.2), but with a modified saturation intensity [71] (and consequently the Kerr index form the eqn. 3.7):

$$\rho_{gg} - \frac{g_g}{g_e}\rho_{ee} = \frac{G_g}{1 + I/I_{s,3L}(\Delta)} \tag{3.20}$$

$$I_{s,3L}(\Delta) = \frac{2\Gamma_t(\Gamma + \Gamma_t)}{\left[\Gamma_{ed} + \Gamma_t(1 + \frac{g_g}{g_e})\right]\Gamma} I_{s,2L}(\Delta) \simeq \frac{\Gamma_t}{\gamma_{ed}} \times I_{s,2L}(\Delta) \tag{3.21}$$

$$n_{2,3L}(\Delta) \simeq \frac{\gamma_{ed}}{\Gamma_t}\frac{\mathrm{Re}\{\chi^{(1)}(\Delta)\}}{2I_{s,2L}(\Delta)} = \frac{\gamma_{ed}}{\Gamma_t} \times n_{2,2L}(\Delta) \tag{3.22}$$

one can notice, that the population inversion in this three level system, given by the eqn. 3.20, takes the same form as in the two-level system (see eqn. 3.2). The intensity dependence in the denominator comes from the definition of the saturation parameter (3.6). This reveals, however, a new saturation intensity, $I_{s,3L}$, which is given in the eqn. 3.21 as function of the saturation intensity of a 2-level system with no optical pumping $I_{s,2L}$ (with $I_{s,2L}$ given by the eqn. 3.10). Note that if $\Gamma_{ed} = \Gamma_t = 0$ and $g_g = g_e$, then both saturation intensities become equal. The second equality in the eqn. 3.21 is a valid approximation, stemming from the fact, that $\gamma_{ed} \gg \Gamma_t$. This result shows that the saturation intensity is drastically ($\Gamma_t/\gamma_{ed} \ll 1$) lowered in presence of the optical pumping and the atomic transit motion. Summarizing up the obtained results, the susceptibility becomes:

$$\chi(\Delta) = \frac{\chi^{(1)}(\Delta)}{G_g}\left(\rho_{gg} - \frac{g_g}{g_e}\rho_{ee}\right) = \chi^{(1)}(\Delta)\frac{1}{1 + I/I_{s,3L}(\Delta)} \tag{3.23}$$

with $\chi^{(1)}$ being the linear susceptibility given in the eqn. 3.3. Finally, one can remark, that logically, neither the optical pumping nor the transit rate affect the linear optical susceptibility.

3.2.3 Discussion and conclusion of the model

The derived optical susceptibility of a three level system taking into account the optical pumping and the transit rate has the same expression as the one of the closed 2 level system but with a modified saturation intensity. This implies that all the scalings of the Kerr index and the saturation intensity, explicited at the beginning of the chapter with the 2-level model, remain valid. However, the value of the on resonant saturation intensity is strongly affected as will be shown in the following.

Saturation intensity in a 3-level system: In order to evaluate the influence of the optical pumping on the non-linear susceptibility and compare it with the closed 2-level model, the results, obtained with the 3-level system, were used for the calculation of the line saturation, the Kerr index and the saturation intensity of the ^{87}Rb D2 line's $F_g = 2_e$ transitions, taking the vapor temperature equal to $T = 150$ °C. The results are shown on figure 3.3. The energy diagram of the involved states is shown on figure 3.3 a). Red arrows show the laser driven transitions allowing the atoms to be excited from the $5S_{1/2}$ $F_g = 2$ state to the $5P_{3/2}$ $F_e = 1, 2, 3$ states, and the gray lines show the possible spontaneous decay channels.

Figure 3.3 b): While the states $5P_{3/2}$ $F_e = 1, 2$ can decay into both $5S_{1/2}$ $F_g = 1, 2$ states, due to the selection rules, the $5P_{3/2}$ $F_e = 3$ state can only decay into the $5S_{1/2}$ $F_g = 2$ state. Therefore the $F_g = 2 \rightarrow F_e = 3$ transition is naturally a closed or the so called "cycling" transition, immune to the optical pumping because $\Gamma_{ed} = 0$, which will serve as the reference for a closed two-level system. For all transitions the results have been calculated independently, i.e. the influence of different transitions on each other was neglected. Figure 3.3 b) shows the relative (with respect to the linear case) variation of the on resonant ($\Delta = 0$) optical susceptibility (see eqn. 3.23) for the three considered transitions as function of their respective closed-two-level saturation parameter $s_{2L} = I/I_{s,2L}$ (with $I_{s,2L}$ given by the eqn. 3.10). The beam waist of ω_0=2 mm was taken for the calculation. The corresponding saturation intensities, corresponding to the x-axis positions where the curves are equal to 0.5, are: 2, 0.7 and 50 W/m^2 for the $F_e = 1, 2, 3$ excited states, respectively. The result for the $F_g = 2 \rightarrow F_e = 3$ transition serving as the reference, one can see, that the saturation of the transitions affected by the optical pumping happens at the 50-times smaller intensity which demonstrates that the optical pumping is the phenomenon, dominating the saturation of these lines.

Figure 3.3 c) and d): Figure 3.3 c) shows the Kerr index n_2, calculated using the 3-level model's saturation intensity $I_{s,3L}$ (eqn. 3.21) in the eqn. 3.7, for the three considered transitions, as function of the input beam waist ω_0. In fact, the beam size dependence emerges from the eqn. 3.13. While, as expected, the Kerr index of the $F_g = 2 \rightarrow F_e = 3$ transition does not depend on the beam waist, the situation drastically changes for the transitions affected by the optical pumping. Indeed, the Kerr index spans almost two orders of magnitude as the beam waist increases from 0.05 to 4 mm. The n_2 scales linearly with ω_0. The increase of n_2 with ω_0 can be explained as follows: as the beam size increases, the transit rate reduces and the optical pumping transfers more efficiently the atoms from the ground to the dark state, leading to a larger saturation of the transition. This means, the saturation intensity drops and the Kerr index increases (eqn. 3.7). This explanation is in agreement with the 3-level model's saturation

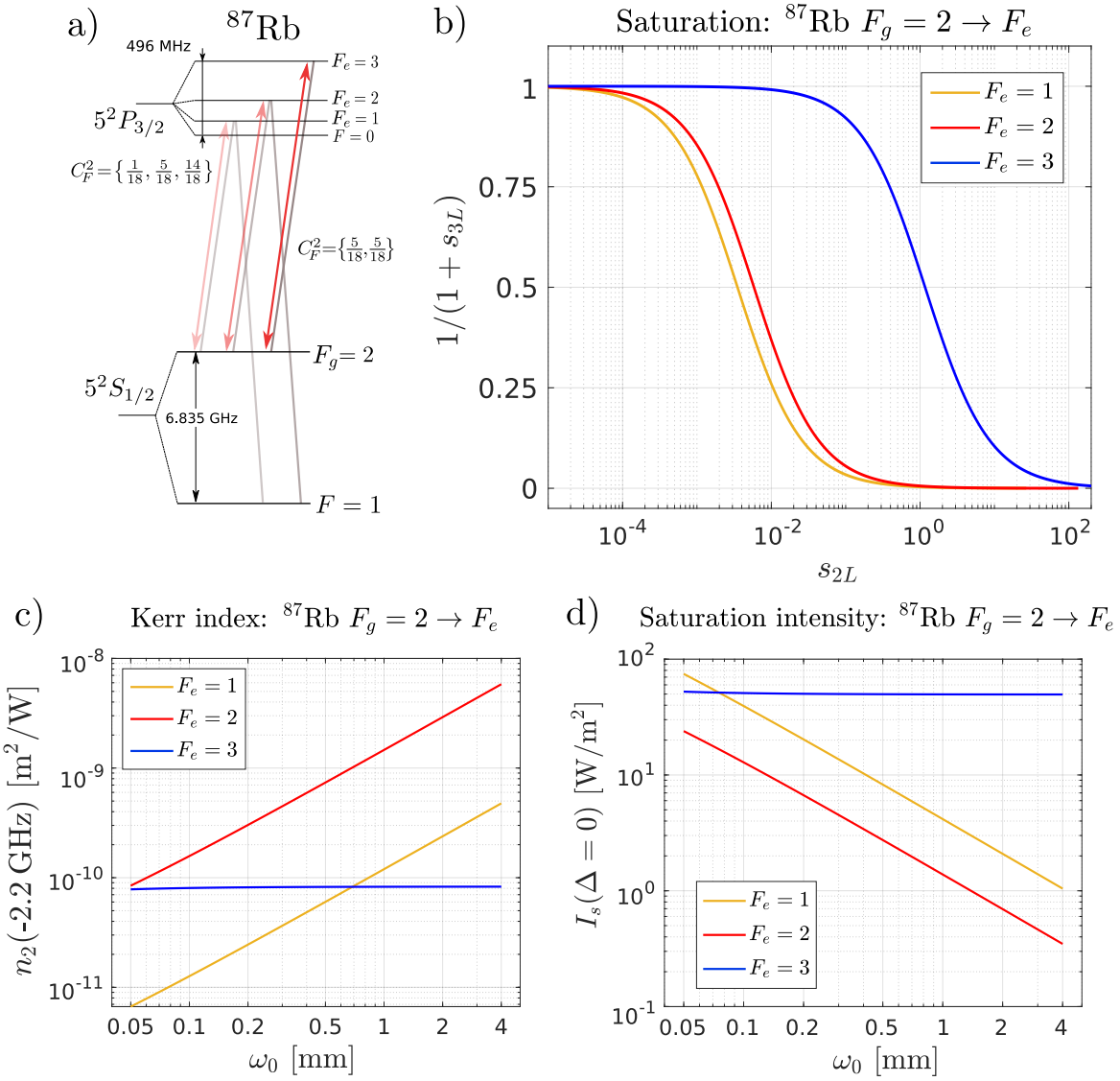

Figure 3.3: Calculated Line saturation, Kerr index and Saturation intensity within a 3-level approximation for ^{87}Rb D2 line's $F_g = 2_e$ transitions, at vapor temperature of $T = 150$ °C and the detuning $\Delta/(2\pi) = -2.2$ GHz. a) Energy diagram of the involved states. Red arrows show the laser driven transitions, the gray lines show the possible decay channels. b) Relative variation (with respect to the linear case) of the on resonant ($\Delta = 0$) optical susceptibility (see eqn. 3.23) for the three considered transitions as function of their respective two level saturation parameter $s_{2L} = I/I_{s,2L}$ (with $I_{s,2L}$ given by the eqn. 3.10, $\omega_0 = 2$ mm). The corresponding saturation intensities are: 2, 0.7 and 50 W/m^2 for the $F_e = 1, 2, 3$ excited states, respectively. c) the absolute value of the Kerr index n_2 (eqn. 3.7) and d) the saturation intensity $I_{s,3L}$ (eqn. 3.21) as function of the input beam waist ω_0, calculated using the 3-level model, for the three considered transitions. Note that Γ_t is given by the eqn. 3.13.

intensity $I_{s,3L}$ (eqn. 3.21), which is shown on figure 3.3 d) as function of the input beam waist ω_0, for the three considered transitions.

Laser coupling the dark state: In the considered three level model the laser only couples the

$g \rightarrow e$ transition, which is a valid approximation in the limit where the saturation parameter of the $d \rightarrow e$ transition is much smaller than that of the $g \rightarrow e$ transition ($s_{ge} \gg s_{de}$). Taking into account the "back-reaction" of the $d \rightarrow e$ transition on the line saturation is necessary for quantitative modeling of the non-linear susceptibility, but is not expected to contribute dominantly to the total result. The theoretical model taking into account simultaneous coupling of both ground states to the excited state by the laser, can be found in [55], where the results of a numerical calculation including both coupling fields, are shown.

Multi-level generalization: The results shown on figure 3.3 assume that the different considered 2-level or 3-level transitions are independent of each other. This assumption is not quite accurate because all transitions share the common ground state therefore the variation of its population affects them all simultaneously. Considering the problem from a different perspective, a commonly used strategy to simplify the hyperfine structure in hot Rb susceptibility consists in averaging over the excited hyperfine stated and considering them as a single effective state. However, this trick is not justified in the present situation, because of drastically different behavior of the open transitions compared with the closed one. In order to further quantitatively model the non-linear optical susceptibility it is needed to extend the study shown here, where all transitions saturate independently, to the case where the saturation of one transition affects the refractive index of other transitions.

Conclusion of the model: This section shows the drastic effect of the presence of two hyperfine ground states in a Rubidium atom, on the vapor's Kerr non-linearity. The line saturation responsible for the Kerr effect, is at least from the theoretical point of view so far, dominated by the optical pumping and the atomic transit motion. While qualitatively the saturation of the susceptibility follows the same law as a "closed" two-level system, the new Kerr index and saturation intensity need to be corrected by factors γ_{ed}/Γ_t and Γ_t/γ_{ed}, respectively, with γ_{ed} the decay rate of the excited state to the "dark" state and Γ_t the atomic transit rate. Importantly, this also results in the laser waist dependence of the considered non-linear coefficients, a feature which will be experimentally investigated in the next section.

3.3 Mach-Zehnder off-axis interferometry

3.3.1 State of the art

Global overview: From the experimental perspective, the non-linear refractive index (NLRI) variation results in the so-called self-phase modulation which alters beam's temporal or spatial characteristics. In the case of a cw laser most of the measurement techniques of the RI variation rely on measurements of: beam deflection [101, 125], its angular dispersion via transmission [139, 133, 7] (known as z-scan techniques), beam's far-field imaging [22, 165], optical bistability in cavity [156, 19], and beam's wavefront measurement [106, 39, 21, 126].

z-scan: For instance, the most commonly used technique in non-linear optics community is the so called "z-scan" technique [139]. This technique consists in the measurement of the normalized transmission through a pinhole aperture placed in the far-field of the sample as function of its position with respect to the waist of a focused Gaussian beam. This technique seems therefore not well suited to measure the Kerr index of different but fixed sized beams. Moreover, it requires therefore multiple transmission measurements to access the index variation at given laser frequency and it is necessary to work with a thin sample in order to minimize the beam extinction and hence have reliable signal.

Far-field rings: Another technique [22],[165] is based on an effect discovered even before the z-scan technique [45]. It relies on imaging intensity dependent annular pattern in the far-field of the sample and counting the number of rings. The origin of the pattern resides in multiwave interference of distinct points within the beam having the same Kerr-effect induced transverse angular direction. These parallel rays only interfere at infinity, what explains the far-field imaging configuration. The number of rings as well as the pattern width increases linearly with laser intensity before saturating at large intensity. The width of the pattern quantifies the beam's angular dispersion (available spatial frequencies) which increases during self phase modulation. At large input intensities (corresponding to more than 10 rings typically), the interference visibility at the centre shrinks. Yet in [22] the authors could successfully reproduce the experimentally observed far-field images with a model taking into account the saturation of NLRI and its anisotropy in the used photorefractive crystal.

Off-axis interferometric cell output imaging: The general idea is to place the non-linear medium in one arm of an interferometer (typically a Mach–Zehnder interferometer) while using a flat collimated reference, and access from an acquired interferogram the beam's phase via Fourier filtering and phase unwrapping algorithms [21, 128, 39]. This method is more precise than the z-scan or ring patterns approaches, easy to implement thanks to a single shot approach, and much more flexible since it allows for thick samples, time resolved measurements and spatial resolution. In this section the implementation of this interferometric measurement the intensity dependent refractive index variation of a Gaussian beam. The goal is twofold: on the one hand to describe the employed technique with the developed image processing procedure, which is, in principle, applicable in all propagating geometry fluid of light platforms, and on the other hand, to apply this technique for the characterization of the Kerr index n_2 as well as the saturation intensity in hot Rb vapors at different conditions. These inferred parameters

are crucial for designing any fluid of light experiment and for analyzing more quantitatively the experimental results.

3.3.2 Off-axis interferometry

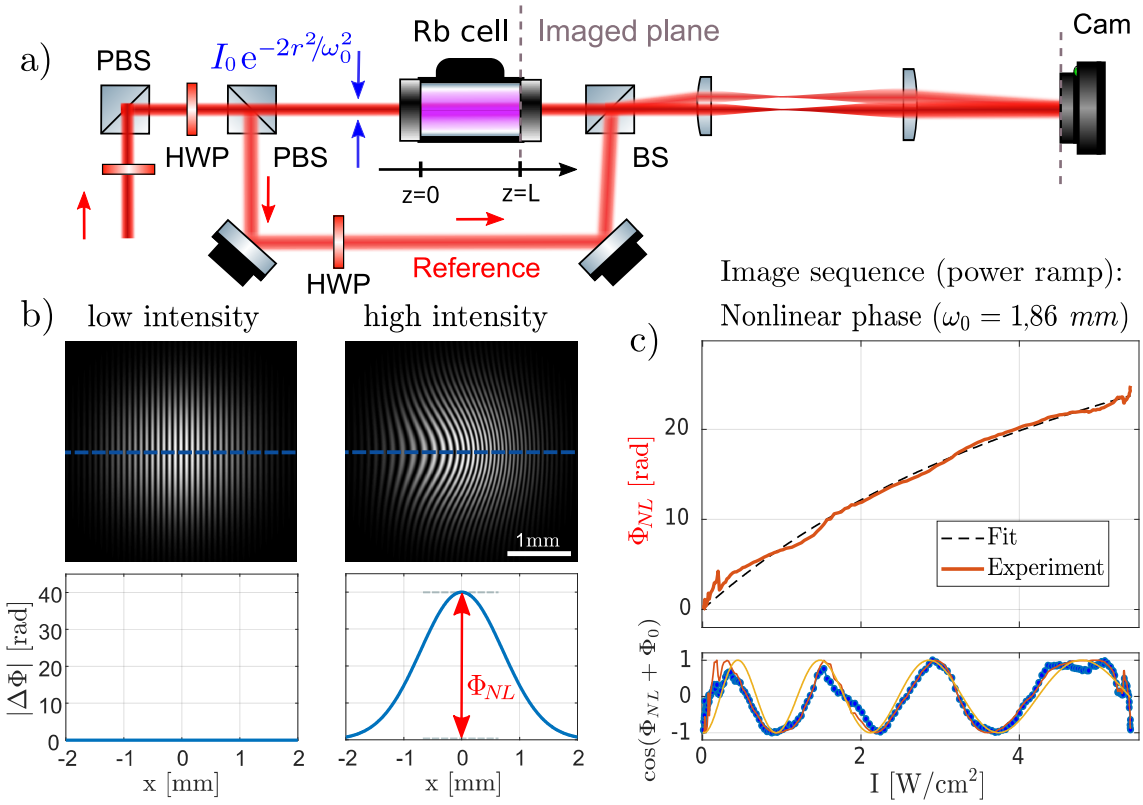

Figure 3.4: a) Experimental setup of the fluid phase measurement (HWP: half-wave-plate, BS: beam-splitter, PBS: polarizing beam-splitter, Cam: imaging camera). The first HWP and PBS serve to control the incident laser intensity. b) The calculated low intensity (left) and high intensity (right) interferogramms acquired by a camera. The reference phase being assumed constant (set to zero), the phase profiles of the measured beam along the dashed blue lines are shown below. The maximal accumulated non-linear phase appears at the beam centre in the intense laser case (dubbed Φ_{NL}). c) The peak (central) non-linear phase Φ_{NL} obtained from an image sequence, recorded during a laser power ramp, as function of the peak intensity of each image. The bottom graph shows the non-linear phase modulated intensity of the interferogramm's central pixel during the power ramp (see 3.3.4).

Interferometric techniques rely on measuring the local phase difference between a reference beam and the beam that has interacted with a non-linear medium. In experiments shown in this work, this is done by inserting the non-linear medium in one arm of a Mach–Zehnder interferometer (see Fig. 3.4 a). Tilting the reference beam by a small angle $\theta_r \simeq 10$ mrad, it is possible to access a spatially resolved image of the phase because the information on the latter becomes spectrally separated from the beam envelope information. The relative tilt between the

two beams leads to a fringe pattern shown in fig. 3.4 b). The left image corresponds to the case of a weak probe while the right image is typically obtained with a strong intensity beam. In the latter case the fringes appear curved at the center and this stems from the intensity dependent phase accumulated over propagation inside the cell with an intensity dependent refractive index. This is the key effect which will allow us to access the Kerr index and the saturation intensity of the medium. The output of the interferometer is recorded on a camera. Both signal and the reference beams are supposed to have the same polarization. When interfering with the signal beam, the reference beam slices a cut of the signal wavefront at a fixed angle. The intensity detected on the camera I_{cam} as function of $\mathbf{r} = (x, y)$ is given by:

$$\begin{aligned} &I_{cam}(\mathbf{r}) \propto |\mathcal{E}(\mathbf{r}, L) + \mathcal{E}_r(\mathbf{r}, L)\mathrm{e}^{i\mathbf{k}_r\mathbf{r}}|^2 = \\ &I(\mathbf{r}, L) + I_r(\mathbf{r}, L) + 2\sqrt{I(\mathbf{r}, L)I_r(\mathbf{r}, L)}\cos\left(\mathbf{k}_r\mathbf{r} + \varphi(\mathbf{r}) + \phi_0\right) \end{aligned} \tag{3.24}$$

For simplicity here I assume that $I = |\mathcal{E}|^2$. In the equation 3.24, $\mathbf{k}_r = k_0\theta_r$ accounts for the relative tilt, I is the intensity of the beams, φ is the signal beam's phase (or more precisely its spatially dependent part), which needs to be accessed and ϕ_0 is a constant stemming from the reference beam's phase. The former quantity allows to access the intensity dependent phase by, for example, comparing its value at the image's most and least intense areas. This measurement can then be performed different input laser powers, giving access to the phase versus laser intensity relationship, an example of which is shown on fig. 3.4 c). This curve can indeed be obtained by the intensity acquisition (see fig. 3.4 c bottom curve) of the pixel corresponding to the beam centre on the camera during a ramp of laser power. In the following, we give a detailed description of two complementary analysis procedures for extracting the non-linear index.

3.3.3 Single shot processing

Mathematical expression of the interferogramm intensity: The different stages of the image processing are shown on figure 3.5. For instance, a raw interferogram acquired is shown in fig. 3.5 a). The off-axis contribution performs a shift in the Fourier space for the last term of equation (3.24). This can be interpreted as a spatial heterodyne detection, with the reference beam shifting the frequencies of the signal, and the demodulation being done numerically. Phase information can therefore be obtained by filtering the complex envelope in Fourier space. Taking the Fourier Transform of this expression yields:

$$\tilde{I}_{\mathrm{cam}}(\mathbf{q}) = \tilde{I}_{\mathrm{s}}(\mathbf{q}) + \tilde{I}_{\mathrm{r}}(\mathbf{q}) + \mathcal{F}\left[\mathcal{E}_{\mathrm{s}}^{i\varphi(\mathbf{r})}\right](\mathbf{q}) * \left\{\mathcal{F}\left[\mathcal{E}_{\mathrm{r}}\right](\mathbf{q} - \mathbf{q}_r) + \mathcal{F}\left[\mathcal{E}_{\mathrm{r}}\right](\mathbf{q} + \mathbf{q}_r)\right\} \tag{3.25}$$

where $\tilde{}$ and $\mathcal{F}$ means the Fourier transform of a quantity and $*$ denotes a convolution product. In practice, the reference beam has a Gaussian profile slightly wider than the signal and the main effect of the convolution product is to shift the information on $\mathcal{E}_s e^{i\varphi(\mathbf{r})}$ in two symmetric satellite peaks on both sides of the peak at the origin, the latter accounting for the envelope of

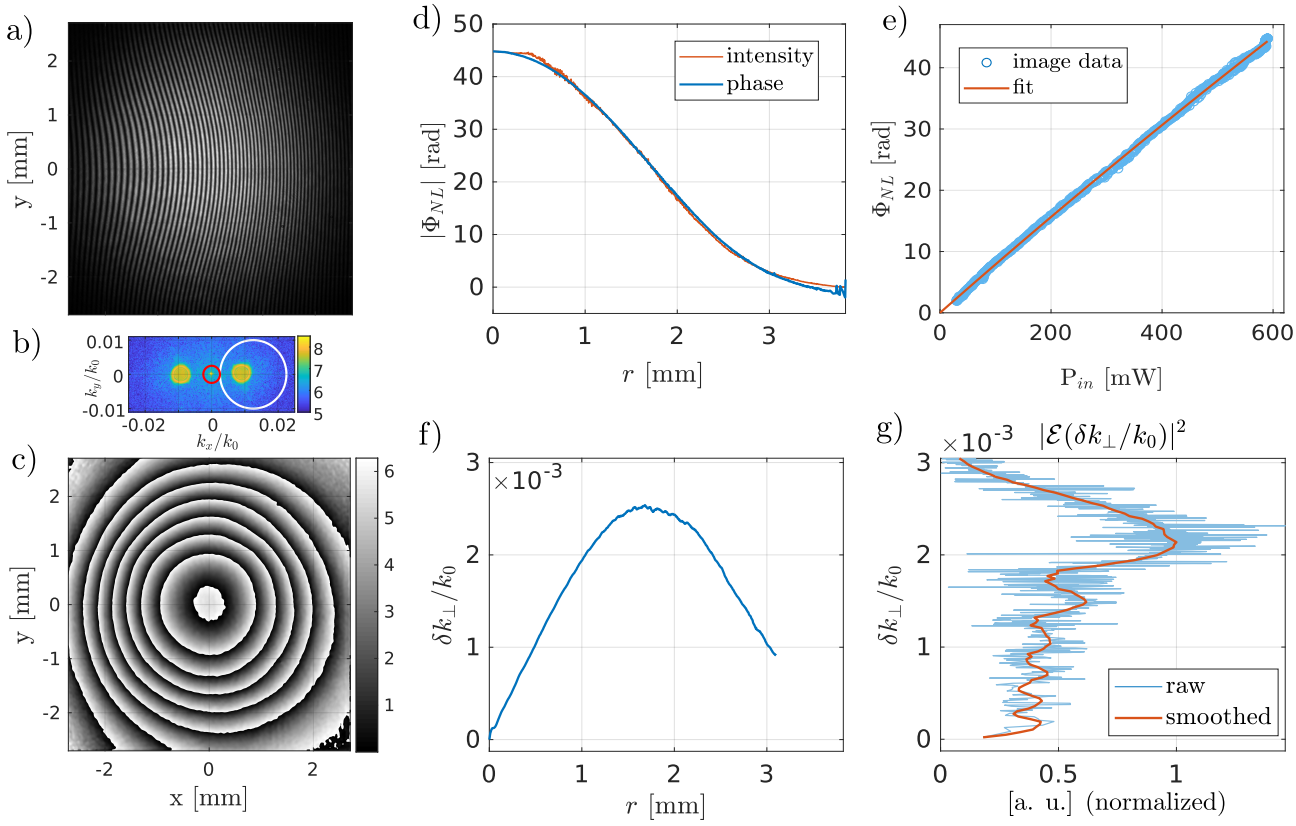

Figure 3.5: Single shot image processing method. a) Raw image. b) Spatial Fourier spectrum of the image. c) The signal beam's wrapped phase retrieved from the filtered complex envelope. d) The azimuthally averaged non-linear phase profile. e) The same radial phase but plotted as function of the radial beam's input intensity, converted into the beam power via the beam size $P = \frac{1}{2}\pi\omega_0^2 I$. f) The local radial beam deflection angle obtained from the radial gradient of the non-linear phase. g) The radial power spectrum of the calculated electric field (intensity $\times$ the non-linear phase from interferogramm).

the intensity. The satellite peaks represent the two first right hand side terms in the eqn. 3.25. An example of a spatial Fourier spectrum of an interferogramm is shown on fig. 3.5 b). After filtering any of the satellite peaks (by setting to zero all around the satellite peak), the inverse Fourier transform is computed to get directly the beam's complex envelope. By taking the argument of this quantity, we recover the total phase $\Phi(\mathbf{r})$:

$$\Phi(\mathbf{r}) = \varphi(\mathbf{r}) + \mathbf{k}_r \cdot \mathbf{r} = \underbrace{\Phi_{\mathrm{NL}}(\mathbf{r})}_{\text{nonlinear phase}} + \overbrace{\varphi_0}^{\text{phase offset}} + \underbrace{k_0(\theta_{r,x}x + \theta_{r,y}y)}_{\text{off-axis contribution}} . \tag{3.26}$$

Accessing the non-linear phase: In order to retrieve the nonlinear phase Φ_{NL} from the total phase, one needs to remove the off-axis contribution, by using the fact that it has a constant phase gradient everywhere on the image. For the calculation of the average phase gradient, one first has to unwrap the phase in order to avoid unphysical phase gradients due to its representation within the $[-\pi, \pi]$ interval. In this work this step was performed with help

of the `phase_unwrap` function on MATLAB [59]. The off-axis contribution is then retrieved from the calculated average phase gradient inside a Region of Interest at the beam centre, and then removed from the total phase. An experimental example of a phase map (in its wrapped representation) after removal of the off-axis contribution, is shown on fig. 3.5 c). This phase, in it unwrapped form, consists of the non-linear phase, that we want to retrieve, and a constant phase offset φ_0. In order to isolate the former, we use the constraint that the non-linear phase has to vanish for vanishing laser intensity. More precisely, one needs to access the dependence of the unwrapped phase versus the beam intensity.

Phase vs intensity to eliminate the offset: For this, a procedure consisting in two steps is employed: the first step uses the symmetry of the Gaussian beam, providing that both phase and intensity should only depend on the radial coordinate. For the first step, the 2D maps of the phase, intensity and the radial coordinate are converted into 1D vectors and they all are arranged according to the increasing radial coordinate, as shown on fig.: 3.5 d). Then as the second step, the radial phase is plotted as function of the radial intensity/power (fig.: 3.5 e)), the latter being retrieved from the central peak of the interferogramm spectrum. The geometrical phase offset φ_0 can be estimated by fitting the phase as function of intensity with the expression:

$$\varphi(I, a, c, b) = \frac{a.I}{1 + I/c} + b \tag{3.27}$$

For the estimation of b, the intensity I does not have to be the true laser intensity but should be a quantity proportional to it (in our case the pixel gray value). This allows to eliminate any constant phase offset. The remaining value of the phase corresponds finally to $\Phi_{NL}(I)$ giving in turn the access to the non-linear refractive index variation averaged over the propagation in presence of extinction, via: $\Delta n = \Phi_{NL}/(k_0 L)$.

Local defocusing and the spectral distribution: Note that calculating the radial phase gradient, one directly accesses the transverse component of the laser wavevector $\delta k_\perp$, showing the beam's focusing/defocusing rate with propagation direction z. An experimental radial transverse wavevector calculated from the radial non-linear phase, is shown in fig.: 3.5 f), where it is expressed as the light ray's local angle with the optical axis, defined as the ratio between the transverse to total wavevector, $\delta k_\perp/k_0$. Finally, the power spectrum of the electric field can be calculated with the knowledge of its amplitude $|\mathcal{E}|$ and phase φ maps, by simply fast Fourier transforming the quantity $|\mathcal{E}|\mathrm{e}^{i\varphi}$ and taking the square of the modulus of the result. The power spectrum, which theoretically corresponds to the far-field image of the beam, possesses the same "radial" symmetry and only depends on the radial coordinate. The calculated (from the same experimental image as the other results of the figure) power spectrum is plotted versus the radial transverse wavevector with inverted x and y axis in fig.: 3.5 g).

Practical considerations: Two important conditions are required for the reconstruction to be successful: the reference beam needs to be collimated (in order to avoid diverging beam phase contributions), and the signal beam must be small enough that it does not fill the whole sensor such as to leave a border of low intensity to serve as a zero reference of the non-linear phase. In practice these conditions are realized by taking a part of the signal beam as reference just

before the non-linear medium with a polarized beam splitter. This beam is then enlarged with a telescope and recombined with the signal beam after the medium with a non polarized beam splitter (after having realigned the polarization). These conditions make this technique perfectly suited for measuring large non-linear phase shifts and accessing the spatially resolved phase maps. On the contrary, weak dephasings (below a few radians) are challenging to measure with this technique as they are comparable to the fluctuations due to convective currents, and therefore we present in the following a complementary phase retrieval method for weak non-linearity.

3.3.4 Interferometric bucket-detector technique

Principle: The single shot technique presented in the previous section relies on the measurement of the spatial non-uniformity of the phase stemming from the spatial non-uniformity of intensity in presence of the Kerr effect. Being given a sufficient spatial resolution on the image many pixels are needed to sample simultaneously different intensity and phase values. It is, however, possible to access the same information by recording the intensity of a single pixel (or any local bucket detector, like a photodiode) while scanning the input laser intensity. Eliminating other phase fluctuation sources than the laser intensity, it is possible to directly retrieve the non-linear phase. This idea constitutes the second non-linear refractive index measurement method and is an interesting alternative in the situation where the use of a camera is not possible. Moreover, if the scanned intensity range is large enough to reach "very" low intensities, where the phase is constant, the absolute intensity dependent phase can be accessed by setting the phase at lowest intensity to zero. As the result, this technique is expected to have a better sensitivity for measuring weak non-linear phase shifts.

Experimental details: From the experimental point of view the setup is the same as shown on fig. 3.4 a). In practice, in this work the power ramp was realized by rotating a half-wave-plate (HWP) placed on an electrically driven rotating mount (Thorlabs K10CR1) followed by a polarizing beam-splitter. The HWP induces the polarization rotation of a linearly polarized beam, which is then transmitted/reflected differently depending on the HWP angle.

Accessing the cosine term: In this approach, we replace the spatially dependent intensity of a Gaussian beam by a temporal intensity ramp (as schematically shown on fig. 3.6 a)) and we acquire (via an image sequence) the evolution of the non-linear phase shift during the ramp by monitoring the intensity of a small region of interest at the center of the beam. The bucket detector can be for example: a photodiode sensor after an iris or a small subgroup of pixels (if we decide to still use a camera) as demonstrated on the panels b,c) of the fig. 3.6. Provided the intensity ramp is slow enough with respect to the response time of the bucket detector, the signal at the center of the image will alternate between bright and dark values as the fringes shift due to dephasing. By normalizing the "central pixel" intensity with the local interference maximum intensity for each image, one can access a cosine curve containing the information on the non-linear phase: $I \propto \cos(\Phi_{NL} + \varphi_0)$. An example of such a curve is shown on fig. 3.6 d).

Access to the Kerr index and the saturation intensity: The Hilbert transform is then employed

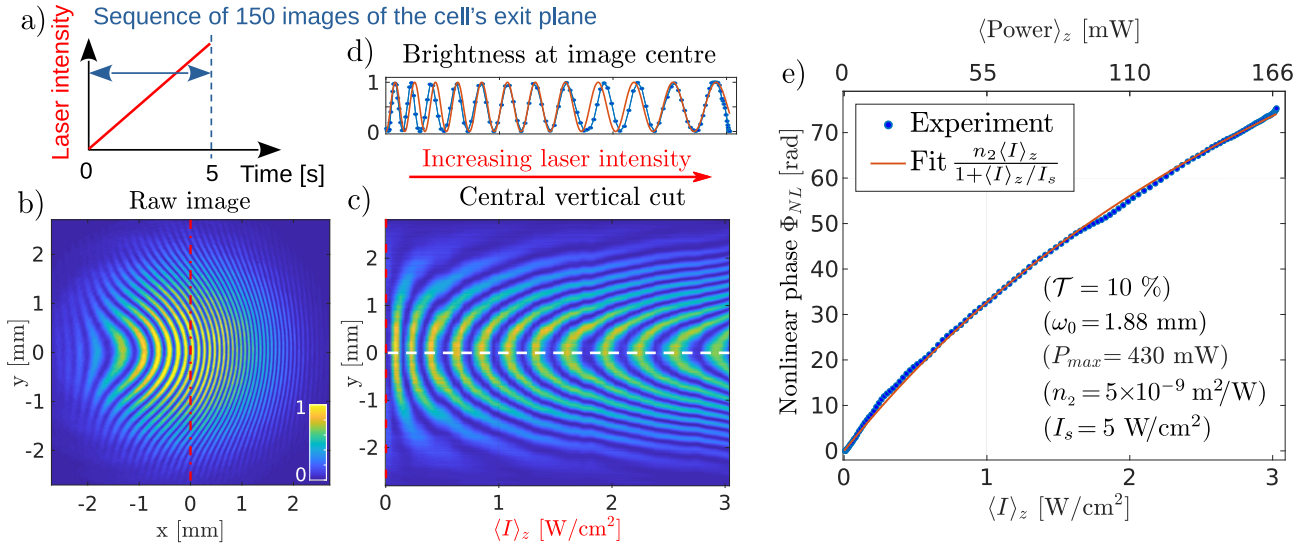

Figure 3.6: Intensity ramp method. A 100 mm long ^{87}Rb cell heated to $T_V = 145(1)$ °C and illuminated at the detuning of $\Delta/(2\pi) = -2.4(0.15)$ GHz with respect to the ^{87}Rb $F_g = 2 \rightarrow F_e = 1$ transition. a) Typical image acquisition timing: a laser ramp from minimal to maximal available laser power is enabled during ≈ 5 s, during the ramp a sequence of ≈ 150 images is acquired on camera imaging the cell exit plane. b) A typical image at the end of the power ramp. c) Vertical intensity cut crossing the image centre plotted for all images of the sequence as function of the cell averaged laser intensity (x-axis). d) Intensity of the image centre (corresponding to the white dashed line in c)), as function of the laser intensity. e) The unwrapped phase reconstructed from d) as function of the laser intensity and power, both averaged over extinction inside the cell.

to access the phase of the cosine. The phase offset φ_0 is eliminated by setting the phase of the lowest intensity image to zero. The laser intensity is calibrated with the measurement of the input laser power, corresponding to the maximal input laser intensity of the ramp $I_{0,max}$, and the fit of the beam waist ω_0, by using the relation: $I_0 = 2P/(\pi\omega_0^2)$. In order to effectively take into account the absorption losses, the power transmission $\mathcal{T}$ through the cell is measured (it is assumed power independent) and the propagation averaged intensity $\langle I_z\rangle = I_0(\mathcal{T}-1)/\ln(\mathcal{T})$. The Kerr index n_2 and the saturation intensity I_s can then be accessed via the fit:

$$\Phi_{NL}(\langle I_z\rangle, n_2, I_S) = \frac{n_2\langle I_z\rangle}{1+\langle I_z\rangle/I_s}k_0 L \tag{3.28}$$

An experimental example of the non-linear phase versus propagation averaged intensity/power, is shown on fig. 3.6 e), along with the corresponding fit using the eqn. 3.28.

Precision and typical conditions: The precision of this method is limited by the stability of the interferometer, which should be stable enough so that the fringes do not shift of more than one period over the measurement time. As explained earlier, the presence of convective currents around the cell, due to the its heating elements, slightly blur the interferogram and it is preferable to have a long exposure time in order to average out these fluctuations (at the

expense of a reduced contrast). If these fluctuations exceed 2π rads, the counting may integrate an extra fringe and falsify the final result. Nevertheless, this method is more accurate for weak dephasings, and is not affected by the phase of the reference.

3.3.5 Comparison of the two phase retrieval methods

The choice of the analysis methods mainly depends on the experimental constraints and requirements. The bucket detector method is suited to measure weak dephasings (but requires about hundred of data points to be accurate), while the Fourier filtering method allows for recovering a spatially resolved Δn from a single picture but is only suited to detect larger phase shifts. This is because the fluctuations due to convective currents around the cell are on the order of a radian. On the contrary, due to the definition of a small region of interest employed in the bucket detector technique, these fluctuations are seen as a constant dephasing and thus shift the fringes around the center of the bin: these fluctuations are mostly erased during averaging as long as they do not exceed π rads. Most importantly, the bucket detector method provides a physically more reliable phase offset value, which is important for an accurate non-linear refraction measurement.
As a general guideline, we suggest to use the bucket detector method (with a camera subregion) for precise calibration of a system (especially for weak non-linearity, bellow a few radians of dephasing) and the Fourier filtering method for a quicker measurement of larger non-linear phase shift.

3.4 Experimental results

In this work we address the question of relevance of the optical pumping and transit broadening for an accurate description of the intensity dependent RI in the regime of high atomic density (typically $10^{13} - 10^{14}$ cm^{-3}). This explains the lack in literature on quantitative comparison between theory and experimental measurement of the intensity dependent RI variation.

3.4.1 Beam size dependence

3.4.1.1 Experimental result

Relevance of this measurement: This section shows the results of investigation of the optical pumping and transit rate effect on the non-linear index in hot Rb vapor, using the off-axis interferometry. As mentioned at the beginning of the chapter, the impact of the optical pumping on the non-linear index has only been discussed very recently [55]. Using the approach developed in [55] and [71], the derivation performed in the first part of this chapter showed (see fig. 3.3) the drastic effect of the beam size on the Kerr index. Indeed, for atomic vapors, this effect has dramatic consequences since it means that due to the thermal distribution of velocities and the random positions of the atoms, not all atoms will spend the same time in the beam. Slower atoms will spend a longer time in the beam and more quickly saturate to a steady

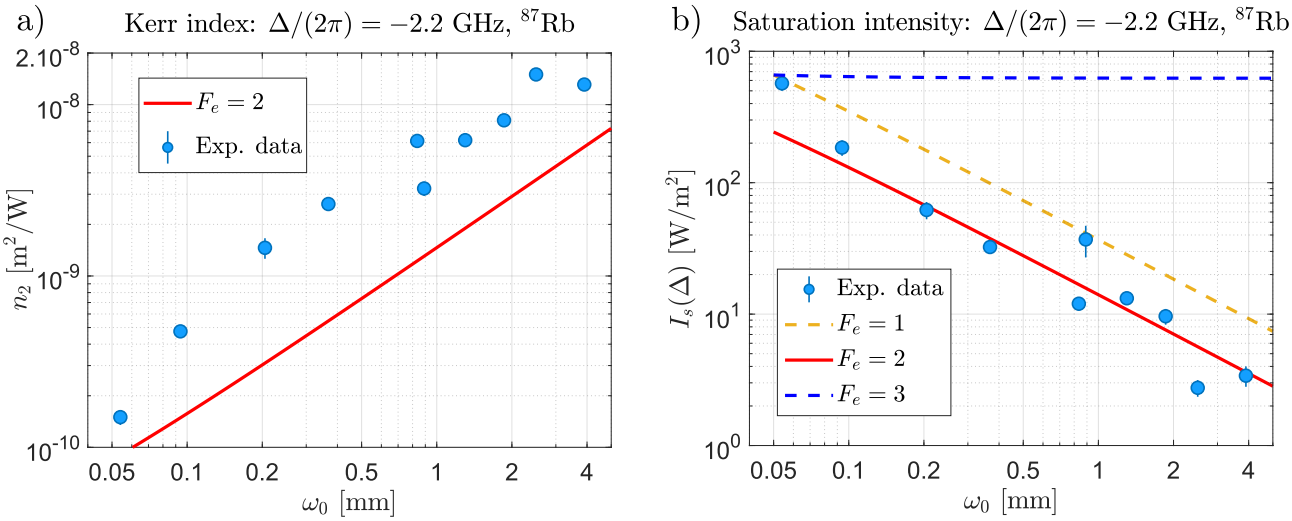

Figure 3.7: Results obtained with the bucket detector technique: a) The Kerr index n_2 and b) the saturation intensity I_s versus the Gaussian beam waist, obtained from the fitted non-linear refractive index variation as function of the laser intensity (averaged over propagation with 40% power losses), measured in a $L = 10$ mm long ^{87}Rb vapor cell heated to 150±5 °C (vapor temperature) at the laser detuning from the ^{87}Rb $F_g = 2 \rightarrow F_e = 1$ fixed at $\Delta/2\pi = -2.2\pm0.15$ GHz. Each point is the least squares fitted parameter of the corresponding measured $\Phi_{NL}(\langle I_z \rangle)$ curve (not shown here). Solid lines correspond to the theoretical predictions based on eqns. 3.22 and 3.21 for separate transitions involving different excited states.

state while faster atoms will interact only for a shorter time. Furthermore, as atoms come in and out of the beam, collision processes, which were neglected in the theoretical description, reshuffle the atoms internal state, and these collisions processes dictate at what speed the atoms will return (or not) in the beam as they govern the mean free path of the atoms in the vapor. A complex combination of these effects is required to model precisely the variation of the non-linear coefficient n_2 and the saturation intensity I_s with the beam size.

Figure description: Figure 3.7 shows the results of various datasets measured using the bucket detector interferometric technique. The non-linear phase versus laser intensity curves were measured for various Gaussian beam waists while keeping the beam always collimated inside the vapor cell. The measurement was performed in a $L = 10$ mm long ^{87}Rb vapor cell heated to 150±5 °C (vapor temperature). The laser intensity (averaged over propagation in presence of absorption) was deduced from the input laser power P, the measured power transmission through the cell $T \simeq 60$ % and the measured (radial intensity profile fit) beam waist ω_0. The fitted values of the Kerr index and the saturation intensity are then analyzed with respect to their dependence on the beam waist. The results are reported in fig. 3.7 a) and b). The variation over two orders of magnitude is observed for both the Kerr index and the saturation intensity as the beam waist is increased from 0.05 mm to 4 mm. This result confirms the important role of the optical pumping and the transit rate in the formation of the non-linear phase in hot Rb vapors.

3.4.1.2 Comparison with theory

Kerr index: In order to compare the measured experimental results with the presented theory, the solid lines on fig. 3.7 show the theoretical predictions based on eqns. 3.22 and 3.21 for separate transitions involving different excited states. From the results shown on fig. 3.3 we know that if all the excited states are taken independently, the dominant contribution to the Kerr index comes from the $F_e = 2$ open state, which promotes the optical pumping and has a larger transition dipole than the transition involving the $F_e = 1$ state. As for the $F_e = 3$ state, although it is involved in the transition with the largest dipole moment, the former is a closed transition and therefore in the absence of the γ_{ed}/Γ_t-fold enhancement, is expected to give negligible contribution with respect to the $F_e = 2$ state especially for an increasing waist. On fig. 3.7 a) the theoretical curve for the Kerr index is roughly two times below the experimental data. This means that the presented model already qualitatively captures well the involved phenomena and the scaling with the beam waist, but there is(are) necessarily some ingredient(s) missing to provide quantitative agreement with the experiment. A possible ingredient which could improve the agreement, is taking into account the "cross talk" between the transitions (especially those involving the $F_e = 2$ and $F_e = 3$ excited states) via the modified common ground state population.

Saturation intensity: Interestingly, for the saturation intensity an excellent agreement (fig. 3.7 b)) is obtained between the experimental data and the calculation involving the $F_e = 2$ excited state. In fact, the transition involving this state has the lowest saturation intensity because it is affected bu the optical pumping and because it has a larger dipole moment than the one involving the $F_e = 1$ state.

Conclusion: This experiment confirmed the importance of taking into account the optical pumping and the transit effect in order to accurately predict the optical saturation behavior in hot Rb vapors. A three level model with one laser coupling (shown at the beginning of the chapter) is sufficient to quantitatively take into account the beam dependence effects emerging from the optical pumping, but it definitely needs to be generalized in order to reach quantitative agreement with the experimental measurements.

3.4.2 Extension for the non-linear temporal response measurement

Interestingly, our setup allows for time-resolved measurement of the non-linear index, not reported so far, for atomic vapors. To demonstrate its potential for characterization, this technique was applied by Guillaume Brochier, intern in our lab in 2021, to retrieve the transient regime at short time for the non-linear index in a hot vapor of rubidium.

The temporal response of the non-linear medium is studied by using the interferometric method in a pulsed configuration. The experimental setup remains unchanged, except that we now gate the reference and signal beams using an AOM as can be seen inside the dashed boxes of Fig. 3.8 a). We turn on the signal beam at a given time and tune the delay to gate the reference beam. We therefore sample the non-linear index at a given delay after the signal has been switched on. The signal beam is between 50 and 20 μs long, while the reference was

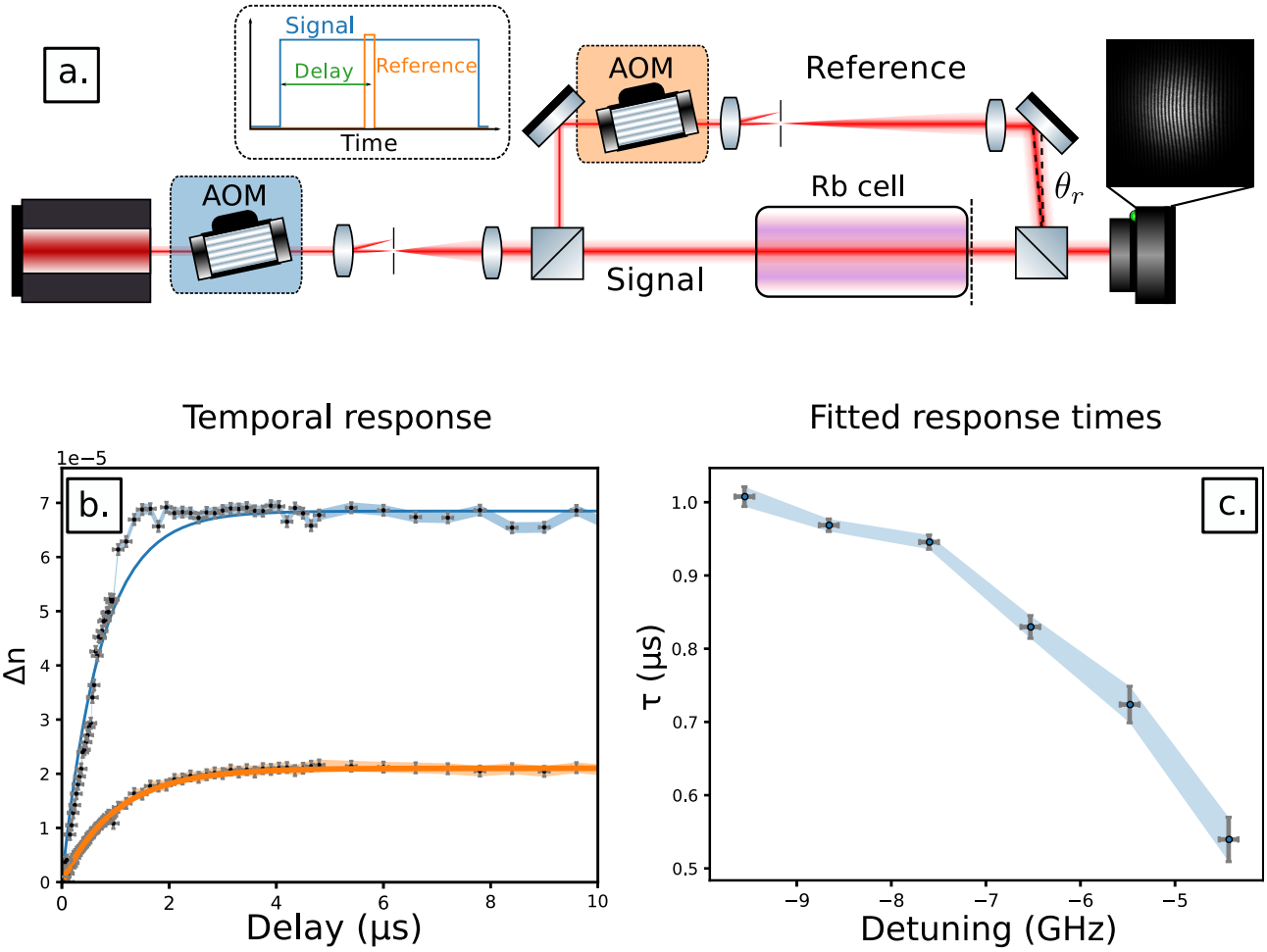

Figure 3.8: a) Upgraded experimental setup for measurement of the transient evolution of the non-linear phase. b) Non-linear index variation Δn as function of the time delay between the signal and reference beams (crosses) for w_0=660 µm, T=140°C, P=400 mW and through a cell of isotopically pure ^{87}Rb of 10 cm. The continuous lines are a fit by $1 - e^{-t/\tau}$. The errorbars are highlighted with the shaded areas. The blue set is at Δ = -2π·5.5 GHz, the orange set is at Δ = -2π·9.5 GHz. c) Fitted value of τ as function of the detuning Δ.

adjusted between 200 and 50 ns (which ultimately defined our temporal resolution) in order to keep a good contrast. We image the non-linear dephasing (essentially the non-linear response of the medium) at this delay. For this experiment, we use the Fourier filtering phase retrieval method.

Experimental results are presented in fig. 3.8 a) for two datasets at different detunings Δ from the signal laser with respect to the D_2 line of Rubidium 87. The response of the medium is fitted by an exponential growth as $\Delta n(t) \propto 1 - e^{-t/\tau}$ with a characteristic timescale τ. For the particular case of our atomic vapor medium, the value of τ can be related to the atomic structure of Rubidium. In the most basic approximation (commonly used for far detuned beam [165]), rubidium can be considered as two-level atoms, and one could expect the time scale τ to be the lifetime of the excited state. However, this approximation failed to describe

quantitatively our results. This analysis was then refined by using a 3-level atomic model, [25] using the eigenvalues of the evolution matrix of the density matrix. This 3-level model gives a good quantitative estimate of τ that is consistent with the experiment within a fixed positive offset of 40%. In fig. 3.8 b), we summarize our measurements of τ as function of Δ: the closer we get to the resonance, the shorter the response time. This effect can be quite large as switching from -6 to -5GHz nearly halves the response time from 0.8 to 0.55 µs. For this range of detunings, the relevant timescale before the medium reaches its steady state is below 1 μs. This is of peculiar interest because this is comparable to the typical transit time of atoms in a beam of 1 mm at a temperature of 400K. This opens interesting perspective for temporally non local interactions [163, 153]. These results highlights the relevance of the transient onset of the non-linearity for time scales of the order of 1 µs. This time scale is almost an order of magnitude larger than the excited state's lifetime in the D2 line $1/\Gamma \simeq 30$ ns, which is typically considered as the time scale for transient optical effects. This observation confirms, that the involved atomic state dynamics is more complex than a two-level system and suggests, that the optical pumping along with the transit rate drive the atomic variables into a more complex steady state which requires more time for being established.

3.5 Outlooks

3.5.1 Non-locality: spatial extent of interactions

3.5.1.1 Introduction

From local to non-local interactions: The "local" Kerr effect, presented in chapter 1, where the non-linear refraction has no other spatial dependence than that, stemming from the local intensity inhomogeneity, is an optical analogue of the contact type interactions in the BECs, where they result from the *s*-wave scattering of the particle wavefunctions. While this assumption is well justified for the BECs in the low-energy regime with no dipolar interactions, the microscopic effects of the light-matter interaction need to be considered in order to verify it in optics. In fact, in a medium with moving and interacting emitters the optical susceptibility can become non-local. Evaluation of the range of the interactions is indeed crucial, because for instance, recalling the ultracold atomic superfluids, the presence of the non-local long range dipole-dipole interactions may lead to new physical phenomena such as supersolidity [107]. This section examines the "local" Kerr effect assumption in hot Rb vapors, based on the state of the art, and presents possible additional contributions to the non-locality of the non-linear refractive index.

Non-local interactions: definition and origins: Here the non-locality means the dependence of the non-linear refractive index at a given position on its values at other (typically neighbouring) locations. Indeed, in presence of the non-locality, the interaction term of the propagation

equation reads [153, 55]:

$$\langle g\rho\rangle(\mathbf{r}) = g\int G(\mathbf{r}-\mathbf{r}')\rho(\mathbf{r}')\mathrm{d}^2\mathbf{r}' = g\langle G*\rho\rangle \tag{3.29}$$

where G is the nonlocal response function, defining the correlation length of the photonic interactions. It is a pair function having its maximum at zero and characterized by its width l and whose shape depends on the mechanism responsible for the non-locality [142] and $\rho = |\mathcal{E}|^2$. Note that the spatial coordinate $\mathbf{r} = (x, y)$ spans only the transverse plane, which is obviously an approximation assuming that the interaction is invariant under the translation in the z coordinate. The optical susceptibility can be non-local in presence of the dipole-dipole interactions or the the dipole motion. In case of the hot (dense) Rb vapor cells both effects are present and could contribute to the non-locality of the photonic interactions.

Non-local interactions: implications for the fluids of light: The non-locality of the photonic interactions can drastically affect the dynamics of a fluid of light [163, 153, 142]. Such dynamics is commonly described with a generalized propagation equation:

$$i\frac{\partial\mathcal{E}}{\partial z} = \left(-\frac{1}{2k_L}\nabla_\perp^2 + g\langle G* |\mathcal{E}|^2\rangle - \frac{i\alpha}{2}\right)\mathcal{E} \tag{3.30}$$

The non-locality significantly complicates the resolution of this equation but can still be included in its numerical simulation (see Appendix B).

3.5.1.2 The known origins for the nonlocality in hot vapor cells

Transfer function of the nonlocal response: Here I review the known effects in hot Rb which lead to the non-local photonic interactions, give the expressions of the corresponding non-local response functions, as well as the estimation of their spatial extents. The calculation of the integral in the eqn.: 3.29 can be done with the convolution theorem, by simply back Fourier transforming the product of the Fourier transforms of the non-local response function $\tilde{G}(\mathbf{q})$ and of the density $\tilde{\rho}(\mathbf{q})$. Therefore only the expressions of $\tilde{G}(\mathbf{q})$ are given here, which can be readily used for the numerical simulations of the NLSE.

Ballistic non-locality: The thermal motion in hot vapors of Rb results in the ballistic displacement of the excited Rb atoms within and around the laser beam. In steady state, at each given position the local atomic density at given time includes the contribution of the atoms arrived from the neighboring positions, as well as the atoms which left the given position. As discussed in this chapter, the non-linear refractive index in hot Rb vapors depends on the atomic population in the excited state, therefore it is affected by the motion of the excited atoms. Assuming the interatomic collisional mean free path much larger than the mean ballistic path of an excited atom, one can calculate a response function of the ballistically moving (in the 2D transverse plane) exited atoms [142, 55], which is given in the Fourier space by:

$$G(\mathbf{q}) = \frac{1}{G(0)}\frac{\mathrm{e}^{(1/lq)^2}}{lq}\mathrm{erfc}\left(\frac{1}{lq}\right) \tag{3.31}$$

where $q = \sqrt{q_x^2 + q_y^2}$ and the normalization by $G(0)$ allows to recover the contact type interactions ($G(q) = 1$) in the limit $l \to 0$.

Diffusive non-locality: In the dense vapor regime the hypothesis of the ballistic motion is not valid anymore, because the interatomic collisional mean free path becomes smaller than the mean ballistic path of an excited atom. Then the atomic transport inside the vapor is described by the diffusion equation [142, 55] resulting in the following transfer function of the nonlocal response:

$$G(\mathbf{q}) = \frac{1}{1 + l^2 q^2} \tag{3.32}$$

3.5.1.3 Possible additional origins for the nonlocality in hot vapor cells

The already listed origins of the nonlocality stem from the transport of the excited atoms. However, using the rate equations for the populations presented in section 3.2.2.3, one can show, that for intensities typically below the saturation intensity I_s, the excited state population is small compared to that of the ground states, which suggests that it is unlikely for the excited atoms to dominantly contribute to the nonlinear susceptibility. Moreover, this chapter shows, that the optical pumping with the atomic transit motion strongly affect the "local" value of the photonic interaction parameters, but could these effects additionally induce the nonlocality of these interactions? This question is sensible because the transport of the atoms, optically pumped into the dark state, away from the brightest area of the beam, can induce the variation of the refractive index at the latter's neighbouring less intense regions. The contribution of this effect to the nonlocality of the Kerr effect could be relevant due to an important atomic fraction involved in the process and because now the range of the nonlocality is not anymore limited by the lifetime of the excited state. Rather, the nonlocal range could now depend on the collisional mean-free path between the ground state atoms. This effect has not been so far considered for modelling the nonlocality in hot Rb vapors but I am convinced that its further investigation could shed new light on better understanding the nonlocality and hence controlling the photonic Kerr interactions in this medium.

3.5.2 Comparison among platforms

In order to better harness the advantages and disadvantages of the hot Rb vapor platform for the experiments with fluids of light, it is sensible to compare its characteristics with different similar experimental platforms based on some common figures of merit. The latter should include the relevant parameters for the exploration of quantum fluids, such as the interaction strength, the attainable propagation lengths and the loss rates. Such comparison could even be done between the spatially multimode platforms such as the hot vapor cells, photorefractive crystalls or thermo-optic media, and monomode platforms, such as the non-linear optical fibers, where the fluid of light's dynamics takes place exclusively in the time coordinate due to the chromatic dispersion [16], while the fiber axis still plays the role of the fluid's effective time. The next generation of the fluid of light experiments will definitely require the tailored design of the experimental platform for achieving specific scientific goals.

Chapter 4

Blast waves in a fluid of light

4.1 Objective of the chapter

The fluid of light concept: Starting with the hydrodynamic formulation of light propagation in a Kerr-type $\chi^{(3)}$ medium I establish the well-known concept of the fluid of light. An important parameter governing the fluid's dynamics is its density dependent speed of sound. The latter is introduced within the linear dispersion relation analysis of weak density/velocity fluctuations on top of a dense background in the long-wavelength limit.

Strong density perturbations of a fluid of light: The discussion is then extended to the case of a strong perturbation where the local speed of sound strongly affects the dynamics of the perturbation spreading. This situation is shown to be analogous to formation of dispersive shock waves. Shock wave is a special type of non-linear waves is characterized by a steepening density/velocity wave profile evolving upon propagation into a discontinuous interface called shock front in the ideal (lossless and dispersionless) case. The wake of the shock front is usually thought to decay exponentially in time and space.

Observation of blast waves: However, in some cases, depending on the geometry and dimensionality of the problem, the exponential decay of the disturbed parameter in the shock front's wake may overshoot the undisturbed value changing the sign until stabilizing subsequently at the equilibrium value. This phenomenon is known as a blast wave and is usually modeled by an empirical model called Friedlander wave. In this chapter 1D and 2D experimental results of the formation of the shock and blast waves in a fluid of light are presented. The blast wave formation is clearly observed in the 2D case while apparently absent in the 1D case. The Friedlander model reproduces well the time history profile of the 2D blast pressure, while in 1D case the latter decays to zero.

4.2 Compressible hydrodynamics with light

4.2.1 Hydrodynamic equations and quantities

4.2.1.1 Propagation equation

We describe the propagation of a linearly polarized monochromatic laser beam in a medium with intensity I dependent reflactive index: $n(I) = n_0 + \Delta n(I)$, with n_0 being the refractive index in the zero intensity limit. We separate the electric field's fast oscillating carrier from the slowly varying (with respect to the laser wavelength) envelope: $E = \mathcal{E}(\mathbf{r}, z)\mathrm{e}^{i(k_L z - k_0 ct)}+$ complex conjugate, where k_L and k_0 are the laser wavevectors in the medium (without including Δn) and in vacuum, respectively. As derived in the introduction chapter 1, under the paraxial approximation, the propagation equation for the envelope $\mathcal{E}$ is the Non-Linear Schrödinger Equation (NLSE) [28]:

$$i\frac{\partial \mathcal{E}}{\partial z} = \left(-\frac{1}{2k_L}\nabla_\perp^2 + g|\mathcal{E}|^2 - \frac{i\alpha}{2}\right)\mathcal{E} \tag{4.1}$$

where α is the additionally added extinction coefficient, accounting for losses due to absorption, and the g parameter is linked to the intensity dependent refractive index variation Δn via: $g|\mathcal{E}|^2 = -k_0\Delta n$ (with k_0 the laser wavevector in vacuum). As highlighted in the previous chapter, the NLSE is analogous to a 2D Gross-Pitaevskii equation describing the dynamics of a quantum fluid in the mean-field approximation. This analogy is possible by mapping the envelope $\mathcal{E}$ to a quantum fluid's many-body wavefunction and the axial coordinate z to an effective evolution time. It is therefore in principle possible to probe the fluid's temporal evolution by simply imaging it at various positions z of the propagation coordinate. The nonlinear refractive index variation plays then the role of a repulsive photon-photon interaction, since all measurements in this work are done in the self-defocusing regime i.e. $\Delta n < 0$ and therefore $g > 0$. Diffraction acts as kinetic energy with the effective mass emerging from the paraxial approximation and given by the laser wavevector k_L=8×10^3 mm^{-1} for a laser wavelength of 780 nm.

4.2.1.2 Hydrodynamic equations

One can rewrite the electric field amplitude $\mathcal{E}$ in a polar form as function of its absolute value $\sqrt{\rho}$ and the phase ϕ, the Nonlinear Schrödinger equation (NLSE, eqn. 4.1) becomes a set of two equations for the quantities ρ and $\mathbf{v}$ that are identified as a density and velocity, respectively. These equations resembling the compressible hydrodynamic equations of mass and momentum conservation, this approach is particularly useful to reveal and get a more profound feeling of the 2D fluid-like behavior of light propagating in a generic $\chi^{(3)}$ Kerr medium.

Hydrodynamic-like equations: Similarly to a quantum wavefunction, the electric field amplitude, being a c-number, can therefore be written as: $\mathcal{E} = \sqrt{\rho}\mathrm{e}^{i\phi}$. This variable substitution is called the Madelung transformation [99]. Defining additionally a velocity: $\mathbf{v} = \frac{c}{k_L}\nabla_\perp\phi$, one can

derive from the NLSE the following equations [76, 155, 95], written for the variables $\{\rho, \mathbf{v}\}$:

$$\frac{\partial \rho}{\partial z} + \nabla_\perp . \left(\rho \frac{\mathbf{v}}{c}\right) = -\alpha\rho \tag{4.2}$$

$$\frac{\partial \mathbf{v}}{\partial z} + \frac{1}{2c}\nabla_\perp \mathbf{v}^2 = -\nabla_\perp \left(\frac{cg\rho}{k_L} - \frac{c}{2k_L^2\sqrt{\rho}}\nabla_\perp^2\sqrt{\rho}\right) \tag{4.3}$$

These equations are mathematically equivalent to hydrodynamic continuity (or local mass conservation) and the Euler's equations, respectively [14, 155, 53, 97, 95]. This analogy gives physical meaning to the variables ρ and $\mathbf{v}$, which rightfully represent the fluid of light's density and velocity. One can also note that the fluid's phase ϕ can now be interpreted as the the fluid's dimensionless velocity potential.

Interpretation: The continuity equation 4.2 states that the fluid's local density changes over "time" z due to its flux in the transverse plane (given by the divergence term) and due to the beam's one-photon extinction [95] via Beer-Lambert's law[1]. The momentum conservation, or Euler's eqn. (4.3) shows that the evolution of the velocity can be due to the convection which is given by the second left hand side term and is driven by a gradient of a pressure stemming from photon interactions and the so-called "quantum pressure" (QP) term due to diffraction.

4.2.1.3 Hydrodynamic quantities

Hydrostatic pressure: The interaction term (proportional to g) in the eqn. 4.3 can indeed be re-expressed as an analogue pressure P as it appears in classical hydrodynamic descriptions: $-1/\rho \cdot \nabla_\perp P$, by using the identity: $-\nabla_\perp \rho = -1/(2\rho)\nabla_\perp \rho^2$. Doing so, one can define the so called bulk hydrostatic pressure P as:

$$P = \frac{\rho^2 c^2 g}{2k_L} \tag{4.4}$$

Eq. (4.4) is the state equation linking the fluid hydrostatic pressure P to its density if one neglects the quantum pressure term. It is the consequence of the mean-field formulation of the interaction. It also implies that the fluid of light is compressible with the compressibility given by:

$$\kappa = \frac{1}{\rho}\frac{\partial \rho}{\partial P} = \frac{k_L}{c^2\rho^2 g} = \frac{1}{2P} \tag{4.5}$$

One can also note that the hydro-static pressure can be rewritten as $\frac{1}{2}\rho c_s^2$ by defining a certain speed of sound as:

$$c_s^2 = c^2 \cdot \frac{g\rho}{k_L} \tag{4.6}$$

or as in classical fluid acoustics, as: $c_s = 1/\sqrt{\kappa\rho}$.

[1]Only "linear" extinction due to light scattering stemming from the imaginary part of the linear susceptibility $\chi^{(1)}$ is considered in this work. This is an assumption justified in the chapter on the atomic medium characterization.

Dynamic pressure: On the other hand, one can assess the strength of the convective term in the eqn. 4.3 by calculating the fluid's dynamic pressure:

$$P_d = \frac{1}{2}\rho \mathbf{v}|\mathbf{v}| \tag{4.7}$$

The dynamic pressure is the fluid kinetic energy flux and accounts for the amount of pressure due to fluid's motion. For instance, the impact force on an obstacle hit by a fluid flow is proportional to its dynamic pressure. Both P and P_d have a dimension of $[density]\times[speed]^2$. Taking into account the above mentioned quantities the analogue Euler equation neglecting the Quantum Pressure reads:

$$\frac{\partial \mathbf{v}}{\partial(z/c)} + \frac{1}{2}\nabla_\perp \mathbf{v}^2 = -\frac{1}{\rho}\nabla_\perp P, \tag{4.8}$$

The quantum pressure term: Unlike the pressure stemming from the interactions, the QP term can not be expressed in a form, analogue to the classical Euler equation, i.e. as $-1/\rho \cdot \nabla_\perp P$. However, the QP is in fact negligible in the long-wavelength limit [76], while becoming important in presence of strong density gradients. It can be rewritten as:

$$\frac{c}{2k_L^2\sqrt{\rho}}\nabla_\perp^2\sqrt{\rho} = -\frac{c}{4k_L^2\rho}\nabla_\perp^2\rho + \frac{c}{8k_L^2\rho^2}\left(\nabla_\perp\rho\right)^2 \simeq -\frac{c}{4k_L^2\rho}\nabla_\perp^2\rho \tag{4.9}$$

The second term which is proportional to the square of the relative density gradient is neglected throughout this work. In other words, with this approximation I assume the square of the relative density gradient to be always smaller than the relative density curvature. The first term can be neglected as well in specific situations such as evolution of the "smooth" average field for which diffraction can typically be neglected in the absence of interactions ($g = 0$) or the evolution times (propagation distances z) small compared with the typical diffraction length $z \ll z_R$, with z_R defined, for instance, for a Gaussian beam of waist ω_0 as, $z_R = \frac{1}{2}k_L\omega_0^2$.

Dissipationless fluid: The eqn. 4.3 also shows that there can be no momentum dissipation due to viscosity in a fluid of light because the eqn 4.3 does not contain any term proportional to the Laplacian of velocity [14]. This means that diffusive momentum transport is impossible in a fluid of light, which is a "perfect fluid" by its nature, unlike classical fluids. Indeed, in classical fluids the non viscous Euler flow is in general an approximation from the Navier-Stokes equations containing the viscous term in the momentum conservation eqn. Yet this approximation is valid at high Reynolds number regimes (fast flow, large spatial extent, low viscosity coefficient) where the convection dominates viscous dissipation or equivalently, the flow's spatial scale is much larger than the thickness of the boundary layer: the region, typically at the vicinity of a flow's solid boundaries, where the previous is strongly affected by viscosity.

Potential flow but with possible vortex production: Finally, the equations above also reveal that the fluid of light's flow is irrotational ($\mathbf{rot}(\mathbf{v}) = 0$) due to the existence of a velocity potential ϕ (such as $\mathbf{v} \propto \nabla_\perp\phi$). This is however true as long as the phase ϕ does not have any discontinuity in the transverse plane. In fact, exceptions to this rule exist in form of

optical vortices: the "points" of zero density surrounded by an azimutally varying phase of a 2π-fold circulation. The latter implies a non-zero value of the curl of the velocity: $\mathbf{rot}(\mathbf{v}) \neq 0$. The vortices can even emerge upon evolution of a fluid of light in presence of an important initial kinetic energy under certain circumstances [127]. The spontaneous vortex production could be a mechanism of dissipation of the excessive kinetic energy in a fluid of light and is to be described within the context of the superfluid turbulence, a field of research attracting significant attention over the last years [58, 127].

4.3 Speed of sound

4.3.1 Weak perturbations: slow and fast variables

Linearization of the hydrodynamic variables: In order to get some insight into the evolution of a fluid of light it is useful to linearize its dynamic variables as is commonly done in various fields where non-linear waves emerge. In the present case it consists in splitting the fluid's dynamic variables into their average, or "slowly varying" part which will be referred to as a "background" $\mathcal{E}_0 = \sqrt{\rho_0}\mathrm{e}^{i\Phi_0(\rho_0)}$ from the "high frequency" fluctuations of the field $\delta\mathcal{E}$ which are ideally small with respect to the background and evolve on top of it. The perturbation $\delta\mathcal{E}$ is generally composed of both contributions due to the density $\delta\rho$ and phase θ fluctuations. Then the total field is: $\mathcal{E} = \sqrt{\rho}\mathrm{e}^{i\phi}$, where: $\rho = \rho_0 + \delta\rho$ is the total density and $\phi = \Phi_0(\rho_0) + \theta$ is the total phase taking into account the background's interaction induced phase $\Phi_0(\rho_0) = -g\rho_0 z$ and the one of the fluctuations. The total velocity can then be calculated as: $\mathbf{v} = \frac{c}{k}\nabla_\perp\phi$ and can, as well as the density, be decomposed into the velocity of the background and the one of the perturbation: $\mathbf{v} = \mathbf{v}_0 + \delta\mathbf{v}$.

Background's evolution: The slowly varying variables $\{\rho_0, \mathbf{v}_0\}$ characterize the dynamics of the background field. They are governed by the equations 4.2 and 4.3 which can be simplified by neglecting the QP term (justified in the long-wavelength regime) thanks to the "slow" nature of the associated variables. The evolution equations read then:

$$\frac{\partial\rho_0}{\partial z} + \frac{\mathbf{v}_0}{c}\nabla_\perp\rho_0 + \rho_0\nabla_\perp.\frac{\mathbf{v}_0}{c} = -\alpha\rho_0 \tag{4.10}$$

$$\frac{\partial\mathbf{v}_0}{\partial z} + \left(\frac{\mathbf{v}_0}{c}.\nabla_\perp\right)\mathbf{v}_0 = -\nabla_\perp\left(\frac{cg\rho_0}{k_L}\right). \tag{4.11}$$

The equations 4.10 and 4.11 are still non-linear because of the coupled contribution of kinetic energy / diffraction and interactions / non-linearity via the rhs terms in the eqn. 4.10 mixing both the density and interaction affected velocity and the term non-linear in $\mathbf{v}$ in the eqn. 4.11. Therefore solving them analytically for an arbitrary beam shape is impossible.

Simplification: neglecting diffraction: Yet a useful regime giving simple analytic results is the one in which diffraction can be neglected, i.e. with the example of a Gaussian beam of waist ω_0, the latter much larger than the laser wavelength $k_L\omega_0 \gg 1$ and the evolution times (propagation distances z) much smaller than typical diffraction (Rayleigh) length $z \ll z_R$, with $z_R = \frac{1}{2}k_L\omega_0^2$.

In this case, assuming a constant initial velocity $\mathbf{v}_0(z=0)/c = \beta_0$, the $\rho_0 \nabla_\perp . \mathbf{v}_0/c$ term can be neglected and the remaining convective terms $\beta_0 \nabla_\perp \rho_0$ and $(\beta_0 . \nabla_\perp)\,\mathbf{v}_0$ can be scaled out with a variable substitution $\mathbf{r}' = \mathbf{r} - \beta_0 z$ and one gets simple evolution equations:

$$\frac{\partial \rho_0}{\partial z} = -\alpha \rho_0 \tag{4.12}$$

$$\frac{\partial \mathbf{v}_0}{\partial z} = -\nabla_\perp \left(\frac{cg\rho_0}{k} \right) \tag{4.13}$$

Which have the following solutions [95]:

$$\rho_0(\mathbf{r}, z) = \rho_0(\mathbf{r}, 0)\, \exp(-\alpha z) \tag{4.14}$$

$$\mathbf{v}(\mathbf{r}, z) = -\frac{cg}{k_L} \nabla_\perp \int_0^z \rho_0(\mathbf{r}, z') dz' \tag{4.15}$$

Weak perturbation dynamics: Bogoliubov dispersion relation: The fast variables $\{\delta\rho, \delta\mathbf{v}\}$ characterize the dynamics of an ideally weak fluctuations around values $\{\rho_0, \mathbf{v}_0\}$ of the background field. Therefore their evolution follows the eqns. 4.2 and 4.3 linearized in $\delta\rho$ and θ ($\delta\mathbf{v}$):

$$\frac{\partial \delta\rho}{\partial z} + \frac{\mathbf{v}_0}{c} \nabla_\perp \delta\rho + \rho_0 \nabla_\perp . \frac{\mathbf{v}}{c} = -\alpha \delta\rho \tag{4.16}$$

$$\frac{\partial \delta\mathbf{v}}{\partial z} + \left(\frac{\mathbf{v}_0}{c} . \nabla_\perp \right) \delta\mathbf{v} = -\nabla_\perp \left(\frac{cg\rho_0}{k_L} - \frac{c}{4k_L^2} \nabla_\perp^2 \right) \frac{\delta\rho}{\rho_0} \tag{4.17}$$

In these equations all terms containing $\mathbf{v}_0$ account for a convective transport of the fluctuating quantities by the background fluid's drift at speed $\mathbf{v}_0$ in the transverse plane. These linear equations can be solved by "diagonalizing" this system of equations. This can be done by using the following decomposition for the density and phase fluctuations:

$$\delta\rho = \sqrt{\rho_0(0)} \mathrm{e}^{-\alpha z} \int \frac{d^2\mathbf{q}}{(2\pi)^2} \left(a_\mathbf{q} f_+(\mathbf{q}) \mathrm{e}^{i(\mathbf{q}\mathbf{r} - \int_0^z \Omega dz)} + a_\mathbf{q}^* f_+^*(\mathbf{q}) \mathrm{e}^{-i(\mathbf{q}\mathbf{r} - \int_0^z \Omega dz)} \right) \tag{4.18}$$

$$\theta = \frac{1}{2i\sqrt{\rho_0(0)}} \int \frac{d^2\mathbf{q}}{(2\pi)^2} \left(a_\mathbf{q} f_-(\mathbf{q}) \mathrm{e}^{i(\mathbf{q}\mathbf{r} - \int_0^z \Omega dz)} - a_\mathbf{q}^* f_-^*(\mathbf{q}) \mathrm{e}^{-i(\mathbf{q}\mathbf{r} - \int_0^z \Omega dz)} \right) \tag{4.19}$$

Such that $\delta\mathbf{v} = (c/k)\nabla_\perp \theta$. In these expressions the introduced on-axial wavevector Ω is allowed to depend on z due to absorption[2]. The equations 4.18 and 4.19 are valid as long as the variation of Ω with z is slow, such that during the system's evolution, the eigenstate and the eigenvalue "adiabatically" follow the slow variation of the parameters (fluid density) on which they depend [95]. The degree of the adiabaticity of the evolution in the case of the "time"

[2]In the case of an inhomogeneous background profile it also locally depends on transverse coordinates over a typical length scale much larger than the one of the fluctuations. If the latter condition is fulfilled then the local frequency can be taken as constant within a local density approximation.

dependent parameters can be calculated using the criterion of adiabaticity developed in [95]. The decomposition coefficients $f_{\pm}(\mathbf{q})$ are linked to the ones of the Bogoliubov transformation (presented in the next chapter) for the field fluctuations $\delta\mathcal{E}$: $f_{+}(\mathbf{q}) = u_{\mathbf{q}}+v_{\mathbf{q}}$ and $f_{-}(\mathbf{q}) = u_{\mathbf{q}}-v_{\mathbf{q}}$ [56, 97], whereas the coefficient $a_{\mathbf{q}}$ is to be matched to initial conditions of the spatial field distribution (which is, for instance, interaction g independent, contrary to the $f_{\pm}(\mathbf{q})$). Inserting these expressions 4.18 and 4.19 in the eqns 4.16 and 4.17, and assuming the absorption rate α small with respect to the coupling due to interactions ($g\rho \gg \alpha$), [95], one gets:

$$\begin{pmatrix} -\Omega(z) + \frac{\mathbf{v}_0}{c}\mathbf{q} & \frac{\mathbf{q}^2}{k_L} \\ \left(g\rho_0(z) + \frac{\mathbf{q}^2}{4k_L}\right) & -\Omega(z) + \frac{\mathbf{v}_0}{c}\mathbf{q} \end{pmatrix} \begin{pmatrix} f_+ \\ f_- \end{pmatrix} = 0 \tag{4.20}$$

Note that we end up with a 2×2 system because exactly the same equations can be obtained for the $\{f_+^*, f_-^*\}$ couple, thanks to the "-" sign in the eqn 4.19. The equation 4.20 is solvable for any $f_{\pm}$ if the matrix determinant equals to zero. This fixes the link between the longitudinal wavevector variation Ω and the transverse wavevector $\mathbf{q}$:

$$\Omega(z) - \mathbf{q}.\mathbf{v}_0 = \pm\sqrt{\frac{\mathbf{q}^2}{2k_L}\left(2g\rho_0(z) + \frac{\mathbf{q}^2}{2k_L}\right)} \tag{4.21}$$

This relation is the Bogoliubov dispersion relation, mathematically equivalent to the one of the density waves in a cold atomic superfluid gas. It has been accurately measured in a fluid of light in several recent experiments by our group [54, 56, 120]. Depending on the sign before the square root, one refers to the "positive" branch or the "negative" branch of the dispersion for the sign "+" and "-", respectively [95]. Throughout this work only the positive branch of the Bogoliubov dispersion is discussed. Note that the background drift modifies the frequency of the Bogoliubov quasiparticles in a way similar to the Doppler effect in classical acoustics. This modification can indeed be interpreted this way noticing that this frequency shift is equivalent to a Galilean change of referential performed by replacing $\mathbf{r}$ by $\mathbf{r} - \mathbf{v}_0\frac{z}{c}$ inside the integrals of eqns 4.18 and 4.19.

Different regimes, peculiarity: The first term comes from the photon interactions and the second from the quantum pressure terms, respectively. The first one is the dominant term in the long-wavelength regime (low $\mathbf{q}$, where the QP is negligible) and gives a linear, sound-like contribution to dispersion of perturbation, while the second one dominates the short wavelength limit (large $\mathbf{q}$) giving a quadratic dispersion. The Bogoliubov dispersion relation, measured in a fluid of light in [54], is shown on figure 4.1. The frontier between the two regimes is given by a characteristic length scale called *healing length*:

$$\xi = \frac{1}{\sqrt{4k_L g\rho_0}} \tag{4.22}$$

All perturbation wavepackets with transverse wavevectors below $1/\xi$ evolve as dispersionless sound waves, while those with wavevectors above $1/\xi$ will evolve as free particles (light rays)

and spread due to the presence of dispersion:

$$\Omega(\mathbf{q}) \simeq \begin{cases} \sqrt{\frac{g\rho_0}{k_L}}|\mathbf{q}| = \frac{c_s}{c}|\mathbf{q}| & \text{if: } q\xi \ll 1 \\ g\rho_0 + \frac{\mathbf{q}^2}{2k_L} & \text{if: } q\xi \gg 1 \end{cases} \tag{4.23}$$

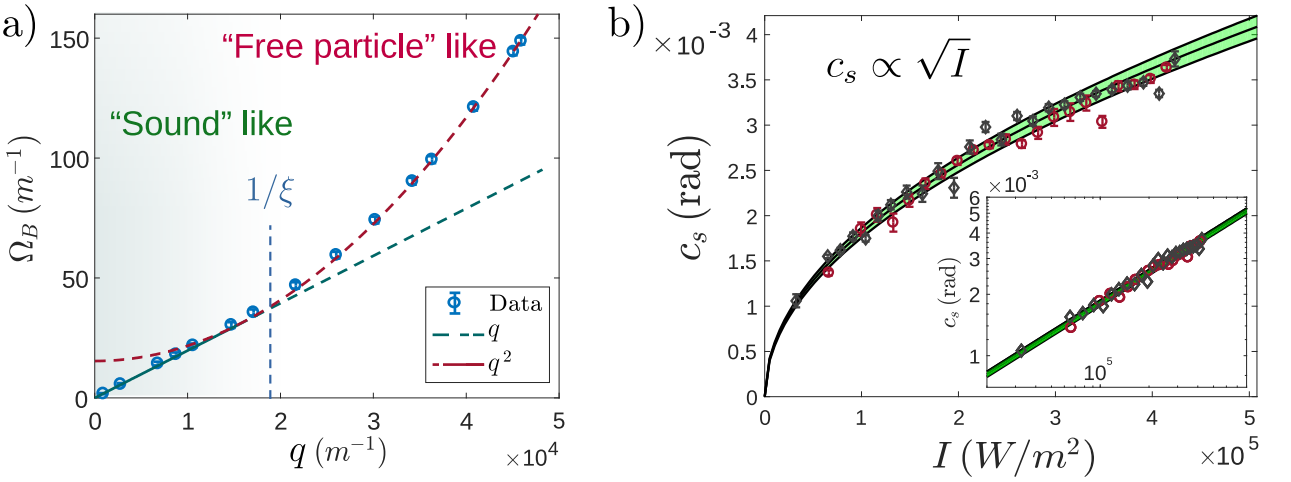

Figure 4.1: Dispersion of weak density perturbations in a paraxial fluid of light, from [54]. a) Bogoliubov dispersion relation $\Omega_B(q)$: the experimental measurement result (dots) and the reproduced theory data, eqn. 4.23 (with independently measured parameters, dashed lines). b) Speed of sound, c_s, (equivalently the slope of the linear regime of the dispersion relation) as function of the photonic background density ρ_0, expressed here with the laser intensity I: the experimentally measured (dots) and theoretically reproduced data (with no fit parameters, solid lines). Figure adapted from [54].

This law defines a highly non-trivial refraction of light rays in presence of photon-photon interactions. One of the most strange features of this results is the emergence of the linear sonic-like regime whereas the ray optics intuition would suggest a quadratic dispersion: $\Omega = k_0 n(I) - \sqrt{(k_0 n(I))^2 - \mathbf{q}^2} \simeq \frac{\mathbf{q}^2}{2k_L}$, which does emerge but only for high spatial frequencies, in the free particle regime $|\mathbf{q}|\xi \gg 1$ and with a shift due to interactions $g\rho_0$. The profound analogy connecting the fluids of light with atomic quantum fluids allows interpreting this result in a very intuitive way using the phenomenology of quantum hydrodynamics. The speed of sound, which is the phase and group velocity deep in the sonic regime coincides with the one defined in equation 4.6. Note that in the present case, assuming the limit of weak perturbations, the speed of sound only depends on the background fluid's density.

4.3.2 Beam expansion

Context: The previous analysis sets useful length scales for describing the fluid's dynamics. Although it is strictly valid within the weak perturbation assumption, one can apply similar reasoning to describe, for example, the expansion of a finite size beam under the effect of the interactions. The present situation is analogous to the Thomas-Fermi regime in cold atomic

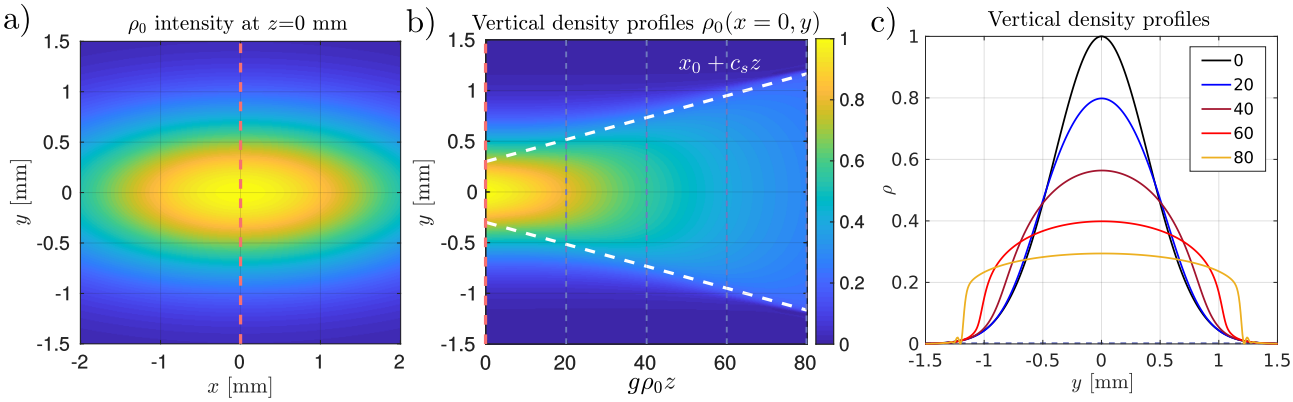

Figure 4.2: Numerical experiment: background fluid's dynamics. An elliptical beam of waists: $\omega_{0,x} = 2.5$ mm and $\omega_{0,y} = 0.8$ mm propagates inside a medium of length $L = 75$ mm with local photon interactions given by $g\rho_0(0,0,z=0) = 1.07$ mm^{-1} and 30 % absorption losses ($\alpha = 0.0048$ mm^{-1}). a) The initial ($z = 0$ mm) density map. b)Time-space map showing the evolution of a vertical density profile passing through the beam centre ($x = 0$ mm). One clearly observes the expansion of the beam during the evolution along z. To compare the observed dynamics to a qualitative description based on the expansion at the speed of sound developed in the main text, the white dashed lines following the trajectories: $\pm x_0 \pm c_s z$ are plotted with arbitrarily chosen $x_0 = 0.3$ mm. c) Density profiles at various times: $g\rho_0 z = \{0; 20; 40; 60; 80\}$, showing the beam shape changing from a Gaussian to an expanding flat-top like profile.

gases, where the interaction dominates the kinetic energy. However, the cold atoms are usually subject to an external potential which spatially confines the system and makes the steady state possible. In difference to the cold atom gases, in the present discussion we don't consider the fluid of light to be confined by an in-homogeneous transverse refractive index landscape. This implies that in our case, the beam expansion under the effect of interactions is an out of equilibrium process which does not reach a steady state within available observation times.

Model: sound wave-like expansion if larger than the healing length: In fact, as mentioned in the description of the eqns 4.10 and 4.11, these equations hardly admit analytic solutions. Nevertheless inspired by the results of the previous section, one can make an analogy between the a low-spatial frequency perturbation and the strong beam itself: once the healing length ξ becomes much smaller than the beam size ω_0 the beam starts to expand at the local speed of sound.

Beam expansion vs beam size: This implies a counter-intuitive conclusion that, taking for instance an example of a Gaussian beam, two beams of different size but having same peak intensity, they will expand by a same spatial range in the $z \ll z_R$ regime. This conclusion is counter-intuitive for an experimentalist, used to observe at constant laser power a faster beam expansion under the effect of interactions for a smaller beam compared to the larger one. Primary explanation of this observation resides in the fact that working with constant laser power the laser intensity decreases quadratically with beam size. On the other hand, taking into account the size dependence of the interaction constant in dense and thermal Rubidium vapors [55], with following scaling: $g \sim \omega_0$, one ends up with the following scaling of the speed

of sound as function of the beam size:

$$c_s \propto \sqrt{gI} \sim \sqrt{\frac{\omega_0}{\omega_0^2}} \sim \sqrt{\frac{1}{\omega_0}} \tag{4.24}$$

This scaling shows that at constant laser power and including the interaction constant linearly increasing with beam size, one still expects to observe a speed of sound decreasing as invserse square root with beam size and therefore a smaller beam non-linearly expanding (defocusing) faster than a larger one, in agreement with experimental observations.

Numerical experiment result/ Figure 4.2 a): Using split-step Fourier method, one can easily numerically integrate the equation 4.1. Figure 4.2 shows the result of such a numerical experiment in which a fluid of light having the density shown in fig. 4.2 a) evolves until the time $z = 75$ mm. An elliptical beam of waists: $\omega_{0,x} = 2.5$ mm and $\omega_{0,y} = 0.8$ mm is used as the initial state. It has local photon interactions given by $g\rho_0(0, 0, z = 0) = 1.07$ mm^{-1} and 30 % absorption losses ($\alpha = 0.0048$ mm^{-1}) at the final stage. In fig. 4.2 b), the density cuts along the clear red vertical dashed line in fig. 4.2 a) crossing the beam centre, are shown as function of the normalized time $g\rho z$ which is the x-axis.

Expansion at c_s/ Figure 4.2 b): The beam expansion is clearly observed during the evolution along z. In order to compare the observed dynamics to a qualitative description based on the expansion at the speed of sound developed in the main text, the white dashed lines following the trajectories: $\pm x_0 \pm c_s(r = 0, z = 0)z$ are plotted. The starting point x_0 is fixed at $x_0 = 0.3$ mm in order to match the beam edge at the maximal propagation time, where it becomes more and more sharp. In fact, one can remark on the space-time diagram b) that as the time advances the beam seems indeed to expand at the speed of sound, according to the trajectory calculated with the beam's initial and central speed of sound.

Beam shape variation / Figure 4.2 c): It is also interesting to observe how the interaction driven dynamics affects the beam shape. This is shown in c) with the density profiles at various times: $g\rho_0 z = \{0; 20; 40; 60; 80\}$. The beam evolves from a Gaussian to an expanding flat-top like profile with the beam edges expanding at the speed of sound.

Experimental measurement: figure 4.3: The figure 4.3 shows the experimental intensity profiles, measured at the vapor cell's exit plane, for increasing interaction strength $g\rho_0 L$ (proportional to the square of the speed of sound, see eqn. 4.6). The panel a) shows the vertical (y) expansion of an horizontally (x) elongated collimated Gaussian beam of the following waist dimensions ($\omega_x = 2.1(0.15)$ mm, $\omega_y = 0.8(0.1)$ mm), which corresponds to a fluid in the quasi 1D geometry, because its expansion dynamics in the horizontal x direction is much slower than in the y direction. The panel b) shows the radial (r) expansion of a 2D centrosymmetric Gaussian beam of waist $\omega = 1.65(0.15)$ mm. On both panels each spatial profile for different $\tau = g\rho_0 L$ values roughly corresponds to one processed image. The interaction strength was measured for each acquired image using the single shot off-axis interferometric technique presented in chapter 3. The different images were acquired at different laser detunings and input powers, therefore each profile's intensity is normalized by its central (maximal) value.

On both panels there are dashed lines, showing the expansion at the speed of sound, calculated

at the beam centre, with an initial "size" y_0 and r_0, chosen to match the beam edges at large interaction strengths. The fig. 4.3 shows clear emergence of a sharp beam edge which becomes more and more pronounced with interaction strength and which expands at the maximal speed of sound $c_s = \sqrt{g\rho_0/k_L}$. Here, the beam edge appears more contrasted in the 1D rather than the 2D case, because of a smaller initial beam size (0.8 mm versus 1.65 mm). Indeed, additional transverse wavevector components, stemming from the beam's intensity inhomogeneity and interactions, emerge at $\delta q = \nabla_\perp \Phi_0(\rho_0(\mathbf{r})) \sim g\rho_0 L/\omega_0$, which have at fixed interaction strength $g\rho_0 L$ has larger values for smaller waist ω_0.

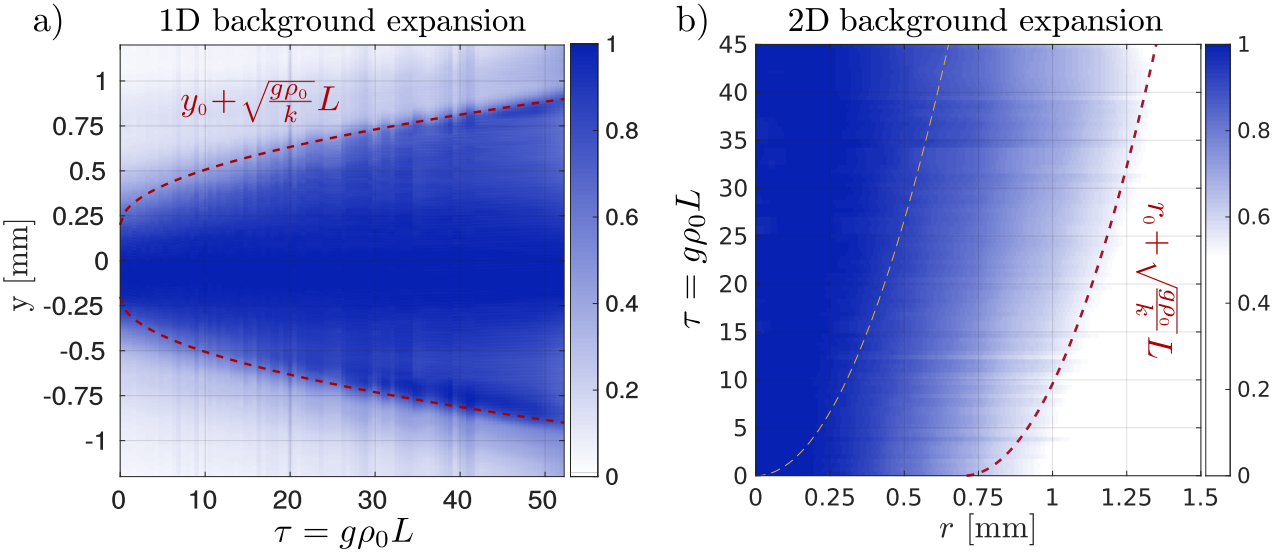

Figure 4.3: Experimentally measured expanding background fluid's normalized density as function of the interaction strength for a) a quasi 1D (horizontally elongated, $\omega_x = 2.1(0.15)$ mm, $\omega_y = 0.8(0.1)$ mm) and b) a 2D (circular, $\omega = 1.65(0.15)$ mm) beam. Dashed lines show a sound like expansion ("size" increasing as $c_s L \propto \sqrt{g\rho_0/k_L}L$) with an arbitrarily chosen position offset: $y_0 = 0.2$ mm in 1D (a) and $r_0 = 0.7$ mm in 2D (b).

Validity range/limitation of the model: It is nevertheless important to notice that the description with eqn. 4.11 is valid for not too long evolution times. Indeed, as it can be seen on fig. 4.2 c) the steepening of the density profile, which happens during the beam's evolution, is accompanied by the emergence of higher spatial frequencies $\mathbf{q}$ in the spectral distribution of the beam. As long as the spectrum only contains the frequencies below the inverse healing length $1/\xi$, the eqn. 4.11 is accurate, but at certain moment this condition is not anymore valid and the beam cannot by anymore within the long-wavelength limit. After this moment the quantum pressure term (eqn. 4.9) becomes relevant. This term is commonly characterized as a "dispersive" one because of its dispersive contribution in the context of the Bogoliubov dispersion relation (eqns. 4.21 and 4.23). Therefore its primary role in beam's evolution consists in splitting the high frequency components according to their different phase velocities $\mathbf{v}_\phi(\mathbf{q}) = \Omega(\mathbf{q})/\mathbf{q}$, which can be calculated from the Bogoliubov dispersion: eqn. 4.21. This results in the emergence of small density oscillations beyond the steep density front. They

stem from the high spatial frequency modes which emerge at the vicinity of the beam edge and have the phase velocity above the speed of sound. The oscillating pattern starts being barely visible in the vertical density profile at $g\rho_0 z = 80$, shown on fig. 4.2 c), yellow colour. It has also been recently experimentally observed in a fluid of light [9].

4.3.3 Strong perturbation on top of a background

Motivation: Having qualitatively modeled the evolution of an interacting background and the one of small perturbations on top the background, it is tempting to consider the evolution of an initial state with strong localized perturbation on top of a background. In the present case the perturbation is considered sufficiently strong to be able to affect the local speed of sound in a non-negligible way. As discussed previously, this implies fast dynamics of the perturbation on top of the background, but variation of speed of sound within the perturbation is expected to strongly affect the perturbation beam's shape. In fact, as will be shown below, this situation gives rise to a special type of non-linear waves, encountered in various fields of physics, called: dispersive shock waves. Analogy and differences between the shock waves in a fluid of light and the ones, emerging, for instance, in non-linear acoustics will be useful to get a comprehensive insight in this phenomenon. This regime is the main focus topic of the present chapter.

Amplitude dependent sound velocity dispersion: Let's consider a Gaussian perturbation of a finite size ω_1, much smaller than the background size ω_0, but larger than the local healing length, $\omega_1 > \xi$:

$$\delta\rho(\mathbf{r}, 0) = \ \rho_1.\exp\left(-2\mathbf{r}^2/\omega_1^2\right) \tag{4.25}$$

If the perturbation is not anymore weak $\rho_1 \sim \rho_0$, then the additional pressure term $\delta P(\mathbf{r}, 0) = g\delta\rho(\mathbf{r}, 0)$ stemming from the interaction term in the eqn 4.3 will act as a repulsive (since $g > 0$) potential pushing the additional density away from the centre. The perturbation will split into two wavepackets spreading towards opposite directions. This symmetry stems from the fact that spatial spectrum of the Gaussian perturbation profile, which is also Gaussian and centered at zero, contains both positive and negative spatial frequencies. The propagation direction of a mode $\mathbf{q}$ is given by the sign of the associated phase velocity $\mathbf{v}_\phi$ which, in turn, equals to the sign of $\mathbf{q}$ for the positive branch of the dispersion relation 4.21. The perturbation's density being comparable to that of the background, the local speed of sound is not anymore fixed by the background density, but rather depends on the total density. This dependence induces significant sound velocity variation within the perturbation, which has a fast spatial density variation. More precisely, at the initial stage, the speed of sound is maximal at the center of the perturbation and equals to $c_{s,0}(r = 0) = \sqrt{g(\rho_0 + \rho_1)/k_L}$ while at its edge, where the perturbation density is small with respect to the one of the background, it reduces to $c_{s,\infty} = \sqrt{g\rho_0/k_L}$. One can hence rewrite the central speed of sound as:

$$c_{s,0} = c_{s,\infty}\sqrt{1 + \tilde{\rho_1}} \ \text{ with: } \ \tilde{\rho_1} = \frac{\rho_1}{\rho_0} \tag{4.26}$$

During the fluid's evolution, the perturbation's center expands faster than its edge, causing fast redistribution of the density and its shape variation. The most dense region moving at fastest speed of sound $c_{s,0}$, accumulates at the vicinity of a front moving at the speed $c_{s,0}$. At the same time the size of the perturbation wavepackets increases with time, due to the amplitude caused dispersion of speed of sound. The wavepacket size should then evolve typically as: $\Delta\omega_1 \simeq (c_{s,0} - c_{s,\infty})z$ while developing a density peak followed by a steep density reduction, called later on the "shock front" at the position given by the propagation at the maximal speed of sound, $c_{s,0}$.

Longer times: QP contribution: The emergence of steep density gradients broadens the spatial spectrum of the fluid and as soon as the involved spatial frequencies exceed the inverse healing length, the quantum pressure term becomes relevant. The associated evolution time is called "wave-breaking" time [76, 18]. As in case of a dense background's evolution at long times, this term gives a dispersive contribution to the wavepacket's propagation. It ensures, that the spatial frequencies above the inverse healing length, emerging due to the shock front's formation, move at phase velocities above the speed of sound and increasing with spatial frequency. This occurs because the quantum pressure term involves higher spatial derivatives than the interaction term in eqn 4.3.

Figure 4.4: Figure 4.4 shows the results of a numerical experiment, in which an elongated Gaussian perturbation of waists $\omega_{1,x} = 0.12$ mm and $\omega_{1,y} = 2.5$ mm on top of an elliptical Gaussian background of waists $\omega_{0,x} = 2.5$ mm and $\omega_{0,y} = 10$ mm, evolves in a medium of length $L = 75$ mm with local photon interactions of strength $g\rho_0 = 0.27$ mm^{-1} and total absorption of 30 %, given by $\alpha = 0.0048$ mm^{-1}. Note that the vertical dimensions being much larger than the horizontal ones, the dynamics along the vertical direction is much slower than the horizontal one and will be neglected in this discussion. This situation is referred to as the quasi 1D case.

Figure 4.4 a) and b): Figure 4.4 a) shows the fluid's normalized spatial density map ($\tilde{\rho} = \rho/\rho_0$) at the initial stage (entrance of the medium) in the case where $\tilde{\rho}_1 = 1.25$ (corresponding to the $|\delta\mathcal{E}(0,0)| = 0.5\sqrt{\rho_0(0, z = 0)}$). Fig. 4.4 b) shows the fluid's density at $z = 75$ mm. As predicted in the previous paragraph, the initial perturbation splits into two wavepackets moving to opposite directions. The shape of the wavepackets is now asymmetric and shows a peaked sharp edge in their direction of motion. The sharp peaked edges are followed by less pronounced density oscillations. The distance between the wavepackets is maximal at the centre ($y = 0$), where the perturbation density is maximal, and slightly decreases as y increases, due to the decreasing perturbation density.

Figure 4.4 c) and d): overdensity: To analyze more precisely the dynamics of the perturbation, the profiles along the horizontal red dashed line in Figure 4.4 b) of the normalized overdensity $\delta\tilde{\rho} = \delta\rho/\rho_0$, are shown as solid curves on the same plot in fig. 4.4 c), and separately in 4.4 d), for various perturbation overdensities $\tilde{\rho}_1$, arranged by increasing colour darkness of the curve. From the clearest to the darkest colour, the perturbation overdensity increases with the values: $\{0.04, 0.21, 0.44, 0.74, 1.25\}$, corresponding respectively to $|\delta\mathcal{E}|/\sqrt{\rho_0} = \{0.02; 0.1; 0.2; 0.32; 0.5\}$,

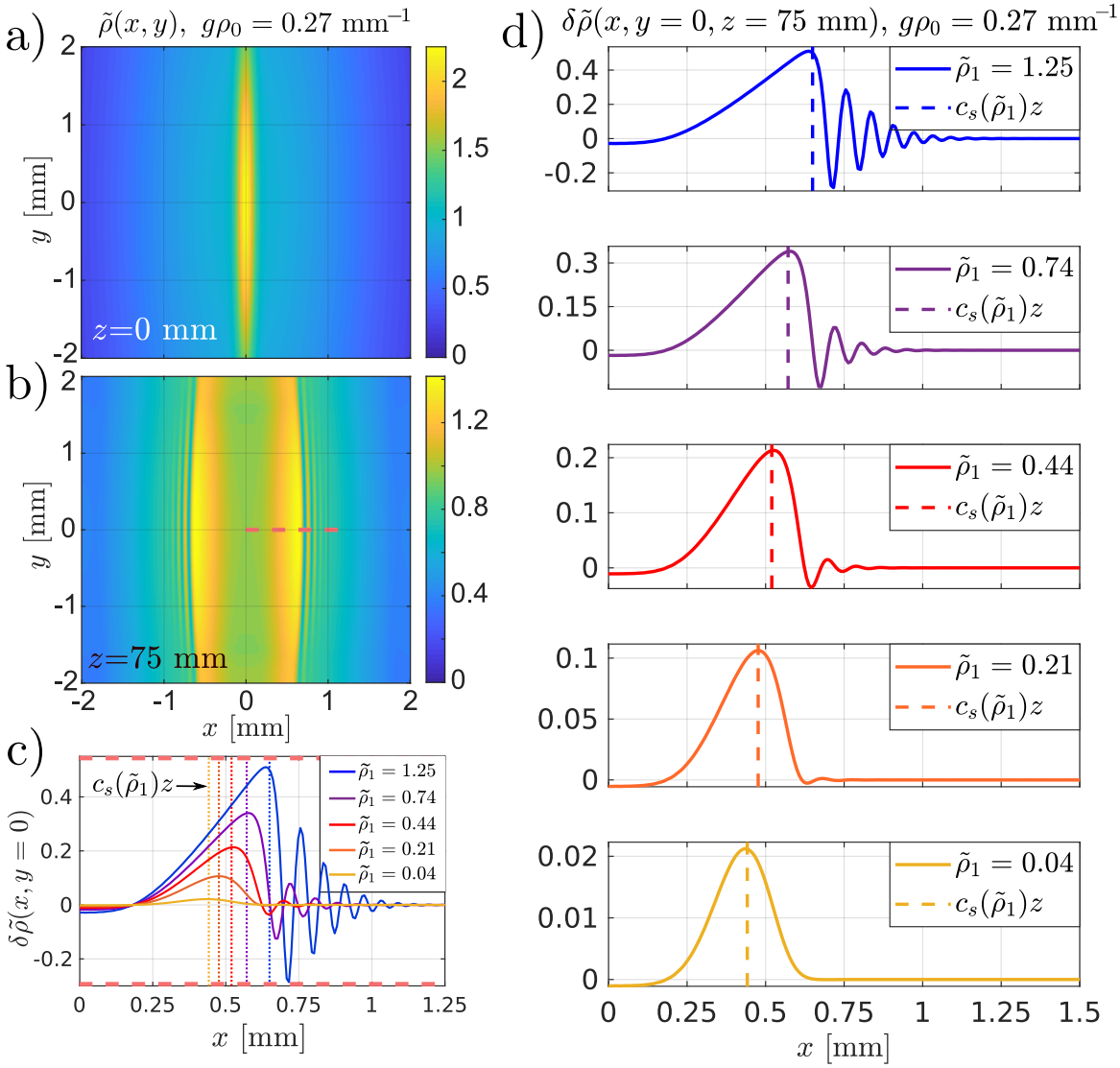

Figure 4.4: Strong perturbation on top of a background fluid. An elongated Gaussian perturbation of waists $\omega_{1,x} = 0.12$ mm and $\omega_{1,y} = 2.5$ mm on top of an elliptical Gaussian background of waists $\omega_{0,x} = 2.5$ mm and $\omega_{0,y} = 10$ mm, evolves in a medium of length $L = 75$ mm with local photon interactions of strength $g\rho_0 = 0.27$ mm^{-1} and total absorption of 30 %, given by $\alpha = 0.0048$ mm^{-1}. a) Initial density map normalized by the background's initial peak density. b) Final density profile at the propagation length of $z = 75$ mm. c) The final state overdensity profiles along the red dashed line in b) showing the simulation results with different initial perturbation strengths quantified with the initial absolute overdensity $\tilde{\rho}_1$ (in the initial background peak density units). The dotted vertical lines show the propagation distance $c_{s,0}L$ at the speed of sound $c_{s,0}$, calculated with the initial total peak density (including the perturbation and given by the eqn. 4.26). d) The same overdensity profiles as in c) but shown separately, with the increasing perturbation strength for bottom to top. The vertical dashed lines show again the shock front position calculated with the initial total speed of sound eqn. 4.26.

according to:

$$\rho_1 = (\rho - \rho_0)|_{(r=0,z=0)} = 2\sqrt{\rho_0}|\delta\mathcal{E}| + |\delta\mathcal{E}|^2 \tag{4.27}$$

One can clearly observe the perturbation shape variation as its strength wrt background increases. For small $\tilde{\rho}_1 = \rho_1/\rho_0 = 0.04$, it simply advances linearly at the speed of sound, imposed by the background fluid, while keeping its initial Gaussian shape during propagation. This is a situation in which the Bogoliubov model (see second part of section 4.3.1) and especially the equation 4.21 are perfectly applicable. As $\tilde{\rho}_1$ increases to 0.2, the perturbation wave's profile starts acquiring an asymmetry making it more peaked towards higher x values. Increasing $\tilde{\rho}_1$ more, the asymmetry becomes even more pronounced and reminds of a saw-tooth function with a linearly rising wave profile dropping to zero at its peaked front edge, called the "shock front". However, as soon as the discontinuity develops, one can observe the density oscillations developing beyond the shock position. As described above, they arise from the dispersive contribution of the quantum pressure, eqn 4.9 at the "wave-breaking" time [76, 18]. An accurate theoretical description of this phenomenon can be found in [76] and a recent experiment from our group succeeded in an impressive quantitative comparison between the proposed theory and the observed results [18].

Figure 4.4 c) and d): calculated sound wave's position: The dashed vertical lines show the calculated perturbation front positions using the perturbation's initial central speed of sound: $c_{s,0} = c_{s,\infty}\sqrt{1+\tilde{\rho}_1}$. Each shown position corresponds to the density profile of the same colour. These positions seem to coincide with the overdensity peaks and can be associated to the shock fronts. Indeed, as the overdensity $\tilde{\rho}_1$ increases, the associated speed of sound increases as well and the shock front moves forward. At long times it is followed by the dispersive density oscillations.

Link to classical shock waves: The notion of the shock front, explored above, highlights the fact, that a strong perturbation's non-linear propagation enhances the formation of a transport of a well localized discontinuity in variables characterizing the fluid's local state (for instance, density and pressure). Such a wave impinging on an obstacle is perceived by the latter as an instantaneous shock impact. Such a phenomenon is commonly encountered various systems in which the wave velocity increases with its amplitude. It may occur in case of surface waves at the sea shore or as a non-linear sound wave during an explosion. All these phenomena have a common description involving the formation and propagation of shock waves. It is therefore interesting to highlight similarities and differences between the shock waves occurring in a fluid of light and, for example, in a classical fluid, within the framework of non-linear acoustics.

Similarity: quadratic state equation favors shock formation: In fact, a quadratic correction to a classical fluid's state equation $P(\rho)$ results in the density dependence of its speed of sound: $c_s^2 = 1/(\rho\kappa) = \frac{\partial P}{\partial \rho} \sim \rho$. This is, in turn, a formation condition for the shock waves in the case of a "strong" density perturbation, exactly as in the case of a fluid of light. In fact, in the latter system, the speed of sound is constant (fixed by ρ_0) for weak perturbations and starts depending on total density as the perturbation ρ_1 becomes important. This results in both systems in a situation in which most dense regions of the perturbation move faster than the less dense ones and form a shock wave front.

Difference: regularization mechanism: As presented above, the discontinuity forming in a fluid of light during a shock wave does not survive at long times due to the dispersive effect arising due to the quantum pressure. As the result, all spectral components supposed to accumulate at the shock front to form a real discontinuity get dephased and spatially delocalised giving rise to the density oscillations beyond the shock. This is a mechanism which regularizes the shock singularity in the case of the quantum fluids. The situation is different fields of shock wave formation. For example, in non-linear acoustics the propagation equations don't contain any dispersive terms, yet the discontinuity is still regularized by an extra damping term stemming from the fluid's viscosity and the wave's eventual non-adiabaticity resulting in heat transfer to the support medium by the propagation of a shock. Interestingly, no such dissipation mechanism is present in quantum fluids despite the presence of the linear absorption term $-\alpha\rho$ in eqn 4.2, specific to the fluids of light in the propagating geometry, which allows to classify the shock waves in these systems as dispersive shock waves. Finally, dispersive shock waves arise in various other fields than quantum fluids, like for example, collisionless plasma physics, where they were predicted for the first time [130, 76].

4.4 Shockwaves in optics

4.4.1 Observation in superfluid systems

In BECs: Their first observation in atomic Bose Einstein Condensates was reported in [72]. The perturbation was produced with an optical pulse focused into the condensate cloud centre, acting as an external potential rapidly pushing the atoms from the condensate center. The condensate density was measured using absorption imaging of the condensate cloud. The authors probed the 2D dynamics of condensate's radial expansion and clearly observed the density depletion at the laser addressed position and the expansion quite rapidly involving the appearance of density oscillations in form of rings due to the quantum pressure's dispersive contribution.

In optics: As highlighted in the previous discussion, a light beam acquires compressible hydrodynamical behavior, including the amplitude dependent speed of sound, in presence of the photon-photon interactions. Depending on the illumination mode (cw or pulsed), the interaction term can mix with either diffraction or/and dispersion to affect the fluid of light's transverse spatial or/and temporal dynamics (see the propagation equations derived in the introduction chapter 1). This suggests that in both cases the variables describing the transverse spatial and temporal coordinates, constitute the 3-dimensional space of a fluid evolving according to an effective time given by the axial coordinate z [96, 97, 95]. At this point it is intriguing to note that the shock wave dynamics has so far never been observed simultaneously in transverse space and time, i.e. in a three dimensional fluid of light.

Spatial domain: First DSW observation in the spatial domain dates back to 2007, where the authors perform the fluid intensity measurements at the exit of a non-linear photorefractive crystal [155] and in other experiments performed in non-linear and non-local thermo-optic

media [14, 36], observing DSW profiles in 2D with a localized point-like perturbation. The authors could confirm that the shock front expands at a rate given by a square root of the density (speed of sound). More recently, an experiment with a fluid of light in hot Rb vapor was performed in the 1D configuration (an elongated perturbation) [18], and successfully validated the theory developed in [76, 77]. Finally, another experiment with fluid of light in a hot Rb vapor observed formation of dispersive shocks during the single beam's (in the absence of a background) interaction driven expansion, noticing the influence of absorption and non-locality of interactions [9].

Temporal domain? DSW ware also observed in the temporal domain with pulsed fluids of light. For this type of experiments well resolved temporal intensity measurement is necessary, while the beam's temporal spectral broadening can be probed with an optical spectrum analyser [50, 161, 112, 109].

4.4.2 Blast waves

Typical shock wave behavior: Phenomenologically, the shock waves arise in situations where sudden and non-adiabatic changes in local hydrodynamic quantities occurs due to their strong perturbation. While this perturbation is spread in space and time according to the local (density dependent) speed of sound by shock waves, the disturbed quantities typically decay exponentially with time after the passage of the shock at a given position. The disturbed quantities eventually reach their ambient (undisturbed) values.

Blast wind: However, there are known situations where the decay of disturbed quantities overshoots below their undisturbed values before eventually stabilizing at the latter. This is the case of the waves produced during explosions. These waves are commonly called blast waves and have a very characteristic behavior of the overpressure evolution, consisting of two stages also called "phases". The first phase consists of the supersonic (with respect to the background speed of sound) passage of the shock front with positive overpressure. It is then followed by the second phase consisting in a negative overpressure. Due to its negative value, it corresponds to the subsonically evolving part of the wave. During the detonations, the negative phase, also called the *blast wind*, has considerable consequence in the wave-matter interaction. Due to its reversed sign of the overpressure, corresponding to the compression stress, it contributes to the damage of material structures it interacts with. More apparently, the negative phase of the blast waves is the direct explanation of the presence of the broken glass pieces inside a building where an explosion happened.

Figure 4.5 of a Friedlander profile: A typical time history of the overpressure is shown on fig. 4.5, highlighting both the positive and negative phases of blast waves. Blast waves are typically modeled with an empirical formula, called Friedlander profile:

$$\frac{P(t) - P_0}{P_0} = P_s \mathrm{e}^{-t/\tau_p} \left(1 - \frac{t}{\tau_p}\right) \tag{4.28}$$

In this equation P_s quantifies the strength of the explosion (usually linked to the total mass of

the explosive) and τ_p corresponds to the duration of the positive phase.

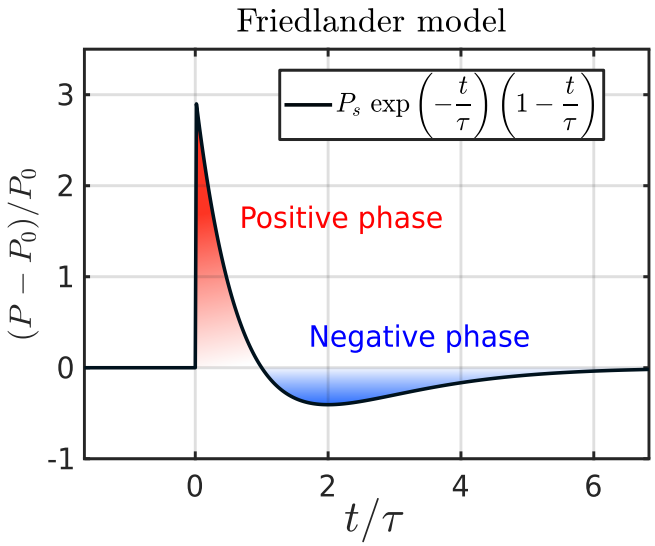

Figure 4.5: A Friedlander wave profile, commonly used to describe the Blast waves.

Analogue blast waves in optics? The overwhelming part of literature on blast waves discusses this phenomenon in the context of the detonation waves. However, to the best of my knowledge, nothing prevents the blast waves to occur in other fields of physics. In the following part of this chapter the experimental study of the shock waves in a paraxial fluid of light is presented, with a particular focus on the possible observation of the analogue blast waves in this experimental system.

4.5 Experimental observation of blast waves

4.5.1 Experimental methods

4.5.1.1 Effective time

Principle: Experimental observation of non-linear hydrodynamics in a fluid of light requires the ability to image the latter at different times. From the chapter 1 we know, that since the propagation direction z plays the role of time, the fluid's temporal dynamics can be studied by accessing its state at different z positions. However imaging is not possible inside a non-linear medium without placing the camera at the imaged position, since the non-linear propagation affects the image in an uncontrolled way. Alternatively, one can instead re-scale the effective time by incorporating fluid interaction [114, 18]. In fact, one can take as definition of time the non-linear phase $\Phi_0 = g\rho_0 L$, that the background beam acquires over the propagation of distance L. This time could be varied by changing the vapor cell length L but now also by changing the interaction strength $g\rho_0$, which can be tuned with the laser frequency and power, while imaging only the cell's exit plane. Re-scaling the time can be mathematically formulated

by defining the rescaled (or normalized) time as:

$$\tau = \int_0^L g\rho_0(z)dz \quad \text{such that:} \quad \delta\tau = g\rho_0(z)\delta z \tag{4.29}$$

From this one can define the following quantities:

$$z_{NL} = \frac{L}{\tau}, \quad \text{non-linear axial length} \tag{4.30}$$

$$\xi = \sqrt{\frac{z_{NL}}{k}}, \quad \text{transverse healing length} \tag{4.31}$$

$$c_s = \frac{c}{k_L \xi}, \quad \text{speed of sound} \tag{4.32}$$

$$\psi = \frac{\mathcal{E}}{\sqrt{\rho_0(0,L)}}, \tag{4.33}$$

Then the space variables can be normalized accordingly as: $\tilde{\mathbf{r}} = \mathbf{r}/\xi$ and $\tilde{\nabla}_\perp = \xi\nabla_\perp$. The propagation equation then reads:

$$i\frac{\partial\psi}{\partial\tau} = \left(-\frac{1}{2}\tilde{\nabla}_\perp^2 + |\psi|^2\right)\psi. \tag{4.34}$$

One can note that dynamics of ψ is not anymore dissipative, due to the normalization with respect to the exponentially decaying density: $\rho(0,L) = \rho(0,0)\exp(-\alpha L)$, measured at at the medium's exit plane. This happens at the expense of a total evolution time τ which is averaged over lossy propagation. Everything happens as if the effective propagation distance were changed while keeping a fixed interaction constant, whereas it is in fact achieved by doing the opposite. It is important to note that the rescaled interaction constant does not depend on the effective time as long as only linear (intensity independent) losses are considered. This formulation is necessary to describe accurately the experimental results of this work probing temporal dynamics of a fluid of light by varying the strength of the optical non-linearity and not the imaged z plane. The effective time $\tau = |\Delta n(\mathbf{r}_\perp = 0, L)|k_0 L$ equals to the maximal accumulated non-linear phase of the background beam. Rewriting the Madelung transformation with the new variables, we obtain:

$$\psi = \sqrt{\tilde{\rho}}\mathrm{e}^{i\phi} = \sqrt{\frac{\rho}{\rho_0(0,L)}}\mathrm{e}^{i\phi}, \quad \tilde{\mathbf{v}} = \frac{\mathbf{v}}{c_s} = \tilde{\nabla}_\perp\phi. \tag{4.35}$$

One gets dimensionless Euler and the continuity equations:

$$\frac{\partial\tilde{\rho}}{\partial\tau} + \tilde{\nabla}_\perp.(\tilde{\rho}\tilde{\mathbf{v}}) = 0 \tag{4.36}$$

$$\frac{\partial\tilde{\mathbf{v}}}{\partial\tau} + \frac{1}{2}\tilde{\nabla}_\perp\tilde{\mathbf{v}}^2 = -\tilde{\nabla}_\perp\left(\tilde{\rho} - \frac{1}{2\sqrt{\tilde{\rho}}}\tilde{\nabla}_\perp^2\sqrt{\tilde{\rho}}\right), \tag{4.37}$$

where the link between Eq. (4.37) and the Euler equation is made by neglecting the quantum pressure.

Validity of the approach: The procedure of rescaling the time, along with the dimensionless formulation of the fluid's evolution, implies the equivalence between the initially dissipative propagation that finally becomes dissipationless evolution with the dimensionless time. This is true as long as the total accumulated non-linear phase Φ_0 from the first case equals the dimensionless time τ of the second case. In other words, no matter what trajectory the normalized time $\tau(z)$ follows between $z = 0$ and $z = L$, as long as $\tau(L)$ is the same, all trajectories (see fig. 4.6 a)) are equivalent and lead to the same final state for the fluid of light. Without rigorous proof of validity of this assumption, let's test it on a simple example of sound-wave like evolution of a localized density perturbation on top of a density background. We want to evaluate the distance that the wavepacket travels after propagation of distance L, on the one hand in presence of an interaction constant g with a loss rate α, and on the other hand, during lossless evolution with the effective interaction strength $\langle g \rangle_z = g\left(1 - \mathrm{e}^{-\alpha L}\right)/(\alpha L)$. In both scenarios the distance will be respectively equal to:

$$\Delta r_1 = \int_0^L c_s(z)dz = c_s(0)\int_0^L \mathrm{e}^{-\alpha z/2}dz = \frac{2\left(1 - \mathrm{e}^{-OD/2}\right)}{OD} \times c_s(0)L \tag{4.38}$$

$$\Delta r_2 = c_s(\langle \rho_0 \rangle_z)L = \sqrt{\frac{1 - \mathrm{e}^{-OD}}{OD}} \times c_s(0)L \tag{4.39}$$

where we introduced the optical depth, $OD = \alpha L$. The numerically calculated prefactors of both results are shown on fig. 4.6 b) as function of the transmitted fraction of power through the cell. They correspond to the normalized (in $c_s(z = 0)L$ units) displacement of the wavepacket and are very close (only 5% deviation at 5% transmission). This result suggests the validity of the dissipationless interpretation of the propagation in presence of absorption losses, using the trick of rescaling the time and working with normalized quantities.

4.5.1.2 Experimental observables: dimensionless hydrodynamic quantities

Initial non-equilibrium state: In this experiment we study the dynamics of a fluid of light disturbed by an initially spatially localized Gaussian over-density:

$$\tilde{\rho}(\mathbf{r}, L) = \tilde{\rho}_0(\mathbf{r}) + \delta\tilde{\rho}(\mathbf{r}, L) \tag{4.40}$$

$$\tilde{\rho}_0(\mathbf{r}, 0) = \tilde{\rho}_0 \cdot \exp\left(-2\mathbf{r}^2/\omega_0^2\right) \qquad \delta\tilde{\rho}(\mathbf{r}, 0) = \tilde{\rho}_1 \cdot \exp\left(-2\mathbf{r}^2/\omega_1^2\right) \tag{4.41}$$

$\tilde{\rho}_1 = \rho_1/\rho_0$ is chosen around unity and $\omega_1 \ll \omega_0$ quantifies the perturbation and the background widths. Indeed, $\tilde{\rho}_0$ depends on $\mathbf{r}$ having a Gaussian shape, much larger than ω_1. The overdensity can also be measured at further normalized times $\tau > 0$:

$$\delta\tilde{\rho}(\mathbf{r}, \tau) = \tilde{\rho}(\mathbf{r}, \tau) - \tilde{\rho}_0(\mathbf{r}, \tau) \tag{4.42}$$

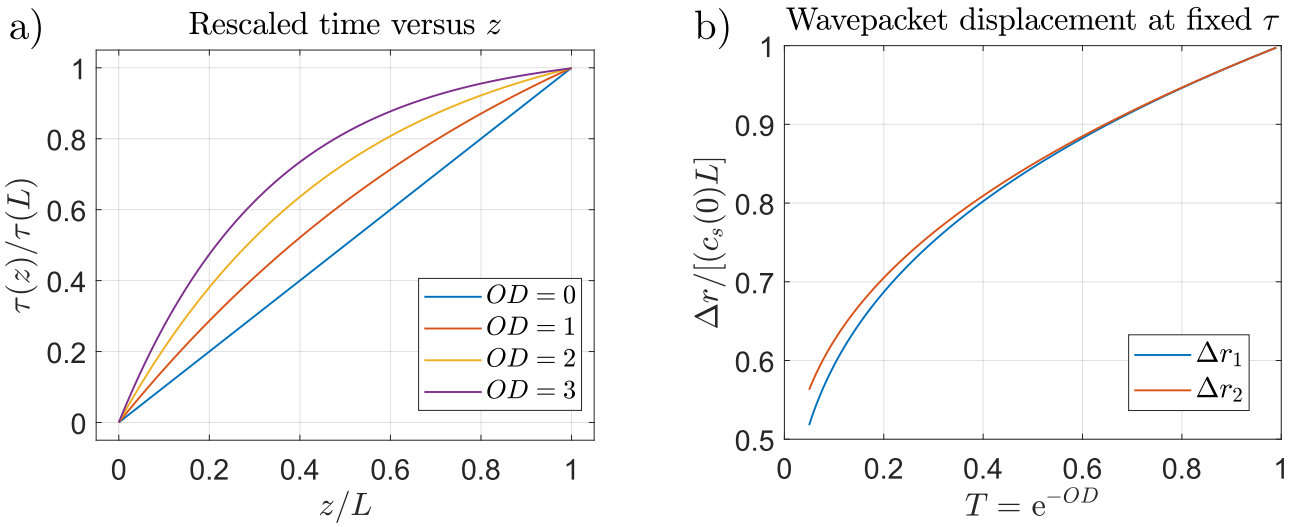

Figure 4.6: a) Normalized time as function of the propagation distance in presence of the linear absorption, quantified with the optical depth, OD. b) Calculated weak density perturbation wavepacket's displacement as function of the total transmission at fixed final time $\tau(L)$.

by simply subtracting the image of background only from the image with the perturbation.

Recalling the hydrodynamic quantities presented in section 4.2.1.3, one can define the dimensionless hydrostatic pressure as:

$$\tilde{P} = \frac{1}{2}\tilde{\rho}^2 \tag{4.43}$$

This pressure can be also easily calculated from the intensity images of the cell's exit plane. One can also define the dimensionless version of the dynamic pressure as:

$$\tilde{P}_d = \frac{1}{2}\tilde{\rho}\tilde{\mathbf{v}}|\tilde{\mathbf{v}}|, \tag{4.44}$$

Expressed in dimensionless units, the dynamic pressure gives the strength of the convection term normalized by the pressure due to the interactions in the Eq. (4.37). In difference to the hydrostatic pressure, the calculation of the dynamic pressure also requires the velocity measurements. The fluid velocity can be accessed from the measurement of the beam's spatial phase, which is realized using off-axis interferometry. Calculating numerically the gradient of the phase, we obtain the background fluid velocity $\mathbf{v}_0$ and the perturbation velocity $\mathbf{v}_1$ by analyzing the images without and with the perturbation, respectively. The over-pressure can be also evaluated from the pressure difference between the case with and without perturbation:

$$\delta\tilde{P}(\mathbf{r},\tau) = \tilde{P}(\mathbf{r},\tau) - \tilde{P}_0(\mathbf{r},\tau). \tag{4.45}$$

Where the involved pressures are calculated using Eq. (4.43). To evaluate the differential pressure $\Delta\tilde{P}(\tau)$, showing the instantaneous difference in pressure between the perturbation

center and the external undisturbed area, we define:

$$\Delta\tilde{P}(\tau) = \tilde{P}(0,\tau) - P_0(r_{ext},\tau). \tag{4.46}$$

The differential pressure $\Delta\tilde{P}(\tau)$ is the most important quantity we study in this work and we expect major differences in the non-linear perturbation dynamics between the 1D and the 2D geometries. We investigate the case $\rho_1 \sim \rho_0$ by analyzing the fluid density, velocity and pressure both in the 1D and 2D geometries, letting the perturbation evolve either primarily in one dimension or isotropically in both $x-y$ directions. The NLSE is known to give rise to sound-like dispersion to the low amplitude waves, governed by the Bogoliubov theory. Here, a perturbation of the same order (or larger) than the background results in the sound velocity variation following the local density inside the perturbation. This is the prerequisite for observing shock waves in our setup. In hydrodynamics, shock waves are usually reported as a time evolution measurement of a physical quantity (pressure, density...) at a fixed point in space. As discussed previously after the passage of a the shock wave front, a blast wind (a negative differential pressure) may occur depending on system parameters and dimensionality. In the next section we report the time evolution as well as the time snapshots (spatial map of a physical quantity at fixed time) typically not accessible in classical hydrodynamics experiments.

4.5.1.3 Setup and data processing

The setup: In this experiment, we investigate the propagation of a near-resonance laser beam through a 75 mm long warm rubidium vapor cell, which induces effective photon-photon interactions [3]. Two configurations are studied: the 2D geometry with a radially symmetric dynamics and the 1D geometry with a background much larger along x than along y which allows for a 1D description of non-linear wave dynamics [18]. The experimental setup is schematically visualized on Figure 4.7 a). A tapered amplified diode laser beam is mode cleaned with a polarization maintaining single mode fiber and then split into a background, a reference and a perturbation beams. The background beam is enlarged with a telescope up to a waist of 2.5±0.5 mm along x and 0.8±0.1 mm along y in the 1D geometry, and 1.8±0.3 mm along the radial coordinate in the 2D configuration. The reference beam (for interferometric phase measurement) is matched to the same dimensions. The cell output is imaged with a ×4.2 magnifying 4-f setup onto a camera. Sets of 4 images (background only, background with reference, background with perturbation and finally background with both perturbation and reference) were acquired for each interaction strength (effective time) in order to access the hydrodynamic observables. For the phase measurement, the reference beam is superimposed with other beams with an angle of 30 milli-radians, giving rise to interferogramms with vertical fringes of average periodicity of 25±1 μm.

Locking the phase between the background and perturbation: The perturbation beam is focused to get the waist of 0.12±0.03 mm in the middle of the cell (the corresponding Rayleigh range is 55 mm). The background and perturbation are recombined with a 90R:10T beam-splitter (BS), such that 90 % of the background beam power is reflected towards the cell. The

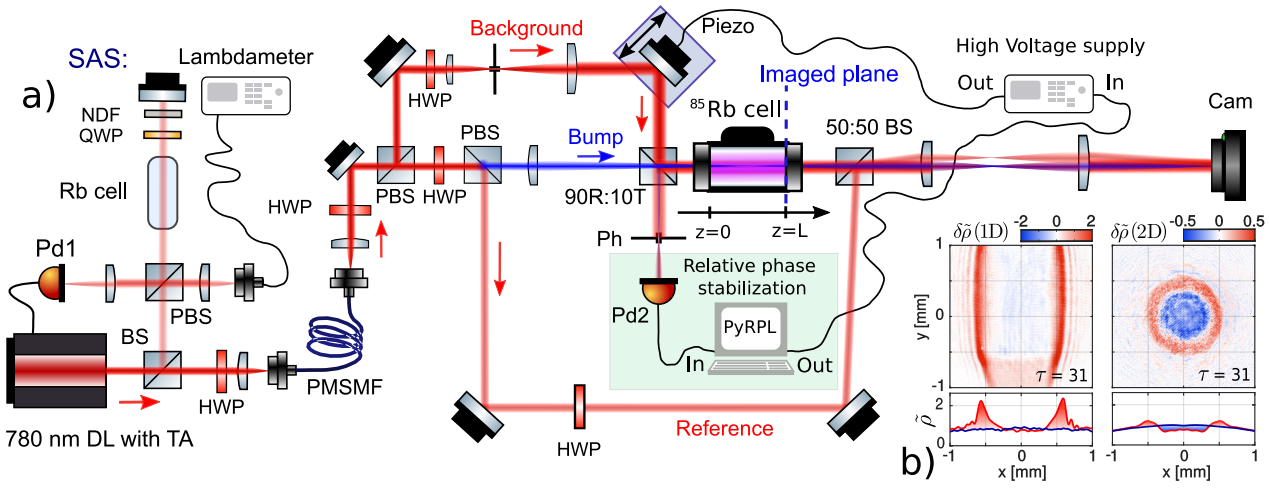

Figure 4.7: a) Experimental setup: a mode cleaned Gaussian laser beam was split into the Background, Bump and the Reference. The Background-Bump interference signal was measured by cropping the overlap area (200 μm diameter pinhole (Ph)) on a photodiode (Pd2) on the Beamsplitter arm complementary to the Rb vapor cell. This signal was transformed via the PyRPL lockbox software into an error signal driving the piezoelectric mirror mount (piezo) to lock the (Pd2) signal on a minimum. This relative phase control enables permanent constructive interference on the vapor cell arm. After propagation in hot Rb vapor, the cell exit plane is image via 4.2 fold magnifying 4f imaging telescope. b) Over-density images obtained image subtraction (see Eq. 4.42) in the 1D and 2D cases, revealing appearance of negative over-density in the 2D case. The centered unperturbed (blue) and perturbed (red) density profiles are shown below.

second arm of the BS is sent through a 200 μm diameter pinhole into a photodiode to stabilize the interferometer. Indeed, the relative phase between the background and the perturbation need to be zero (and stable in time) for the beam going into the cell, in order to realize correctly the state given in the eqn. 4.41. The relative phase is controlled with the photodiode signal of the BS's second arm: its minimum corresponds to the constructive interference on the arm, going into the cell, and vice-versa. Therefore the signal needs to be locked to its minimum value. For this the photodiode signal was transformed into an error signal using the Pound-Drewer-Hall technique [20], allowing for active relative phase correction.

In practice, the error signal was realized with a RedPitaya FPGA run by the PyRPL software [108]. PyRPL allows (among others) to visualize as on a scope and process the photodiode signal, transferred to Red-Pitaya, by mixing it with an additionally created modulation signal to produce in particular the $\pi/2$ phase shifted version of the photodiode signal. The latter can now be used as an error signal, because it has a shape of a linear slope around the lock-point corresponding to the zero phase. The error signal was then used by a PID (also available as a PyRPL module) before being fed (via a high voltage generator) into a piezoelectric mirror mount directly acting on the relative phase.

Control of the photonic interactions: Cell temperature is 149±2° C, leading to an atomic den-

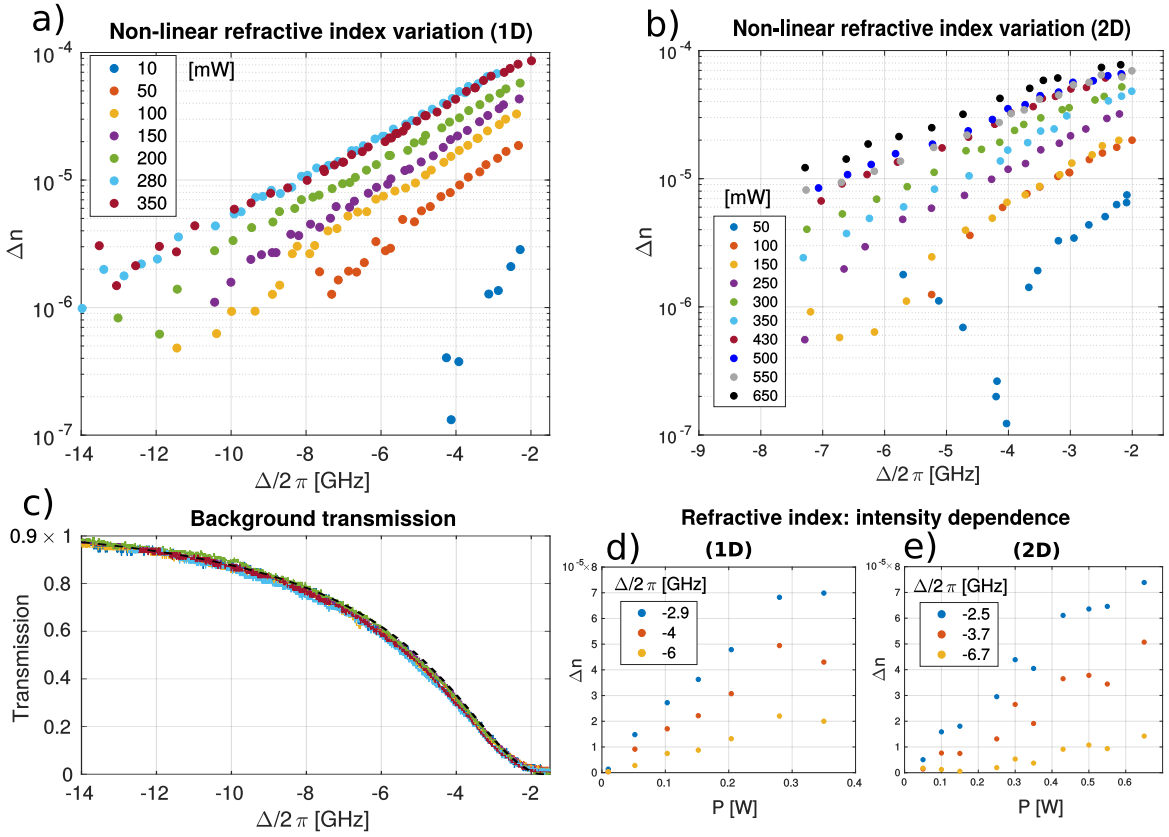

Figure 4.8: Vapor's transmission and its intensity dependent refractive index measurement. a) and b) show the maximal refractive index variation calculated from the off-axis interferograms of the background beam with a reference, in 1D and 2D geometry, respectively. c) Background beam's transmission spectrum with respect to ^{85}Rb $F_g = 3 \rightarrow F'$ transition measured at different input powers. Dashed line is the theory of a linear multilevel vapor at temperature 150 °C and 0.5 % the isotopic fraction of ^{87}Rb inside the cell. d) and e) show the variation of the refractive index with laser power at fixed laser detuning in both geometries.

sity of $8.3\pm0.8\times10^{13}$ cm^{-3}. In order to vary/control the interaction strength and consequently the effective time τ, the different images were acquired at different input powers $\mathcal{P}$ ranging from 50 to 600 mW and different laser detunings Δ from the ^{85}Rb D2 line $F = 3 \rightarrow F'$ transition are taken (see fig. 4.8 for details). The associated time $\tau = |\Delta n|k_L L$ is calculated from the nonlinear index Δn via the single-shot off-axis interferometric measurement (see chapter 3) for each experimental configuration $(\mathcal{P}, \Delta)$.

4.5.2 Results

4.5.2.1 Density

The density is an important physical parameter needed to compute the static and hydrodynamic pressure. It is directly given by the intensity measurement. In figure 4.7 b) we present the experimental images of the over-density $\delta\tilde{\rho}$ at time $\tau = 31$, using image subtraction as described

in Eq.(4.42), in the 1D and 2D geometries, respectively. From this images, as well as the corresponding centered profiles given below, one can notice the key difference in the evolution of the Bump in both geometries: the appearance of a negative over-density after the Bump's expansion (corresponding to times above $\tau > 20$) in the 2D geometry. Interestingly, this effect seems absent in the 1D case, which on the contrary, shows clear steepening of the perturbation front and the development of dispersive shock waves in form of an oscillating pattern developing in beyond the shock front with effective time τ, the effect less pronounced in the 2D case. These feature have direct consequences on the evolution of the over-pressure and the differential pressure. The negative differential density has a direct consequence on the sign change in the differential pressure calculated using Eq. (4.46).

4.5.2.2 Static pressure

Over-pressure and shock front: To isolate the effect of the perturbation on the static pressure, we compute the over-pressure from images of the background with and without the bump taken at same effective times $\tau(\mathcal{P}, \Delta)$, using Eq. (4.45) and (4.43). The over-pressure as a function of time τ is shown in Fig. (4.9) b) and d) and profiles averaged along y in the 1D case and radially in the 2D case are presented in Fig. (4.9) a) and c) for various times. The trajectory of a density pulse spreading with no dispersion at the speed of sound can be expressed as follows: $r = c_s(\tau) \times (L/c)$. The coefficient can be calculated using the time dependence of the sound velocity: $c_s = c\sqrt{\tau/(k_L L)}$ obtained from Eqs. (4.30) and (4.32). It directly leads to $\tau = k_L r^2/L$ and knowing that: $L = 75$ mm and $k_L = 8 \times 10^3$ mm^{-1}, one gets: $\tau = 107 \times r^2$. The coefficient does not depend on the dimensionality of the system. In the pressure maps (Fig. (4.9) b) and d)), we have added a black dashed line following this trend: $\tau = 107 \times x^2$ (1D) and $\tau = 107 \times r^2$ (2D). As expected, this trajectory follows closely the shock front in the 1D geometry. The differential pressure is defined as the pressure difference between inside and outside of the shock as expressed in Eq. (4.46). The undisturbed pressure as function of time is evaluated along the same trend line $\tau = 107 \times (r_{ext} - r_0)^2$, translated $r_0 = 250$ μm in 1D and $r_0 = 200$ μm in 2D, which corresponds to ~ 1.5 times the perturbation beam waist (blue dashed line). In 2D, the shock front expansion is slower than the calculated trajectory, as described in [18], and the blue dashed line can therefore still used to define the undisturbed pressure.

Differential pressure: The temporal evolution of the differential static pressure (at $x = 0$) is presented in Fig. 4.10. 1D (red circles) and 2D (gray triangles) geometries are compared from $\tau = 0$ to $\tau = 45$. An important difference can be seen between the two geometries: in the 2D situation the differential pressure becomes negative at $\tau = 20$ as it goes to zero in the 1D case. The observation of the negative pressure is the typical signature of a blast wind. This measurement reveals the dramatic impact of the geometry on blast wind in a fluid of light and exemplifies the analogy with classical hydrodynamics. To quantify this analogy, we use the Friedlander waveform model which is known to describe the dynamics of physical quantities in a free-field (i.e. in a open 3-dimensional space) blast wave [43]. In this model the differential

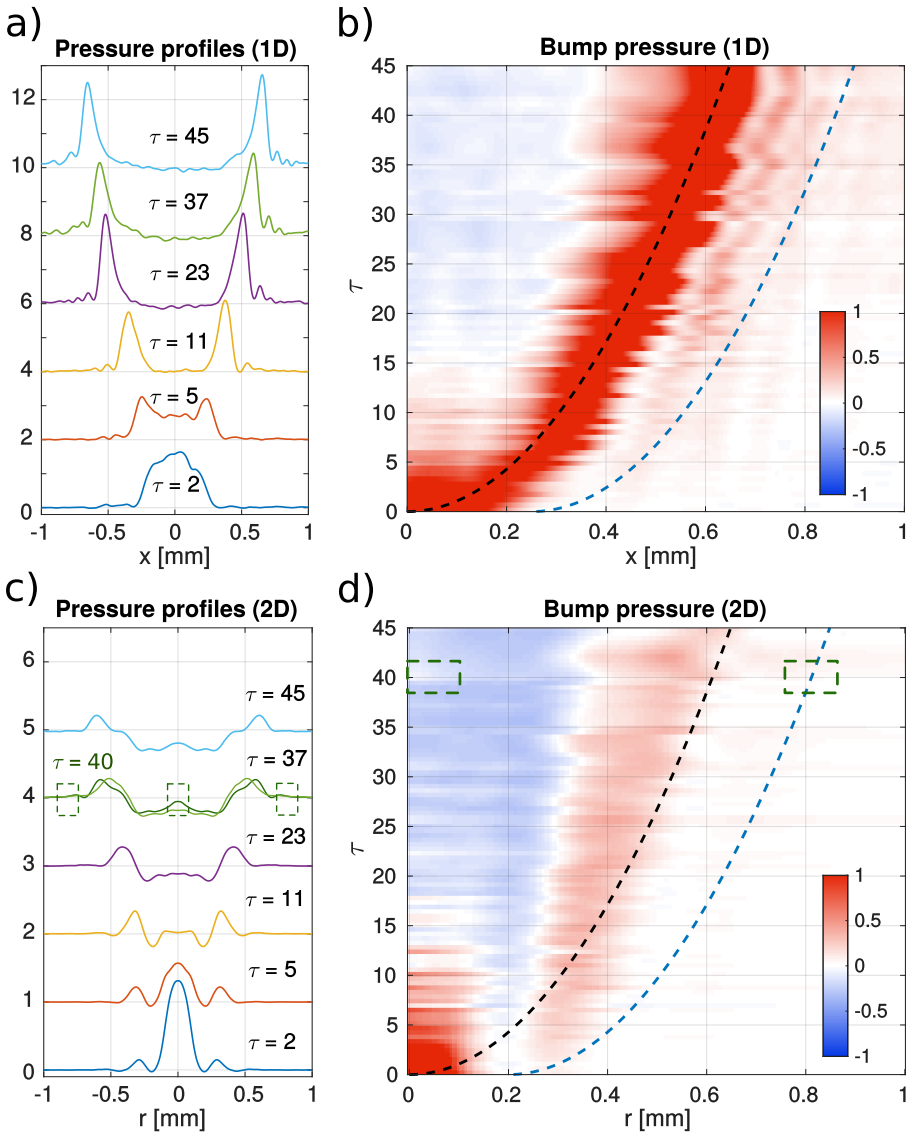

Figure 4.9: Pressure analysis: a),c): Over-pressure profiles evaluated at different effective times τ. Each following profile shifted vertically by 2 for better visibility. b),d) show the 1D and 2D spatio-temporal diagrams of the over-pressure evolution, respectively. The dotted black lines show an expansion trajectory at the speed of sound according to $\tau = k_L r^2/L$, ($k_L/L = 107$ mm^{-2}) in both geometries. The blue dotted lines show the same trajectories shifted horizontally by 250 μm in 1D (200 μm in 2D) case, used as external undisturbed area used for the measurement of the differential pressure. Dashed green rectangles around $\tau = 40$ show the presence of a second shock due to an increasing differential pressure.

pressure follows an exponential decay of the form:

$$\Delta\tilde{P} = P_s e^{-\tau/t^*}(1 - \tau/t^*), \tag{4.47}$$

where P_s and t^* are two parameters which corresponds respectively to the peak differential pressure immediately behind the shock and to the time when the differential pressure becomes

negative. The period when the hydrostatic pressure is above the ambient value is known as the positive phase, and the period when the properties are below the ambient value is the negative phase. We use $P_s = 1$ (since the differential pressure is normalized) and $t^* = 20$ (the parameters best fitting the experimental data) and plot the corresponding model with a black dashed line in Fig. 4.10. An intriguing feature can also be seen in the 2D time evolution at $\tau = 40$. Close to the minimum of the negative phase, a second peak of differential pressure is observed (the single point at $\tau = 40$ Fig. 4.10 is the average of several realizations with errors bars indicating the standard deviation of the measurement) in our optical analogue which is reminiscent of the second shock observed in classical explosion. In classical blast wave dynamics, this second shock is believed to be a consequence of the expansion and subsequent implosion of the detonation products and source materials. Our results suggest that this second shock might be of more general nature than currently thought.

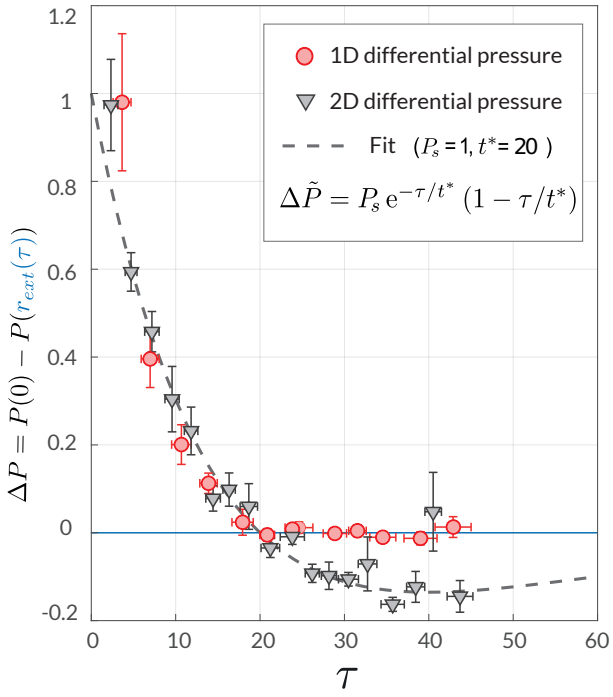

Figure 4.10: Differential pressure calculated from Eq. (4.46) for the 1D (circular dots) and the 2D cases (square dots). The uncertainty bars correspond to the statistical analysis of multiple images. The pressure is normalized as described in the main text. Blue line is the ambient pressure outside of the shock. Black dashed line is the Friedlander model for a blast wave described in Eq. (4.47) with $P_s = 1$ and $t^* = 20$ obtained from fit to experimental data.

4.5.2.3 Velocity

Additional thermodynamic quantities: For blast waves, there are no simple thermodynamic relationships between the physical properties of the fluid at a fixed point [154]. This means that the temporal evolution of the static pressure measured at a fixed point is not sufficient

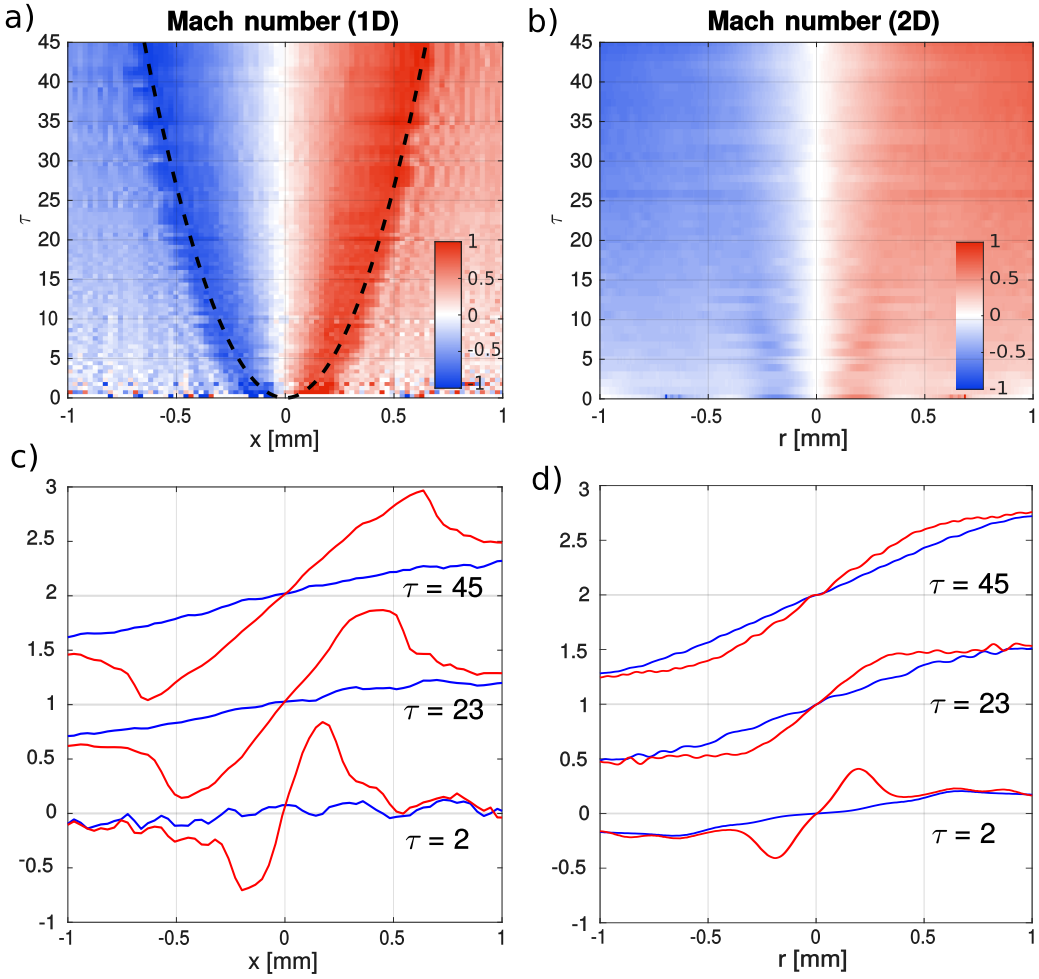

Figure 4.11: Fluid velocities from the off-axis interferometry. a),b) Space-time evolution of the Mach number with respect to the background's local speed of sound, in the 1D and 2D geometry, respectively. The dotted black line in a) shows the calculated trajectory of expansion at the speed of sound (see main text). c),d) show the background's $\tilde{v}_0$ (blue) and total $\tilde{v}$ (red) Mach number profiles, at different times, for the 1D (x coordinate) and 2D geometry (radial coordinate), respectively. Each following profile shifted vertically (spacing of 1) for visibility.

to calculate the temporal evolution of the velocity or the dynamic pressure from that single measurement. To fully describe the physical properties of a fluid in a blast wave it is necessary to independently measure at least three of the physical properties, such as, the static pressure, the density and the fluid velocity or the dynamic pressure. In the last section of this work, we report the measurement of last two physical properties, which are vector quantities.

Velocity calculation: The fluid velocity is calculated from its phase (see Eq. (4.35)) which is measured using off-axis interferometric imaging. The off-axis configuration consists in the tilted recombination of the signal beam with the reference beam on the camera plane. This results in the set of linear fringes evolving along the relative tilt direction and locally deformed (stretched or compressed) according to the beams relative curvature. Using a collimated Gaussian beam as the reference, the measured curvature is the one of the signal beam. The acquired interfero-

gramm carries the information on the beam phase via its amplitude modulated term. This term shows spatial periodicity and in the Fourier space it translates to two peaks shifted by a distance proportional to the off-axis tilt angle, symmetric with respect to the origin. By numerically calculating the spatial spectrum and filtering one of these peaks, the inverse Fourier transform gives the beam complex envelope with a spatial resolution bound by the fringe wavelength. The measured phase is unwrapped and the contribution due to the relative tilt is removed by subtracting the phase ramp. The resulting phase is averaged and numerically differentiated to get the velocity map.

Different contributions to the velocity: Using this procedure, the off-axis interferograms of the background fluid and of the background fluid with the perturbation are analyzed to give access to $v_0(r,\tau)$ and $v(r,\tau)$, respectively. The difference of these quantities gives the perturbation velocity $v_1(r,\tau)$. The non-zero velocity v_0 of the background fluid arises from its finite size causing its expansion due to a non-zero pressure gradient. The knowledge of v_0 is essential to calculate the effective interaction g and therefore the time τ and the sound velocity. Indeed, $\phi_0 = \tau\tilde{\rho}_0$ can be accessed by integrating v_0 over the transverse coordinate and using the fact that $\phi(\tilde{r} \to \infty, \tau) \to 0$. Knowing τ, the sound velocity is $c_s(\mathbf{r}_\perp, \tau) = c\sqrt{\tau\tilde{\rho}_0(\mathbf{r}_\perp, \tau)/(k_0 L)}$. The velocity maps normalized by the local sound velocity (in Mach number units) are presented in figure 4.11 a) and b) for the 1D and 2D configurations, respectively. Since velocity is a vector quantity, negative values correspond to a propagation along $-x$ direction. Figure 4.11 c) and d) show the corresponding profiles obtained for three specific times $\tau = 2;\ 23$ and 45. The maximal speed of sound at these times is 0.18, 0.62 and 0.86 percent of the speed of light in vacuum. Positive outward velocity, as well as zero velocity at the center is observed at all times both in the 1D and 2D cases. Whereas it is intuitively expected in the 1D geometry with the differential pressure never dropping to negative values, it also holds in the 2D case in which a negative phase for the differential pressure exists. A possible explanation lies in the fact that when the negative phase is reached for the differential pressure, the perturbation has already expanded enough such that the net resulting force is smaller due to a larger distance. It is also worth noting that the velocity is at least 2 times larger in the 1D geometry than in 2D, as seen by comparison of the y-axis scales in Figure 4.11 c) and d). Additionally, a steepening of the velocity profiles is observed in the 1D case reaching a Mach number of 1 at the steepest.

4.5.2.4 Dynamic pressure

Alternatively, we can measure the dynamic pressure to compute a third thermodynamic quantity: the total pressure. The dynamic pressure is also a vector quantity and can be obtained from a phase measurement similar to fluid velocity using Eq. (4.44). The dynamic pressure maps are presented in Figs. 4.12 a) and b). Once again Figs. 4.12 c) and d) show dynamic pressure profiles for three selected times. In 1D, the dynamic pressure forms a steep overpressure characteristic of the shock front which increases as function of time. In the 2D geometry, on the contrary the dynamic pressure reaches a plateau at the shock front without forming a steep overpressure peak. This behavior is in agreement with the velocity distributions presented previously.

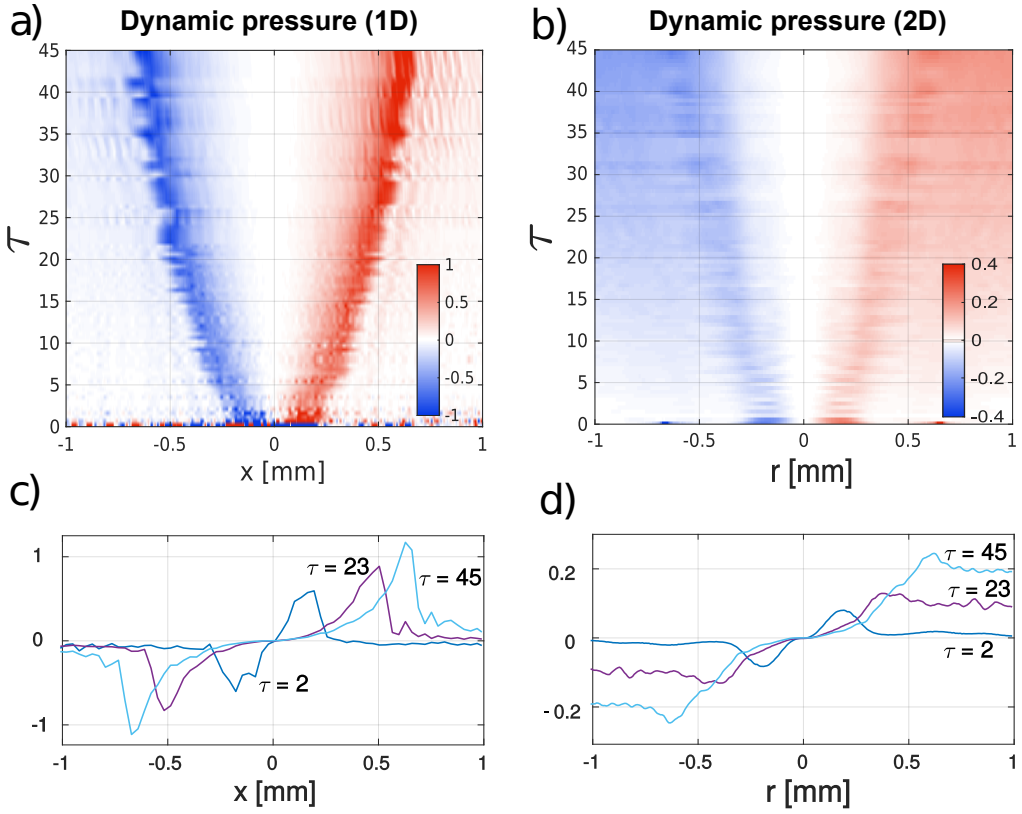

Figure 4.12: Dynamic pressure analysis. a) and b) show the spatio-temporal evolution maps of the dynamic pressure profiles, for the 1D (the x component) and 2D geometry (the radial component), respectively. Below, the c) and d) panels show various superimposed dynamic pressure profiles at different times, in 1D and 2D geometry, respectively.

4.6 Numeric experiments

4.6.1 Goal of investigation

Experimental results suggest that the shock front moves at the background imposed speed of sound. This interesting result seems in disagreement with the numerical simulations presented at the beginning of the chapter (see for instance fig. 4.4), the latter showing clear agreement between the shock front velocity and the calculated generalized speed of sound, including the perturbation contribution. This section presents the results of several numerical experiments performed in attempt to reproduce the experimental over-pressure data. Details on the implemented split-step method to perform numerical experiments, are shown in Appendix B. Starting with the theoretical description of this chapter, I then generalize it by including extra effects in order to reproduce more realistically the observed results. The influence of two effects possibly explaining the perturbation's slower speed of sound is investigated separately with help of numerical simulations: the saturation and non-locality of interactions. It is shown, that adding strong non-locality in the interactions allows to reproduce reasonably well the experimental data.

4.6.2 Saturation of the interactions

The photon-photon interactions in Rubidium vapors tend to saturate as the laser intensity increases. This phenomenon was derived in the first part of chapter 3 and results in the interaction strength given by:

$$g(\rho)\rho = \frac{g_0\rho}{1+\rho/\rho_s} \tag{4.48}$$

with ρ_s the fluid's saturation density. This implies, that in presence of saturation, the local speed of sound at the center of the perturbation contributing same density as the background fluid (total density equal to twice the background's density) is necessarily less than $\sqrt{2}\times$ the background's speed of sound, theoretically expected for Kerr-type interactions. This effect can indeed explain slower experimentally observed shock front expansion than predicted by Kerr-type interactions. Numerical simulations, including the saturation effect, were performed for different values of the saturation parameter ρ_0/ρ_s, while keeping fixed τ. However, adding saturation did not result in satisfying agreement between the numerical simulations and the experimental data. Moreover, the experimental measurements of the non-linear refractive index for this experiment, reported in fig. 4.8 don't show any significant saturation of of interaction strength with laser intensity. I therefore conclude that the interaction saturation effect is not sufficient to explain the deviations between the experiment and the model.

4.6.3 Influence of the non-locality

Why non-locality? Non-locality of interactions is another effect possibly important in our experimental platform and neglected in the theoretical description of this chapter. While it can stem from various physical origins like thermal motion of or/and interaction (collisional or dipole-dipole type interactions) among particles (atoms) involved in mediation of photon-photon interactions, the effect of non-locality on the photon-photon interactions amounts to spatially smooth them. Indeed, in presence of the non-locality, the interaction term of the propagation equation reads [153, 55]:

$$\langle g\rho\rangle(\mathbf{r}) = g\int G(\mathbf{r}-\mathbf{r}')\rho(\mathbf{r}')\mathrm{d}^2\mathbf{r}' \tag{4.49}$$

where G is a function characterized by its width l and whose shape depends on the mechanism responsible for the non-locality [142]. This implies for a perturbation region a speed of sound which is no more local in density but rather a spatial average over a region extending beyond the perturbation's boundary. As the consequence, the perturbation's motion takes place at a reduced effective speed of sound and the shock front appears more blurred compared to the local interaction case [14].

Fig. 4.13: To illustrate this effect, the Fig. 4.13 shows the radial profiles of the fluid over-density as function of the propagation coordinate z, in presence of local a) and non-local b) photonic interactions. Diffusive non-locality ($G(\mathbf{q}) = [1+l^2q^2]^{-1}$) with $l = 180$ µm was used for the

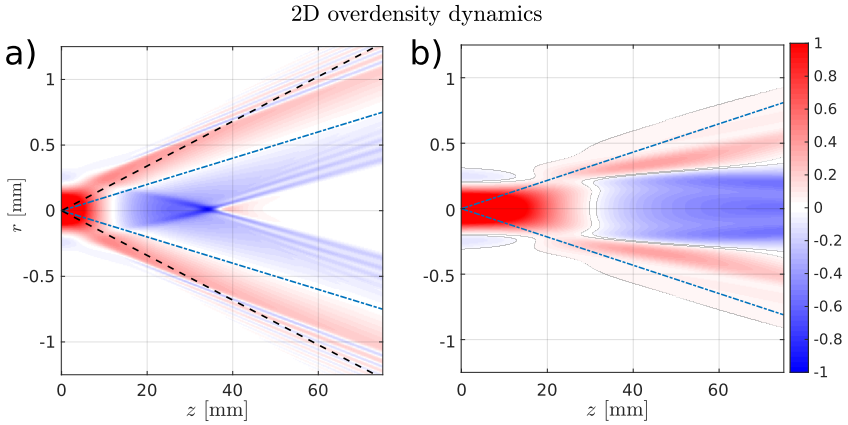

Figure 4.13: Numerically simulated radial over-density $\delta\tilde{\rho}$ as function of the propagation "time z "inside the cell". a) Over-density evolution in a medium with local photon interactions. a) Over-density evolution in a medium with non-local photon interactions. The blue dash-dotted line shows the light cone of an expansion at the background imposed speed of sound, while the black dotted line shows the sound wave-like expansion at the speed of sound including the perturbation density contribution $c_s\sqrt{1+\tilde{\rho}_1}$.

simulation. The initial state taken for the simulation was:

$$\psi(\mathbf{r}, z=0) = \mathrm{e}^{-\frac{r^2}{\omega_0^2}} + \delta\tilde{\psi}\cdot\mathrm{e}^{-\frac{r^2}{\omega_1^2}+i\frac{kr^2}{2R_0}+i\varphi} \tag{4.50}$$

where $\delta\tilde{\psi} = 0.85$ corresponds to the initial maximal over-density $\delta\tilde{\rho}(0,0) = \tilde{\rho}_1 = 1.42$, $\omega_1 = 0.09$ mm, $\omega_0 = 1.8$ mm, $R_0 = z_c + z_R^2/z_c$ (with $z_R = k\omega_1^2/2$) accounts for the focusing of a Gaussian beam with $z_c = -37.5$ mm (waist in the middle of the cell) and the phase $\varphi = \pi/4$ accounts here for the Gouy phase plus the unknown contribution by the phase lock procedure used in the experiment. The used interaction strength is $g\rho_0 = 0.8$ mm^{-1}. The transverse spatial grid has 512×512 points and corresponds to a 4×4 mm region. The axial coordinate spans from 0 to 75 mm within 500 points. The blue dash-dotted line shows the light cone of an expansion at the background imposed speed of sound, while the black dotted line shows the sound wave-like expansion at the speed of sound including the perturbation density contribution $c_s\sqrt{1+\tilde{\rho}_1}$. In the local interaction case, as expected, the shock front (the red region of the perturbation) position is better predicted by the black dotted line, while in the non-local case, the perturbation's expansion is clearly limited within the blue dash-dotted line. Comparing both space-time diagrams one notices indeed that the non-locality explains well the reduced extent of the shock front expansion. Moreover, the shape of the over-density profiles is drastically affected as well.

Fig. 4.14: In order to compare more precisely the shape of the disturbed hydrodynamic quantities between the experiment and the calculated evolution in presence of non-locality, the Fig. 4.14 shows the space-time diagrams of the hydrostatic pressure difference due to the presence of a 2D perturbation, calculated as: $\tilde{\rho}^2 - \tilde{\rho}_0^2$, both with a) and without b) non-locality. For comparison with the corresponding experimental data (shown on Fig. 4.14 c)), the effec-

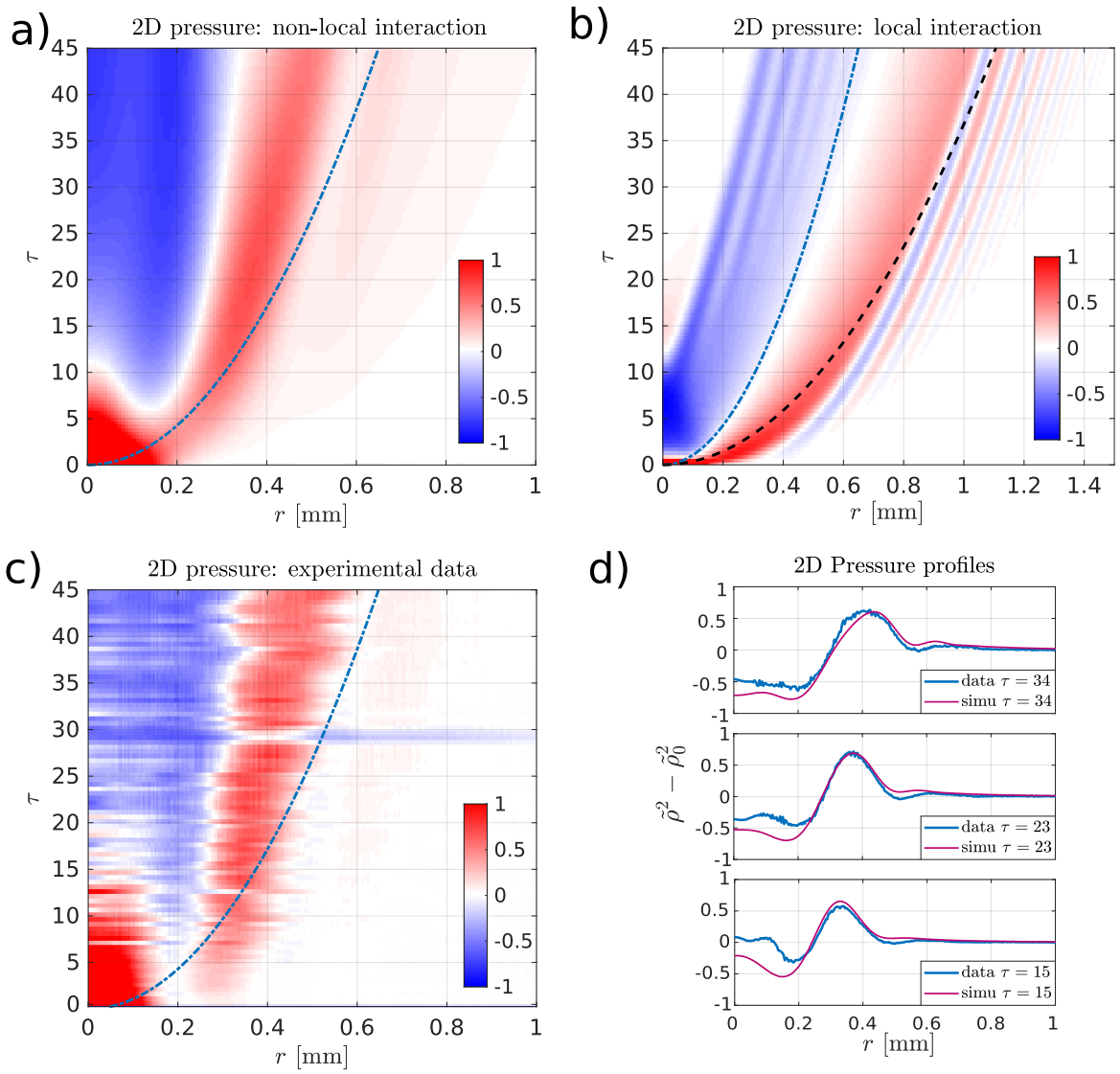

Figure 4.14: 2D perturbation's pressure: matching numerical simulation to experimental data. a) and b) show the space-"normalized time" diagrams of the hydrostatic pressure difference due to the perturbation, in presence and the absence of non-locality, respectively. The blue dash-dotted line shows the light cone of an expansion at the background imposed speed of sound, while the black dotted line shows the sound wave-like expansion at the speed of sound including the perturbation density contribution. c) Shows the experimental data for comparison with a) and b). d) Numerically calculated (with non-locality, purple curves) versus experimental (blue curves) radial over-pressure profiles at three different effective times $\tau = \{15; 23; 34\}$

tive time was varied by means of the interaction strength, as in experiment. The panel d) compares numerically calculated (with non-locality, purple curves) versus experimental (blue curves) radial over-pressure profiles at three different effective times $\tau = \{15; 23; 34\}$.

Agreement: One can conclude that the numerical simulation with the non-locality reproduces rather well the experimental pressure profiles at all three times. This would definitely be im-

possible with any simulation using local and even weakly saturable interactions, if one used the same values for the interaction strengths as those measured experimentally. The smoothened shape of the shock front with almost absent oscillations beyond the shock, observed in the calculation involving the non-locality, also seem in better agreement with the experiment. Note that the shown results correspond to the same used perturbation's initial parameters as in fig. 4.13 and correspond to the best obtained matching between the numerical simulations and the experiment. As the result, the non-locality could be the missing ingredient for quantitative agreement between the experiment and the theoretical model. However, the used value for the non-local range l is significantly larger than any reported value in our experimental platform [9, 142] and we currently have no established model to explain it. Yet, knowing that the range of non-locality has not been measured experimentally in hot Rb vapors, this leaves some room for the uncertainty of its value, which could be lifted in future works.

4.7 Conclusion

Relying on detailed measurements of all thermodynamic quantities in a fluid of light blast wave, we have demonstrated for the first time the occurrence of a blast wave in a fluid of light. We compare 1D and 2D geometry and report the observation of a negative phase during the blast only for the 2-dimensional case. The differential pressure in the 2D geometry is compared to the classical hydrodynamics of Friedlander blast-wave and we see a very good agreement with this model. Velocity maps and dynamic pressure are finally presented to complete the study. Our work opens the way to precise engineering of a fluid of light density and velocity distribution which will prove to be a valuable tool to design new experiments studying superfluid turbulence [127] or analogue gravity where an excitation of a fluid of light changes from a subsonic to a supersonic region.

Chapter 5

Post-quench evolution of the spatial noise spectrum in a quantum fluid of light

5.1 Outline of the chapter

Global scope: In this chapter I show, that the fluid of light, introduced in the previous chapters, also possesses the quantum features, stemming from its photonic nature. They are primarily linked to the *shot-noise* of a coherent state, describing the laser radiation, and this noise results in spatial and temporal density and phase fluctuations of the quantum fluid of light. These fluctuations become correlated in the presence of the photonic interactions, therefore the measurement of the correlations allows to reveal the fluid's non-equilibrium evolution following its sudden perturbation. Such evolution occurs, for example, after a sudden change, called further "a quench", of the fluid's interaction strength g. Experimentally, a fluid of light, crossing the vapor cell's entrance and exit planes, experiences two interaction quenches, where recalling the mapping between the axial coordinate and time, the photonic interactions are suddenly turned on and then off, respectively. The fluid's response to these quenches can be probed with the *Static Structure Factor*, this chapter's main observable, expressing the power spectrum of the spatial density fluctuations.

Results and discussion: This chapter presents the measurement of the static structure factor in a fluid of light at different "times" after the two interaction quenches, occurring at the vapor cell interfaces. The static structure factor shows distinct oscillations in the momentum and spatial domains at fixed times. Importantly, the correlations of the density fluctuations at given modes are also shown to oscillate in "time". The interpretation of these oscillations involves the dynamics of the Bogoliubov quasi-particles. It turns out, that they can also be viewed as an analogue of the Sakharov oscillations [75], a cosmological model explaining the emergence of the density fluctuations (anisotropy) during the initial stage of an expanding Universe, resulting nowadays in the so-called *acoustic peaks* of the Cosmic Microwave Background.

5.2 Quantum description of a fluid of light

Small introduction: Throughout this chapter we deal with (very) small fluctuations stemming from the quantum nature of light and measure and calculate their spatial power spectrum at fluid's different times. It is therefore useful to first describe the propagation/evolution of a quantum fluid's field in presence of photon-photon interactions, then extend the discussion to the response to interaction quenches and finally use the obtained results in order to calculate the evolution of its static structure factor.

5.2.1 Shot noise and quantized field

Definition of the quantized field: Up to now, the electric field envelope was described within the mean-field approach by a complex function. This approach is perfectly valid for the fields containing huge number of photons and where the spatial/temporal fluctuations of light's intensity and phase either stem from the light source itself or are artificially produced by shaping the beam. In particular, in this regime all the effects stemming from the corpuscular nature of light are negligible. One of such effects is the noise which is necessarily present even in the coherent states of light, produced by laser sources, and is called shot noise. This noise is typically weak for intense coherent states, because it scales as the square root of the photonic density $\sim \sqrt{\rho}$. However, the accurate modelling of the experiments, where shot noise is measured, requires the quantum description of light. This is usually done by assuming a quantum field with "classical" average value and quantized fluctuations [56, 96]:

$$\hat{\mathcal{E}}(\mathbf{r},z) = \sqrt{\rho_0} + \delta\hat{\mathcal{E}}(\mathbf{r},z) \tag{5.1}$$

$$\delta\hat{\mathcal{E}}(\mathbf{r},z) \propto \int \frac{\mathrm{d}^2\mathbf{q}}{(2\pi)^2}\hat{a}_{\mathbf{q}}(z)\mathrm{e}^{i\mathbf{q}.\mathbf{r}} \quad \text{and:} \quad \delta\hat{\mathcal{E}}^\dagger(\mathbf{r},z) \propto \int \frac{\mathrm{d}^2\mathbf{q}}{(2\pi)^2}\hat{a}^\dagger_{-\mathbf{q}}(z)\mathrm{e}^{i\mathbf{q}.\mathbf{r}} \tag{5.2}$$

where $\hat{a}_{\mathbf{q}}$ and $\hat{a}^\dagger_{\mathbf{q}}$ are the photon annihilation/creation operators in a spatial mode $\mathbf{q}$, obeying the commutation relation: $[\hat{a}_{\mathbf{q}}, \hat{a}^\dagger_{\mathbf{q}'}] = \delta(\mathbf{q}-\mathbf{q}')$. The quantized fluctuations then account for the shot noise. In the following parts of this chapter we define the time as: $\tau = z/c$.

5.2.2 Photonic interactions - interaction Hamiltonian

Photonic Hamiltonian and its physical origins: Recalling that the z direction plays the role of time, we deal with time dependent operators whose evolution is governed by the system's Hamiltonian. In presence of the photonic Kerr interactions, the Hamiltonian of a fluid of light composed of $N = \rho V$ photons reads [32]:

$$\hat{H} = \frac{1}{V}\sum_{\mathbf{q}} \frac{\hbar^2\mathbf{q}^2}{2m}\hat{a}^\dagger_{\mathbf{q}}\hat{a}_{\mathbf{q}} + \frac{1}{2V}\sum_{\mathbf{k},\mathbf{k}',\mathbf{q}'} U(\mathbf{q}')\hat{a}^\dagger_{\mathbf{k}-\mathbf{q}'}\hat{a}^\dagger_{\mathbf{k}'+\mathbf{q}'}\hat{a}_{\mathbf{k}}\hat{a}_{\mathbf{k}'} \tag{5.3}$$

where $m = \hbar k_L/c$ and V is the mode volume. In this expression the first term accounts for the kinetic energy and stems from the paraxial approximation, being the first order term of the

free photonic energy at mode $\mathbf{q}$: $E(\mathbf{q}) = \hbar c\sqrt{k_L^2 + \mathbf{q}^2} \simeq \hbar c k_L[1 + \mathbf{q}^2/(2k_L^2)]$ (with k_L being the axial component of the laser wavevector). The second term of eqn. 5.3 accounts for the Kerr interactions. If the interactions are local (no non-locality), one gets: $U(\mathbf{q}') = g$, a contact-type interaction constant. It expresses the energy of a field $\mathcal{E}_x$ coupled to the dielectric polarization it induces: $E_d = -P_x^*.\mathcal{E}_x/2$, with: $P_x \propto -\tilde{n}_2|\mathcal{E}_x|^2\mathcal{E}_x$, and can be obtained by inserting the definition of the quantized field (eqn. 5.1) into the expression of E_d in Fourier space. This term can be interpreted as the interaction Hamiltonian, coupling pairs of photons with initial spatial modes $\mathbf{k}$ and $\mathbf{k}'$ and final modes $\mathbf{k} - \mathbf{q}'$ and $\mathbf{k}' + \mathbf{q}'$. During the "collision" process the photons scatter and exchange the momentum $\mathbf{q}'$, respecting the momentum conservation ($\mathbf{k} - \mathbf{q}' + \mathbf{k}' + \mathbf{q}' = \mathbf{k} + \mathbf{k}'$), also known in non-linear optics as the phase-matching condition [32]. Note that all operators correspond to the same ω_L frequency ($-\omega_L$ for the hermitian conjugates) which guarantees the energy conservation during the interaction and corresponds well to the Kerr effect (degenerate four-wave-mixing process).

5.2.3 Bogoliubov approximation and pair production/annihilation

"Quadratized" Hamiltonian: If the interactions are sufficiently weak and the $\mathbf{q} \neq 0$ modes are initially only populated due to the field's quantum fluctuations, one can then rightfully assume that large fraction of the photons populates the $\mathbf{q} = 0$ mode, meaning: $\hat{a}_0^\dagger\hat{a}_0 = N_0 \simeq N$. This also allows to replace the creation and annihilation operators by numbers: $\hat{a}_0 = \hat{a}_0^\dagger \simeq \sqrt{N_0}$ (neglecting hence the quantum correlations stemming from the non-commutation of $\hat{a}_0^\dagger$ and $\hat{a}_0$). This approximation is known as the Bogoliubov approximation and it helps simplifying the interaction term of the Hamiltonian (eqn. 5.3). Indeed, the latter necessarily includes its most dominant terms $\propto N_0^2 = \hat{a}_0^\dagger\hat{a}_0^\dagger\hat{a}_0\hat{a}_0$ (no operators at $\mathbf{q} \neq 0$) and several terms $\propto N_0 = \hat{a}_0^\dagger\hat{a}_0$ (containing two operators at $\mathbf{q} \neq 0$), then less dominant terms containing $\sqrt{N_0}$ with three operators at non-zero momentum and finally the terms with all four operators occupying non-zero momenta. The Hamiltonian 5.3 can be significantly simplified by keeping only the terms with up to quadratic dependence in non-zero momentum operators, resulting in a so-called "quadratized" Hamiltonian:

$$\hat{H}_{eff} \simeq \frac{1}{V}\sum_{\mathbf{q}} \frac{\hbar^2\mathbf{q}^2}{2m}\hat{a}_{\mathbf{q}}^\dagger\hat{a}_{\mathbf{q}} + \frac{g}{2V}\hat{a}_0^\dagger\hat{a}_0^\dagger\hat{a}_0\hat{a}_0 + \frac{g\rho_0}{2}\sum_{\mathbf{q}\neq 0}\left(3\hat{a}_{\mathbf{q}}^\dagger\hat{a}_{\mathbf{q}} + \hat{a}_{-\mathbf{q}}^\dagger\hat{a}_{-\mathbf{q}} + \hat{a}_{\mathbf{q}}^\dagger\hat{a}_{-\mathbf{q}}^\dagger + \hat{a}_{\mathbf{q}}\hat{a}_{-\mathbf{q}}\right) \quad (5.4)$$

The terms inside the bracket are obtained by setting in the eqn. 5.3 $\{\mathbf{k} = \mathbf{q}', \mathbf{k}' = 0\}$, $\{\mathbf{q}' = \mathbf{k}' = 0\}$ and $\{\mathbf{q}' = \mathbf{k} = 0\}$ to obtain $\hat{a}_{\mathbf{q}}^\dagger\hat{a}_{\mathbf{q}}$, then $\{\mathbf{k}' = -\mathbf{q}', \mathbf{k} = 0\}$ to obtain $\hat{a}_{-\mathbf{q}}^\dagger\hat{a}_{-\mathbf{q}}$ and finally $\{\mathbf{k} = \mathbf{k}' = 0\}$ and $\{\mathbf{k}' = -\mathbf{k} = -\mathbf{q}'\}$, to obtain $\hat{a}_{\mathbf{q}}^\dagger\hat{a}_{-\mathbf{q}}^\dagger$ and $\hat{a}_{\mathbf{q}}\hat{a}_{-\mathbf{q}}$ respectively.

Note that the term $\frac{g}{2}\hat{a}_0^\dagger\hat{a}_0^\dagger\hat{a}_0\hat{a}_0$ cannot be directly replaced by N_0^2 but should be worked out as

follows [35]:

$$\begin{aligned}\hat{a}_0^\dagger\hat{a}_0^\dagger\hat{a}_0\hat{a}_0 = \hat{a}_0^\dagger(\hat{a}_0\hat{a}_0^\dagger - 1)\hat{a}_0 = N_0^2 - N_0 = \left(N - \sum_{\mathbf{q}\neq 0}\hat{a}_{\mathbf{q}}^\dagger\hat{a}_{\mathbf{q}}\right)^2 - \left(N - \sum_{\mathbf{q}\neq 0}\hat{a}_{\mathbf{q}}^\dagger\hat{a}_{\mathbf{q}}\right) \\ \simeq N(N-1) - (2N-1)\sum_{\mathbf{q}\neq 0}\hat{a}_{\mathbf{q}}^\dagger\hat{a}_{\mathbf{q}} \simeq (N)^2 - 2N\sum_{\mathbf{q}\neq 0}\hat{a}_{\mathbf{q}}^\dagger\hat{a}_{\mathbf{q}}\end{aligned} \tag{5.5}$$

Then by using this result and approximating the total density to the condensed one $N/V = \rho \simeq \rho_0$ in the eqn. 5.4, one gets:

$$\hat{H}_{eff} \simeq \frac{g\rho N}{2} + \frac{1}{V}\sum_{\mathbf{q}}\frac{\hbar^2\mathbf{q}^2}{2m}\hat{a}_{\mathbf{q}}^\dagger\hat{a}_{\mathbf{q}} + \frac{g\rho_0}{2}\sum_{\mathbf{q}\neq 0}\left(\hat{a}_{\mathbf{q}}^\dagger\hat{a}_{\mathbf{q}} + \hat{a}_{-\mathbf{q}}^\dagger\hat{a}_{-\mathbf{q}} + \hat{a}_{\mathbf{q}}^\dagger\hat{a}_{-\mathbf{q}}^\dagger + \hat{a}_{\mathbf{q}}\hat{a}_{-\mathbf{q}}\right) \tag{5.6}$$

The eqn. 5.6 is obtained with the Bogoliubov approximation, assuming that most particles of the system occupy the $\mathbf{q} = 0$ mode. The eqn. 5.6 tells us then, that the dominant effect stemming from the photonic Kerr interactions consists in creating (annihilating) the pairs of photons with opposite momenta from (into) the "condensate" $\mathbf{q} = 0$ mode, as well as the "number conserving" scattering of the non-zero momentum photons through the photons in the condensed mode. This means, that the onset of interactions creates correlations between the non-zero opposite momentum modes.

Bogoliubov quasiparticles: The effective Hamiltonian (eqn. 5.6) allows to write the Heisenberg (evolution) equation for the operators $\{\hat{a}_{\mathbf{q}}, \hat{a}_{-\mathbf{q}}^\dagger\}$ [35]:

$$i\hbar\frac{\partial\hat{a}_{\mathbf{q}}}{\partial\tau} = [\hat{a}_{\mathbf{q}}, \hat{H}_{eff}] = E_{tot}\hat{a}_{\mathbf{q}} + g\rho_0\hat{a}_{-\mathbf{q}}^\dagger \tag{5.7}$$

$$i\hbar\frac{\partial\hat{a}_{-\mathbf{q}}^\dagger}{\partial\tau} = [a_{-\mathbf{q}}^\dagger, \hat{H}_{eff}] = -E_{tot}\hat{a}_{-\mathbf{q}}^\dagger - g\rho_0\hat{a}_{\mathbf{q}} \tag{5.8}$$

where $\tau = z/c$ and $E_{tot} = \hbar^2q^2/(2m) + g\rho_0$. This is a set of coupled differential equations which can be solved by defining the following set of operators $\{\hat{b}_{\mathbf{q}}, \hat{b}_{-\mathbf{q}}^\dagger\}$:

$$\hat{b}_{\mathbf{q}} = u_{\mathbf{q}}\hat{a}_{\mathbf{q}} + v_{\mathbf{q}}\hat{a}_{-\mathbf{q}}^\dagger \tag{5.9}$$

$$\hat{b}_{-\mathbf{q}}^\dagger = v_{\mathbf{q}}\hat{a}_{\mathbf{q}} + u_{\mathbf{q}}\hat{a}_{-\mathbf{q}}^\dagger \tag{5.10}$$

which are supposed to evolve in presence of the interactions simply as: $\hat{b}_{\mathbf{q}}(\tau) = \hat{b}_{\mathbf{q}}(0)\mathrm{e}^{-i\Omega\tau}$. Then solving the eqns.: 5.7 and 5.8 amounts to diagonalizing the following matrix:

$$\begin{pmatrix} E_{tot} & -g\rho \\ g\rho & -E_{tot}\end{pmatrix}\begin{pmatrix} u_{\mathbf{q}} \\ v_{\mathbf{q}}\end{pmatrix} = \hbar\Omega\begin{pmatrix} u_{\mathbf{q}} \\ v_{\mathbf{q}}\end{pmatrix} \tag{5.11}$$

This implies for the eigenfrequency Ω the following condition, known as the Bogoliubov disper-

sion relation:

$$\Omega(\mathbf{q},\tau) = \pm\sqrt{c_s^2(\tau)\mathbf{q}^2 + \left(\frac{\hbar\mathbf{q}^2}{2m}\right)^2} \tag{5.12}$$

with $c_s(\tau) = \sqrt{g(\tau)\rho_0(\tau)/m}$ the local speed of sound of the quasi-particles in the low $\mathbf{q}$ regime. This means, that as soon as the photonic interactions are switched on, the photonic fluctuations evolution can be viewed in terms of the freely evolving quasi-particles obtained with the Bogoliubov transformation. One can find the coefficients $u_\mathbf{q}$ and $v_\mathbf{q}$ by summing/subtracting the rows of the eqn. 5.11 and using the fact that $u_\mathbf{q}^2 - v_\mathbf{q}^2 = 1$ (stemming from the condition $[\hat{a}_\mathbf{q}, \hat{a}_\mathbf{q}^\dagger] = 1$):

$$u_\mathbf{q} = \frac{1}{2}\left[\left(\frac{\hbar\Omega}{E_{kin}}\right)^{1/2} + \left(\frac{E_{kin}}{\hbar\Omega}\right)^{1/2}\right], \qquad v_\mathbf{q} = \frac{1}{2}\left[\left(\frac{\hbar\Omega}{E_{kin}}\right)^{1/2} - \left(\frac{E_{kin}}{\hbar\Omega}\right)^{1/2}\right] \tag{5.13}$$

where $E_{kin} = (\hbar\mathbf{q})^2/(2m)$. Indeed, one has: $u_\mathbf{q} = u_{-\mathbf{q}}$ ($v_\mathbf{q} = v_{-\mathbf{q}}$). In the limit of small $q\xi \ll 1$ both u and v diverge as $\sim (q\xi)^{-1/2}/2$, while for large $q\xi \gg 1$, u tends to 1, wlile v tends to zero as $\sim (q\xi)^{-2}/4$, with $\xi = \hbar/(mc_s)$ the fluid's healing length. Note, that recalling the definition of the quantum fluctuations of the field (eqn. 5.2), they can be rewritten as:

$$\delta\hat{\mathcal{E}}(\mathbf{r},z) \propto \mathrm{e}^{-ig\rho z/c}\int\frac{\mathrm{d}^2\mathbf{q}}{(2\pi)^2}\left(u_\mathbf{q}\hat{b}_\mathbf{q}(z) - v_\mathbf{q}\hat{b}_{-\mathbf{q}}^\dagger(z)\right)\mathrm{e}^{i\mathbf{qr}} \tag{5.14}$$

One can show, that eqn. 5.14 is still a solution of the linearized propagation equation for the fluctuations:

$$i\frac{\partial\delta\hat{\mathcal{E}}}{\partial z} = \left(-\frac{1}{2k_L}\nabla_\perp^2 + 2g|\mathcal{E}_0|^2\right)\delta\hat{\mathcal{E}} + g\mathcal{E}_0^2\delta\hat{\mathcal{E}}^\dagger \tag{5.15}$$

These results indicate, that the presence of the photonic interactions $g \neq 0$ results, among others, in the production of the opposite momentum photon pairs, composing the field fluctuations. These can be interpreted as quasi-particles, with the characteristic Bogoliubov dispersion 5.12. The operator $\hat{b}_\mathbf{q}^\dagger$ corresponds to the creation of a quasiparticle in mode $\mathbf{q}$, oscillating at frequency $\Omega(\mathbf{q},\tau)$. The transformation between the quasi-particle and photonic pictures is performed with the eqns. 5.9 and 5.10, involving the Bogoliubov coefficients $u_\mathbf{q}, v_\mathbf{q}$, which in turn depend on the interaction strength via eqns. 5.13.

Interaction quenches: How do the spatial laser shot noise fluctuations behave after sudden changes (called quenches) of the interaction constant (discontinuous changes in $g(\tau)$)? As will be shown below, the interaction quenches induce spontaneous or stimulated production of the Bogoliubov quasi-particles. These quasi-particles possess correlations between the opposite momentum modes due to their synchronized production. It turns out that these variations directly appear in an experimentally measurable observable, called the static structure factor, which basically measures the power spectrum of spatial density fluctuations.

5.3 Static structure factor

Here I present the calculation of the static structure factor, necessary for understanding the experimental results shown later. Several effects are included phenomenologically into the model, such as the absorption and spontaneous reemission of photons as well as the finite imaging resolution, with special focus on their influence on the shape of the structure factor.

5.3.1 Before the first quench

Definition and the approximate expression within the Bogoliubov approach: We study the response of a quantum fluid of light to the interaction quenches using the static structure factor, which is the power spectrum of the fluid's density fluctuations. For a system of $N = \rho V$ particles (photons in our case) it is given by [35, 75]:

$$S(\mathbf{q}, \tau) = \frac{\langle \delta\hat{\rho}^\dagger(\mathbf{q}, \tau)\delta\hat{\rho}(\mathbf{q}, \tau)\rangle}{N} \tag{5.16}$$

where $\mathbf{q}$ is the Fourier mode $\mathbf{q}$, $\delta\rho(\mathbf{q}, \tau)$ is the spatial Fourier transform of the density fluctuation at time $\tau = z/c$, and N is the total number of particles in the fluid. Since in this chapter we consider the fluctuations stemming from the shot noise of light, it makes sense to express the structure factor with the photon creation/annihilation operators $\hat{a}^\dagger_{\mathbf{k}}/\hat{a}_{\mathbf{k}}$, describing a quantized light in a spatial mode $\mathbf{k}$. For this we express the density fluctuation $\delta\hat{\rho}(\mathbf{q})$ operator as function of the quantum field operator [35]:

$$\delta\hat{\rho}(\mathbf{q}, \tau) = \int \frac{\mathrm{d}^2\mathbf{r}}{(2\pi)^2} \left[\hat{\mathcal{E}}^\dagger(\mathbf{r}, \tau)\hat{\mathcal{E}}(\mathbf{r}, \tau) - \rho_0(\mathbf{r})\right] \mathrm{e}^{-i\mathbf{q}\mathbf{r}} \tag{5.17}$$

then using the definition and properties ($\langle\hat{\delta}\mathcal{E}\rangle = 0$) of the definition of the field fluctuations (eqn. 5.2) one gets:

$$\delta\hat{\rho}(\mathbf{q}) = \sum_{\mathbf{k}'} \hat{a}^\dagger_{\mathbf{k}'+\mathbf{q}}\hat{a}_{\mathbf{k}'} \simeq \sqrt{N_0}\left(\hat{a}^\dagger_{\mathbf{q}} + \hat{a}_{-\mathbf{q}}\right) \tag{5.18}$$

$$\delta\hat{\rho}^\dagger(\mathbf{q}) = \sum_{\mathbf{k}'} \hat{a}^\dagger_{\mathbf{k}'}\hat{a}_{\mathbf{k}'+\mathbf{q}} = \sum_{\mathbf{k}} \hat{a}^\dagger_{\mathbf{k}-\mathbf{q}}\hat{a}_{\mathbf{k}} \simeq \sqrt{N_0}\left(\hat{a}^\dagger_{-\mathbf{q}} + \hat{a}_{\mathbf{q}}\right) \tag{5.19}$$

While these results can be rigorously derived [75, 35], it has an intuitive interpretation: the density fluctuation operator at mode $\mathbf{q}$ measures the probability of killing a photon at all possible modes $\mathbf{k}$, which is performed by $\hat{a}_{\mathbf{k}}$, and creating a new one in the Fourier mode shifted by $\mathbf{q}$, $\hat{a}^\dagger_{\mathbf{k}+\mathbf{q}}$. The continuous sum over modes was replaced by a discrete one just for the simplicity of notation. The last shown expressions are obtained within the Bogoliubov approximation, allowing to replace $\hat{a}_0 = \hat{a}^\dagger_0 \simeq \sqrt{N}$. Using this result, the static structure factor

becomes:

$$S(\mathbf{q}) = \frac{1}{N}\sum_{\mathbf{k},\mathbf{k}'}\left\langle \hat{a}^\dagger_{\mathbf{k}-\mathbf{q}}\hat{a}_{\mathbf{k}}\hat{a}^\dagger_{\mathbf{k}'+\mathbf{q}}\hat{a}_{\mathbf{k}'}\right\rangle \simeq \left\langle \hat{a}^\dagger_{\mathbf{q}}\hat{a}^\dagger_{-\mathbf{q}}\right\rangle + \langle \hat{a}_{\mathbf{q}}\hat{a}_{-\mathbf{q}}\rangle + \left\langle \hat{a}_{\mathbf{q}}\hat{a}^\dagger_{\mathbf{q}}\right\rangle + \left\langle \hat{a}^\dagger_{-\mathbf{q}}\hat{a}_{-\mathbf{q}}\right\rangle \tag{5.20}$$

where the different terms have been obtained by setting: $\{\mathbf{k} = \mathbf{k}' = 0\}$, $\{\mathbf{k} = \mathbf{q}, \mathbf{k}' = -\mathbf{q}\}$, $\{\mathbf{k} = \mathbf{q}, \mathbf{k}' = 0\}$ and $\{\mathbf{k} = 0, \mathbf{k}' = -\mathbf{q}\}$, respectively, or by simply using the approximated expressions in the eqns. 5.18 and 5.19. We can regroup the terms corresponding to the average photonic populations: $N_a(\mathbf{q}) = \langle \hat{a}^\dagger_{\mathbf{q}}\hat{a}_{\mathbf{q}}\rangle = \langle \hat{a}^\dagger_{-\mathbf{q}}\hat{a}_{-\mathbf{q}}\rangle = \langle \hat{a}_{\mathbf{q}}\hat{a}^\dagger_{\mathbf{q}}\rangle - 1$, and the photonic correlations: $C_a(\mathbf{q}) = \langle \hat{a}_{\mathbf{q}}\hat{a}_{-\mathbf{q}}\rangle$ (and $C^*_a(\mathbf{q}) = \langle \hat{a}^\dagger_{\mathbf{q}}\hat{a}^\dagger_{-\mathbf{q}}\rangle$). Then the expression of the static structure factor becomes:

$$S(\mathbf{q}, \tau) = 1 + 2N_a(\mathbf{q}) + 2\mathrm{Re}\{C_a(\mathbf{q})\} \tag{5.21}$$

With this definition a non-interacting gas has $S(\mathbf{q}) = 1$ (the only remaining term of $\langle \hat{a}_{\mathbf{q}}\hat{a}^\dagger_{\mathbf{q}}\rangle$) reflecting the presence of spatial shot noise (quantum fluctuations) and the absence of other sources for either average photonic populations at any non-zero mode $\mathbf{q}$ or correlations between the opposite $\mathbf{q}$ modes.

5.3.2 The first quench

First quench: cell's input plane, substitution with the quasi-particle operators: As light crosses the cell's input plane, the photonic interactions are suddenly switched on, giving rise to the first interaction quench. Let's note the time point associated to this quench $\tau_0 = -L/c$. The presence of photonic interactions induces production of photons at non-zero $\mathbf{q}$ modes and the correlation among the opposite $\mathbf{q}$ modes, it is therefore preferable to switch from the photonic operators to new operators whose evolution is not coupled to that of other modes. This is why the operators before and after the quench are related by the same Bogoliubov transformation, which links the interacting photonic operators to the non-interacting quasi-particles operators (eqns. 5.10 and 5.9) where the Bogoliubov coefficients are given by eqns. 5.13. Since in presence of interactions, the quasi-particle evolution is a simple oscillation: $\hat{b}_{\mathbf{q}}(\tau) = \hat{b}_{\mathbf{q}}(\tau_0)\mathrm{e}^{-i\Omega(\tau-\tau_0)}$, it is sensible to express the structure factor inside the medium with quasi-particle operators by using the substitution derived from the eqns. 5.9 and 5.10:

$$\hat{a}_{\mathbf{q}} = u_{\mathbf{q}}(\tau_0)\hat{b}_{\mathbf{q}} - v_{\mathbf{q}}(\tau_0)\hat{b}^\dagger_{-\mathbf{q}} \tag{5.22}$$

$$\hat{a}^\dagger_{-\mathbf{q}} = -v_{\mathbf{q}}(\tau_0)\hat{b}_{\mathbf{q}} + u_{\mathbf{q}}(\tau_0)\hat{b}^\dagger_{-\mathbf{q}} \tag{5.23}$$

and inserting it into the definition of the density perturbation operators, eqns. 5.18 and 5.19:

$$\delta\hat{\rho}(\mathbf{q}, \tau) \simeq \sqrt{N_0}\left[u_{\mathbf{q}}(\tau) - v_{\mathbf{q}}(\tau)\right]\left(\hat{b}^\dagger_{\mathbf{q}} + \hat{b}_{-\mathbf{q}}\right) \tag{5.24}$$

$$\delta\hat{\rho}^\dagger(\mathbf{q}, \tau) \simeq \sqrt{N_0}\left[u_{\mathbf{q}}(\tau) - v_{\mathbf{q}}(\tau)\right]\left(\hat{b}^\dagger_{-\mathbf{q}} + \hat{b}_{\mathbf{q}}\right) \tag{5.25}$$

Then by using the fact that: $\langle \hat{b}_{-\mathbf{q}} \hat{b}^\dagger_{-\mathbf{q}} \rangle = \langle \hat{b}^\dagger_{-\mathbf{q}} \hat{b}_{-\mathbf{q}} \rangle + 1 = \langle \hat{b}^\dagger_{\mathbf{q}} \hat{b}_{\mathbf{q}} \rangle + 1$, and after defining the quasi-particle populations $N_b = \langle \hat{b}^\dagger_{\mathbf{q}} \hat{b}_{\mathbf{q}} \rangle$ and their correlations $C_b = \langle \hat{b}_{\mathbf{q}} \hat{b}_{-\mathbf{q}} \rangle = \langle \hat{b}^\dagger_{\mathbf{q}} \hat{b}^\dagger_{-\mathbf{q}} \rangle^*$ between the opposite $\mathbf{q}$ modes, the structure factor becomes:

$$S(\mathbf{q}, \tau) = S_0(\mathbf{q}, \tau) \left[1 + 2N_b(\mathbf{q}, \tau) + 2\mathrm{Re}\{C_b(\mathbf{q}, \tau)\} \right] \tag{5.26}$$

In this expression $S_0(q) = (u_{\mathbf{q}} - v_{\mathbf{q}})^2 = E_{kin}/(\hbar\Omega(\tau))$. Note that the correlations $C_b(\mathbf{q}, \tau) = \langle \hat{b}_{\mathbf{q}}(\tau_0) \hat{b}_{-\mathbf{q}}(\tau_0) \rangle \mathrm{e}^{-2i\Omega(\mathbf{q},\tau_0)(\tau-\tau_0)}$ between the opposite $\mathbf{q}$ modes oscillate in time at the frequency corresponding to the double of their Bogoliubov frequency.

Quasi-particle statistics: spontaneous and stimulated contributions: The photon annihilation operators ($\hat{a}_{\mathbf{q}}$) describe what happens before the quench, and the one for quasi-particles ($\hat{b}_{\mathbf{q}}$) after the quench. In order to calculate the populations and the opposite mode correlations of the Bogoliubov quasi-particles, one needs to express them as function of the "initial" photonic populations $N_a = \langle \hat{a}^\dagger_{\mathbf{q}} \hat{a}_{\mathbf{q}} \rangle$ and correlations $C_a = \langle \hat{a}_{\mathbf{q}} \hat{a}_{-\mathbf{q}} \rangle$ before the quench. Using the eqn. 5.9 and 5.10, one has for $\tau_0 < \tau < 0$:

$$N_b(\mathbf{q}, \tau) = v^2_{\mathbf{q}}(\tau_0) + \left[u^2_{\mathbf{q}}(\tau_0) + v^2_{\mathbf{q}}(\tau_0) \right] N_a + 2u_{\mathbf{q}}(\tau_0) v_{\mathbf{q}}(\tau_0) \mathrm{Re}\left\{ C_a \right\} \tag{5.27}$$

$$C_b(\mathbf{q}, \tau) = \left(u_{\mathbf{q}}(\tau_0) v_{\mathbf{q}}(\tau_0) + 2u_{\mathbf{q}}(\tau_0) v_{\mathbf{q}}(\tau_0) N_a + \left[u^2_{\mathbf{q}}(\tau_0) C_a + v^2_{\mathbf{q}}(\tau_0) C^*_a \right] \right) \mathrm{e}^{-2i\Omega(\mathbf{q},\tau_0)(\tau-\tau_0)} \tag{5.28}$$

This result shows the different sources for the quasi-particle populations and correlations, highlighting the fact that they may be stimulated through the presence of the photonic populations and correlations (terms proportional to N_a and C_a) before the quench, but also arise spontaneously as soon as there are non-zero interactions (stemming from $v_{\mathbf{q}} \neq 0$). The spontaneous production of the quasi-particles stems from the quantum fluctuations of the fluid of light, or more precisely from the non-commutation of the photon annihilation and creation operators.

Quasi-particle statistics: experimental arrangement: We can now use the experimental configuration of a coherent laser beam of a Gaussian shape, sent into the non-linear medium. As mentioned above, in this case only the shot noise contributes to the structure factor and, in particular, there are no photonic correlations $C_a = \langle \hat{a}_{\mathbf{q}}(\tau < \tau_0) \hat{a}_{-\mathbf{q}}(\tau < \tau_0) \rangle = 0$, while we may allow finite amount of the photonic populations $N_a = \langle \hat{a}^\dagger_{\mathbf{q}}(\tau < \tau_0) \hat{a}_{\mathbf{q}}(\tau < \tau_0) \rangle$ due to the beam imperfections and additional sources for spatial intensity fluctuations within the beam. Then the quasi-particle populations and correlations become:

$$N_b(\mathbf{q}, \tau) = v^2_{\mathbf{q}}(\tau_0) + \left[u^2_{\mathbf{q}}(\tau_0) + v^2_{\mathbf{q}}(\tau_0) \right] N_a + N'_b(\tau) \tag{5.29}$$

$$C_b(\mathbf{q}, \tau) = u_{\mathbf{q}}(\tau_0) v_{\mathbf{q}}(\tau_0)(1 + 2N_a) \mathrm{e}^{-2i\Omega(\mathbf{q},\tau_0)(\tau-\tau_0)} \tag{5.30}$$

In the eqn. 5.29 the first term accounts for the quasi-particles spontaneously produced during the quench, the second term accounts for the those, stimulated by the initial photonic density fluctuations, and finally the last term, N'_b was added artificially to account for the possible additional "incoherent" contribution which may stem from local inhomogeneity of the atomic density or the spontaneous emission from the atoms into the considered mode during the

evolution inside the vapor cell (see section 5.3.4).

5.3.3 The second quench

From quasi-particles to photons: As the fluid of light quits the vapor cell it undergoes a second quench during which the photonic interactions are suddenly switched off. We set the time corresponding to the second quench to zero. Then for $\tau > 0$ the photonic operators are again the "eigen"-operators evolving without being coupled to other modes. In order to distinguish the operators after the second quench and those before the first quench, we call the photon annihilation operator after the 2-nd quench $\hat{c}_{\mathbf{q}}$ and define it as:

$$\hat{c}_{\mathbf{q}} = u_{\mathbf{q}}\hat{b}_{\mathbf{q}} - v_{\mathbf{q}}\hat{b}^{\dagger}_{-\mathbf{q}} \tag{5.31}$$

$$\hat{c}^{\dagger}_{-\mathbf{q}} = -v^{*}_{\mathbf{q}}\hat{b}_{\mathbf{q}} + u^{*}_{\mathbf{q}}\hat{b}^{\dagger}_{-\mathbf{q}} \tag{5.32}$$

In comparison with the previous substitution from $\hat{b}$ to $\hat{a}$, here we allow the Bogoliubov coefficients to be complex in order to account for possible (absorption) losses inside the cell, as will be described in more details later. In order to express the structure factor with these new operators we refer again to the density perturbation operators which are given by the same expressions as the eqns. 5.18 and 5.19 but with the $\hat{a}$ operators replaced by the $\hat{c}$ operators. Then the structure factor after the second quench ($\tau > 0$) reads:

$$S(\mathbf{q},\tau) = 1 + 2N_c(\mathbf{q},0) + 2\mathrm{Re}\left\{C_c(\mathbf{q},0)\mathrm{e}^{-2i\Omega(\mathbf{q},0)\tau}\right\} \tag{5.33}$$

with $N_c(\mathbf{q},0) = \langle\hat{c}^{\dagger}_{\mathbf{q}}\hat{c}_{\mathbf{q}}\rangle$ and $N_c(\mathbf{q},0) = \langle\hat{c}_{\mathbf{q}}\hat{c}_{-\mathbf{q}}\rangle$. The variable substitution allows us to calculate the photonic populations and correlations, which are the building blocks of the structure factor, as function of the analogous quantities of the quasi-particles just before the second quench:

$$N_c(\mathbf{q},0) = |v_{\mathbf{q}}(0)|^2 + \left(|v_{\mathbf{q}}(0)|^2 + |u_{\mathbf{q}}(0)|^2\right)N_b(\mathbf{q},0) - 2\mathrm{Re}\left\{u_{\mathbf{q}}(0)v^{*}_{\mathbf{q}}(0)C_b(\mathbf{q},0)\right\} \tag{5.34}$$

$$C_c(\mathbf{q},0) = u^2_{\mathbf{q}}(0)C_b(\mathbf{q},0) + v^2_{\mathbf{q}}(0)C^{*}_b(\mathbf{q},0) - u_{\mathbf{q}}(0)v_{\mathbf{q}}(0)\left(1 + 2N_b(\mathbf{q},0)\right) \tag{5.35}$$

The final result: At this stage one can gather these results and neglecting the absorption, obtain the following structure factor just after the second quench:

$$\begin{aligned} S(\mathbf{q},\tau) = 1 &+ 2\left\{|v_{\mathbf{q}}(0)|^2 + \left[|v_{\mathbf{q}}(0)|^2 + |u_{\mathbf{q}}(0)|^2\right]N_b(\mathbf{q},0) - 2\mathrm{Re}\left[u_{\mathbf{q}}(0)v^{*}_{\mathbf{q}}(0)C_b(\mathbf{q},0)\right]\right\} \\ &+ 2\mathrm{Re}\left\{\left(u^2_{\mathbf{q}}(0)C_b(\mathbf{q},0) + v^2_{\mathbf{q}}(0)C^{*}_b(\mathbf{q},0) - u_{\mathbf{q}}(0)v_{\mathbf{q}}(0)\left[1 + 2N_b(\mathbf{q},0)\right]\right)\mathrm{e}^{-2i\Omega(\mathbf{q},0)\tau}\right\} \end{aligned} \tag{5.36}$$

By injecting now the expressions of N_b and C_b given in the eqns. 5.29 and 5.30, we get:

$$\begin{aligned}
S(\mathbf{q},\tau) &= 1 + 2|v_{\mathbf{q}}(0)|^2 + 2\left(|v_{\mathbf{q}}(0)|^2 + |u_{\mathbf{q}}(0)|^2\right)\left(v_{\mathbf{q}}^2(\tau_0) + \left[u_{\mathbf{q}}^2(\tau_0) + v_{\mathbf{q}}^2(\tau_0)\right]N_a + N_b'(0)\right) \\
&- 4\mathrm{Re}\left[u_{\mathbf{q}}(0)v_{\mathbf{q}}^*(0)u_{\mathbf{q}}(\tau_0)v_{\mathbf{q}}(\tau_0)(1+2N_a)\mathrm{e}^{2i\Omega_{\mathbf{q}}(\tau_0)\tau_0}\right] \\
&+ 2\mathrm{Re}\left[u_{\mathbf{q}}^2(0)u_{\mathbf{q}}(\tau_0)v_{\mathbf{q}}(\tau_0)(1+2N_a)\mathrm{e}^{-2i(\Omega_{\mathbf{q}}(0)\tau-\Omega_{\mathbf{q}}(\tau_0)\tau_0)}\right] \\
&+ 2\mathrm{Re}\left[v_{\mathbf{q}}^2(0)u_{\mathbf{q}}(\tau_0)v_{\mathbf{q}}(\tau_0)(1+2N_a)\mathrm{e}^{-2i(\Omega_{\mathbf{q}}(0)\tau+\Omega_{\mathbf{q}}(\tau_0)\tau_0)}\right] \\
&- 2\mathrm{Re}\left[u_{\mathbf{q}}(0)v_{\mathbf{q}}(0)\left(1+2v_{\mathbf{q}}^2(\tau_0)+2\left[u_{\mathbf{q}}^2(\tau_0)+v_{\mathbf{q}}^2(\tau_0)\right]N_a+2N_b'(0)\right)\mathrm{e}^{-2i\Omega_{\mathbf{q}}(0)\tau}\right]
\end{aligned} \tag{5.37}$$

The equation 5.37 is the final result of the structure factor, based on a reasonable assumption of the absence of the initial photonic correlations before the first interaction quench ($C_a = 0$) and neglecting the possible effects of absorption (photonic losses) on the interaction strength inside the cell due to the exponential decay of the photonic density.

Physical sense and simplification: Before readdressing the last approximation in the next section, it is useful to get the physical sense of the different terms of the eqn. 5.37: the first line includes the increased density fluctuations at mode $\mathbf{q}$ as the result of both quenches creating quasi-particle populations both spontaneously and stimulated by the fluctuations already present in the fluid of light. The second line is the contribution to the populations after the 2-nd quench, arising from the quasi-particle correlations just before it. The following two lines are the cross-couplings between the correlations before and after the 2-nd quench, while the last term accounts for the correlations after the 2-nd quench, arising both spontaneously and from the quasi-particle populations before the 2-nd quench.

The eqn. 5.37 can in fact be simplified in the limit of large momenta, $q\xi \gg 1$, implying: $u_{\mathbf{q}} \simeq 1,\ v_{\mathbf{q}} \simeq 0$. Keeping only the terms up to the first order in $v_{\mathbf{q}}$, one gets:

$$\begin{aligned}
S(\mathbf{q},\tau) &= 1 + 2\left[N_a + N_b'(0)\right] + 2v_{\mathbf{q}}(\tau_0)(1+2N_a)\cos\left(2\Omega_{\mathbf{q}}(0)\tau - 2\Omega_{\mathbf{q}}(\tau_0)\tau_0\right) \\
&- 2v_{\mathbf{q}}(0)\left[1+2(N_a+2N_b'(0))\right]\cos(2\Omega_{\mathbf{q}}(0)\tau)
\end{aligned} \tag{5.38}$$

where $\Omega_{\mathbf{q}}(\tau_0) = \sqrt{c_s^2(\tau_0)q^2 + (\hbar q^2/2m)^2}$ and $\Omega_{\mathbf{q}}(0) = \hbar q^2/2m$ are the Bogoliubov frequencies between the quenches and after the second quench, respectively, and τ_0 is the time difference between the quenches. This result shows in particular the presence of two oscillating terms. Both oscillate at the same frequency $2\Omega_{\mathbf{q}}(0)$ in time, while the first one is shifted by twice the phase acquired by a quasi-particle inside the cell. The temporal oscillations of various modes witness the synchronization and coherence of the quasi-particles induced by the interaction quenches. At the same time, at a given time τ, the oscillating terms reveal two different frequencies ($2c_s(0)\tau$ and $2[c_s(0)\tau - c_s(\tau_0)\tau_0]$ for the sonic quasi-particles within $|\mathbf{q}| < 1/\xi = \hbar/(mc_s(\tau_0))$) when plotted as function of $\mathbf{q}$. Importantly, the presence of two spectral frequencies is the consequence of the conserved "memory" from both "on" and "off" interaction quenches.

5.3.4 Influence of absorption inside the cell

Generalized Bogoliubov coefficients: Inside the vapor cell the light is partially absorbed and scattered isotropically via spontaneous emission. This leads, on average, to an exponentially decaying photonic density, leading to additional time dependence of the interactions inside the cell. Therefore in presence of absorption can affect the definition of the Bogoliubov coefficients defining the quasi-particle operators, which now obey:

$$i\hbar\frac{\partial}{\partial\tau}\begin{pmatrix}u_{\mathbf{q}}\\ v_{\mathbf{q}}\end{pmatrix}=M(\tau)\begin{pmatrix}u_{\mathbf{q}}\\ v_{\mathbf{q}}\end{pmatrix},\quad\text{with:}\quad M(\tau)=\begin{pmatrix}\frac{ic\alpha}{2}+E_{tot}(\tau) & -g\rho(\tau)\\ g\rho(\tau) & -\frac{ic\alpha}{2}-E_{tot}(\tau)\end{pmatrix}\tag{5.39}$$

where α is the absorption coefficient of the medium. Since the evolution matrix M is now time dependent, two scenarios are possible for the solution of these equations. The first one is the so called adiabatic evolution [96]: the absorption rate is small enough such that the quasi-particle picture is still valid but has now a dispersion relation which follows the variation of the interaction strength.

Incoherent quasi-particle source due to the spontaneous emission: A second more subtle effect of the spontaneous emission resides in its probabilistic nature and the local atomic density inhomogeneity. These details result in the effects on the light propagation, going beyond the "effective medium" regime, where the latter is just described by a space independent complex refractive index. While the exact theoretical evaluation of this effect requires more advanced numerical tools and goes beyond this work, phenomenologically, we model it as a "white noise" like additional source of density fluctuations N_b'. It is supposed incoherent with respect to the Bogoliubov quasi-particles, due to the finite temporal coherence range of the spontaneous emission process.

5.3.5 Influence of the limited imaging resolution

Upper bound of accessible spatial mode frequency: While theoretical calculation allows to calculate the density fluctuations at infinite momentum $\mathbf{q}\to\infty$, in practice any spatial imaging apparatus is spectrally bound by its Point Spread Function (PSF). Supposing a PSF of a Gaussian profile, the effect of the finite imaging resolution on the structure factor can be written as:

$$S(\mathbf{q},\tau)=1+(S_{th}(\mathbf{q},\tau)-1)\cdot\mathrm{e}^{-R(\tau)^2\mathbf{q}^2}\tag{5.40}$$

with S_{th} is the theoretically calculated structure factor and R is the minimal resolvable length scale, related to the Numerical Aperture NA of the system: $R(\tau)=1/(\mathrm{NA}(\tau)k_L)$, where the NA is supposed to decrease with τ.

5.4 Interaction quenches and the link with cosmology

Quenches at the medium's interfaces: In any experimental platform involving non-linear optical media (including ours) the photons interact only inside the hot medium. Recalling that

the fluid of light's propagation direction plays the role of time, the planes corresponding to the medium's interfaces necessarily correspond to the time points where interactions are suddenly switched on (entrance plane) and off (exit plane).

Cosmology: Recalling the analogy of our platform with cold interacting atomic gases, the situation, where the interactions are suddenly quenched to zero when the laser beam exits the vapor cell [96], can be mapped to an expanding universe, as illustrated in Fig. 5.1 d), since a rapid reduction of the interactions causes a sudden red shift of the energy spectrum [75]. In fact, the reverse process takes place at the cell entrance, in which the interaction suddenly appears. This could then be interpreted as a suddenly contracting universe, following the logic of the analogue cosmology experiments. The expansion of a universe stretches all length scales, including the wavelengths of the particle modes. Thus, the frequencies of the modes evolve with time [135], which implies that the modes at early and late times are related by a Bogoliubov transformation [111]. This field theory approach avoids the microscopic details, and predicts the spontaneous production of cosmological particles, including the primordial density fluctuations, which led to the acoustic peaks, characteristic oscillations revealing the correlations in the cosmic microwave background (CMB) spectrum [67, 27, 115]. It is particularly relevant since the acoustic peaks can be described by linear perturbation theory [74]. The field theory approach inspired the subject of analogue cosmological particle creation, in which laboratory experiments mimic the dynamics of scalar fields in curved space times [11, 51, 123]. In a two-dimensional atomic Bose-Einstein condensate, a qualitative comparison with cosmological particle creation was reported [75]. In this experiment we simulate expanding and contracting universes in a quantum fluid of light, and we observe time-resolved analogue cosmological particle creation out of vacuum fluctuations. As will be shown with the structure factor measurements, both processes (each of the quenches) produce pairs of so called quasi-particles, or correlated density/phase fluctuations of the field, produced in all dimensions, in analogy with cosmological particle creation. The precision of our experiment allows for the observation of the interferences between these two sets of the quasi-particles.

5.5 Experimental methods

To create the fluid of light, we use a 100 ns laser pulse with a 4 mm Gaussian waist and a power of 100 mW, propagating in an ^{85}Rb vapor cell heated to 150 °C. The laser is detuned -1.5(0.2) GHz (90 natural linewidths Γ_0, 6 times the Doppler broadening σ_D) from the D2 $F_g = 3 \rightarrow F'_e$ resonance. The interaction energy is determined by the nonlinear change in the refractive index Δn which is computed from the experimental parameters (laser detuning, vapor temperature, the reported 2-level saturation intensity [37] for a π polarized far detuned light). By taking into account the compression factor, this configuration leads to a weakly interacting photon gas with a thickness of 2 mm in the z coordinate.

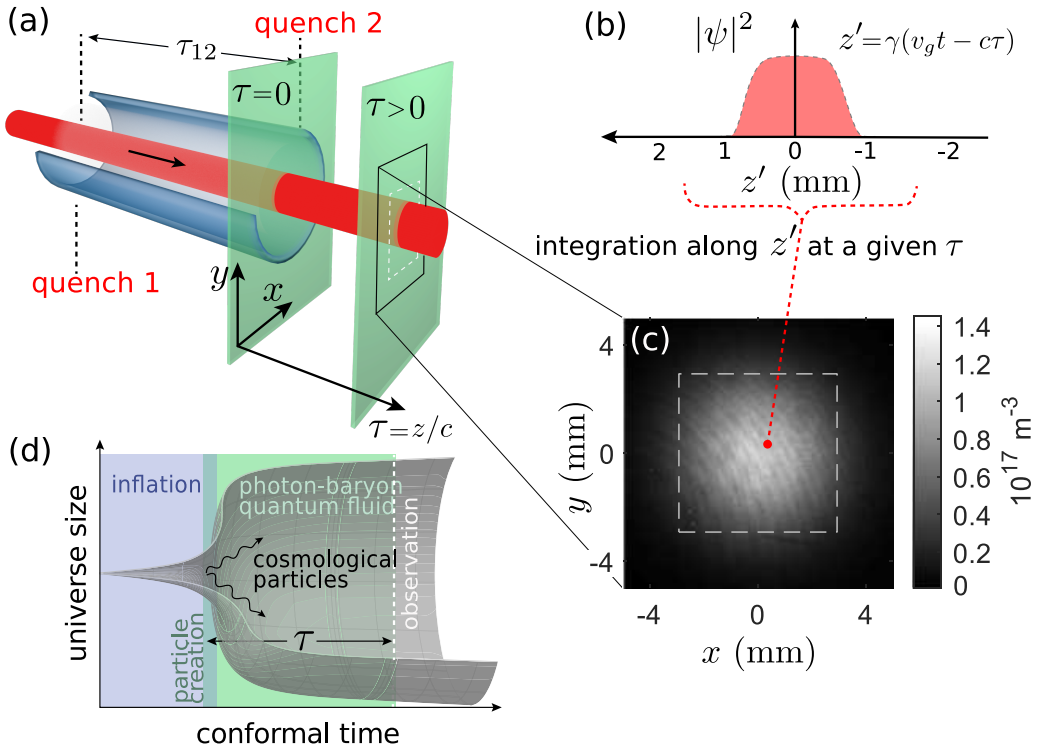

Figure 5.1: Schematic description of the interaction quenches in a 3D fluid of light and their analogy with a cosmological model of particle creation.

5.5.1 Pulsed illumination: third "spatial" dimension

Theoretical consideration: Using the results (eqns. 1.17 and 1.18) derived in the introduction chapter 1, let's remind that the electric field envelope of a nearly mono-chromatic pulsed light within the slowly varying envelope and the paraxial approximations obeys the following propagation equation in the comoving frame:

$$\frac{i}{v_g}\frac{\partial \mathcal{E}}{\partial \tau} + \frac{1}{2k_L}\nabla_\perp^2 \mathcal{E} - \frac{v_g^2 D_0}{2}\frac{\partial^2 \mathcal{E}}{\partial \zeta^2} + g|\mathcal{E}|^2\mathcal{E} = 0 \tag{5.41}$$

where $\tau = z/v_g$ is defined as the ratio between the propagation direction coordinate and the group velocity of the pulse and $\zeta = v_g t + z$ is linked to the "true" time but playing the role of a 3-rd spatial dimension. Recalling, that the fluid's mass in its third dimension $m_\zeta = -1/(v_g^2 D_0)$ may differ in magnitude (sometimes even in sign) from its mass m in other directions, we assume $D_0 < 0$ a negative group velocity dispersion parameter, giving a positive mass. Using this fact we "correct" the dimensional anisotropy via contraction of the third dimension by a factor: $\sqrt{m_\perp/m_{z'}} = \sqrt{k_L v_g^2 D_0}$. In the end the following transformation is used to switch from the lab frame to the compressed comoving frame:

$$z' = \sqrt{\frac{m_\perp}{m_{z'}}}\zeta = \sqrt{k_L v_g^2 D_0}(v_g t + z), \quad \text{and:} \quad \tau = \frac{z}{v_g} \tag{5.42}$$

In this case one gets an equation analogous to a 3D Gross Pitaevskii Equation:

$$i\hbar\frac{\partial\mathcal{E}}{\partial\tau}+\frac{1}{2m}\nabla^2\mathcal{E}+g|\mathcal{E}|^2\mathcal{E}=0 \tag{5.43}$$

Where the Laplacian is now written for three "spatial" dimensions of the fluid.
Practical consideration: while switching from the cw to pulsed illumination adds the conceptually new feature of an additional spatial dimension, there is a simple practical motivation for it. In fact, the measurement of the spatial intensity correlations in the shot noise regime forbids using any attenuating element between the imaged plane and the camera, because this would randomize the correlations. However, the high enough light intensity, required for noticeable photonic Kerr interactions, would necessarily result in the camera saturation, which can be successfully avoided by switching to the pulsed illumination at fixed laser intensity.

5.5.2 Fluid's parameters

In this experiment it is essential to normalize the electric field envelope $\mathcal{E}$ such that the mean of $|\mathcal{E}|^2$ is the photon density: $\rho\simeq 7\times10^{16}$ m^{-3}. In practice this corresponds to a laser beam of power $P=100$ mW with a Gaussian spatial shape of waist $\omega_0=4$ mm and approximately square temporal shape with width of 100 ns. Also, for comparison with cold atom experiments, the effective photon mass is $m=\hbar k_L/c\simeq 2.8\times10^{-36}$ kg. The mean-field interaction energy (the chemical potential)is given by $g\rho=\hbar\omega_L\Delta n$, with Δn the non-linear refractive index variation measured with the off-axis interferometry. With laser detuning $\Delta/(2\pi)=1.5(0.2)$ GHz from the ^{85}Rb's D2 $F_g=3\rightarrow F_e'$ transition, and a $L=10$ mm long pure ^{85}Rb isotopic vapor cell heated to $T_V\simeq 150$ °C, $\Delta n\simeq 8(2)\times10^{-6}$ was measured. Laser transmission at the given detuning was $T=20$ %. Furthermore, the healing length is given by $\xi=1/(k_L\sqrt{|\Delta n|})\simeq 60$ μm, where $c_s=c\sqrt{|\Delta n|}$ is the speed of sound for the Bogoliubov excitations. The group velocity was estimated from the calculated linear refractive index spectrum to be equal to $v_g=0.007c$. The length scale associated with group velocity dispersion is given by $\xi_{z'}=\xi\sqrt{m/m_{z'}}\simeq 6$ mm. In order for the eqn. 5.43 to be valid, the frequency interval $v_g\xi_{z'}/(2\pi)\simeq 50$ MHz should be much less than the laser detuning $\Delta/(2\pi)=1.5(0.2)$ GHz, which is indeed the case. The effective s-wave scattering length is $a_s=mg/(4\pi\hbar^2)=3.1\times10^{-10}$ m.

5.5.3 Experimental setup

The experimental setup is shown on figure 5.2. A cw beam of the Kilimandjaro laser (see ch.:2) was send to an Acousto-Optic Modulator (AOM) double pass setup for the pulse production. The laser frequency was controlled with a saturable absorption spectroscopy (SAS) by locking the SAS signal to a slope (side of fringe lock) at the vicinity of the Doppler broadened ^{87}Rb $F_g=2\rightarrow F'$ line. After the pulse production the beam is spatial mode cleaned with a polarization maintaining single mode optical fiber. After collimation, it is then magnified with a $\times4$ telescope before reaching the vapor cell. After the cell, a given axial position z is

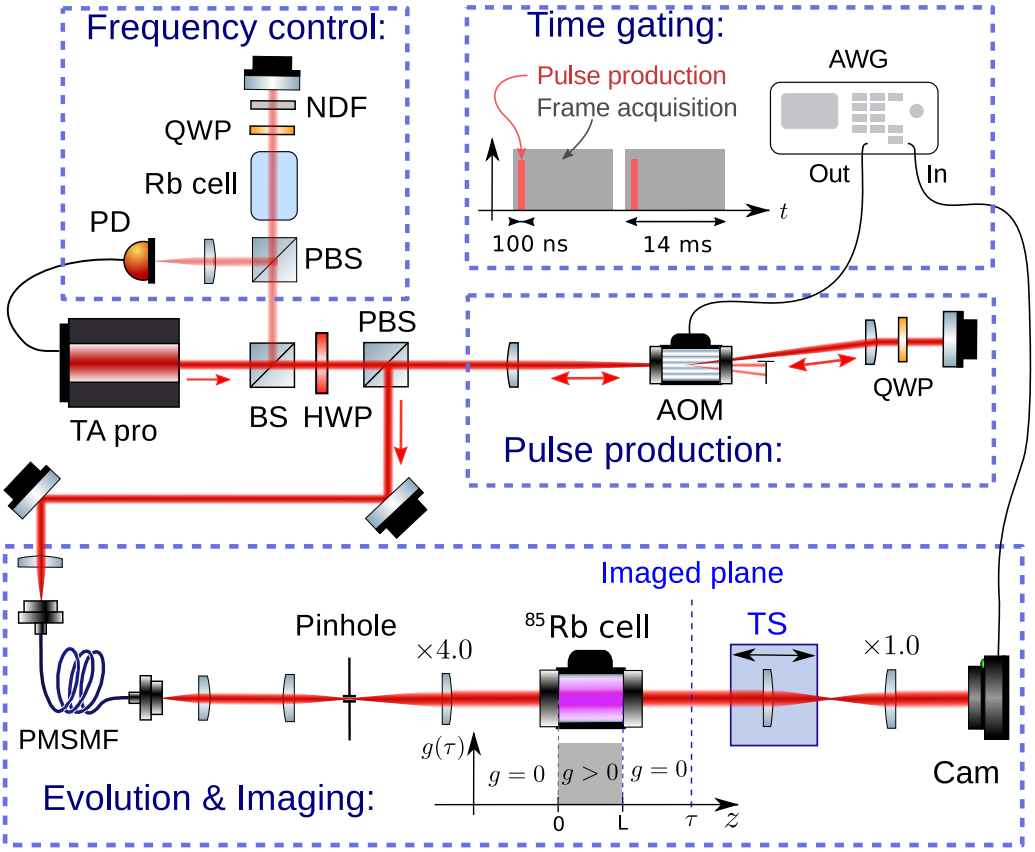

Figure 5.2: Experimental setup of the fluid's spatial noise spectrum measurement. Laser frequency was controlled and locked at $\Delta/(2\pi) = -1.5(0.15)$ GHz with respect to the ^{85}Rb $F_g = 3 \rightarrow F'$ transition with a saturable absorption spectroscopy setup. The beam is then temporally modulated with a double pass AOM setup to produce pulses of width 100 ns. The pulse is then spatially mode-cleaned with a Polarization Maintaining Single Mode Fiber (PMSMF) and a $\times 4$ magnifyinig telescope with a pinhole in the Fourier plane, before being collimated with the waist $\omega_0 = 4$ mm at the entrance of the vapor cell. The $L = 10$ mm long vapor cell is heated to $T = 150°$ C (corresponding to the $\mathcal{T} = 20$ % transmission for a 100 ns pulse at the given laser frequency). Various $z = c\tau$ planes after the cell's exit plane are imaged on a CMOS camera with a $\times 1$ magnifying 4-f setup with the first lens placed on a Translation Stage (TS). During the acquisition, the AOM pulse production is triggered by the beginning of camera's frame acquisition through an Arbitrary Waveform Generator (AWG).

imaged with a ($\times 1$ magnifying) 4f setup on a Hamamatsu Orca Flash 4.2 camera. The imaged plane's position can be varied by displacing the first lens after the cell, which is mounted on a translation stage. The synchronization between the camera acquisition and the pulse production was enabled by triggering the AOM driver with the output trigger of the camera. Finally, the imaging resolution of the setup was estimated to be equal to $R = 5$ μm [146].

5.5.4 Image acquisition and processing

Acquisition: The fluid of light is imaged on a CMOS camera, as shown in Fig. 5.1 c). We tune the imaging system to pick out a certain z position after the cell, and the camera integrates over true time, as illustrated in Fig. 5.2. Thus, each image shows the density integrated in the z' direction, at an effective time τ after the second quench. For each τ, an ensemble of 200 images is obtained in approximately 5 seconds, and the power spectrum $S(q_x, q_y, q_{z'} = 0, \tau)$ is computed by 2-dimensional Fourier transforms within the dashed square shown in Fig. 5.1 c). The computation partially removes the effects of any drifts such as thermal convection, and accounts for the measured quantum efficiency of the camera, as will be elaborated in the next section.

Processing: In fact, due to the lack of temporal resolution in the fluid's imaging, the experimentally accessible power spectrum (static structure factor) $S(\mathbf{q})$ slightly differs from its definition given in eqn. 5.16. We can first recall the definition of the density fluctuation spectrum:

$$\delta\rho(q_x, q_y, q_{z'}, \tau) = \int_{\mathbb{R}^2} \mathrm{d}x\mathrm{d}y \left(\int_{\mathbb{R}} \mathrm{d}z' \delta\rho(x, y, z', \tau) \mathrm{e}^{-iq_{z'}z'} \right) \mathrm{e}^{-i(q_x x + q_y y)} \tag{5.44}$$

Setting $q_{z'} = 0$ the term inside the brackets corresponds to the density fluctuation obtained from images acquired on the camera: $\delta\rho(x, y, \tau)$. As the result, one gets: $\delta\rho(q_x, q_y, q_{z'} = 0, \tau)$ and the static structure factor is: $S(q_x, q_y, q_{z'} = 0, \tau)$. The density fluctuation is calculated as $\delta\tilde{\rho} = \tilde{\rho} - \langle\tilde{\rho}\rangle_5$ for each image, where $\langle\tilde{\rho}\rangle_5$ is the average of 5 adjacent images rather than the average $\langle\tilde{\rho}\rangle$ over the entire ensemble. This technique reduces the effects of drifts in the experimental parameters. As mentioned in relation to fig. 5.3 c), the relative density fluctuation $\delta\tilde{\rho}/\langle\tilde{\rho}\rangle$ is on the order of 10^{-3}, so small drifts can play a role. The 2-dimensional Fourier transform of $\delta\tilde{\rho}(x, y, \tau)$ is computed for each image within the dashed square of fig. 5.1 c). The power spectrum $S(q_x, q_y, q_{z'} = 0, \tau)$ is computed by using the eqn. 5.16 with N_p obtained as the average sum over pixels inside the considered region of interest (dashed square of fig. 5.1 c)). The use of $\langle\tilde{\rho}\rangle_5$ rather than $\langle\tilde{\rho}\rangle$ reduces the fluctuations by a factor of 4/5. Thus, the result, $S(q_x, q_y, q_{z'} = 0, \tau)$ is multiplied by 5/4 to correct this effect. Furthermore, the finite quantum efficiency $QE = 0.485$ of the camera tends to randomize the photon density and bring $S(q_x, q_y, q_{z'} = 0, \tau)$closer to unity. Thus, $S(q_x, q_y, q_{z'} = 0, \tau) - 1$ is multiplied by the factor $1/QE$.

5.6 Results

5.6.1 Oscillations in the momentum and spatial domains

Spectral oscillations: In Fig. 5.3 a) we observe ring patterns in $S(q_x, q_y, q_{z'} = 0, \tau)$, oscillating as a function of $q = \sqrt{q_x^2 + q_y^2}$. These oscillations are the experimental signature of the Bogoliubov quasi-particle creation. Note that in the context of analogue cosmological experiments, these oscillations are in close analogy with the acoustic peaks in the angular spectrum of the cosmic microwave background (CMB) [75]. They occur because the modes q are generated synchronously at the moment of the quench, and oscillate with different frequencies $\Omega(q)$. The

rings shrink with τ since lower frequencies take longer to develop oscillations. The radius of the first minimum is seen to be in good agreement with the theoretical prediction of eqn. 5.38, indicated by the dashed green curve. The azimuthal averages of the spherically-symmetric $S(q)$ are indicated in black in fig. 5.3 b). The red curves are calculated from the eqn. 5.37, taking into account the two quenches, and the variations in u_q, v_q, and $\Omega(q)$, which result from the measured absorption, as well as the effect of the finite imaging resolution.

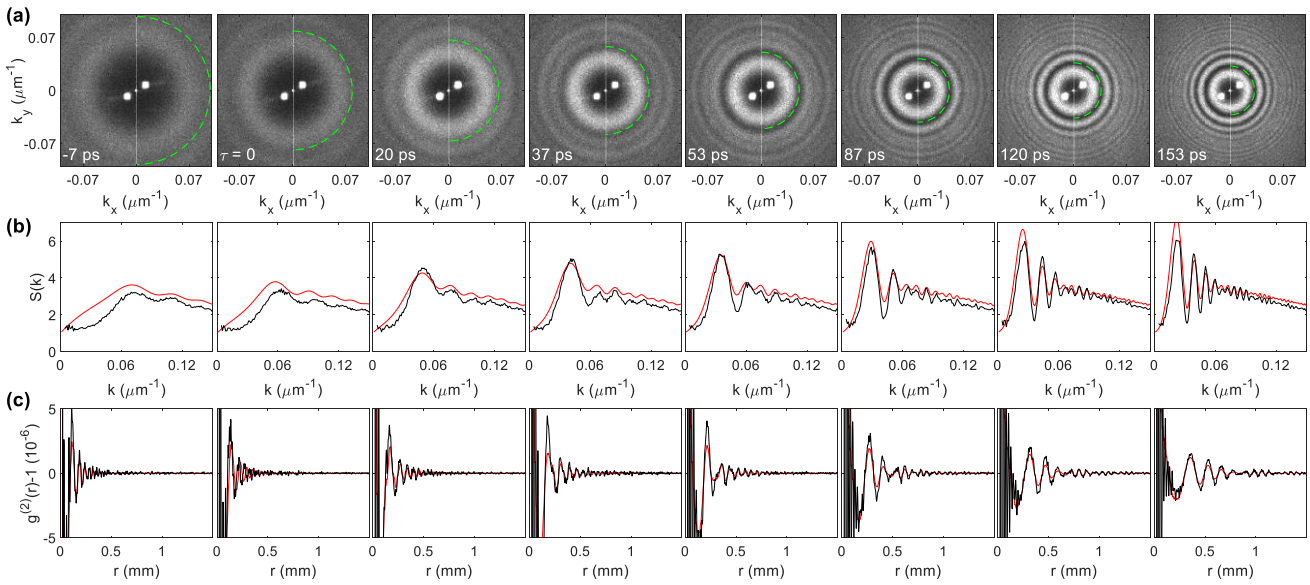

Figure 5.3: a) The static structure factor $S(q_x, q_y, q_z = 0)$ at various times after the second quench. The dashed green curves indicate the first minimum of the red curves in b). The symmetric white points near the center of all panels are due to spurious fringes in the imaging system. b) Radial profiles of a). The black curves are the experimental data. The red curves are the prediction for analogue cosmological particle creation, from the eqn. 5.37 including absorption, finite imaging resolution and the quantum efficiency of the camera. c) Density-density correlations. The experimental (black) and theoretical (red) curves are obtained from b) by the spherical Fourier transform of eqn. 5.45.

Spatial oscillations: We also determine the spatial density correlations produced by the analogue cosmological particle creation. We derive the density-density correlation function $g^{(2)}(\Delta r)$ from $S(q)$ by the 3-dimensional spherically-symmetric Fourier transform:

$$g^{(2)}(\Delta r) - 1 = \frac{1}{2\pi^2 \rho_0} \int_0^\infty q^2 \mathrm{d}q \frac{\sin(q\Delta r)}{q\Delta r} (S(q) - 1) \tag{5.45}$$

Note that here we have: $q = \sqrt{q_x^2 + q_y^2 + q_z^2}$. Figure 5.3 c) shows $g^{(2)}(r) - 1$, found by applying the eqn. 5.45 to Fig. 5.3 b). The oscillations are spherical shells propagating outward. The correlations are seen to reach increasing distances as time increases. They are on the order of 10^{-6}, which implies that the relative density fluctuations are on the order of 10^{-3}. The oscillations are clear despite the small signal, due to the high sensitivity of the optical detection. The theoretical red curves are obtained by applying the eqn. 5.45 to the eqn. 5.26, and quantitative

agreement with the experimental curves is seen.

5.6.2 Analysis of the correlations

5.6.2.1 Nature of the density fluctuations

Spontaneous vs stimulated density fluctuations? The low-q behavior of $S(q)$ provides a window into the early times before the quenches, since the frequency of these modes approaches zero, so the modes do not have sufficient time to evolve during the experiment. The cut-off frequency is on the order of $1/\tau$, stemming from the time necessary for the quasi-particles to realize the first oscillation at the given mode (with the rate given by the Bogoliubov frequency) which corresponds to the first peak in $S(q)$. Well below this q-value, the eqn. 5.38 reduces to $S(q) = 1 + 2N_a$, where N_a is the incoherent population before the first quench. Thus, the value of $S(0)$ gives a direct measure of N_a. Fig. 5.4 a) shows the $S(q)$ curves for all τ plotted together. We observe that $S(q)$ is at most 1.4 for low q, as indicated by the dashed green line, giving $N_a \leq 0.2$ according to the eqn. 5.38. This value is finite, which implies a negligible thermal component, since a thermal population diverges like $1/q$. Furthermore, it is less than unity, implying that the spontaneous contribution dominates. Thus, the analogue cosmological particle creation is spontaneous in the first quench. This is verified by the blue and green curves in fig. 5.4 c), which show that stimulation in the first quench by thermal noise and white noise, respectively, would produce larger values of $S(q)$ than those of the experiment, for low q. The quasiparticles spontaneously created during the first quench stimulate pair creation in the second quench. However, if the particle production in the second quench were stimulated by the first-quench quasiparticles only, $S(q)$ would oscillate about unity, as indicated by the magenta curve in fig. 5.4 d). The upward shift of $S(q)$ allows us to identify the presence of background quasiparticles, due to spontaneous and superradiant emission of photons from the atomic medium, which cause additional stimulation in the second quench. The downward slope of $S(q)$ observed at large q is due to the finite resolution of the imaging system, measured to be 10 μm and is included in all theoretical curves.

Incoherent background population: Other than this slope, $S(q)$ oscillates about the value $1 + 2(N_a + N_b')$, where N_b' is the background population present in the fluid between the two quenches (phenomenologically added as the contribution of the spontaneous emission). In our experimental configuration, we calculate that the contribution of spontaneous and superradiant emission leads to an incoherent population of $N_b' = 1.2$. The theoretical curves in fig. 5.3 b)include this additional stimulation with no adjustable parameters, and confirm the origin of the background population. While this incoherent, flat spectrum of 1.2 quasiparticles per mode implies that the fluid is not in its ground state, like a finite-temperature Bose-Einstein condensate, it does not negate the oscillatory behavior of $S(q)$, and it even enhances the visibility of the oscillations. We can control this population by tuning the atomic density, the pulse duration, intensity, and detuning. In fig. 5.4 e) we verify that this population vanishes for long weak pulses, as expected for spontaneous and superradiant emission.

5.6.2.2 Effective temperature of the fluctuations?

How cold is our quantum fluid of light? Although our fluid of light is not in thermal equilibrium between the two quenches, we can put an upper limit on the effective temperature of the thermal component before the second quench. The blue curve in fig. 5.4 d) includes thermal stimulation with an effective temperature $2mc_s^2 = 30$ mK, which results in a greatly enhanced first peak, absent from the experimental curve. Thus, we estimate the effective temperature of the thermal component to be less than $2mc_s^2$, as in an atomic Bose-Einstein condensate. For the second quench, the thermal fraction does not diverge like $1/q$ since the zero-temperature static structure factor in the fluid of light goes to zero for low q [119].

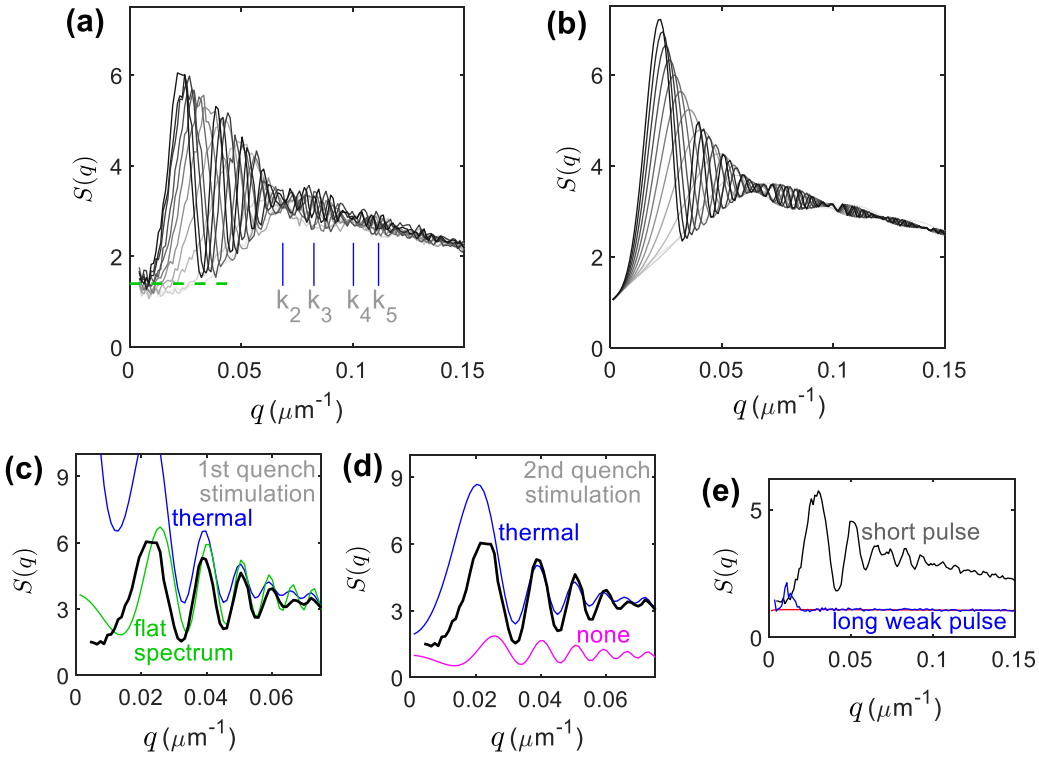

Figure 5.4: Analysis of the radial static structure factor with respect to the various phenomenological contributions. Experimental a), and theoretical b) superimposed radial structure factors at at different times τ. The k_p mark the nodes and antinodes. These graphs first show the beating of the oscillations, confirming the presence of two interaction quenches, and second allow to quantify the photonic population before the first quench N_a since $S(0) \simeq 1+2N_a$. c) The effect of stimulation in the first quench, on $S(q, \tau = 153$ ps) after both quenches. The blue curve includes additional stimulation by a thermal distribution in the first quench. The green curve includes stimulation by a flat distribution in the first quench rather than the second. d) The effect of stimulation in the second quench. The blue curve includes additional stimulation by a thermal distribution in the second quench. The magenta curve includes no extra stimulation in either quench. e) Effect of the interactions. The black curve is $S(q, \tau = 87$ ps). The blue curve employs a pulse which is 500 times weaker and longer. The red curve is the theoretical prediction for the long, weak pulse.

Signature of the presence of two quenches: Fig. 5.4 a) exhibits a beating pattern in the envelope of the various curves, resulting from interference between analogue cosmological particles created in the two quenches. The theoretical curves in fig. 5.4 b) show a similar pattern. We

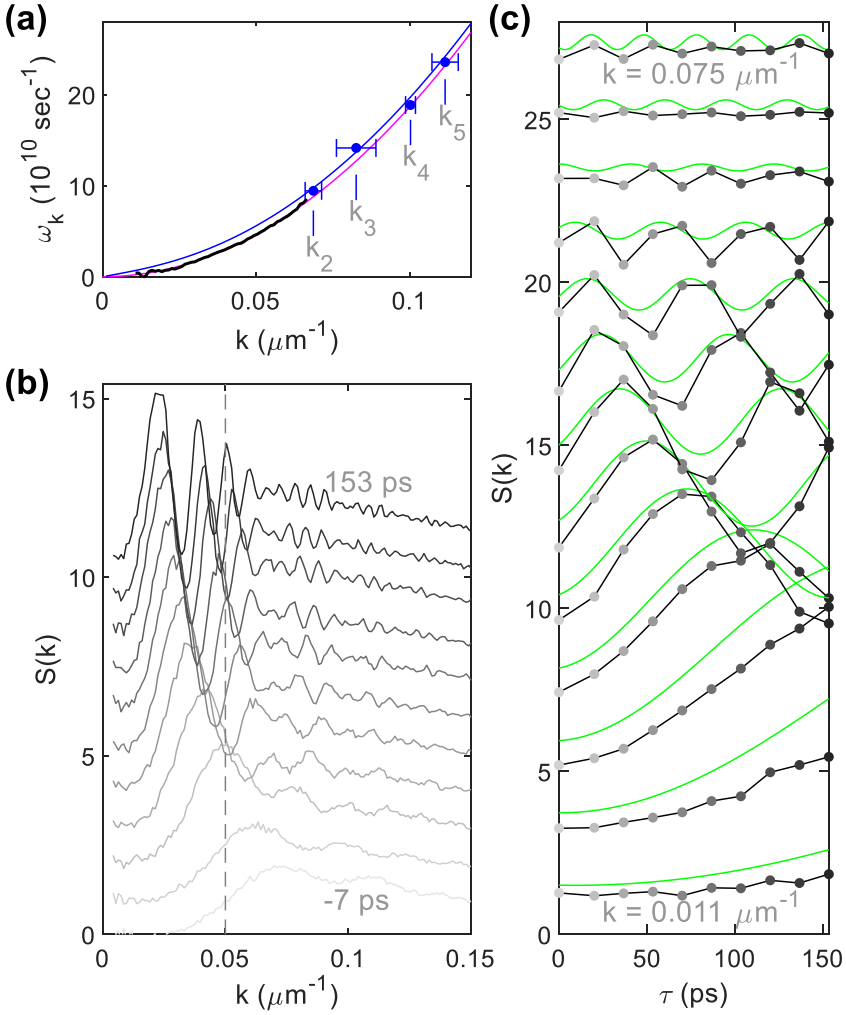

Figure 5.5: Individual modes of the analogue cosmological particles. a) The dispersion relation, obtained by measuring (for details see the b) and c) panels) the oscillation frequency of the different momenta. The blue points correspond to the (anti-)node positions k_p, identified in fig. 5.4 a), stemming from the $\tau_0 = L/c = 33$ ps long evolution after the 1-st quench in presence of interactions. The error bars indicate one standard deviation. The black curve is obtained by sinusoidal fits to the gray curves in c). The magenta curve is the calculated free-particle dispersion relation. The blue curve is the dispersion relation in the interacting fluid (before the 2-nd quench). b) The static structure factor at various times. The curves are from Fig. 5.4 a), and are shifted vertically. The vertical dashed line is used to find the values in c). c) Each curve shows the -dependence of a definite q, given by the values along a vertical line in b), such as the dashed line. The grayscale is the same as in b). The k-values shown are equally spaced by 5.4×10^{-3} μm^{-1}. The green curves are computed with the eqn. 5.37. Each pair of black and green curves has been shifted vertically.

can recall the simplified expression for the structure factor, eqn. 5.38, obtained by neglecting

absorption and approximating $u_q \simeq 1$ and $v_q \ll 1$, which is valid for all but the lowest values of q. As already mentioned above, this expression shows two distinct frequencies when plotted versus q. This results in the observed beating with an envelope showing nodes and antinodes at $\Omega_{\mathbf{q}}(\tau_0) = \pi p/(2\tau_0)$, where p is an integer. By identifying each (anti-)node position k_p as shown in fig. 5.4 a), 4 points on the dispersion relation are found, as indicated by blue points in fig. 5.5 a). These points agree well with the dispersion relation in the medium, calculated from the interactions, and indicated by the blue curve.

5.6.3 Temporal dynamics of the correlations

Fig. 5.5 b) shows the curves of Fig. 5.4 a), one above the other. By plotting the $S(q)$ values along the dashed line, we obtain the time dependence of a given mode q, as shown in Fig. 5.5 c). Each mode is seen to oscillate sinusoidally after the second quench. We observe as much as 3 full oscillation periods. The frequencies of the oscillations, indicated by the black curve in Fig. 5.5 a), agree well with the free-particle spectrum, indicated by the magenta curve. This result shows that the fluctuations produced during the quenches are synchronized, i.e. the different populated quasi-particle modes are phase coherent and their interference results in the temporal oscillations of the static structure factor upon their temporal evolution. These oscillations appear without noticeable damping, confirming the conservative nature of the evolution Hamiltonian and suggesting the absence of any relaxation mechanisms in a weakly disturbed quantum fluid of light within the considered short time scales.

5.7 Conclusion

This experiment establishes the paraxial fluid of light as a quantum fluid. In our platform the fluid of light appears to have an effective temperature less than twice the chemical potential, which is comparable to many ultracold atomic Bose-Einstein Condensates. The results demonstrate that quantum field theory applies to a system in which a spatial coordinate plays the role of time. The direct detection of the photon fluid allowed to observe the response to two interaction quenches. We observe both spontaneous and stimulated quasiparticle creation which we interpret as the analogue cosmological particle creation in a quantum fluid of light. The particle production in the first quench is seen to be spontaneous, while the second includes stimulation by the first quench quasiparticles, as well as by an incoherent background. We quantitatively confirm the quantum field-theoretical prediction. The long wavelength part of the spectrum provides a window into early times before the particle creation. We can therefore conclude that these results open a new avenue in the analogue gravity experiments in quantum fluids of light.

Chapter 6

Pre-thermalization and power-law to exponential transition of spatial coherence in a fluid of light

6.1 Outline of the chapter

In this chapter the observation of a pre-thermal state in a non-equilibrium, 2D fluid of light is reported. Direct measurements of the coherence function of the fluid reveal the dynamical emergence of algebraic correlations, a quasi steady-state with properties close to those of thermal superfluids. By a controlled increase of fluctuations, we observe a cross-over from algebraic to short-range (exponential) correlations. We conjecture that this phenomenon is a non-equilibrium precursor of the Kosterlitz-Thouless transition.

6.2 Introduction

6.2.1 What is prethermalization?

The relaxation dynamics of isolated many-body systems has revealed a rich variety of scenarios in the past decades [122, 62]. While a general understanding of how a quantum system returns to its equilibrium after a perturbation is still elusive, several intriguing phenomena have been identified. Examples include the non-equilibrium dynamics of near-integrable systems [86], the relaxation towards thermalization [150] or the spontaneous emergence of universal scaling laws [124, 49, 60] following a quantum quench. Ultracold atomic quantum gases have been a particularly relevant platform in this context, with quench experiments allowing to probe the non-equilibrium dynamics in a controlled fashion and under conditions close to isolation. In non-equilibrium many-body systems, the phenomenon of pre-thermalization plays a central role [17, 89, 100]. Pre-thermalization describes the fast relaxation toward a quasi-steady state following a perturbation, with the evolution to full thermalization occuring on a much longer time scale. In a pre-thermal state, the system has a partial memory of its initial conditions,

while showing a strong resemblance to its true thermal equilibrium state. Experimentally, this mechanism has been observed in one-dimensional (1D) Bose gases [66, 92, 93], where the presence of a trapping potential weakly breaks the system integrability, a sufficient condition for the dynamical emergence of a pre-thermalized state. More recently, signatures a of pre-thermalized state were also identified in a unitary Bose gas [47].

6.2.2 Prethermalization in fluids of light?

In this chapter I report on the direct observation of a pre-thermal state in a two-dimesnional (2D) fluid of light realized by propagating a laser beam through a nonlinear atomic vapor. Upon entering the medium, the beam experiences a sudden change of the nonlinear refractive index, which effectively reproduces the non-equilibrium dynamics of a Bose gas after an interaction quench. This analogy has been previously exploited to observe the dynamical formation of dispersive shock waves [129, 164, 18], analogue cosmological Sakharov oscillations [146] or the formation of optical condensates [147, 165]. In our experiment, the dynamical emergence of correlations characteristic of pre-thermalization is achieved by imprinting weak spatial fluctuations to the laser, analogous to thermal fluctuations in a Bose gas, an idea put forward in the recent proposal [13]. Unlike in [66, 92, 93], however, the non-equilibrium dynamics of our fluid of light is 2D, which leads to *algebraic* correlations spreading within a light cone [13, 137, 30]. This behavior, which we probe by direct measurement of the fluid's coherence function, is the non-equilibrium counterpart of the well-known algebraic order of 2D thermal Bose superfluids [117, 104, 69, 33]. By increasing the strength of fluctuations, we further observe a cross-over where the fluid correlations turn from algebraic to exponential. This phenomenon, which echoes the celebrated Kosterlitz-Thouless transition expected at thermal equilibrium, suggests the existence of precursors of thermodynamic phase transitions even at the fully non-equilibrium level.

6.3 Spatial coherence of an inhomogeneous fluid of light

Approach description: In this section the spatial coherence function of a fluid of light is calculated based on the results presented in [13] and [12]. Using an approach similar to the one presented in section 4.3.1 based on the separation of the background's slow variations from the fluctuations' fast variables, the first order correlation function is derived for the case of a finite sized Gaussian background beam within the so-called Local Density Approximation (LDA). Indeed, here we take special attention to the fact that the background is not uniform in space and slightly generalize the result presented in [13].

6.3.1 Statistics of the initial state

The initial state of the fluid can be written as:

$$\mathcal{E}(\mathbf{r},0)=\sqrt{\rho_0(\mathbf{r})}\,(1+\varepsilon.\delta\psi(\mathbf{r}))\quad\text{with:}\quad\rho_0(\mathbf{r},z)=\rho_0(0,0).\exp\left(-\frac{2\mathbf{r}^2}{\omega_0^2}\right)\tag{6.1}$$

It is composed of a spatially "slowly" depending background field $\sqrt{\rho_0(\mathbf{r})}$ and the "fast" fluctuations $\delta\psi$. The strength of the fluctuation field with respect to background is quantified by the parameter ε. The fluctuations are supposed to have Gaussian statistics and follow a spatial correlation $\gamma(\Delta\mathbf{r})$. Translated into the language of optics, the fluctuations are represented by a well developed optical speckle pattern with following characteristics:

$$\delta\psi(\mathbf{r})=\delta\psi_r(\mathbf{r})+i\delta\psi_i(\mathbf{r})\quad\text{such that :}\quad\langle\delta\psi_r(\mathbf{r}+\Delta\mathbf{r})\delta\psi_i(\mathbf{r})\rangle=0\tag{6.2}$$

$$\langle\delta\psi^*(\mathbf{r}+\Delta\mathbf{r})\delta\psi(\mathbf{r})\rangle=\langle\delta\psi_r(\mathbf{r}+\Delta\mathbf{r})\delta\psi_r(\mathbf{r})\rangle+\langle\delta\psi_i(\mathbf{r}+\Delta\mathbf{r})\delta\psi_i(\mathbf{r})\rangle=\gamma(\Delta\mathbf{r})\tag{6.3}$$

In this work we use Gaussian fluctuations such as: $\gamma(\Delta\mathbf{r})$ =exp$(-\Delta r^2/(4\sigma^2))$. This correlation function reveals a correlation length of the fluctuations σ, which is also the typical variation scale of the fluctuations and roughly corresponds to the average speckle grain size. This length is supposed much smaller than the waist $\sigma\ll\omega_0$. Assuming $\varepsilon\ll1$ weak fluctuations, one can link the initial field fluctuations to those of its density and phase:

$$\delta\rho(\mathbf{r},0)=\rho_0(\mathbf{r},0)\left(\left[1+\varepsilon\delta\psi_r(\mathbf{r})\right]^2+\varepsilon^2\delta\psi_i(\mathbf{r})\right)-\rho_0(\mathbf{r},0)\simeq2\varepsilon\rho_0(\mathbf{r},0)\delta\psi_r(\mathbf{r})\tag{6.4}$$

$$\theta(\mathbf{r},0)\simeq\varepsilon\delta\psi_i(\mathbf{r})\tag{6.5}$$

This result shows that the real part of the fluctuation field primarily contributes to the intensity fluctuations, while the imaginary part of the fluctuations primarily contributes to the phase fluctuations.

6.3.2 Observable: spatial coherence function

The main observable of this chapter is the equal time spatial coherence. It is defined for spatially invariant systems as:

$$g^{(1)}(\Delta\mathbf{r},z)=\langle\mathcal{E}^*(\mathbf{r},z)\mathcal{E}(\mathbf{r}+\Delta\mathbf{r},z)\rangle\tag{6.6}$$

However, one can immediately notice that, as soon as the background field is a finite sized spatially dependent beam, the spatial invariance is broken. In this case the spatial coherence depends both correlated points $\mathbf{r}$ and $\mathbf{r}'$. Taking into account the radial symmetry of the Gaussian background beam, it is convenient to cross correlate the points which are symmetric to the center of the beam $\mathbf{r}'=-\mathbf{r}$:

$$g^{(1)}(\mathbf{r},-\mathbf{r},z)=\langle\mathcal{E}^*(\mathbf{r},z)\mathcal{E}(-\mathbf{r},z)\rangle\tag{6.7}$$

This definition is more appropriate for the description of the experimental results of this work and will therefore be used in the following discussion. In particular, it has several advantages providing similar results for the case of an inhomogeneous background compared to the case of an homogeneous one (plane wave), as will be shown later.

Independent contributions: intensity and phase fluctuations: In this paragraph we shall see that the coherence can be conveniently be expressed with the field's intensity and phase fluctuations: for this we use the Madelung transformation, as in the chapter 4:

$$\mathcal{E}(\mathbf{r},z)=\sqrt{\bar{\rho}(\mathbf{r},z)+\delta\rho(\mathbf{r},z)}\mathrm{e}^{i\phi(\mathbf{r},z)},\quad \text{with: } \phi(\mathbf{r},z)=\phi_0(\rho_0(\mathbf{r},z))z+\theta(\mathbf{r},z) \tag{6.8}$$

Note that the average density: $\bar{\rho}=\rho_0(1+\varepsilon^2)$ includes the average density of the fluctuations [13]. Inserting the eqn.: 6.8 into 6.7 one gets:

$$g^{(1)}(\mathbf{r},-\mathbf{r},z)=\bar{\rho}(\mathbf{r})\left\langle\sqrt{\left(1+\frac{\delta\rho(\mathbf{r},z)}{\bar{\rho}}\right)\left(1+\frac{\delta\rho(-\mathbf{r},z)}{\bar{\rho}}\right)}\right\rangle\left\langle\mathrm{e}^{i(\phi(\mathbf{r},z)-\phi(-\mathbf{r},z))}\right\rangle \tag{6.9}$$

Where the average density could be factorized using $\bar{\rho}(-\mathbf{r})=\bar{\rho}(\mathbf{r})$. This expression assumes that the field's density and phase fluctuations are uncorrelated. This assumption holds for the case of $\{\psi_r,\psi_i\}$ uncorrelated and following same Gaussian statistics, which is a common requirement in case of well developed speckle beams.

Intensity dependent factor:

$$\sqrt{\bar{\rho}+\delta\rho(\mathbf{r},z)}\simeq\sqrt{\bar{\rho}}\left(1+\frac{1}{2}\frac{\delta\rho}{\bar{\rho}}-\frac{1}{8}\frac{\delta\rho^2}{\bar{\rho}^2}+\mathcal{O}\left(\frac{\delta\rho}{\bar{\rho}}\right)^3\right) \tag{6.10}$$

Indeed, at this point we suppose small density fluctuation ($\varepsilon\ll 1$) in order the expansion of the square root be valid. Note that, this does not imply anything on the initial phase fluctuations, which may not be as well, but this feature isn't necessary. As we'll see later, they get amplified with time, giving rise to the long range correlations. Note that the expansion at least up to the 2-nd order in $\delta\rho/\bar{\rho}$ is required, because the density fluctuation is on average zero. Therefore the density contribution to the field correlation is given, up to the 2-nd order in $\delta\rho$, by:

$$\begin{aligned}&\left\langle\sqrt{1+\frac{\delta\rho(\mathbf{r},z)}{\bar{\rho}}}\sqrt{1+\frac{\delta\rho(-\mathbf{r},z)}{\bar{\rho}}}\right\rangle\simeq\\&1-\frac{1}{8}\frac{\langle\delta\rho(\mathbf{r},z)^2\rangle}{\bar{\rho}^2}-\frac{1}{8}\frac{\langle\delta\rho(-\mathbf{r},z)^2\rangle}{\bar{\rho}^2}+\frac{1}{4}\frac{\langle\delta\rho(\mathbf{r},z)\delta\rho(-\mathbf{r},z)\rangle}{\bar{\rho}^2}+\mathcal{O}\left(\frac{\delta\rho}{\bar{\rho}}\right)^3\simeq\\&1-\frac{\left\langle[\delta\rho(\mathbf{r},z)-\delta\rho(-\mathbf{r},z)]^2\right\rangle}{8\bar{\rho}^2}\simeq\exp\left(-\frac{\left\langle[\delta\rho(\mathbf{r},z)-\delta\rho(-\mathbf{r},z)]^2\right\rangle}{8\bar{\rho}^2}\right)\end{aligned} \tag{6.11}$$

The last equality required the use of the Taylor expansion of an exponential around zero.

Phase dependent factor: The the phase dependent factor can be expressed in a similar manner:

$$\left\langle \mathrm{e}^{i(\phi(\mathbf{r},z)-\phi(-\mathbf{r},z))} \right\rangle \simeq \exp\left(-\frac{1}{2}\left\langle [\phi(\mathbf{r},z)-\phi(-\mathbf{r},z)]^2 \right\rangle\right) \tag{6.12}$$

where I apply an approximation commonly used in wave physics in complex media. For a radially symmetric beam, the two-point phase difference depends only on the fluctuation phase because the background's phase $\Phi_(\rho_0)$ cancels out due to the radial symmetry: $\phi(\mathbf{r},z)-\phi(-\mathbf{r},z) = \theta(\mathbf{r},z)-\theta(-\mathbf{r},z)$. This is the main advantage of choosing $\mathbf{r}' = -\mathbf{r}$ in the inhomogeneous background case.

Total result: Combining both density and phase dependent factors, one gets:

$$g^{(1)}(\mathbf{r},-\mathbf{r},z) = \bar{\rho}.\exp\left(-\frac{\left\langle [\delta\rho(\mathbf{r},z)-\delta\rho(-\mathbf{r},z)]^2 \right\rangle}{8\bar{\rho}^2} - \frac{1}{2}\left\langle [\theta(\mathbf{r},z)-\theta(-\mathbf{r},z)]^2 \right\rangle\right) \tag{6.13}$$

This result expressed the equal time first order spatial coherence as function of the fluid's density and phase fluctuations. Remarkably, same result holds for the spatial coherence of BEC-s.

Simplification: Finally, the ensemble averaged terms of the eqn. 6.13 read:

$$\frac{\left\langle [\delta\rho(\mathbf{r},z)-\delta\rho(-\mathbf{r},z)]^2 \right\rangle}{8\bar{\rho}^2} = \frac{\langle \delta\rho(\mathbf{r},z)^2\rangle - \langle \delta\rho(\mathbf{r},z)\delta\rho(-\mathbf{r},z)\rangle}{4\bar{\rho}^2} \tag{6.14}$$

$$\frac{1}{2}\left\langle [\theta(\mathbf{r},z)-\theta(-\mathbf{r},z)]^2 \right\rangle = \left\langle \theta(\mathbf{r},z)^2 \right\rangle - \langle \theta(\mathbf{r},z)\theta(-\mathbf{r},z)\rangle \tag{6.15}$$

In each of these equations the two variance terms are equal: ($\langle \delta\rho(\mathbf{r},z)^2\rangle = \langle \delta\rho(-\mathbf{r},z)^2\rangle$ and $\langle \theta(\mathbf{r},z)^2\rangle = \langle \theta(-\mathbf{r},z)^2\rangle$), because of the radial background density symmetry in the inhomogeneous case and because of the spatial invariance in the homogeneous case.

Conclusion: in this section, this chapter's main observable, the spatial coherence, was introduced and reexpressed in terms of the fluid of light's density and phase fluctuations. Within the assumption of uncorrelated density and phase fluctuations, as well as up to the 2-nd order in these quantities, it is shown, that the spatial coherence depends on the variance and the 2-point correlations of both density and phase fluctuations.

6.3.3 Coherence within the Bogoliubov approximation

6.3.3.1 The link with prethermal states

Before showing the derivation of the results, it is important to mention, that here we derive the coherence of an interaction quenched fluid of light possessing weak fluctuations. Using this approximation, we shall use the Bogoliubov approach and find out a result very similar to that for the 2D equilibrium superfluids. This result will be shown accurate at short times, confirming the fluid's fast relaxation towards the state described by this analytical theory. Nonetheless, being obtained within the "quadratic Hamiltonian" approximation, the result appears less accu-

rate at long times, where the Bogoliubov quasi-particles start interacting [12, 13]. This results in a slow deviation of the fluid's coherence from the Bogoliubov theory, which is precisely the signature of the onset of prethermal states, which can be viewed as metastable states during the system's relaxation towards equilibrium.

6.3.3.2 Evolution

Evolution equations: In this section the coherence function, defined in the eqn. 6.7, is calculated analytically [12] in the case of a background fluid disturbed by weak fluctuations. The total field evolves according to the NLSE and can be written with hydrodynamic variables:

$$i\partial_z \mathcal{E}(\mathbf{r},z) = \left[-\frac{1}{2k}\nabla_\perp^2 + g|\mathcal{E}(\mathbf{r},z)|^2 - \frac{i\alpha}{2}\right]\mathcal{E}(\mathbf{r},z) \tag{6.16}$$

Exactly in the same way as shown in section 4.3.1, we can first write the evolution equations for total density and phase, then rewrite them for the slowly varying background and fast fluctuations, using: $\mathcal{E}(\mathbf{r},z) = \sqrt{\bar{\rho}(\mathbf{r},z) + \delta\rho(\mathbf{r},z)}\mathrm{e}^{i\phi_0(\rho_0)z + i\theta(\mathbf{r},z)}$. In this way one applies the local density approximation, assuming the in-homogeneous background with fluctuations developing on top of it and following its relatively slow spatial dependence parametrically. For simplicity, here we assume the background fluid at rest ($\mathbf{v}_0 = 0$). Then the background variables evolve as given by the eqns 4.12 and 4.13, supposing the decay of density due to the absorption $\bar{\rho}(\mathbf{r},z) \simeq \bar{\rho}(\mathbf{r},0)\exp(-\alpha z)$, and the phase given by: $\phi_0(\mathbf{r},z) = -g\langle\bar{\rho}\rangle_z z$, with $\langle\bar{\rho}(\mathbf{r},z)\rangle_z$ the time z averaged background density.

Evolution of fluctuations: Still in the regime where $\varepsilon \ll 1$ the fluctuations follow the linearized hydrodynamic eqns:

$$\frac{\partial\delta\rho}{\partial z} + \alpha\delta\rho = -\bar{\rho}\nabla_\perp.\frac{\mathbf{v}}{c} \tag{6.17}$$

$$\frac{\partial\delta\mathbf{v}}{\partial z} = -\nabla_\perp\left(\frac{cg\bar{\rho}}{k} - \frac{c}{4k^2}\nabla_\perp^2\right)\frac{\delta\rho}{\bar{\rho}} \tag{6.18}$$

In this regime one can use again the results derived in the section 4.3.1 within the Bogoliubov theory: with $\mathbf{v}_0 = 0$ the eqns 4.20 become:

$$\begin{pmatrix} -\Omega(z) & \frac{\mathbf{q}^2}{k} \\ \left(g\bar{\rho}(z) + \frac{\mathbf{q}^2}{4k}\right) & -\Omega(z) \end{pmatrix}\begin{pmatrix} f_+ \\ f_- \end{pmatrix} = 0 \tag{6.19}$$

Giving the Bogoliubov dispersion relation, that I now rewrite as function of the kinetic energy $K_{kin} = \mathbf{q}^2/2k$:

$$\Omega(\mathbf{q},z) = \sqrt{K_{kin}(\mathbf{q})\left(2g\bar{\rho}(z) + K_{kin}(\mathbf{q})\right)} \tag{6.20}$$

For the solutions given in eqns 4.18 and 4.19. Replacing $a_\mathbf{q} f_\pm(\mathbf{q})$ by $b_\pm(\mathbf{q})$, and using first eqn of 6.19 ($b_-(\mathbf{q}) = \frac{\Omega}{K_{kin}} b_+(\mathbf{q})$), one can reexpress the eqns 4.18 and 4.19 in a simpler form with

the only coefficient $b_+(\mathbf{q})$ which is now called $b(\mathbf{q})$:

$$\delta\rho(\mathbf{r},z) = \sqrt{\rho_0(0)}\mathrm{e}^{-\alpha z}\int \frac{d^2\mathbf{q}}{(2\pi)^2}\left(b(\mathbf{q})\mathrm{e}^{i(\mathbf{q}\mathbf{r}-\langle\Omega\rangle_z z)} + b^*(\mathbf{q})\mathrm{e}^{-i(\mathbf{q}\mathbf{r}-\langle\Omega\rangle_z z)}\right) \tag{6.21}$$

$$\theta(\mathbf{r},z) = \frac{1}{2i\sqrt{\rho_0(0)}}\int \frac{d^2\mathbf{q}}{(2\pi)^2}\frac{\Omega(\mathbf{q},z)}{K_{kin}(\mathbf{q})}\left(b(\mathbf{q})\mathrm{e}^{i(\mathbf{q}\mathbf{r}-\langle\Omega\rangle_z z)} - b^*(\mathbf{q})\mathrm{e}^{-i(\mathbf{q}\mathbf{r}-\langle\Omega\rangle_z z)}\right) \tag{6.22}$$

Matching initial conditions: The coefficient $b(\mathbf{q})$ depends on the initial distribution of field fluctuations:

$$\delta\rho(\mathbf{q},0) = \sqrt{\rho_0(0)}\left(b(\mathbf{q}) + b^*(-\mathbf{q})\right) \simeq 2\varepsilon\rho_0(0)\delta\psi_r(\mathbf{q}) \tag{6.23}$$

$$\theta(\mathbf{q},0) = \frac{\Omega/K_{kin}}{2i\sqrt{\rho_0(0)}}\left(b(\mathbf{q}) - b^*(-\mathbf{q})\right) \simeq \varepsilon\delta\psi_i(\mathbf{q}) \tag{6.24}$$

Where $\psi_{r,i}(\mathbf{q})$ is the Fourier transform of $\psi_{r,i}(\mathbf{r})$ and $b_\pm(-\mathbf{q})$ was introduced by making a variable substitution $\mathbf{q}" = -\mathbf{q}'$ in the b^* terms of the eqns 6.21 and 6.22, in order to express both terms as a single Fourier transformation. Inverting the eqns 6.23 and 6.24, one gets $b(\mathbf{q})$ for each disorder configuration, given by:

$$b(\mathbf{q}) = \varepsilon\sqrt{\rho_0(0)}\left(\delta\psi_r(\mathbf{q}) + i\frac{K_{kin}}{\Omega}\delta\psi_i(\mathbf{q})\right) \tag{6.25}$$

$$b^*(-\mathbf{q}) = \varepsilon\sqrt{\rho_0(0)}\left(\delta\psi_r(\mathbf{q}) - i\frac{K_{kin}}{\Omega}\delta\psi_i(\mathbf{q})\right) \tag{6.26}$$

6.3.3.3 Coherence calculation of a weakly disturbed quenched fluid

2-point density/phase correlations: first stage: Now that the expressions for the density/phase fluctuations are obtained (eqns: 6.25,6.26 and 6.21,6.22), one can calculate the building blocs of the coherence function, namely the two-point density and phase correlations. For this, one needs to insert the eqns 6.21 and 6.22 into the eqns 6.14, 6.15 and perform the disorder averaging:

$$\frac{\langle\delta\rho(\mathbf{r},z)\delta\rho(\mathbf{r}+\Delta\mathbf{r},z)\rangle}{\rho_0^2} =$$

$$2\varepsilon^2\int\frac{\mathrm{d}^2\mathbf{q}\mathrm{d}^2\mathbf{q}'}{(2\pi)^4\rho_0}\mathrm{Re}\left\{\langle b(\mathbf{q})b(\mathbf{q}')\rangle\mathrm{e}^{i(\mathbf{q}+\mathbf{q}')\mathbf{r}+i\mathbf{q}'\Delta\mathbf{r}-i(\langle\Omega\rangle_z+\langle\Omega'\rangle_z)z} + \langle b(\mathbf{q})b^*(\mathbf{q}')\rangle\mathrm{e}^{i(\mathbf{q}-\mathbf{q}')\mathbf{r}-i\mathbf{q}'\Delta\mathbf{r}-i(\langle\Omega\rangle_z-\langle\Omega'\rangle_z)z}\right\} \tag{6.27}$$

$$\langle\theta(\mathbf{r},z)\theta(\mathbf{r}+\Delta\mathbf{r},z)\rangle =$$

$$\frac{\varepsilon^2}{2}\int\frac{\mathrm{d}^2\mathbf{q}\mathrm{d}^2\mathbf{q}'}{(2\pi)^4\rho_0}\frac{\Omega^2}{K_{kin}^2}\mathrm{Re}\left\{\langle b(\mathbf{q})b^*(\mathbf{q}')\rangle\mathrm{e}^{i(\mathbf{q}-\mathbf{q}')\mathbf{r}-i\mathbf{q}'\Delta\mathbf{r}-i(\langle\Omega\rangle_z-\langle\Omega'\rangle_z)z} - \langle b(\mathbf{q})b(\mathbf{q}')\rangle\mathrm{e}^{i(\mathbf{q}+\mathbf{q}')\mathbf{r}+i\mathbf{q}'\Delta\mathbf{r}-i(\langle\Omega\rangle_z+\langle\Omega'\rangle_z)z}\right\} \tag{6.28}$$

In these eqns we re-introduced the two-point position difference $\Delta\mathbf{r}$, which is equal to $2|\mathbf{r}|$.
Quasi-particle correlations: Since only the coefficient $b(\mathbf{q})$ depends on each disorder configu-

ration, the ensemble averaging reveals in all cases the following correlations: $\langle b(\mathbf{q})b(\mathbf{q}')\rangle$ and $\langle b(\mathbf{q})b^*(\mathbf{q}')\rangle$, which can be worked out knowing the statistical properties of the input fluctuations. Using the eqn. 6.25 one gets:

$$\frac{\langle b(\mathbf{q})b(\mathbf{q}')\rangle}{\varepsilon^2\rho_0} = \langle\psi_r(\mathbf{q})\psi_r(\mathbf{q}')\rangle - \frac{K_{kin}}{\Omega}\frac{K'_{kin}}{\Omega'}\langle\psi_i(\mathbf{q})\psi_i(\mathbf{q}')\rangle + \frac{K'_{kin}}{\Omega'}\langle\psi_r(\mathbf{q})\psi_i(\mathbf{q}')\rangle + \frac{K_{kin}}{\Omega}\langle\psi_r(\mathbf{q}')\psi_i(\mathbf{q})\rangle \tag{6.29}$$

$$\frac{\langle b(\mathbf{q})b^*(\mathbf{q}')\rangle}{\varepsilon^2\rho_0} = \langle\psi_r(\mathbf{q})\psi^*_r(\mathbf{q}')\rangle + \frac{K_{kin}}{\Omega}\frac{K'_{kin}}{\Omega'}\langle\psi_i(\mathbf{q})\psi^*_i(\mathbf{q}')\rangle - \frac{K'_{kin}}{\Omega'}\langle\psi_r(\mathbf{q})\psi^*_i(\mathbf{q}')\rangle - \frac{K_{kin}}{\Omega}\langle\psi^*_r(\mathbf{q}')\psi_i(\mathbf{q})\rangle \tag{6.30}$$

I decided to show this simple but lengthy intermediate result to highlight that the "quasi-particle" correlations generally depend on both the auto- and cross-correlations of the input fluctuations' real and imaginary parts. But since we assume here the uncorrelated and identically distributed real and imaginary part of the input fluctuations (this holds in both real and Fourier spaces), one can safely neglect the cross terms $\langle\psi_r(\mathbf{q})\psi_i(\mathbf{q}')\rangle$, while the auto-correlations are expressed using the eqn. 6.3 and the fact that $\psi_{r/i} \in \mathbb{R}$ are real functions: $\langle\psi_{r/i}(\mathbf{q})\psi_{r/i}(\mathbf{q}')\rangle = (2\pi)^2\delta(\mathbf{q}+\mathbf{q}')\gamma(\mathbf{q})/2$ and $\langle\psi_{r/i}(\mathbf{q})\psi^*_{r/i}(\mathbf{q}')\rangle = (2\pi)^2\delta(\mathbf{q}-\mathbf{q}')\gamma(\mathbf{q})/2$. Applying these results one gets:

$$\langle b(\mathbf{q})b(\mathbf{q}')\rangle = \varepsilon^2\rho_0\frac{(2\pi)^2}{2}\delta(\mathbf{q}+\mathbf{q}')\gamma(\mathbf{q})\left(1-\frac{K^2_{kin}}{\Omega^2}\right) \tag{6.31}$$

$$\langle b(\mathbf{q})b^*(\mathbf{q}')\rangle = \varepsilon^2\rho_0\frac{(2\pi)^2}{2}\delta(\mathbf{q}-\mathbf{q}')\gamma(\mathbf{q})\left(1+\frac{K^2_{kin}}{\Omega^2}\right) \tag{6.32}$$

2-point density/phase correlations: final result: Using the expressions of the quasi-particle correlations after several steps reported in details in C.1 (in order to simplify the main text), one gets the final results for the density/phase correlations:

$$\frac{\langle\delta\rho(\mathbf{r},z)\delta\rho(\mathbf{r}+\Delta\mathbf{r},z)\rangle}{\bar{\rho}^2} \underset{\varepsilon\ll 1}{\simeq} 2\varepsilon^2\int\frac{\mathrm{d}^2\mathbf{q}}{(2\pi)^2}\gamma(\mathbf{q})\left(1+\left[\frac{K^2_{kin}}{\Omega^2}-1\right]\sin^2(\Omega z)\right)\cos(\mathbf{q}\Delta\mathbf{r}) \tag{6.33}$$

$$\langle\theta(\mathbf{r},z)\theta(\mathbf{r}+\Delta\mathbf{r},z)\rangle = \frac{\varepsilon^2}{2}\int\frac{\mathrm{d}^2\mathbf{q}}{(2\pi)^2}\gamma(\mathbf{q})\left(1+\left[\frac{\Omega^2}{K^2_{kin}}-1\right]\sin^2(\Omega z)\right)\cos(\mathbf{q}\Delta\mathbf{r}) \tag{6.34}$$

Note that the density/phase variances can be obtained from these equations by simply setting $\Delta\mathbf{r} = 0$. The coherence function then becomes:

$$g^{(1)}(\mathbf{r},-\mathbf{r},z) = \rho_0(1+\varepsilon^2).\exp\left(-\varepsilon^2\int\frac{\mathrm{d}^2\mathbf{q}}{(2\pi)^2}\gamma(\mathbf{q})\left(1-\cos(\mathbf{q}\Delta\mathbf{r})\right)\left[1+\frac{2(g\bar{\rho})^2}{\Omega^2}\sin^2(\Omega z)\right]\right) \tag{6.35}$$

6.3.3.4 Simplification: polar coordinates

Coherence function result in polar coordinates: In order to simplify the previous result (eqn. 6.35) we just need to replace the the fluctuation correlation spectrum $\gamma(\mathbf{q})$ and Bo-

goliubov dispersion relation $\Omega(\mathbf{q})$ by their known expressions (see eqns 6.20 and 6.2). I recall them here by writing the latter in the normalized form and insisting on the Gaussian fluctuation statistics assumption:

$$\Omega(\mathbf{q},z) = 2(g\rho_0)q\xi\sqrt{1+(q\xi)^2} = 2g\rho_0\tilde{\Omega}(\mathbf{q},z) \quad \text{with: } q = |\mathbf{q}| \tag{6.36}$$

$$\gamma(\Delta\mathbf{r}) = \exp\left(-\frac{\Delta r^2}{4\sigma^2}\right), \quad \text{implying:} \quad \gamma(\mathbf{q}) = 4\pi\sigma^2 \mathrm{e}^{-\sigma^2 q^2} \tag{6.37}$$

Then the $g^{(1)}$ can be rewritten using a variable substitution: $u = q\sigma$ and $\phi_0 = g\rho_0 z$:

$$g^{(1)}(\Delta\mathbf{r},\tau) = \bar{\rho}.\exp\left(-2\varepsilon^2\int_0^\infty u\mathrm{d}u\mathrm{e}^{-u^2}\left[1-J_0\left(u\frac{\Delta r}{\sigma}\right)\right]\left[1+\frac{\sin^2\left(2\tilde{\Omega}(u)\Phi_0(z)\right)}{2\tilde{\Omega}(u)^2}\right]\right) \tag{6.38}$$

$$\text{with: } \tilde{\Omega}(u) = \frac{u\xi}{\sigma}\sqrt{1+\frac{u^2\xi^2}{\sigma^2}} \tag{6.39}$$

The only polar angle ϕ dependent contribution, stemming from: $\mathbf{q}.\Delta\mathbf{r} = q.\Delta r.\cos(\phi)$ results in the J_0 Bessel function upon angular integration, using the identity:

$$J_n(x) = \frac{1}{2\pi}\int_{-\pi}^{+\pi} \mathrm{e}^{-i(n\phi - x.\sin(\phi))}d\phi \tag{6.40}$$

Conclusion and comment on the LDA: The eqn. 6.38 is the final result of the analytical derivation of the spatial coherence of a weakly interacting Bose gas. Its further calculation requires a numerical integration over rescaled momentum u and can be easily performed using the trapezes method and numerically truncating the integral between $u = 0.01$ and $u = 10$, while sampling the grid with at least 1000 points. The result presented here is a slight generalization of the result presented in [13] to the case of a non-uniform background, more suitable to the description of the experimental results shown in this chapter. In fact, I assumed the initial state of the background beam to have a Gaussian shape ($\rho_0(\mathbf{r}) = \rho_0(0)\exp(-2r^2/\omega_0^2)$). This has two main consequences on the $g^{(1)}$ function: the most obvious one stems from the total average density ρ which appears as the multiplication factor in eqn. 6.38 and due to its finite size imposes the maximal size of the available measurement range of the $g^{(1)}$ function. The second consequence is the local dependence of the fluid's density dependent variables ξ and Φ_0 which appear as parameters in the integral of the eqn. 6.38. The obtained expression takes identical form to the one reported in [13] but with parameters which are not constant in space and time, and the key idea behind the LDA consists in saying that the variation of the $g^{(1)}$ due to the local variation of the density can be calculated by simply evaluating the eqn. 6.38 with the fluid's local total density value.

6.3.4 Characteristic scaling and physical interpretation

Fig 6.1: The fastest way to get a physical understanding of the derived result eqn. 6.38 is to plot it for various input parameters. For this reason, the fig. 6.1 shows theoretical plots of coherence

function based on the eqn. 6.38 and highlighting its features, which are then described in details below.

6.3.4.1 Quasi-particle light cone

Control parameters: As can be seen from the eqn. 6.38, the coherence function depends on $\Delta r/\sigma$, the relative position difference re-scaled by the input fluctuation correlation length σ via the Bessel function term. It also depends on the interactions via the sin term containing the healing length ξ, which is also rescaled wrt fluctuation correlation length σ, and the non-linear phase ϕ_0 accumulated by the background. The latter parameter linearly depends on the "time" z indicating that the temporal evolution of spatial coherence is governed by the sin term.
Fig 6.1 a) Light cone spreading, homogeneous background case: In order to follow the space-time dynamics of the $g^{(1)}$, Fig 6.1 a) shows a colorplot of the coherence normalized by the fluid's central density, as function of the time and space, for the homogeneous background (for simplicity and better visibility) having interactions of magnitude $g\rho_0 = 4$ mm^{-1} and small ($\varepsilon = 1\%$) $\sigma = 25$ μm correlated fluctuations on top of it. One can remark that as the time evolves, the coherence decays in a uniform way for large displacements. One can also notice at small displacements an area of slower decay, which seems to linearly increase with time z. In fact, deep in the phononic regime of the Bogoliubov dispersion, i.e. $\xi/\sigma \ll 1$, the argument of the sin term can be rewritten in terms of the background's speed of sound:

$$2\tilde{\Omega}(u)\phi_0(z) \simeq 2\phi_0(z)\frac{u\xi}{\sigma} = q \cdot (2c_s z) = qL_c(z) \tag{6.41}$$

This result reveals an important length scale L_c, called the Lieb-Robinson bound, of the light-cone of the Bogoliubov quasiparticles. Plotting $L(z)$ on top of the colorplot fig. 6.1 a), one recognizes the frontier of the slower decaying central area $\Delta r < L_c(z)$ and the uniformly decaying large displacement $\Delta r > L_c(z)$ area. This frontier corresponds physically to the maximal distance between a pair of two oppositely moving low-momentum Bogoliubov phonons after a time z of evolution.

6.3.4.2 Algebraic decay within the light cone

Fig 6.1 b): Spatial coherence profiles with a Gaussian background at different propagation "times" z: In order to visualize how the coherence decays within the Bogoliubov quasi-particle light-cone, the Fig 6.1 b) shows spatial coherence profiles at different propagation "times" z, calculated with same parameters as in fig 6.1 a) except the background fluid's shape which is this time a Gaussian of waist $\omega_0 = 2$ mm ($\rho_0(\mathbf{r}) = \rho_0(0).\exp(-2r^2/\omega_0^2)$). The most remarkable feature of the $g^{(1)}$ (from eqn. 6.38) calculated in a 2D space, is the emergence of an algebraic decay. Although not directly apparent from the eqn. 6.38 the coherence develops several different regimes in its spatio-temporal dependence. For instance, at short times, when the sin term

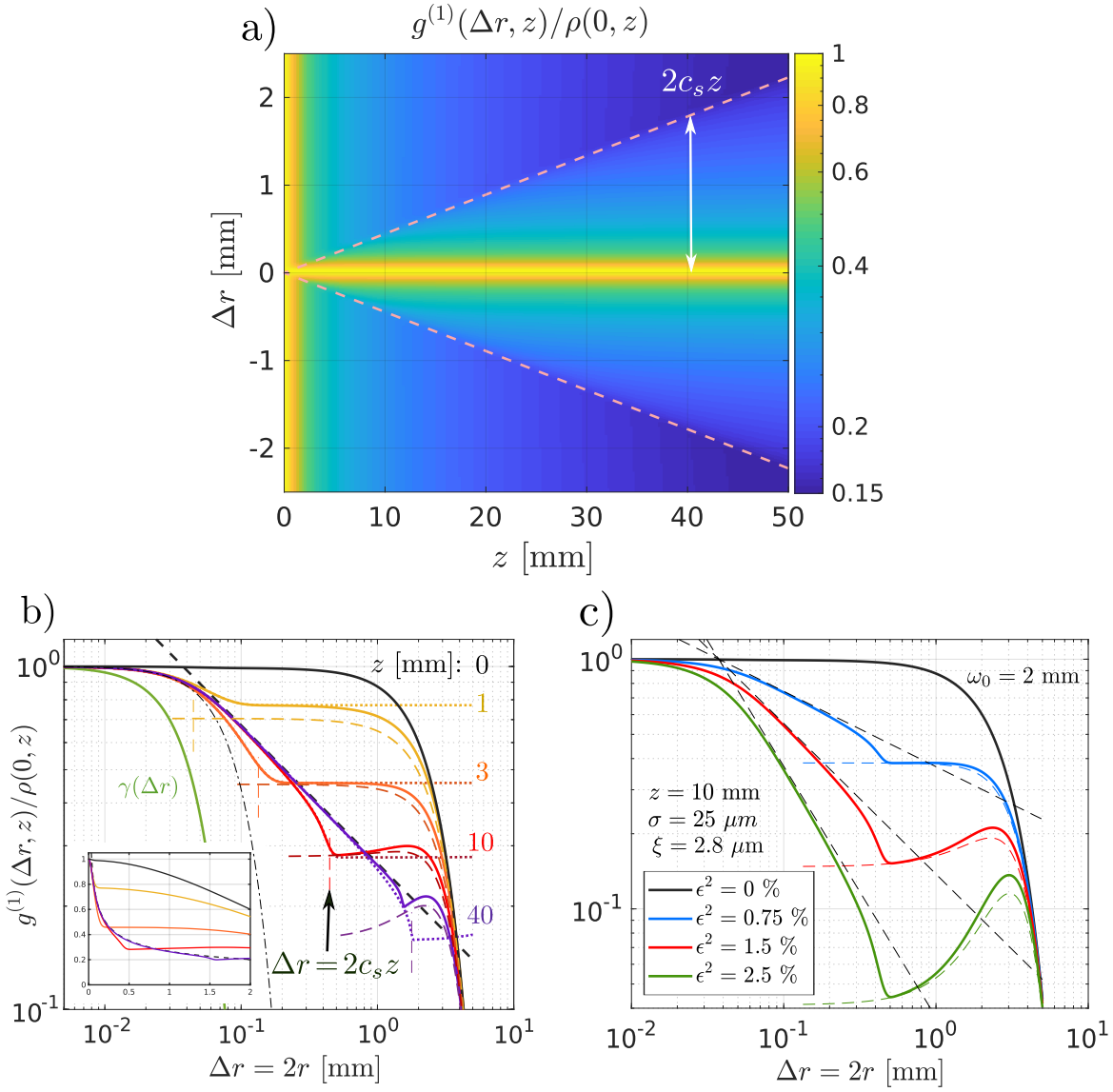

Figure 6.1: Theoretical result for the spatial coherence, calculated with eqn. 6.38. a) shows the normalized $g^{(1)}(\Delta r, z)$ plotted with a log scale colormap versus "time" z and displacement Δr for the case of an uniform background with small $\varepsilon^2 = 1\%$ fluctuations. b) shows the normalized $g^{(1)}(\Delta r)$ profiles at different propagation "times" z in log-log scale, calculated with same parameters as in a) except the Gaussian background shape. The dotted curves show the result with a uniform (plane wave) background. The black dashed line is the power law calculated with the eqn. 6.44, the colored dashed horizontal & vertical lines show the calculated light cone position $L(z)$ (eqn. 6.41) and the plateau from eqn. 6.45 corresponding to the $g^{(1)}$ curves of same color. The inset shows same $g^{(1)}$ curves in the linear scale. The solid green curve is the fluctuation correlation function $\gamma(\Delta r)$ (eqn. 6.37) and the dash-dotted line is the Gaussian approximation for small times and displacements (eqn. 6.43). c) shows the normalized $g^{(1)}$ with a Gaussian background at fixed time $z = 10$ mm for different initial fluctuation fractions ε. Black dashed lines show the corresponding power law approximations using eqn. 6.44, the colored dashed lines show the plateau calculated with eqn. 6.45 within the LDA. In all subfigures the interaction strength was set to $g\rho_0 = 4$ mm^{-1} and the fluctuation correlation length to: $\sigma = 25$ μm. The Gaussian background shape in b) and c) is defined as: $\rho_0(\mathbf{r}) = \rho_0(0).\exp(-2r^2/\omega_0^2)$ with waist $\omega_0 = 2$ mm.

is negligibly small, the equation 6.38 gives simply:

$$g^{(1)}(\Delta\mathbf{r}, g\rho_0 z \ll 1) = \rho_0 \left(1 + \varepsilon^2 \gamma(\Delta\mathbf{r})\right) = \rho_0 \left[1 + \varepsilon^2 \exp\left(-\frac{\Delta\mathbf{r}^2}{4\sigma^2}\right)\right] \tag{6.42}$$

At reasonably small times or more precisely in the regime $g\rho_0 z \sim 1$, the argument of the sin term is still small and the former can be linearized, resulting in the coherence function which still decays as a Gaussian but within a spatial scale not anymore depending on σ:

$$g^{(1)}(\Delta\mathbf{r} \sim \sigma, g\rho_0 z \sim 1) \simeq \rho_0(1 + \varepsilon^2)\exp\left(-\frac{\varepsilon^2 \Delta r^2}{16\xi^2}\right) \tag{6.43}$$

This is shown with the dash-dotted line in Fig 6.1 b), which roughly captures the behavior of the coherence at small spatial scales. Finally, as the time z evolves more, as soon as and in presence of interactions, the coherence builds up an algebraically decaying tail developing until the relative displacement $L_c = 2c_s z$, linearly increasing in time:

$$g^{(1)}(\Delta r < 2c_s z) \simeq \rho_0(1 + \varepsilon^2)\mathrm{e}^{\frac{\eta}{2}\psi(\frac{1}{2})}\left(\frac{4\sigma}{\Delta r}\right)^{\eta} \quad \text{with:} \quad \eta = \frac{\varepsilon^2}{2}\frac{\sigma^2}{\xi^2} \tag{6.44}$$

Where $\Psi(1/2) \approx -1.96$ is the value of a mathematical function Ψ, linked to the Euler's di-Gamma function [12]. At first glance this behavior reminds of a disordered to quasi-ordered phase transition in a 2D system at thermal equilibrium where the emergence of the quasi-long range order is accompanied by a "slower" decay of the system's correlation function which starts decaying as a power-law rather than exponentially. In difference to the equilibrium systems in 2D, the fluid of light undergoes a non-equilibrium evolution during the beam's propagation, implying that the coherence function is not stationary (but depends on the "time"). This feature manifests itself in the fact that the algebraic decay develops first in the small displacement area of the coherence function and then reaches larger and larger displacements at a pace $2c_s z$ given by the Bogoliubov quasi-particle light-cone.

Exponent: Fig. 6.1 c) shows the normalized $g^{(1)}$ with a Gaussian background at fixed time $z = 10$ mm for different initial fluctuation fractions ε. The power-law approximations calculated with eqn. 6.44 using corresponding parameters, are shown in fig. 6.1 b) and c) as black dashed lines. In c) they show that the power-law exponent η increases with the fluctuation fraction as given by the eqn. 6.44. Note that the exponent also depends on the correlation length σ and the interaction strength via the healing length ξ. For example, curves similar to those shown in Fig 6.1 c) could have been shown by keeping constant ε and increasing σ, while variation of ξ would additionally influience the light cone position $L(z)$. The latter is shown as colored dashed vertical lines in fig 6.1 b), calculated using the eqn. 6.41 and corresponding to the $g^{(1)}$ curves of same color.

6.3.4.3 Reminiscent coherent plateau beyond the light cone

Beyond the light-cone there is no algebraic decay and the coherence simply follows the prefactor density profile, shifted vertically due to the algebraic decay until the light cone position. The corresponding approximated expression is given by [12, 13]:

$$g^{(1)}(\Delta r > 2c_s z) \simeq \rho_0(1+\varepsilon^2)\mathrm{e}^{\frac{\eta}{2}\psi(\frac{1}{2})}\left(\frac{\sigma}{c_s z}\right)^{\eta} \tag{6.45}$$

It is simply given by the density profile multiplied by the locally constant value equal to the initial power-law within the light cone, eqn. 6.44, but evaluated far beyond the light cone, at $\Delta r = 2L_c = 4c_s z$. This detail comes from the fact that the coherence starts to slightly deviate from the approximated power-law, eqn. 6.44 by decreasing faster just before the light cone. Interestingly, the discontinuity of slopes arising at the light cone position between the algebraic decay regime and the vertically rescaled background shape is already encoded in the expression 6.38.

Fig 6.1 c): Spatial coherence profiles with a Gaussian background at fixed propagation time but different speckle fractions ε**:** The colored dashed lines in fig 6.1 b) and c) show the plateau calculated with eqn. 6.45 within the LDA. Note that within the LDA the locally constant prefactor after the density in the eqn. 6.45 becomes space dependent due to the density dependence of the speed of sound c_s and the healing length ξ inside the exponent η. This effect is clearly seen in the plateaux shown in Fig 6.1 c) at hither exponent η values, and manifests itself with the plateau height increasing with displacement Δr due to the exponent's local variation with inhomogeneous background density $\eta(\rho_0)$, before being dominated by the density profile appearing as prefactor in eqn. 6.45.

6.3.4.4 Validity limits

In this section we derived the spatial coherence of an interaction quenched fluid of light within the Bogoliubov approximation. This approach allows to obtain an analytical result for the coherence at different times, but what is the range of the validity of this theory? This question was addressed theoretically in [13, 12] by means of numerical simulations, compared to the theoretical result presented above. The comparison is nicely summarized on fig. IV.8 of the PhD thesis of Tamara Bardon-Brun [12]: it shows that the Bogoliubov theory describes accurately the coherence for short times, while at later times the deviation arises between theory and the numerical result. The deviation was explaied by the higher order non-linearities in the interaction Hamiltonian gaining in significance with the fluid's effective time. They can also be interpreted as the interaction between the Bogoliubov quasi-particles. This effect was taken into account by an additional phenomenological parameter, which was included into the model [12]. The question of exact modelling of the fluid's coherence at longer times is currently investigated theoretically in the group of Nicolas Cherroret. It is also important to mention that the Bogoliubov theory, being valid for weak perturbations, breaks down as ε increases, making the linearization of the perturbations not anymore valid.

6.4 Experiment

Necessary building blocks, outline: The experimental observation of the pre-thermalization in a fluid of light requires several building blocks: the preparation of an initial state, its evolution in presence of photon-photon interactions and finally the measurement of spatial coherence. In this section I describe first how to create a background beam with random fluctuations of controllable parameters, explaining in details the SLM created input state and its statistical properties, and switch then to the description of a Mach-Zehnder interferometric spatial coherence measurement apparatus, used to produce the results shown in this chapter, and finally I describe the used automatized data acquisition, as well as image processing techniques before switching to the presentation of the results in the next section.

6.4.1 SLM produced speckle

6.4.1.1 Different speckle production strategies

Fluctuations with specific statistics? Observation of pre-thermalization for a fluid of light, described by the model developed in the previous section, requires the possibility to generate an input state with well controlled statistical properties (obeying the conditions 6.2 and 6.3) of the fluctuations produced on top of a background. For instance, while deriving the coherence function, I assumed a fluctuation field with equal variance of its real and imaginary parts and no cross correlation between them.

How to customize speckle fluctuations? These conditions are, in fact, quite simple to implement with a speckle beam produced by propagation of a laser beam through a slab of scattering medium or a transparent material with rough surface, like for example, a layer of white scotch. With this choice different disorder configurations can be easily accessed by simply moving the scattering layer in the transverse plane, for example by mounting it on a rotating stage. In this case however, one needs to provide an appropriate imaging configuration in order to be able to control not only the average speckle grain size σ, but also the shape of the correlation function, which, under certain imaging conditions may be described by, for example, a Bessel [42] rather than Gaussian function. Experiments with scattering slab generated speckle fluctuations were performed during this work and are described in the Appendix D. Despite the reasonable simplicity and low cost of this strategy, it has two main inconveniences. Firstly, scattering of a laser beam through a diffuser induces inevitably significant laser power losses even for the weakly scattering slabs, due to the back-reflection from the slab and due to polarization mixing (typically 50% of the transmitted power has cross polarization with respect to the background's polarization). Secondly, the speckle grain size control through the variation of the illuminated area on a scattering slab strongly affects the beam divergence of the speckle beam while it is recombined with a strong background at the cell entrance.

Speckle with SLM: An alternative strategy to produce speckle fluctuations was used in the experiments presented in this chapter. It consists in printing with an SLM a pixel table of random phases on the background beam and let it evolve a certain distance in free space. The

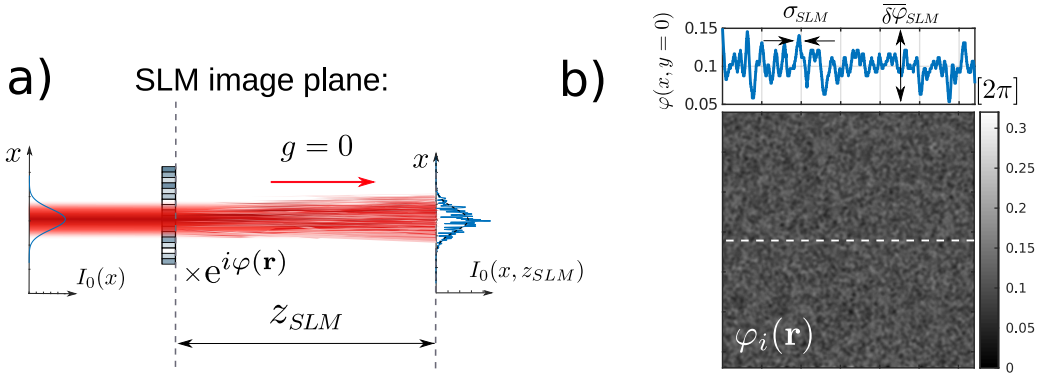

Figure 6.2: SLM produced speckle: figure a) shows the experimental configuration, in which an initially collimated Gaussian beam is phase modulated by an SLM with an example of phase a mask shown in b) (note that in real experiment the SLM was used in reflection), and propagates by a distance z_{SLM} after the SLM plane. Diffraction of the SLM induced phase fluctuations enables mixing of the phase and intensity fluctuations.

free space propagation after the SLM plane is crucial for the phase fluctuations to diffract and give rise/ mix with the density fluctuations, realizing this way the required characteristics for the input fluctuations. Different disorder configurations can now be realized by printing new random patterns on the SLM. For instance, imposing Gaussian statistics for the imprinted SLM pixel values enables Gaussian statistics for the phase fluctuations. On the other hand, one can already intuitively guess that adding a finite correlation length for the neighbouring pixel values, it is possible to increase the speckle correlation length σ, and by controlling the variance of the SLM pixel values $\overline{\delta\varphi}_{SLM}$, the resulting strength of the phase fluctuations will control the speckle intensity fraction ε. The phase modulation by the SLM does not alter the beam's polarization and is equivalent to a reflecting surface with a well controllable variable roughness, thus reducing the loss of power. It should be however remarked, that it is not obvious to separate the SLM produced speckle from the background, since the fluctuations are imprinted on the background itself and take the density from the latter.

Figure SLM speckle scheme: The figure 6.2 a) shows a typical experimental configuration of the generation of an input state consisting of a background with controllable speckle fluctuations. Figure 6.2 b) shows a typical phase mask (converted into a phase map) displayed on the SLM to produce phase fluctuations. It has a phase variance of the order of $0.1\times 2\pi$ and a correlation length of several pixels. It is useful to investigate how the input fluctuation strength ε and correlation length σ depend on the background beam and SLM controlled parameters.

6.4.1.2 Properties of the SLM produced input state

Theoretical results: Given the experimental input parameters σ_{SLM} and $\overline{\delta\varphi}_{SLM}$ of the phase pattern displayed on the SLM as depicted in fig. 6.2 a), it is important to understand what happens to the field once it propagates over a distance of z_{SLM} between the SLM image plane and the vapor cell's input plane. In the performed experiment this distance equals to $z_{SLM} \simeq$

200 mm. For instance, two main questions I respond in this paragraph are: what is the total field's spatial correlation at the cell's input plane and do the fluctuation statistics fulfill the requirements (see eqn. 6.3) necessary for obtaining the result given in eqn. 6.38? Answering these questions requires calculating the propagation of the field which is assumed known at the SLM plane and given by:

$$\mathcal{E}(\mathbf{r}, z=0) = \mathcal{E}_0.\exp\left(-\frac{\mathbf{r}^2}{\omega_0^2}\right).\mathrm{e}^{i\varphi(\mathbf{r})} \tag{6.46}$$

over a certain distance z_{SLM} in free space after the SLM plane. Then the knowledge of the statistics of $\varphi(\mathbf{r})$ will allow to deduce the total field's statistical characteristics at this new plane. Assuming the paraxial approximation, the propagation is only governed by diffraction and is described by the eqn:

$$\left[i\partial_z + \frac{\Delta_{\mathbf{r}}}{2k_0}\right]\mathcal{E}(\mathbf{r}, z) = 0 \tag{6.47}$$

The calculation was done with help of Nicolas Cherroret and its detailed derivation is given in C.2. To keep discussion short, I give here only the main results necessary for the following discussion. The beam waist ω_0 is assumed large enough ($z/z_R \ll 1$ with $z_R = k_0\omega_0^2/2$) in order to neglect the variation of the average field's size, the additional phase due to the Gaussian beam's defocusing and the Gouy phase. This assumption is fulfilled in the performed experiments by working with a $\omega_0 = 1.8$ mm large beam. With this assumption the field at cell entrance reads:

$$\mathcal{E}(\mathbf{r}, z=z_{SLM}) = \frac{\mathcal{E}_0}{\sqrt{1+\varepsilon^2}}\left[\exp\left(-\frac{\mathbf{r}^2}{\omega_0^2}\right) + \varepsilon\delta\mathcal{E}(\mathbf{r}, z_{SLM})\right] \tag{6.48}$$

The normalization by $\sqrt{1+\varepsilon^2}$ is required to take into account the fact that the total laser power (controlling the density ρ_0) is fixed and the fluctuation strength ε is increased at the expense of reducing the background power. Indeed this configuration is specific to the SLM generated fluctuation case in which the phase fluctuations are directly "imprinted" on the Gaussian background. This gives the following coherence at the cell input:

$$g^{(1)}(\mathbf{r}, -\mathbf{r}, 0) = \tfrac{\rho_0}{1+\varepsilon^2}.\left[\exp\left(-\tfrac{\Delta\mathbf{r}^2}{2\omega_0^2}\right) + \varepsilon^2\exp\left(-\tfrac{\Delta\mathbf{r}^2}{4\sigma'^2}\right)\right] \tag{6.49}$$

$$\text{with:}\quad \varepsilon^2 \propto \overline{\delta\varphi}^2, \quad \sigma' \propto z_{SLM} \tag{6.50}$$

In this result the typical speckle grain size $\sigma' \ll \omega_0$ is supposed to be much smaller than the beam size ω_0. This condition is realizable for sufficiently small SLM pixel size. For instance, in the experiment, the SLM (with 12.5 μm pixel size) was imaged with a de-magnifying telescope of ratio $\times 0.5$ making the effective pixel size equal to 6.25 μm which is largely sufficient to achieve $\sigma' \ll \omega_0$.

Normalization of the $g^{(1)}$***:*** Note that with the $1/\sqrt{1+\varepsilon^2}$ normalization of the field, the $g^{(1)}(\Delta r = 0) = \rho_0$, which is a convenient definition for comparison with the experimental data in which the fringe contrast, proportional to the $g^{(1)}$, can simply be normalized by its value at zero displacement $\Delta r = 0$. In order to take into account this normalization in the

previously derived results, one simply needs to replace $\rho_0(1+\varepsilon^2)$ by ρ_0.
Simu result: Moreover, numerical simulation of the field's free space propagation after SLM induced phase modulation (as shown schematically in fig. 6.2 a)) was performed and the corresponding results are shown in C.2. The numerical simulation showed that the fluctuation field's real and imaginary part mix quite fast during the propagation after the SLM plane. In particular, the fluctuation field's real and imaginary parts (or the intensity and phase fluctuation respectively) have equal variances after several cm of propagation after SLM. Moreover, the numerical experiment showed (fig. C.1) that the real-imaginary part's cross-correation is not zero but very small (typically ε^2 % with respect to the fluctuation field's strength ε^2).
Conclusion: This allows to conclude that speckle production on top of a Gaussian background implemented in this work with phase only modulation by an SLM placed at the $z_{SLM} \simeq 200$ mm distance before the vapor cell input generates an initial state which has suitable statistics for the observation of pre-thermalization of light via its spatial coherence (eqn. 6.38).

6.4.2 Imaging and auto-correlation

How to measure the final state's $g^{(1)}$***?*** The input state created by the SLM evolves in the hot vapor cell mediating the photon-photon interactions. In order to measure the fluid's spatial coherence at the final state of evolution, one needs to image the cell's output plane with a camera. This is done with help of two imaging lenses in 4f configuration magnifying the image by factor of $\times 2.46 \pm 0.05$. However, accessing the coherence function requires superimposing the field with itself at a given relative displacement. This is the reason why the beam is split and then recombined with 50:50 beam splitters within a Mach-Zehnder interferometer between the cell output and the camera planes.
Superimposing a beam with itself but flipped: As explained in the model derivation, the optimal choice for two point correlation with a radially symmetric background is the correlation of pairs of points symmetric with respect to the beam centre. By doing so, it is possible to access all relative displacements with a single frame, in which the central position corresponds to the zero relative displacement and the latter continuously increases as one moves away from beam center. All the points sharing same radius r with respect to the beam center, correspond hence to the two-point relative displacement equal to $2r$. Experimental implementation of this condition requires flipping the images of the two arms oppositely with respect to each other.
Dove prisms for flipping the beam: This is the role of the Dove prisms placed on rotating mounts at each interferometer arm (see fig. 6.3 a)). Dove prism is a trapezoidally shaped prism which flips the image wrt a symmetry direction in the transverse plane, the latter depending on the prism's orientation angle around the optical axis. Putting the prism's largest side horizontally at the one arm and vertically at the other arm, one ends up after recombination with a superposition of respectively vertically $(x, y) \to (x, -y)$ and horizontally $(x, y) \to (-x, y)$ flipped fields with respect to the field before the interferometer. In order to continuously fine-tune the relative angle between the prism flipped images, at least one of the prisms is mounted on a rotating mount (Thorlabs PS992M prisms used in this work).

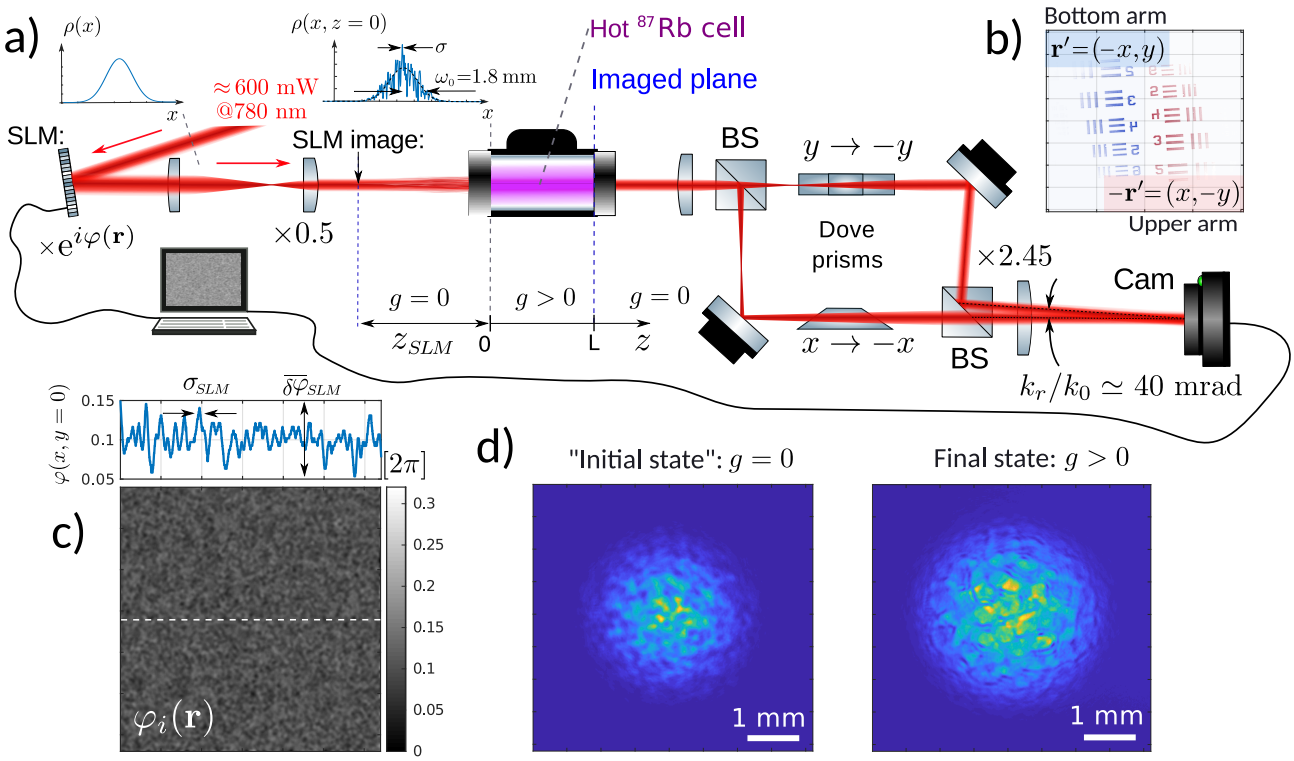

Figure 6.3: Experimental setup of the spatial coherence measurement: a) shows a schematic visualization of the experimental setup. A collimated Gaussian beam of waist 3.6 mm is phase modulated by an SLM which acts as a reflecting surface with controllable roughness. The SLM image is then 2-fold demagnified with a 4f telescope and allowed to propagate in free space over a distance $z_{SLM} \simeq 200$ mm before reaching the cell input. The resulting initial state then evolves in a $L = 10$ mm long ^{87}Rb vapor cell heated to 150 °C. The laser detuning is chosen to give 50 % power transmission at $P = 560$ mW input power (and beam waist $\omega_0 = 1.8$ mm). The cell's exit plane is imaged with a $\times 2.46$ magnifying 4f telescope on a camera via two paths interfering in a balanced Mach-Zehnder configuration and perfectly overlapping at the camera plane. The images of both arms are inverted with respect to each other with help of the two Dove prisms each put on a different beam path in perpendicular configuration: the one inverts the image horizontally (the bottom one on the scheme) and the other vertically (the upper one on the scheme). b) shows the image of a USAF 1951 target image coming from both interference arms (distinguished by the image colormap): if both arms are well aligned, the blue image is the perfect opposite of the red one with respect to the camera centre. c) shows an example a phase pattern displayed on the SLM, the phase profile above corresponds to the horizontal dashed white line at the centre of the phase pattern. It defines the disorder control parameters: the pattern's Gaussian correlation length σ_{SLM} controlling the fluctuation correlation length and the phase variance which controls the fluctuation strength ε. d) shows typical intensity images of the cell exit plane coming from the one of the amrs in the absence (left) and in presence (right) of photon-photon interactions.

Alignment procedure: However, proper matching of the opposite positions coming from the two arms at the camera plane requires accurate alignment. This was done in two steps: first the Gaussian beam of any arm (called reference arm) is centered on the imaging camera. Then a USAF1951 target is placed at the imaged plane before the interferometer, giving via the two arms its two superimposed images which are almost inverted with respect to each other. The second arm's path is then adjusted with respect to the reference one: its position via a mirror acting only on the second arm and its orientation via the Dove prism's angle on the rotating mount. The goal is to align the second arm's beam with respect to the reference arm until its image appears as symmetrically opposite of the reference arm's image with respect to camera's central pixel (1024,1024). In practice this condition is equivalent to checking that a given point of the USAF target (say the edge of any line-pair) appears on its image from both arms at the same distance and opposite angles to the camera center. An experimental alignment result used for this chapter's experiment is shown in fig. 6.3 b) with each arm's image being distinguished by a different color.

What is seen on camera? The both beams are superimposed at the camera plane with a relative angle $\theta_r = (\theta_{r,x}, \theta_{r,y})^t$, typically of the order of 40 mrad, corresponding to a relative transverse wavevector $\mathbf{k}_r \simeq k\theta_r$. Noting $\mathbf{r}$ the spatial coordinate of any of both beams, say $\mathbf{r} = (-x, y)$, the total intensity on the camera reads:

$$\begin{aligned} &I_{cam}(\mathbf{r}) \propto |\mathcal{E}(\mathbf{r}, L) + \mathcal{E}(-\mathbf{r}, L)\mathrm{e}^{i\mathbf{k}_r\mathbf{r}}|^2 = \\ &|\mathcal{E}(\mathbf{r}, L)|^2 + |\mathcal{E}(-\mathbf{r}, L)|^2 + 2\mathrm{Re}\{\mathcal{E}^*(\mathbf{r}, L)\mathcal{E}(-\mathbf{r}, L)\mathrm{e}^{i\mathbf{k}_r\mathbf{r}}\} \end{aligned} \tag{6.51}$$

In this expression we neglect the delay accumulated between the two arms, because of the balanced configuration (splitting and recombining beam-splitters not on the incident beam path direction) of the Mach-Zehnder interferometer used for this experiment.

What happens once ensemble averaged? The total field $\mathcal{E}$ depends on the initial phase disorder φ imprinted on it by the SLM. The previous expression can be therefore easily ensemble averaged by acquiring multiple images, each corresponding to a different initial phase disorder numerically calculated using a random number generating function and printed by the SLM on the field's input state. The ensemble averaging of the final state imaging interferograms gives:

$$\langle I_{cam}(\mathbf{r})\rangle \propto 2\rho_0(\mathbf{r}, L)\left(1 + \frac{g^{(1)}(\mathbf{r}, -\mathbf{r}, L)}{\rho_0(\mathbf{r}, L)}\cos(\mathbf{k}_r\mathbf{r})\right) \tag{6.52}$$

where I used that: $\langle|\mathcal{E}(-\mathbf{r}, L)|^2\rangle = \langle|\mathcal{E}(\mathbf{r}, L)|^2\rangle = \rho_0(\mathbf{r}, L)$ and also that: $g^{(1)}(\mathbf{r}, -\mathbf{r}, L) = \langle\mathcal{E}^*(\mathbf{r}, L)\mathcal{E}(-\mathbf{r}, L)\rangle$, assuming that it has no or a vanishing imaginary part. This result (eqn. 6.52) assumes that the phase difference due to the relative tilt $\Delta\phi = \mathbf{k}_r\mathbf{r}$ is constant during whole acquisition process, neglecting thus any additional dephasing mechanisms, such as convective air currents. This assumption turned out to be reasonable in this experiment because of high reproducibility of the results, among others, thanks to the special care to isolate both interfering beam paths from air currents. It is however possible that these additional dephasing mechanisms do contribute to the noise floor of the sensitivity in the $g^{(1)}$ measurement (typically

$\simeq 10^{-2}$ later in the results section).

Conclusion: In this section I showed that a simple optical imaging setup containing an off-axis Mach-Zehnder interferometer with Dove prism assisted image inversion is an efficient way to measure spatial coherence. Ensemble averaging can be performed with an SLM imprinting different calculated phase disorder configurations. Finally I showed that averaging over the acquired images gives a result containing the spatial coherence function. The goal of the next section is to give more information on the experimental details and to explain how I proceeded to numerically retrieve it from the averaged images.

6.4.3 Data acquisition and image processing

6.4.3.1 Data acquisition

Cam+SLM synchronization. Description of the setup figure: Interferometric imaging necessary for the $g^{(1)}$ measurement was performed with a Hamamatsu Orca Flash 4.0 (2048×2048 pixels of size 6.5 μm) camera throughout the whole experiment. The evolution result of a single disorder realization was obtained by first numerically calculating a phase mask, displaying it on the SLM (Hamamatsu, LCOS-SLM X13138, 1272×1024 pixels of 12.5 μm pitch) and only then acquiring an image is on camera. This is necessary in order to avoid integrating on camera the transient images appearing during the phase display process on the SLM which is not instantaneous. The realization of such an acquisition order presumes necessarily synchronization between the SLM and camera. In this work this was done by running both SLM and camera with the same program, a python code which calculates the phase pattern, displays it on the screen duplicated with the SLM and then acquires an image with the camera. In order to control the Hamamatsu camera with python code the Hamamatsu dcam library (available online) was used. The SLM rise time during the experiment was measured to be approximately 25 ms while image acquisition using dcam functions took typically 200 ms plus the required camera exposure time. Ensemble averaging the measurement consisted in repeating the image acquisition for different random phase patterns of given correlation length σ_{SLM} and variance $\overline{\delta\varphi}_{SLM}$ and adding the result to an image which is a sum over disorder realizations. The advantage of running the experiment with a program is that the ensemble averaging requiring many repetitions can simply be written as a loop over disorder realisations.

Data acquisition: Measurement of the coherence function for a given experimental configuration $(\sigma, \varepsilon, \xi)$ required typically 2000 (at least 1000 realizations were verified to be necessary in order to obtain a well averaged $g^{(1)}$) disorder realizations which were saved as 20 interferogramm images, each of them being a sum over 100 realizations. For each experimental configuration an additional measurement of the spatial coherence in the absence of fluctuations was performed. As shown in previous section, although this result simply corresponds to the background density profile, it allows to identify (and correct, as will be shown below) the "static" beam imperfections causing its small density/phase fluctuations other than the ones added by the SLM. For this measurement an average over only 50 images was acquired a single image.

6.4.3.2 Image processing to access the coherence function

Fringe contrast via Fourier filtering: Given a disorder averaged image result corresponding to the eqn. 6.52 and shown as an example on fig. 6.4 a), one can retrieve the coherence function using Fourier filtering. In fact, calculating the spatial spectrum of the image, one can notice that thanks to the relative tilt θ_r between the two interfering paths, the cosine modulated term containing the $g^{(1)}$ in the eqn. 6.52 appears, according to the convolution theorem, as two peaks symmetric with respect to the origin and shifted from it by a distance equal to $k_0\theta_r$. An example of such spectrum is shown in fig. 6.4 b). This means that filtering the area (white circle in fig. 6.4 b)) around any of these two peaks and and setting the remaining parts of the spectrum to zero, one obtains the spectrum of the complex part of the cosine term in the eqn. 6.52. The absolute value of the Fourier inversed filtered spectrum gives then a quantity directly proportional to the $g^{(1)}$ or the fringe contrast. Normalizing the result such that $g^{(1)}(\Delta r = 0) = 1$, one gets the map of the normalized coherence function, as shown in fig. 6.4 c).

Raw radial $g^{(1)}(\Delta r)$***:*** This map has the radial symmetry and depends only on $r = \sqrt{x^2 + y^2}$. One can therefore replot this map as a 1D function versus each corresponding pixel's distance from the beam centre. An example of such curves is shown with the relatively noisy curves in fig. 6.4 d). The clear blue one corresponds to the case where no fluctuations were added to the beam $g^{(1)}_{0,\mathrm{raw}}(\Delta r) = \rho_{0,\mathrm{raw}}(r)$ while the yellow one $g^{(1)}_{\mathrm{raw}}(\Delta r)$ corresponds to the case of $\varepsilon^2 = 9$ % fluctuation strength as defined in eqn. 6.49, $\sigma = 27 \pm 2$ μm and the photon interaction strength given by $\Phi_{NL} = \langle g\rho_0 L\rangle_z = 28$ rad. The interpolated (smoothed) versions of these curves are shown with the thin orange and dark red curves, respectively. Slight deviations from a Gaussian shape especially around the beam centre are clearly observable for the coherence of background only. This is due to the imperfections within the beam which do not carry relevant physical information, (e.g. defects on vapor cell walls).

Background imperfection correction: These background imperfections were corrected by the following procedure: the background's coherence map (fig. 6.4 c)) was smoothed with a Gaussian filter of 200 μm correlation length (using Matlab's `imgaussfilt` function). The smoothed background $\rho_{0,sm}$ was then again represented as function of the radial coordinate $\Delta r = 2r$ and interpolated to 500 radial positions logarithmically spanning the whole accessible radial interval. This last step is responsible for azimuthal averaging because the new interpolated value is an average over values of many points sharing same (or very close) radius and corresponding to different polar angles. An example of a corresponding result is shown with thick black curve in fig. 6.4 d). In order to remove the imperfect background noise in the raw coherence profile $g^{(1)}_{\mathrm{raw}}(\Delta r)$ (yellow curve in fig. 6.4 d)), the corresponding raw coherence map was divided by the raw background coherence and then multiplied by its smoothed version:

$$g^{(1)}(x,y) = \frac{g^{(1)}_{\mathrm{raw}}(x,y)}{\rho_{0,\mathrm{raw}}(x,y)}\rho_{0,sm}(x,y) \tag{6.53}$$

Dividing the raw coherence map of the $\varepsilon > 0$ case by the "noisy" background, one gets rid of this

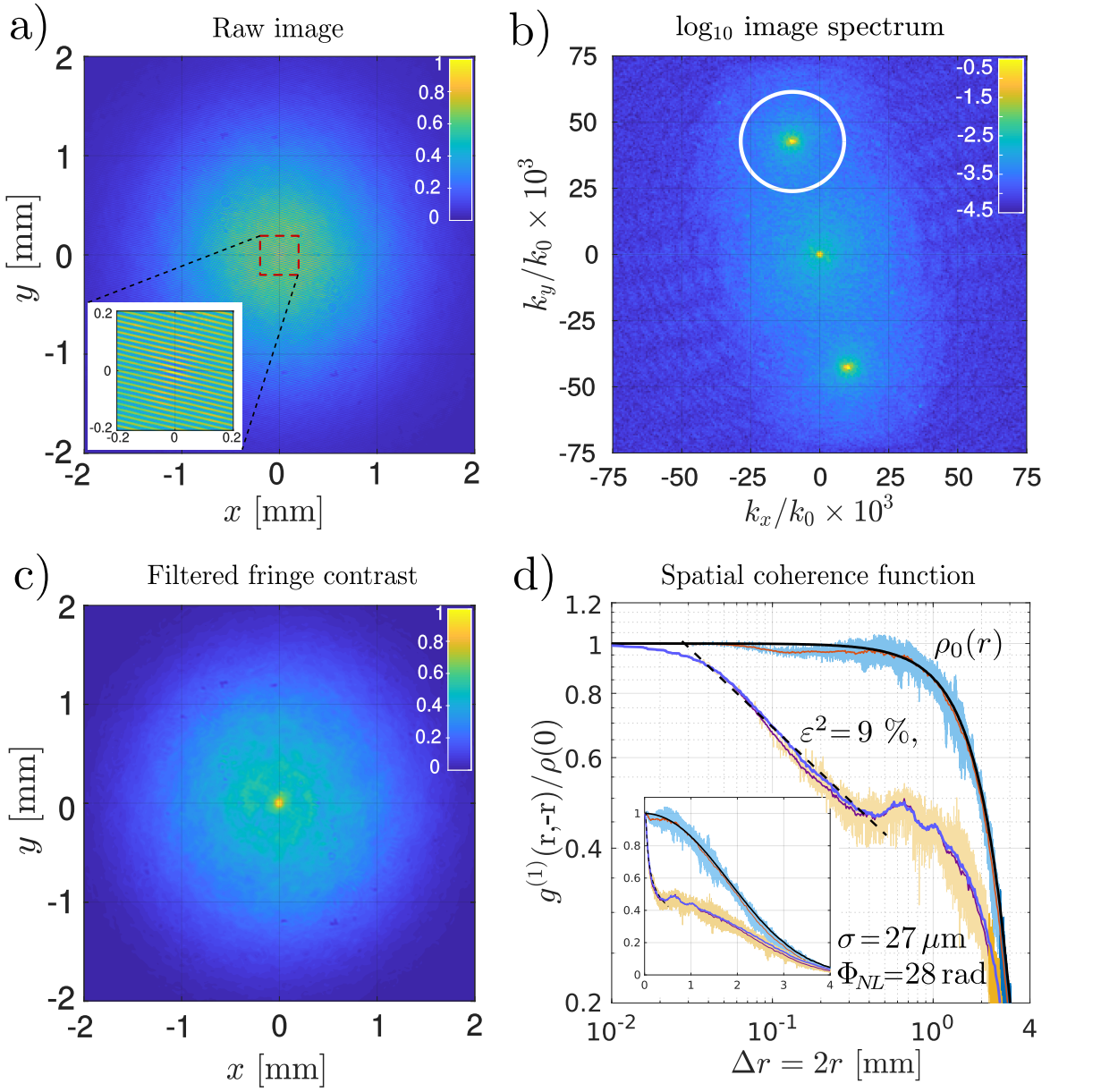

Figure 6.4: Image processing for accessing spatial coherence function. a) shows a sum over 100 disorder realizations of the cell exit plane's interferogram image superimposed with its inverted version at an angle of roughly 40 mrad, acquired by camera. The inset shows the zoomed square area of size 0.4 mm around the image centre, on which one can distinguish interference fringes with higher contrast at the centre. b) shows the numerically calculated spatial spectrum of the image shown in a). The white circle shows the boundary of the area filtered in order to access the cosine term in the eqn. 6.52. c) shows the interference fringe contrast map of the image a), which is the absolute value of the Fourier inversed filtered spectrum, containing only the information inside the white circle area of the spectrum b). d) shows the final spatial coherence in log-log scale obtained by averaging over the polar angle the fringe contrast c). The curves next to subscription $\rho_0(r)$ were obtained without adding phase fluctuations into the beam ($\varepsilon = 0$, $\overline{\delta\varphi}_{SLM} = 0$) and correspond hence to the background density. The curves next to subscription ε^2 =9 % were obtained for the average phase variance on the SLM equal to $\overline{\delta\varphi}_{SLM} = 0.12 \times 2\pi$ and $\sigma_{SLM} = 2$ pixels (12.5 μm at the SLM image plane) giving the input correlation length $\sigma = 25$ μm. The inset in d) shows the same spatial coherence but in the lin-lin scale. The dashed black line is the power law fit performed within $\Delta r \in [0.04, 0.45]$ mm using the eqn. 6.57 and with obtained parameters: $\beta = 0.94$, $\eta = 0.17$.

background induced noise in the coherence map, and multiplying the result by the smoothed background $\rho_{0,sm}$ amounts to obtain the coherence function as it would be if the background had initially its smoothed shape. As in the case of the background, the corrected coherence $g^{(1)}(x,y)$ The corresponding interpolated result of the coherence function is the final result of the image processing and is presented the normalized $g^{(1)}(\Delta r)$ function. An example of such result is shown in fig. 6.4 d) with the thick blue curve. The background imperfection correction turns out to be a crucial step to increase the $g^{(1)}$ measurement sensitivity especially in the case of small fluctuation and interaction strengths.

6.4.3.3 Measuring auxiliary parameters

Fluctuation parameters: Accurate analysis of the measured spatial coherence requires the knowledge of fluctuation strength ε and correlation length σ, as well as the background's healing length ξ which governs the power-law exponent (eqn. 6.44). In case of the SLM generated initial state, the first two parameters were determined by measuring the spatial coherence at the cell's output plane $z = L$ in the absence of photon-photon interactions ($g = 0$). In fact, since the cell length used in this work is much smaller than the distance between the SLM image plane and the cell input plane $L = 10$ mm $\ll z_{SLM} \simeq 200$ mm, no significant change in the coherence function is expected between the cell input and output planes (in absence of interactions, of course). The absence of interactions was realized by detuning the laser frequency to at least -6 GHz away from the ^{87}Rb $F_g = 2 \rightarrow F'$ atomic resonance and reducing the laser power to several tens of mW. Using the theoretical results derived above (eqn. 6.49), the obtained coherence function was then fitted with the equation (with σ and ε^2 set as free parameters):

$$g^{(1)}(\Delta r) = \frac{1}{1+\varepsilon^2}\left[\exp\left(-\frac{\Delta \mathbf{r}^2}{2\omega_0^2}\right) + \varepsilon^2 \exp\left(-\frac{\Delta \mathbf{r}^2}{4\sigma^2}\right)\right] \tag{6.54}$$

Interaction parameters and justification for the short cell: The healing length was not directly measured in this work. Recalling the definition of the background's non-linear phase $\Phi_{NL} = \langle g\rho_0 L\rangle_z$, which was measured during all experiments, the healing length was calculated using:

$$\xi = \sqrt{\frac{L}{4k_0\Phi_{NL}}} \tag{6.55}$$

This equation shows that for a given non-linear phase the healing length (and therefore the ξ/σ ratio) is smaller for a shorter cell. This justifies the choice of a 10 mm long cell for this experiment. The constant non-linear phase assumption can be justified by the fact that at equivalent transmission (T =exp($-\alpha L$)), the longer propagation length L in $\Phi_{NL} = g\rho_0 L$ is compensated in case of a short cell by larger interaction constant g. The measurement was performed via the off axis Mach-Zehnder interferometry with a collimated external reference, as described in chapter 3. The typical values for the healing length in this work lie in the range of 5-10 μm. For this experiment the healing length was controlled by varying the laser power.
Light-cone position: In the same manner as the healing length, the background's speed of

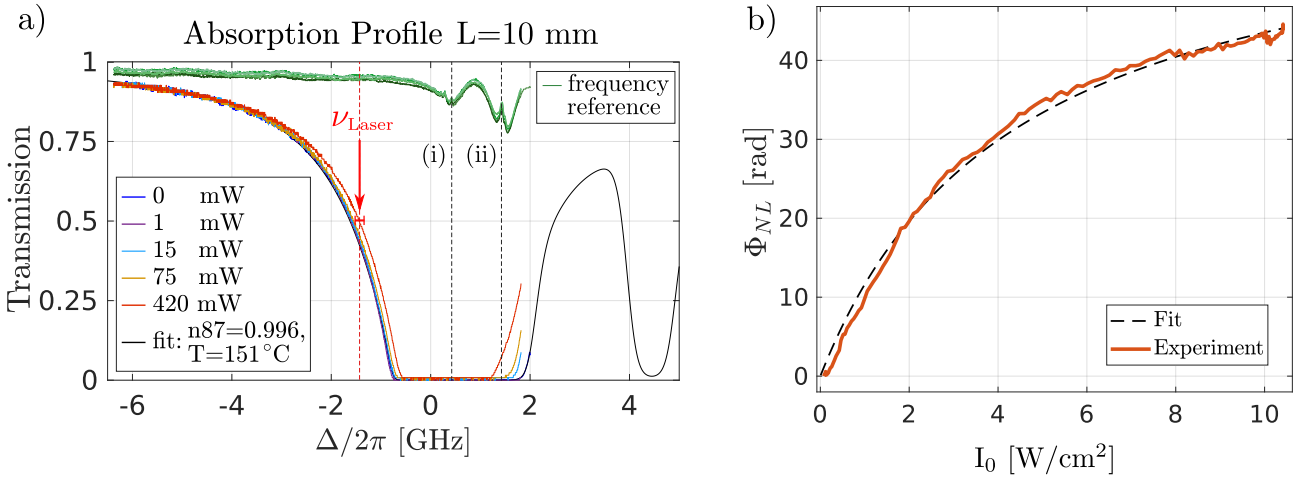

Figure 6.5: Control of atomic vapor dependent interaction parameters: a) Transmission spectrum at the vapor's operation temperature $T_v = 150$ °C for different input laser powers. Green curves are the reference curves for frequency calibration, obtained from a saturable absorption spectroscopy setup and showing 2 calibration points: (i) the ^{87}Rb's $F = 2 \rightarrow F' = 3$ and (ii) the ^{85}Rb's $F = 3 \rightarrow F'$ transition within the Rb D2-line. The black curve is the fit of the weak probe transmission spectrum, revealing the vapor temperature and the isotopic fraction of Rb. b) The non-linear phase $\Phi_{NL} = g\langle\rho_0\rangle_z L$ as function of the input laser intensity, measured with the interferometric Bucket detector technique (see chapter 3).

sound c_s at the beam center was calculated from the measured corresponding non-linear phase Φ_{NL} and the cell length L using: $c_s = \sqrt{\Phi_{NL}/(k_0 L)}$. This gives also access to the estimation of the light cone position:

$$L_c = 2\sqrt{\Phi_{NL} L/k_0} \tag{6.56}$$

Power-law exponent: Finally, in order to measure experimentally the power-law exponent η one can fit the power-law region of the coherence function by the the following expression:

$$g^{(1)}(\Delta r) \simeq \beta.\rho(r).\mathrm{e}^{\frac{\eta}{2}\psi(\frac{1}{2})}\left(\frac{4\sigma}{\Delta r}\right)^{\eta} \quad \text{with:} \quad \Delta r \in [4\xi/\varepsilon, 2c_s z] \tag{6.57}$$

The fitted value of β is usually around 1, while η typically ranges from 0 to 2. The theoretical reason of the possibility for β's variation with time lies in the deviation of the behavior of Bogoliubov quasiparticles from the theory exposed here due to their mutual interference [13]. In practice the fitted β value different from 1 could also stem from the uncertainty on the measurement of σ. An example of such fit is shown in fig. 6.4 d) with the black dashed line giving following results: $\eta = 0.17$, $\beta = 0.94$. The fitted exponent value can then be compared to the one calculated from other measured parameters on which it depends. This is done using the formula:

$$\eta = \frac{2\varepsilon^2 k_0 \Phi_{NL} \sigma^2}{L} \tag{6.58}$$

Atomic vapor parameters: control of interactions: All measurements in presence of photon-photon interactions were performed at the laser detuning of $-1.5(0.1)$GHz with respect to the

$F = 2 \rightarrow F' = 1$ transition of the D2-line of ^{87}Rb at $\lambda_0 = 2\pi/k_0 = 780$ nm corresponding to 50 % of power transmission through a $L = 10$ mm long cell purified with the ^{87}Rb isotope (isotopic fraction above 99 %) and heated to 150±3 °C (see fig. 6.5 a)). The interaction strength corresponding to each laser power used for the $g^{(1)}$ experiments, was deduced from an auxiliary Φ_{NL} measurement (see section 6.4.3.3) with the bucket detector technique presented in section 3.3.4 (see fig. 6.5 b)).

Conclusion: This section summarized the data acquisition strategy employed to measure the spatial coherence function, the image processing methods, as well as the measurement techniques of the auxiliary quantities necessary for the analysis of the measured spatial coherence function. The results of the spatial coherence function measurements, as well as their analysis is consequently described in the next section.

6.5 Results

Various series of results are reported in this section, showing the measured spatial coherence for various interaction strengths, fluctuation strengths and the fluctuation correlation lengths. In order to structurize the results and make their presentation most clear this section is divided into the following parts:

- the first part focuses on the results showing the spatial coherence variation as function of the interaction strength $g\rho_0$ (see section 6.5.1),
- the second part shows the variation of the coherence for different moderate values of the fluctuation strength ε (see section 6.5.2),
- the third part compares the coherence results obtained with two different initial fluctuation correlation lengths σ (see section 6.5.3),
- finally the fourth part's results obtained at maximal photon interaction strength $g\rho_0$ revealing the change of behavior of the spatial coherence from an algebraic to exponential decay when the fluctuation strength is increased to large values (see section 6.5.4).

All these results are analyzed with tools presented in section 6.4.3.3. For instance, plotting the coherence $g^{(1)}(\Delta r)$ in log-log scale is particularly useful to identify the spatial region where it decays algebraically because any power-law function appears with this scale as a linear function. This region's upper bound is then compared with the light-cone position estimation from eqn. 6.56. The coherence within the algebraically decaying area is fitted using the eqn. 6.57. The obtained exponent η_{fit} is then compared with its estimation from eqn. 6.58.

6.5.1 Increasing interaction strength at small fluctuation strengths

Experimental conditions: In order to test how photon-photon interactions alter the coherence of an initially partially coherent state, the $g^{(1)}(\Delta r, z = L)$ was measured at relatively small

initial fluctuation strength for various input laser powers ranging from 20±5 to 560±20 mW. It is important to note that the healing length varied with different input powers but according to its estimation using the eqn. 6.55, its value is typically around (and mostly below) 5 μm. The fluctuation correlation length σ was fixed by setting the correlation length $\sigma_{SLM} = 2$ pixels (12.5 μm at the SLM image plane) of the random patterns produced by the SLM and measured as described in section 6.4.3.3, giving: $\sigma = 25 \pm 2$ μm at the cell input plane. The fluctuation strength corresponding to the measurements at different input laser powers was fixed by setting the same SLM induced phase variance $\overline{\delta\varphi}_{SLM} = 0.04 \times 2\pi$ for all disorder realizations, giving the measured fluctuation strength $\varepsilon^2 = 2$ %. Additional datasets at different input powers were also acquired for several higher values of the SLM's phase variance, $\overline{\delta\varphi}_{SLM} = \{0.08, 0.12, 0.16\} \times 2\pi$ corresponding respectively to the measured values $\varepsilon^2 = \{5, 9, 18\}$ %.

Figure 6.6 a): $g^{(1)}$ ***profiles, qualitative analysis:*** The measured coherence profiles of the $\varepsilon^2 =$ 2 % are shown on figure 6.6 a). Each curve is the result of averaging over 2000 disorder realizations. The solid black line is the background density profile obtained by extracting the fringe contrast in the absence of SLM induced fluctuations. From clear blue to dark red, the colored solid curves correspond to the $g^{(1)}$ functions measured at increasing laser powers. As the interaction strength increases, the decay of coherence at large relative displacements becomes more and more pronounced. Plotting the graph in log-log scale makes the power-law decay of coherence appear as a straight line. The former becomes more and more clearly observable as the interaction strength increases, in agreement with a higher theoretically expected exponent (eqn. 6.57). The dashed black lines plotted on top of the colored solid curves correspond to the fitted power-law functions (eqn. 6.57). The fit was performed within the displacement range where the curves are shown, the upper bound being fixed by the light-cone position calculated from the auxiliary Φ_{NL} measurement at the corresponding input powers, using eqn. 6.56. The fitted curves reproduce well the experimental data, confirming the observation of the algebraic decay of coherence. For the curves acquired at highest input powers, one can clearly state that the power-law decay stops just at the vicinity of the calculated light-cone position, where it is followed by a short plateau which is then "truncated" by the background's Gaussian envelope. Before switching to the quantitative analysis of the results of this data set, one can already confirm a qualitative agreement with the theoretical model derived in the section 6.3 based on the observation of the algebraic decay of spatial coherence until a light-cone position, giving further place to a plateau dominated by the background's density profile.

Figure 6.6 b) quantitative analysis: exponent: The power-law fit of the spatial coherence until the light cone gives access to the power law exponent. The fitted power-law exponents are plotted as function of the interaction strength Φ_{NL} in fig. 6.6 b) for the different datasets corresponding to $\varepsilon^2 = \{2, 5, 9\}$ %. The fitted exponent increases linearly with interaction strength, in qualitative agreement with the model (eqn. 6.58). Comparing the fitted exponents with the corresponding calculated values from eqn. 6.58, one gets an expected slope for the $\eta(\Phi_{NL})$ which is roughly 8.3 times higher than the measured one. This inconsistency is observed for all datasets presented in this chapter and certainly requires a deeper investigation. A possible missing ingredient which could explain it is discussed further in section 6.6. Yet, in

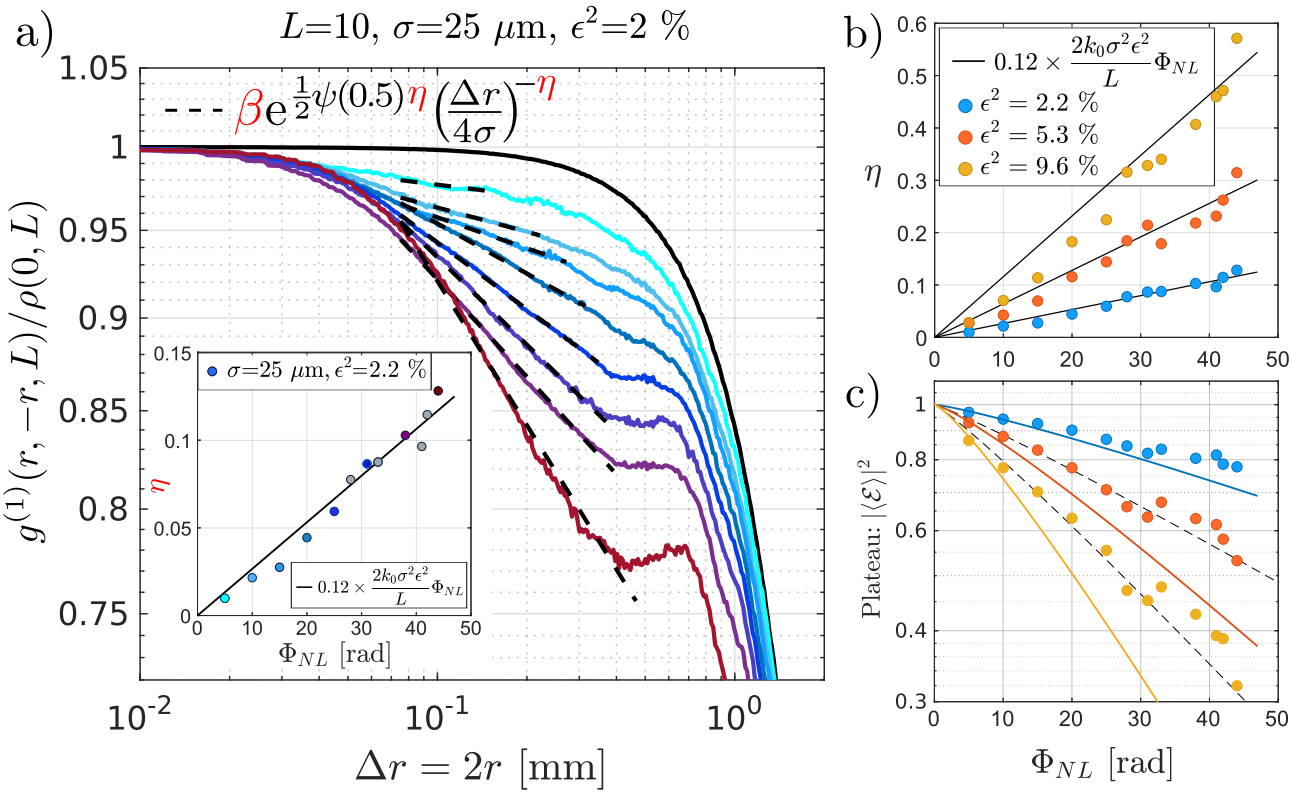

Figure 6.6: Measured coherence function with small (ε^2 =2% wit respect to background density) fluctuations: a) Solid lines show in log-log scale the coherence function versus the 2-point relative displacement, measured at different incident laser powers controlling the the fluid density and accordingly the interaction strength $g\rho_0$. The dashed black lines on top of the solid curves are the corresponding power-law fits performed between $\Delta r = 0.08$ mm and the light cone position $L_c = 2c_sL$ calculated from the measured background's non-linear phase Φ_{NL} using eqn. 6.56. Fitted power-law exponent η, (b), and the coherence plateau height (c) as function of the interaction strength $g\rho_0$ expressed in terms of the measured non-linear phase accumulated by the background $\Phi_{NL} = g\langle\rho_0\rangle_z L$.

order to compare the fitted exponents with the model, the equation eqn. 6.58 calculated with the measured parameters (σ, ε and ξ calculated with the eqn. 6.55) is additionally multiplied by 0.12 and plotted as the solid line in fig 6.6 b). Interestingly this time the agreement is achieved for all three curves corresponding to different fluctuation strengths.

Figure 6.6 b) quantitative analysis: plateau height: To study how the plateau height beyond the light cone decays with interaction strength, the values of the $g^{(1)}$ curves shown on fig. 6.6 a) are sampled at $\Delta r = 1.1 \times L_c$ with L_c the calculated light cone position for each curve. The corresponding result is shown in fig. 6.6 c) as point data and plotted in lin-log scale versus the interaction strength $g\rho_0$ expressed via the non-linear phase: $\Phi_{NL} = \langle g\rho_0\rangle_z L$. The theoretically expected plateau calculated from the eqn. 6.45 with the power-law exponents multiplied by 0.12 is shown with solid lines of same colors as the corresponding experimental data. Good

agreement is observed for the data set taken at small fluctuation fraction $\varepsilon^2 = 2$ %. For data sets acquired at larger fluctuation strengths the experimentally observed plateaus start to deviate appearing slightly above compared to the expected values. This discrepancy for data at non-negligible fluctuation fraction, could stem from the deviation from the perfect applicability regime of the derived model.

6.5.2 Increasing the fluctuation strength at moderate interactions

Experimental conditions: Now that the algebraic decay and the light cone have been evidenced in the previous section within the best applicability regime of the derived model (small fluctuation strength), another set of measurements was performed to study the influence of the fluctuation strength on the coherence function and more specifically on the power-law exponent at fixed interaction strength and correlation length σ. For the data presented here the fluctuation correlation length σ was fixed by setting the correlation length to $\sigma_{SLM} = 5$ pixels (31.2 μm at the SLM image plane) of the SLM patterns and measured as described in section 6.4.3.3, giving: $\sigma = 35 \pm 2$ μm at the cell input plane and the interaction strength $\langle g\rho_0 \rangle_z = 2 \pm 0.2$ mm^{-1}, deduced from the measured non-linear phase acquired by the background $\Phi_{NL} = 20 \pm 2$ rad.
Figure 6.7 a): The corresponding coherence profiles are shown on figure 6.6 a) in log-log scale. Each curve is a result of an average over 2000 disorder realizations. The solid black line is again the background density profile or the fringe contrast in the absence of SLM induced fluctuations. From yellow to purple, the colored solid curves correspond to the $g^{(1)}$ functions measured at fixed laser power (and frequency) and increasing fluctuation fraction ε controlled by fixing the variance of the displayed SLM patterns. Following phase variances were tested: $\overline{\delta\varphi}_{SLM}$ ={2,3,4,5,6,8,10,12}%$\times 2\pi$, corresponding to the measured (input state's $g^{(1)}$ fit described in section: 6.4.3.3): $\varepsilon^2 = \{0.027, 0.04, 0.05, 0.07, 0.11, 0.16, 0.23, 0.35\}$ % with the relative uncertainty of 10 % for smaller values and 2 % at higher values. As expected, the increasing fluctuation fraction, accelerates the decay of coherence at large relative displacements. One can still clearly recognize the power-law decay of coherence which appears as a straight line which becomes more and more pronounced as the fluctuation fraction increases, again in qualitative agreement with theory (eqn. 6.57). The dashed black lines plotted on top of the colored solid curves correspond to the fitted power-law functions (eqn. 6.57). The fit was performed within the displacement range where the curves are shown, the upper bound being fixed by the calculated light-cone position $L_c = 0.32$ mm, using eqn. 6.56. The fitted curves reproduce well the experimental data, still confirming the observation of the algebraic decay of coherence as expected theoretically by the model derived in section 6.3.
Light cones, strange plateaus: On all curves one can clearly separate the upper limit of the power-law decay corresponding well to the calculated light-cone position $L_c = 0.32$ mm, where the former is followed by an oscillating plateau with oscillations getting damped with increasing relative displacement until the plateau gets decimated by the background's Gaussian envelope. It was verified that these oscillations are not a numerical artefact of the Fourier filtering used to extract the fringe contrast from interferograms. While exact reason for the oscillations is not

yet established, a possible explanation of this effect is discussed further in section 6.6. Finally, one can remark slight growth of plateau height for the $g^{(1)}$ measured at maximal fluctuation fraction ε^2 which can be explained by the background's in-homogeneity within the local density approximation.

Quantitative analysis, exponent's comparison to theory at small ε^2, fig. 6.7 b): As in the previous subsection, the power-law fits within the light cone position give access to the experimentally measured exponents which can be compared to the theory. The fitted power-law exponents are plotted as function of the fluctuation fraction ε^2 in fig. 6.7 b). For small fluctuation fraction, the fitted exponent increases linearly, in qualitative agreement with the model (eqn. 6.58). Comparing the slope of the $\eta(\varepsilon^2)$ curve at small ε^2 with the model given by the eqn. 6.58 and calculated from experimentally measured parameters, one gets again an expected slope which is roughly 8.3 times higher than the measured one, as in the sets where the interaction strength was increased at fixed fluctuation fraction. Similarly to those sets, in order to scale the fitted exponents with the model, the equation eqn. 6.58 calculated with the measured parameters, is additionally multiplied again by 0.12 and plotted as the dashed line in fig 6.7 b) achieving this time agreement with experimental data.

Quantitative analysis, exponent's saturation at large ε^2, fig. 6.7 b): However, at larger fluctuation fractions ε^2 the fitted exponent saturates around the value $\eta \simeq 1$ and therefore behaves differently than in case of increasing interaction strength at constant fluctuation fraction and correlation length, where it kept increasing linearly even for large Φ_{NL}. This behavior is not captured by the derived model (eqn. 6.58) but can be explained by the invalidity of the Bogoliubov theory at larger fluctuation strengths ε.

Quantitative analysis of the plateaus: fig. 6.7 c): To quantify the dependence of the plateau height beyond the light cone on the fluctuation fraction, the values of the $g^{(1)}$ curves shown on fig. 6.7 a) are sampled at $\Delta r = 1.1 \times L_c = 0.35$ mm. The corresponding result is reported in fig. 6.7 c) as point data and plotted in lin-log scale versus the fluctuation fraction ε^2. The theoretically expected plateau calculated from the eqn. 6.45 with the power-law exponents multiplied by 0.12 is shown as solid line. Fair agreement can be concluded at small fluctuation fraction ε^2. At larger fluctuation strengths the experimentally observed plateau starts to strongly deviate appearing much above than it is expected to be. This observation is in agreement with the one reported in the previous section: at non-negligible fluctuation fraction the observed plateaus deviate and are above the expected values, suggesting that they correspond to experimental conditions going beyond the validity of the derived model.

6.5.3 Different initial fluctuation correlation lengths

Various acquired data sets with two different fluctuation correlation lengths $\sigma = 25 \pm 2$ μm and $\sigma = 35 \pm 2$ μm allow determine how the power-law exponent depends on σ and compare the result with theory.

Fig. 6.8 a) fixed fluctuation fraction: In order to do it, multiple data sets acquired at different input laser powers but at fixed fluctuation fraction $\varepsilon^2 = 5$ % (corresponding to $\overline{\delta\varphi}_{SLM} = 8$ % and

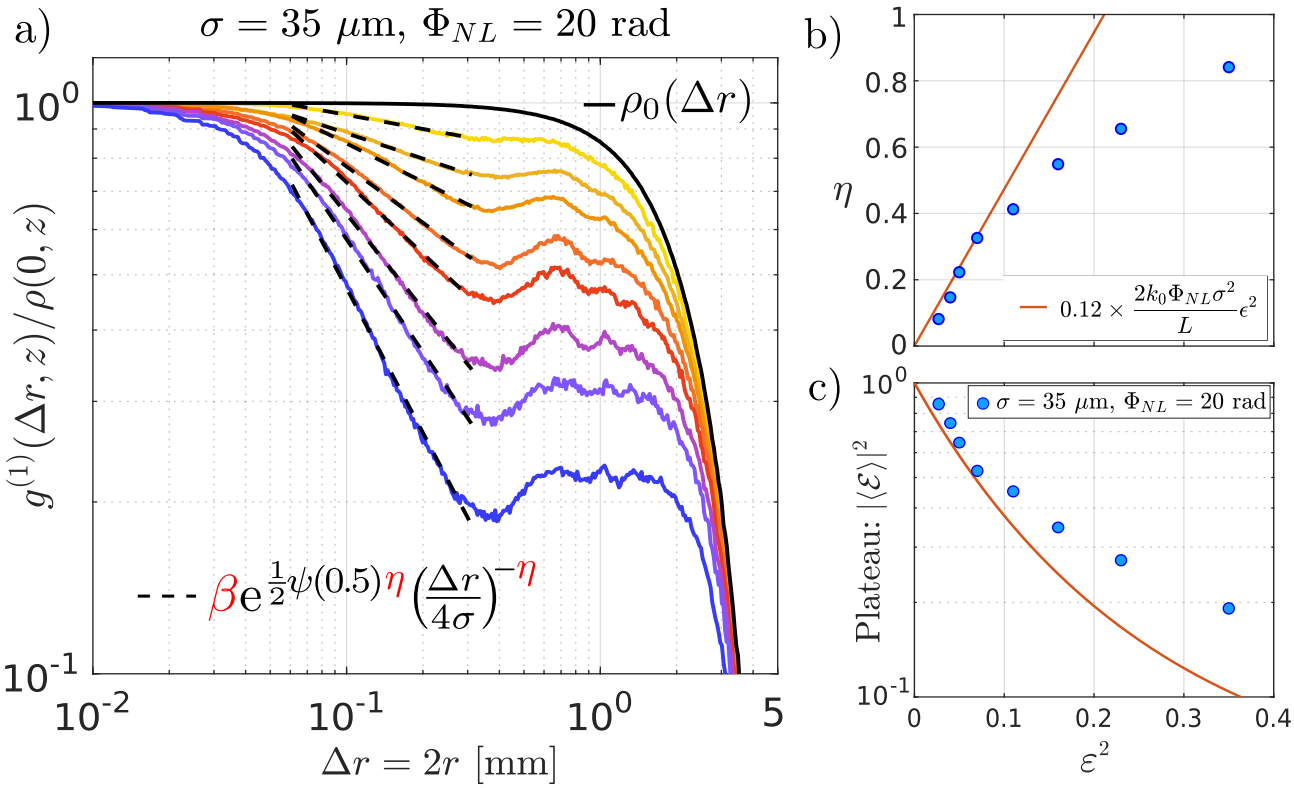

Figure 6.7: Coherence function at increasing fluctuation fraction with moderate interactions. a) shows the measured spatial coherence profiles at the interaction strength equal to: $g\langle\rho_0\rangle_z = 0.2 \pm 2$ mm^{-1} for different fluctuation fractions increasing from the yellow to the dark blue curve. Solid black line is the background's coherence profile ($\varepsilon^2 = 0$ case), the dashed black lines are the power-law fits performed within the range where they appear. b) fitted power law exponents and c) the plateau height as function of the fluctuation fraction. The solid lines correspond to the adjusted ($\times 0.12$) calculated theoretical exponent and the plateau height.

4 % $\times 2\pi$) have been analyzed for the two available fluctuation correlation lengths $\sigma = 25 \pm 2$ µm and $\sigma = 35 \pm 2$ µm. The corresponding fitted power-law exponents obtained from the procedure described in section 6.4.3.3, are shown once divided by σ^2, on figure 6.8 a). The circular points correspond to $\sigma = 25\ \mu$m and the square points correspond to $\sigma = 35\ \mu$m. the solid curve is the expected exponent from eqn. 6.57 multiplied by 0.12. The two experimental curves overlap well especially for Φ_{NL} up to 30 rad and follow rather well the adjusted theoretical prediction.
Fig. 6.8 b) fixed interaction strength: On the other hand, same analysis has been performed with multiple data sets sharing the same Φ_{NL} for various fluctuation fractions and corresponding to the same two correlation lengths. The result is shown with fitted power-law exponents divided by σ^2, on figure 6.8 b). Again, the data from both correlation lengths collapses rather well on the same solid curve showing the theoretically expected value times 0.12.
Conclusion: These both results are in agreement with the theoretical scaling of the power-law exponent with fluctuation's initial correlation length.

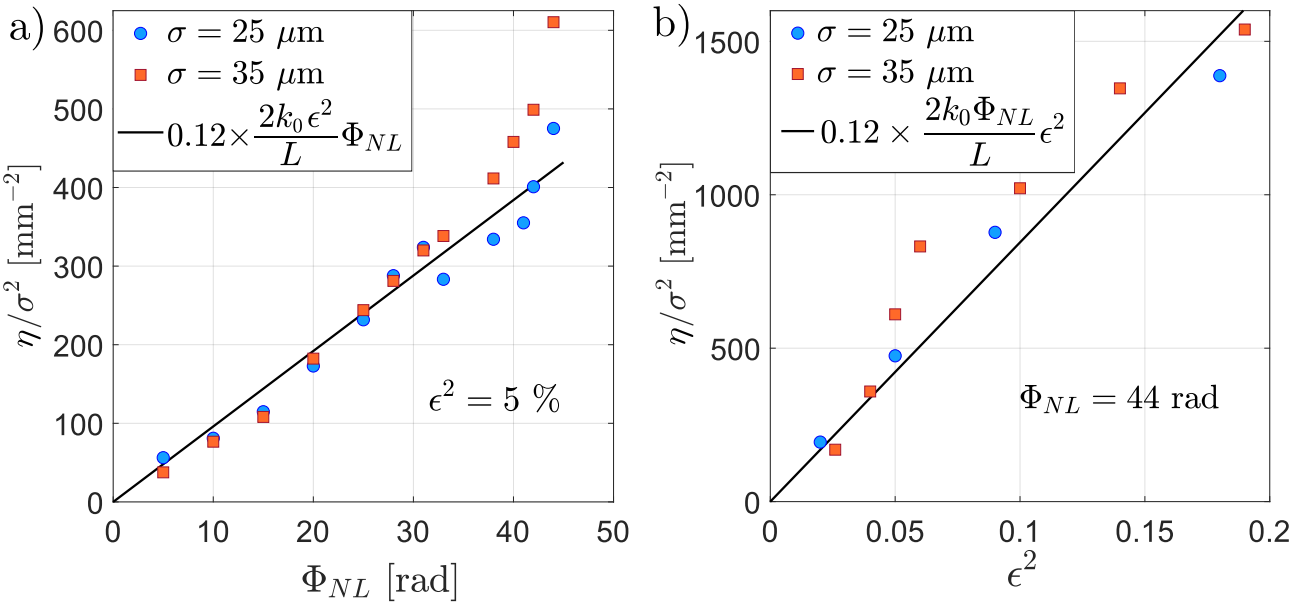

Figure 6.8: Influence of the fluctuation's initial correlation length σ on the power-law exponent of coherence. Fitted power law exponents divided by the square of the correlation length σ are shown in a) versus interaction strength expressed with $\Phi_{NL} = g\langle\rho_0\rangle_z L$ at $\varepsilon^2 = 5\ \%$, and in b) versus fluctuation strength at $\Phi_{NL} = 44$ rad for the datasets with $\sigma = 25 \pm 2\ \mu$m and $\sigma = 35 \pm 2\ \mu$m. Solid lines correspond to the calculates theoretical values multiplied by 0.12.

6.5.4 Power-law to exponential decay transition

Upper limit of the derived model: Previous sections presented the results allowing to analyze separately the influence of interactions, fluctuation fraction and fluctuation correlation length on the spatial coherence. The corresponding coherence data showed algebraic decay with exponents rising typically up to the value of unity or slightly above. It is however intriguing to investigate what happens in the regime where the power-law exponent is pushed to even higher values. This regime goes clearly beyond the theoretical model derived at the beginning of the chapter, opening the avenue into the strongly non-linear behavior of the system. Indeed, increasing the power-law exponent presumes increasing the magnitude of density fluctuations and interactions to the point where neither the second order expansion in density fluctuations used for the coherence function derivation is a valid assumption, nor the Bogoliubov-type description for the evolution of fluctuations on top of a background fluid.

Experimental strategy:

To further characterize the non-equilibrium dynamics of our fluid of light, we have also studied the evolution of $g^{(1)}(\Delta\boldsymbol{r})$ up to larger values of ε, setting a stronger interaction strength $\Phi_{\mathrm{NL}} = 44$ rad. A relatively high fluctuation correlation length $\sigma = 35 \pm 2$ µm was chosen by setting $\sigma_{SLM} = 5$ pixels for the SLM displayed patterns. Finally, the fluctuation fraction is the parameter which changes from one measurement to the other increasing to the maximal value of $\varepsilon^2 = 1$ achieved with the SLM phase variance $\overline{\delta\varphi}_{SLM} = 0.18 \times 2\pi$.

Figure 6.9 a): The corresponding series of results are shown on fig. 6.9 a) as the $g^{(1)}$ profiles

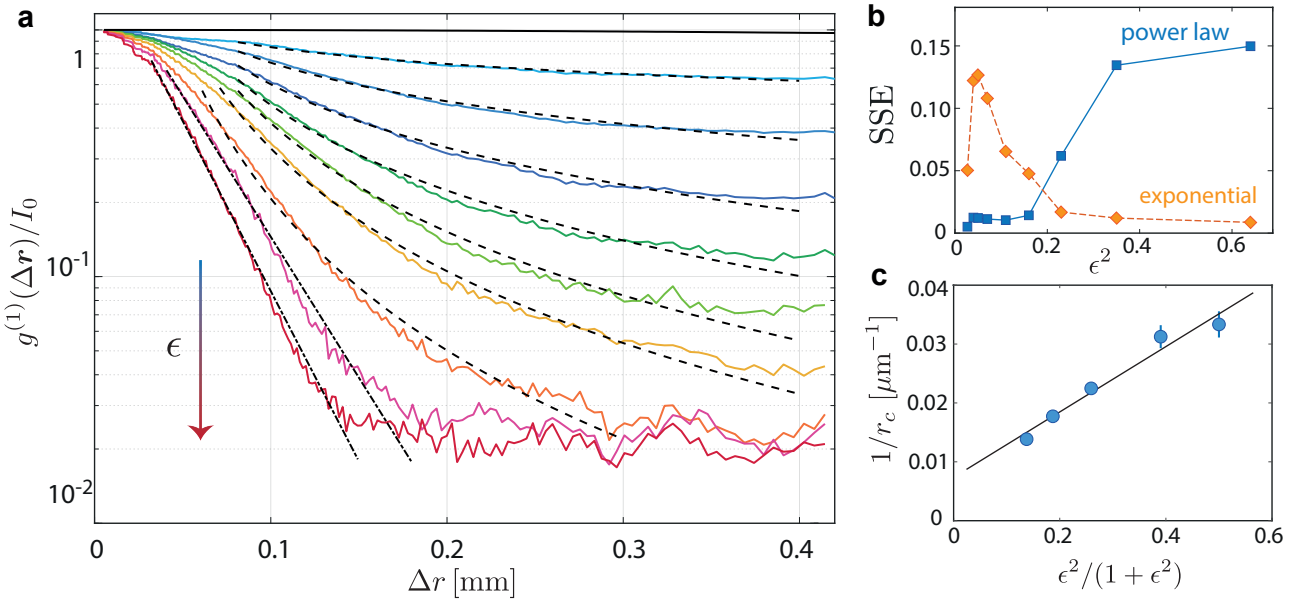

Figure 6.9: Cross-over from algebraic to short-range (exponential) correlations at stronger fluctuation amplitudes, with the interaction strength set to a value $\Phi_{\rm NL} = 44$ rad twice larger than in the previous data (notice the log scale). (a) Normalized coherence function $g^{(1)}(\Delta \boldsymbol{r})/\rho_0$ vs Δr when increasing more significantly ε ($\varepsilon^2 = 0, 0.027, 0.04, 0.05, 0.07, 0.11, 0.16, 0.23, 0.35, 0.64$ from top to bottom). Here $\sigma = 35$ μm is fixed. (b) Sum-squared error between the experimental data and an exponential (orange) vs algebraic (blue) fit. For $\varepsilon^2 > 0.35$ the exponential fit becomes more accurate than the algebraic fit. (c) Rate $1/r_c$ of the exponential decay, see Eq. (6.59), vs the fluctuation amplitude. The linear fit (black) confirms the theroretical scaling of Eq. (6.60).

plotted in lin-log scale for increasing fluctuation fraction corresponding to the solid line curves ranging from clear blue to the red color. The solid black curve corresponds to the background's profile, the dashed lines are the power-law fits while the dash-dotted lines are the exponential decay fits, performed within the spatial range where they appear. The lin-log scale makes exponential decay appear as a straight line while a power-law decay as a convex curved line.
From the above discussion, one could naively expect that, upon increasing ε, the low-energy state (6.44) leaves room to a non-universal dynamics, where no pre-thermalization stage arises and where $g^{(1)}(\Delta \boldsymbol{r})$ has no specific structure. Instead, we have experimentally observed that the coherence function smoothly turns from algebraic to exponential as ε is increased:

$$g^{(1)}(\Delta \boldsymbol{r}) \sim \exp(-\Delta r/r_c). \tag{6.59}$$

The cross-over from Eq. (6.44) to this exponential behavior is presented in the measurements of Fig. 6.9(a). We have confirmed it by a computation of the sum of squared estimate of errors (SSE) that measures the discrepancy between the $g^{(1)}$ data and a fit to either Eq. (6.44) or (6.59), see Fig. 6.9(b). Note that such an exponential decay differs from the Gaussian correlations of the initial speckle and, in that, is associated with a genuine new dynamical

regime emerging from the quench. We have also observed this cross-over in *ab initio* numerical simulations presented in the Supp. Mat., and have found it to be a generic feature of $g^{(1)}$ in the pre-thermal regime as ε or Φ_{NL} are increased to moderate values. This phenomenon was also previously pointed out in [13]. At a physical level, we conjecture that this algebraic-to-exponential crossover is reminiscent of the celebrated Kosterlitz-Thouless (KT) transition, which drives 2D Bose gases at thermal equilibrium from a superfluid to a normal-fluid state when the temperature is raised. Although out-of-equilibrium, our fluid of light displays a very similar behavior in the pre-thermal regime. This unexpected phenomenon can be understood by noticing that, at low ε and/or small interaction strength, the energy injected into the system during the quench is small, and so is the effective pre-thermalization "temperature". This results in an pre-thermal state with quasi long-range order, which can be seen as the dynamical counterpart of a 2D, equilibrium superfluid at low temperature. When ε and/or g is increased, on the other hand, one reaches a pre-thermal state of effectively larger temperature. The resulting fluid displays exponentially-decaying correlations, analogous to the normal phase of a 2D Bose gas above the KT temperature.
To gain more insight on the pre-thermal regime of exponential correlations, we have also studied the dependence of the correlation length r_c of the exponential decay, see Eq. (6.59), on the initial fluctuation amplitude ε. To unveil this dependence, one can take advantage of the conservation of the total energy $E_t = \int d\boldsymbol{r}(1/(2k_L)|\nabla\psi(\boldsymbol{r})|^2 + g/2|\psi(\boldsymbol{r})|^4)$ during the non-equilibrium evolution. Equating E_t to the energy of the normal state (6.59), we obtain:

$$\frac{1}{r_c} \propto \frac{\varepsilon^2}{1+\varepsilon^2} \sim T_i^2. \tag{6.60}$$

We have also confirmed this law from extensive numerical simulations presented in the Supp. Mat. Experimental values of $1/r_c$, extracted from our measurements of $g^{(1)}$, are also shown in Fig. 6.9(c). When plotted vs $\varepsilon^2/(1+\varepsilon^2)$, they show a good agreement with the prediction (6.60).

6.6 Discussion and conclusion

6.6.1 Deviations from theory

6.6.1.1 Exponent inconsistency

Exponent's discrepancy with theory: neglected effects? Comparison of the measured power-law exponents with the theoretically expected values based on the the independently measured auxiliary parameters revealed a discrepancy requiring for all presented experiments to multiply the theoretical exponent by 0.12 in order to match the experimental data. Here I try to list several effects neglected in the derivation of the coherence function but present in in the experiment and discuss their possible impact on the observed inconsistency.
Absorption: density loss during evolution: During the calculation of the coherence function

the background's "slow" variations with space and the propagation direction are taken into account within the LDA. In practice it means that the dispersion relation for the fluctuations adiabatically follows the the background density during the system's evolution. In practice, to make link with experiment performed with 50 % losses, I suppose that the result for the coherence function in the absence of absorption is still valid if I replace the interaction by its propagation averaged value measured via the non-linear phase shift. Generalizing this approach to the power-law exponent, one can speculate that the latter being proportional to the background density via Φ_{NL}, should decrease in presence of the absorption by the factor: $(T-1)/\ln(T) \simeq 0.72$ for T=0.5. But this factor is already taken into account in the measured value of Φ_{NL}. Furthermore, even multiplying the value of the exponent by the final transmission, which would correspond to the "worst case" scenario of a loss-less evolution of the final density, one gets the a correction of 0.5 for the exponent, still much above the observed value. This analysis allows to rule out safely the absorption as an explanation for the exponent inconsistency.

Saturation of the interactions: Another effect present in most systems mediating the photon-photon interactions, including the atomic vapor cells, is the saturation of the interactions. Taking into account this effect makes the calculation of the coherence function non-analytical. As discussed in [48], the saturation affects the dispersion relation for the fluctuations in a fluid of light and in order to take it into account one needs to replace the "non-saturated" interaction strength in the Bogoliubov dispersion relation 6.20 by the saturated one. In our experiment the interaction strength as well as the healing length is calculated from the measured non-linear phase which already incorporates the saturation, therefore no additional corrections are expected due saturation from this point of view. Moreover, it is known that the saturation parameter $s = \rho/I_s$ depends on the input laser intensity and is negligibly small at low input power. This property suggests that the deviation from the theoretically expected behavior for the power-law exponent in presence of saturation should increase gradually with interaction strength and in particular, that no deviation should be observed at reasonably low input powers corresponding to the saturation parameter well below one. This argument allows to discard the saturation as the dominant effect responsible for the exponent discrepancy.

Non-local interactions: The non-locality is an effect spatially smoothing the interactions. As already mentioned, this effect can strongly affect the evolution of a fluid of light [142]. Its influence depends on the ratio between the non-local range l, a length scale setting a lower bound on the spatial resolution of the interaction strength, and the healing length ξ [153]. Putting some figures on the latter, one gets from eqn. 6.55 the healing length as small as: $\xi \simeq 3$ µm$< l_b = 8$ µm at the interaction strength of $\Phi_{NL} = 44$ rad, which is smaller than the most optimistic (small) length scale l_b for the ballistic non-locality in Rubidium vapor at the temperature $T = 150$ °C [55]. Even reducing the interaction strength by a factor of 4, $\Phi_{NL} = 11$ rad, one still gets the "local" healing length $\xi \simeq 6$ µm$< l_b = 8$ µm. This implies for the experimental results presented in this chapter, that the fluid of light's evolution should be strongly affected by the non-locality. Considering this fact, it is important to understand how the non-locality acts on the power-law exponent. The major implication of the presence

of the non-locality is the modification of the dispersion relation for the fluctuations, which, for example, in presence of the diffusive non-locality takes the form [153, 55]:

$$\Omega(q) = \sqrt{K_{kin}(q)\left(\frac{2g\rho_0}{1+l_c^2q^2} + K_{kin}(q)\right)} \tag{6.61}$$

with $K_{kin} = \mathbf{q}^2/2k$. This eqn tells that the role of the non-locality on the dispersion simply consists in killing the effect of interactions at momenta above $1/l_b$. Possible approaches to include the non-locality into the model of the coherence function presented in this work would be to modify the dispersion relation used to derive the final result (eqn. 6.38) by the one given in the eqn. 6.61 or to make an assumption that the influence of non-locality "simply" results in a variation of the healing length, and hence defining an effective healing length taking into account the non-locality, one can plug it into the expression of the power-law exponent and get the corrected result. The question of the healing length redefinition in presence of the non-locality has been addressed in: [90, 116]. However it was found that the in case of the repulsive interactions the re-scaled healing length is smaller than the one corresponding to the local case, which does not improve things at all. Therefore this result rules out the second approach to include the non-locality, but it does exclude the effect itself as a possible explanation for the exponent inconsistency. Taking several steps back, one can recall the eqn. 6.35, which is still a valid result for modified versions dispersion relation and re-express it in a more formal way:

$$g^{(1)}(\mathbf{r},-\mathbf{r},z) = \rho.\exp\left(-\varepsilon^2\int\frac{d^2\mathbf{q}}{(2\pi)^2}\gamma(\mathbf{q})\left(1-\cos(\mathbf{q}\Delta\mathbf{r})\right)\left[1+\frac{(\Omega^2-K_{kin}^2)^2}{2\Omega^2K_{kin}^2}\sin^2(\Omega z)\right]\right) \tag{6.62}$$

The only term depending on the dispersion relation, also the one responsible for the emergence of an algebraic coherence, is the sin term. In the "local" case, its prefactor times the fluctuation fraction ε^2 controls the final power-law exponent η. The former can now be elaborated in the non-local case:

$$\frac{(\Omega^2-K_{kin}^2)^2}{2\Omega^2K_{kin}^2} = \frac{\varepsilon^2(2g\rho_0)^2/2}{K_{kin}(q)\left[2g\rho_0(1+l_c^2q^2)+K_{kin}(q)(1+l_c^2q^2)^2\right]} \tag{6.63}$$

Comparing the three length scales involved in the game, namely σ, ξ and l_c, one can simplify this result. Let's first recall, that all performed experiments were performed in the $\sigma/\xi \simeq 10 \gg 1$ regime, corresponding to the deep "phononic" regime of the "local" dispersion. This implies that the non-local dispersion can be simplified to:

$$\Omega(q) \simeq \sqrt{\frac{g\rho}{k}\frac{q^2}{1+l_c^2q^2}} \tag{6.64}$$

suggesting that in the eqn. 6.63 the term proportional to K_{kin}^2 can be neglected, giving finally:

$$\frac{(\Omega^2-K_{kin}^2)^2}{2\Omega^2K_{kin}^2} = \frac{\varepsilon^2\sigma^2}{2\xi^2}\frac{1}{1+l_c^2q^2} \tag{6.65}$$

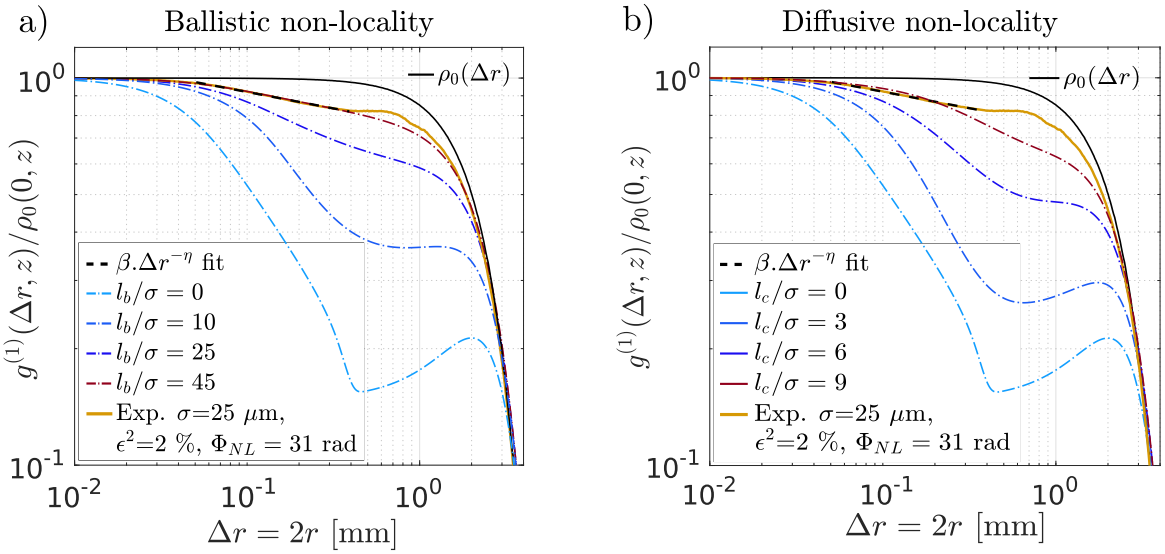

Figure 6.10: Influence of the non-locality on the spatial coherence of the fluid of light. a) b)

where I used the standard "local" definition of the healing length. This result reveals that the power law exponent, being a constant for the local interactions, acquires spatial (spectral dependence on q) dependence as the interactions become non-local. One can also conclude that the non-local contribution reduces the expression in the eqn. 6.65. It is therefore interesting to evaluate the exact result of the coherence function with the non-local dispersion relation. In fact, this calculation was easily implemented by numerically calculating the Fourier integral in eqn. 6.62 with the modification given by eqn. 6.65. The results are shown on figure 6.10 for the ballisctic a) and diffusive b) types of non-locality.

Describe fig. 6.10: The idea is to take a reference experimental coherence measurement and compare it first with the corresponding "local" theory and then step-by-step increase the range of non-locality. One can observe that the increasing non-local range "raises" the local spatial coherence in both cases. The coherence result with ballistic non-locality [55] on fig. 6.10 a) shows better agreement with experimenal data than the diffusive non-locality in fig. 6.10 b). However, extremely high non-local range, of the order of 1 mm has to be included in order to obtain the agreement with the experimentally observed power-law decay. It is important to mention that for the moment there is no possible explanation for such high non-local range.

Conclusion: Summing up this discussion, I can say that the numerically calculated expression of the coherence function in a medium with non-local interactions leads to the reduced algebraic exponent. However, in order to obtain the agreement with experimental data, unrealistically high non-local range needs to be supposed. For the moment, no effect considered in this work is able to explain such high non-local range.

6.6.1.2 Oscillating plateau

Correlated disorder? On the experimental coherence profiles shown in previous sections one can observe oscillations of the plateau right after the light cone position, which get damped as

the relative displacement increases. Such oscillations are observed only in case of the SLM produced speckle and are absent in the coherence function results obtained with input fluctuations obtained with speckle produced by a scattering slab (see D). These oscillations are not predicted by the theoretical model presented in this chapter. Revisiting the approximations used during the derivation, one can notice that the cross correlations of the initial fluctuation's real and imaginary parts have been neglected in the model, while the SLM produced speckle does not guarantee this condition. Moreover, the numerical simulation of the SLM produced speckle (see C.2) reveals that although very small, this correlation is not zero. In fact as shown in eqns. 6.29 and 6.30, the real-imaginary part cross-correlations of the fluctuation do contribute to the final result of the coherence function. These contributions could explain the observed oscillations on top of the plateau.

6.6.2 Conclusion

In summary, this work's experimental description of a 2D fluid of light through a direct probe of its spatial coherence has revealed the dynamical emergence of algebraic pre-thermalization following an interaction quench. Unlike previous studies involving near-integrable systems in 1D, in our case pre-thermalization emerges as a result of the weak-breaking of translation invariance after the quench. Our results further point toward the existence of a cross-over from algebraic to exponential correlations in the pre-thermal regime of 2D systems, an intriguing phenomenon that we interpret as a non-equilibrium precursor of the thermodynamic KT transition. We believe that this effect opens exciting perspectives for further studies of non-equilibrium quantum fluids. While a comprehensive description of 2D thermalization processes remains open, our analysis emphasizes the assets of photon fluids for its characterization, and more generally for probing the dynamics of far-from-equilibrium many-body systems.

General conclusion and outlook

The concept of fluids of light englobes the experiments where light propagation in a nonlinear Kerr medium mimics the temporal evolution of a 2D superfluid, with the propagation coordinate playing the role of time. The scope of research of the fluid of light community spans from the exploration of hydrodynamic phenomena for light to bridging the gap between quantum optics and many-body physics of quantum fluids. The long term goal is to realize a photonic quantum simulator, as counterpart to the simulators based on ultracold atoms, for example. In this work hot Rubidium vapor cells were used to produce a fluid of light. While this medium has been used for decades for quantum optics experiments, it only recently emerged as a platform for the fluids of light, with the Kerr effect, relying on the near-resonant saturation of the refractive index. While a textbook model of a 2-level system was known to give typical scalings, allowing to control the Kerr effect, it is completely inappropriate for a quantitative comparison and appears to miss the dependence on the beam size. This has been first suggested by our group's previous PhD student Quentin Fontaine, who developed a more complete model, including the excited state's additional decay channel into a second ground state and the atomic transit motion [55]. In this work an off-axis interferometric imaging technique has been developed to characterize more precisely the hot Rubidium vapor's non-linear parameters: the Kerr index n_2 and the saturation intensity I_s, controlling the This tool allowed to evidence for the first time (to the best of my knowledge) the drastic variation of the vapor's non-linear parameters with laser beam size. Moreover, the off-axis technique was adapted to measure the transient onset of the optical non-linearity, which arises essentially exponentially with time, and revealed a slower rise time than the one expected from a two-level system. These both observations validate the relevance of the hyperfine optical pumping and the atomic transit motion for the Kerr interaction modelling in Rb vapor.

Another important milestone, realized before I joined the group, consisted in observing the Bogoliubov dispersion relation for weak density perturbation in our paraxial fluids of light [54]. In this work, the investigation of a density perturbation dynamics has been extended to the case, where the over-density is of the same order of magnitude as the background. Previous works in fluids of light in the similar regime reported the formation of analogue shock waves, which are non-linear waves, characterized by the emergence of a steep shock front giving eventually rise to an oscillating pattern moving with the phase velocity above that of the shock front. In the shock waves in a fluid of light were studied in analogy with their classical counterpart occurring during explosions. In fact, a well known phenomenon in the detonation physics is called blast

waves: a special type of the non-linear shock waves characterized by a negative over-pressure in the wake of the shock front. This phenomenon is one of the key factors of the destructive effect of explosions and explains, for example, the remaining glass pieces of broken windows following an explosion inside a building. This work reports the observation of analogue blast waves in the fluid of light's over-pressure [2]. Interestingly, the blast waves were shown to arise only in case of a 2D perturbation while absent for the elongated quasi 1D perturbation. The off-axis interferometric tools were also successfully used to access other hydrodynamic quantities, as the local velocity, the dynamic pressure, which provided a complementary analysis of the blast wave dynamics. It is shown, that the blast waves can be observed for the fluid's over-density and differential static pressure, but not for the dynamic pressure nor for the fluid velocity. Finally this experiment allowed to compare the shock front velocity to the theoretical prediction given by a model with local Kerr interactions. The measured shock front velocity seems to be only given by the background's speed of sound which is in disagreement with the model. Revisiting the approximation of the local interactions, numerical simulations corresponding to the experimental parameters were performed by adding the diffusive non-local range of interaction as a free parameter. The agreement between the numerical simulation and the experimental data was achieved for a large non-local range of $\approx 180\mu$m. This high value of the non-local range can so far not be explained by any existing model and could be an object of further investigations.

The blast wave experiment is an example of the common strategy to drive a fluid of light out of equilibrium by means of a strong perturbation. This state becomes a noneqilibrium state as soon as the photonic interactions are "turned on" at the cell's input interface. However, an important result of this work (see chapter 5) shows that even in the absence of the perturbation, the sudden variations of the fluid's interaction constant at cell's interfaces result in its non-equilibrium evolution. The fluid's response to interaction quenches, occurring at the vapor cell's interfaces, was probed with its intrinsic fluctuations stemming from the shot noise of the laser beam. The measurement of the fluid's static structure factor revealed the emergence of the acoustic peaks as the result of two interaction quenches, as well as their temporal evolution at short times. The behavior of the static structure factor was successfully reproduced by the Bogoliubov theory including several additional experimental effects, such as the finite imaging resolution and the contribution of the spontaneous reemission to the incoherent quasiparticle population. The structure factor signal at high momentum modes appears at short times, while the low momentum modes appear at longer times in agreement with the increasing quasiparticle oscillation period. Importantly, the static structure factor at different spatial Fourier modes is shown to oscillate in time as the result of the interference These results may be interpreted in a way analogous to cosmological model of the Sakharov oscillations explaining the primordial density fluctuations of the Universe and predicting the similar acoustic peaks, but in a completely different context of the cosmic microwave background's power spectrum [146].

The fluid's nonequilibrium evolution also inevitably raises the question of the fluid of light's relaxation to a possible equilibrium state. A recent theoretical model [13], predicted the dynamic emergence of the algebraic spatial coherence decay within the light cone of the Bogoliubov

quasiparticles, similar to the case of the 2D superfluids at thermal equilibrium. However, this state is the so-called prethermal state, emerging at short times, showing strong ressemblance with an eauilibrium state, but undergoing very slow evolution towards a final equilibrium state. Prethermal states have been recently studied in the context of thermalization of isolated quantum many-body systems. They have been identified in the nearly-integrable systems, i.e. systems, showing strong ressemblence with the analytically solvable systems but possessing sightly more degrees of freedom than the constants of evolution. Inspired by this theoretical result an experiment was set up to measure the fluid of light's short-time relaxation. Disturbing a Gaussian initial state with multiple realizations of SLM-induced small random fluctuations the fluid's spatial coherence was measured. To experimentally access the spatial coherence, the light beam, exiting the vapor cell is superimposed to its inverted version, produced by means of Dove prisms inside a Mach-Zehnder interferometer. This setup allowed to observe the emergence of long range power-law decay of the spatial coherence. The spatial extent of the algebraic decay is shown in agreement with the calculated light cone of the sonic excitations using the independently measured interaction strength. The fitted power-law exponent increases in agreement with the theory, linearly with the interaction strength and fluctuation strength (for low fluctuation strengths) and as the square of the initial fluctuation correlation length. In order to explore beyond the integrable regime (small fluctuations) where the Bogoliubov theory is already expected to be inaccurate, the fluctuation strength was increased and led to a dynamic emergence of a transition from long range algebraic to short range exponential decay of spatial correlations. This transition strongly ressembles to the superfluid to normal fluid transition in 2D, also well known as the Berezinskii-Kosterlitz-Thouless (BKT) transition in equilibrium systems. However, in our case, this transition occurs in a nonequilibrium fluid. We therefore interpreted this result as a non-equilibrium counterpart of the BKT transition. While these results already show several remarkable aspects of the fluid's nonequilibrium evolution, they all were obtained at short evolution times and leave the fate of the fluid's long-time evolution an open question, which will hopefully be explored in future works. This work will hopefully provide the necessary tools and insightful ideas for the further research. For instance, one of the emerging topics, where the fluids of light can be considered as a successful experimental platform, is quantum turbulence. As already discussed in this work, the fluid's evolution can be described with hydrodynamic equations for a dispersive and non-dissipative fluid with pressure proportional to the square of the density. The interplay between the photonic interactions (non-linearity) and kinetic energy (diffraction) can give rise to the wave turbulence phenomena, where the energy dissipation due to the interaction with an obstacle or collision with a counter-streaming fluid occurs via spontaneous generation of vortices. These phenomena can be observed and quantitatively studied using the available observation tools in our fluids of light and are currently explored by Wei Liu and Myrann Abobaker, PhD students in our group.
Switching from the continuous wave to pulsed illumination may add new degree of freedom to the fluid of light's dynamics due to the medium's chromatic dispersion. In particular the temporal direction now plays the role of the fluid of light's 3-rd spatial dimension. Theoretically [96] one can show that the fluid's dynamics in the third dimension may or not be analogous

to the to its dynamics in the transverse spatial dimensions, depending on the relative signs of the group velocity dispersion and the non-linear refractive index variation. In case where the behaviour in all three dimensions is analogous, one can define the speed of sound and the healing length in the third dimension. A future project could focus on the development of the experimental techniques to measure these quantities in a three dimensional fluid of light. Furthermore, a new tool explored during this works is the density power spectrum, used for the measurement of the response to interaction quenches. This tool can be further used to explore the quantum fluctuations and correlations in the 3D fluid of light. This topic will be further explored by Tangui Aladjidi, a PhD student of our group. Finally, a non less important knob, that has not at all been explored in this work, is the external potential. The multi-level structure of Rb provides indeed multiple degrees of freedom to optically tailor an external potential for a fluid of light. Adding an optical potential for light can allow to explore physics analogous to the ultracold atoms in optical lattices. A long-term open question to explore could be the possibility of the observation of quantum phase transitions such as Superfluid-Mott insulator transition, for the fluid of light.

Appendix A

Steady state of the three level rate equations

The Optical Bloch Equations for the density matrix elements of a three level system with a laser coupling the $g-e$ transition, read:

$$\frac{\mathrm{d}\rho_{gg}}{\mathrm{d}t} = -\mathrm{Im}\left\{\sigma_{eg}\Omega_{ge}\right\} + \Gamma_{eg}\rho_{ee} + \Gamma_t(\rho_{gg}^{(0)} - \rho_{gg}) \tag{A.1}$$

$$\frac{\mathrm{d}\rho_{ee}}{\mathrm{d}t} = \mathrm{Im}\left\{\sigma_{eg}\Omega_{ge}\right\} - (\Gamma + \Gamma_t)\rho_{ee} \tag{A.2}$$

$$\frac{\mathrm{d}\rho_{dd}}{\mathrm{d}t} = (\Gamma - \Gamma_{eg})\rho_{ee} + \Gamma_t(\rho_{dd}^{(0)} - \rho_{dd}) \tag{A.3}$$

$$\frac{\mathrm{d}\sigma_{eg}}{\mathrm{d}t} = -\frac{i\Omega_{ge}}{2}(\rho_{ee} - \rho_{gg}) - \left(\frac{\Gamma}{2} - i\Delta\right)\sigma_{eg} \tag{A.4}$$

In this approach we suppose that the laser couples only the $g-e$ transition, because the laser is significantly more detuned from the $d-e$ transition. Again, one can search for the steady-state solution (dρ/dt=0) of the density matrix in order to evaluate the medium's susceptibility in the cw illumination case. At steady state the eqn. A.4 becomes:

$$\sigma_{eg} = \frac{\Omega}{2\gamma}\frac{i - \Delta/\gamma}{1 + (\Delta/\gamma)^2}(\rho_{gg} - \rho_{ee}) \tag{A.5}$$

Then we can make a substitution:

$$\mathrm{Im}\left\{\sigma_{eg}\Omega_{ge}\right\} = \frac{\Omega^2}{2\gamma}\frac{1}{1 + (\Delta/\gamma)^2}(\rho_{gg} - \rho_{ee}) = \gamma s_{ge}(\rho_{gg} - \rho_{ee}) \tag{A.6}$$

where s_{ge} is the (intensity dependent) saturation parameter of the transition $g \to e$. In case if the ground and the excited states have different degeneracies g_i, the population inversion factor $(\rho_{gg} - \rho_{ee})$ has to be replaced by: $\left(\rho_{gg} - \frac{g_g}{g_e}\rho_{ee}\right)$. Using the eqn. A.6, one can rewrite the Bloch

equations as rate equations in steady state:

$$0 = -\gamma s_{ge}\left(\rho_{gg} - \frac{g_g}{g_e}\rho_{ee}\right) + \Gamma_{eg}\rho_{ee} + \Gamma_t(\rho_{gg}^{(0)} - \rho_{gg}) \tag{A.7}$$

$$0 = \gamma s_{ge}\left(\rho_{gg} - \frac{g_g}{g_e}\rho_{ee}\right) - (\Gamma + \Gamma_t)\rho_{ee} \tag{A.8}$$

$$0 = (\Gamma - \Gamma_{eg})\rho_{ee} + \Gamma_t(\rho_{dd}^{(0)} - \rho_{dd}) \tag{A.9}$$

The equilibrium populations of the ground states $\rho_{gg}^{(0)}$ can already be explicited as the fractional degeneracies: $\rho_{ii}^{(0)} = g_i/(\sum_j g_j) = G_i$. The second and the first equations become:

$$\rho_{ee} = \frac{\gamma s_{ge}}{\Gamma_t + \Gamma + \frac{g_g}{g_e}\gamma s_{ge}}\rho_{gg} \tag{A.10}$$

$$\rho_{gg} = \frac{\Gamma_t G_g + (\Gamma_{eg} + \frac{g_g}{g_e}\gamma s_{ge})\rho_{ee}}{\Gamma_t + \gamma s_{ge}} \tag{A.11}$$

Using the equation A.10 in the equation A.11, after some rearrangements, one gets:

$$\rho_{gg} = \frac{\Gamma_t G_g\left(\Gamma + \Gamma_t + \frac{g_g}{g_e}\gamma s_{ge}\right)}{\Gamma_t(\Gamma + \Gamma_t) + \left[\Gamma_{ed} + \Gamma_t(1 + \frac{g_g}{g_e})\right]\gamma s_{ge}} \tag{A.12}$$

$$\rho_{ee} = \frac{\Gamma_t G_g \gamma s_{ge}}{\Gamma_t(\Gamma + \Gamma_t) + \left[\Gamma_{ed} + \Gamma_t(1 + \frac{g_g}{g_e})\right]\gamma s_{ge}} \tag{A.13}$$

One can now calculate the population inversion to access the atomic coherence responsible for the optical susceptibility and consequently the saturation intensity and the Kerr (using the eqn. 3.7):

$$\rho_{gg} - \frac{g_g}{g_e}\rho_{ee} = \frac{G_g}{1 + I/I_{s,3L}(\Delta)} \tag{A.14}$$

$$I_{s,3L}(\Delta) = \frac{2\Gamma_t(\Gamma + \Gamma_t)}{\left[\Gamma_{ed} + \Gamma_t(1 + \frac{g_g}{g_e})\right]\Gamma} I_{s,2L}(\Delta) \simeq \frac{\Gamma_t}{\gamma_{ed}} I_{s,2L}(\Delta) \tag{A.15}$$

$$n_{2,3L}(\Delta) \simeq \frac{\gamma_{ed}}{\Gamma_t}\frac{\mathrm{Re}\{\chi^{(1)}\}}{2I_{s,2L}(\Delta)} = \frac{\gamma_{ed}}{\Gamma_t} n_{2,2L}(\Delta) \tag{A.16}$$

Appendix B

Numerical simulations

The propagation of the electric field envelope can be efficiently implemented using the split-step method.

Principle

We want to numerically integrate the following partial differential equation:

B.1 Implementing non-locality

In presence of the transverse non-locality the propagation equation reads:
One can notice the

Appendix C

Supplemental material: spatial coherence measurement

C.1 Intermediate derivation steps: density/phase correlations

Here I give the calculation details allowing to get the eqns 6.34 from the eqns 6.27 and 6.28. Using the calculated quasi-particle correlations (eqns 6.31 and 6.32) one gets:

$$\frac{\langle\delta\rho(\mathbf{r},z)\delta\rho(\mathbf{r}+\Delta\mathbf{r},z)\rangle}{\rho_0^2} = \epsilon^2\int\frac{d^2\mathbf{q}}{(2\pi)^2}\gamma(\mathbf{q})\left(\left[1+\frac{K_{kin}^2}{\Omega^2}\right]\cos\left(\mathbf{q}\Delta\mathbf{r}\right)+\left[1-\frac{K_{kin}^2}{\Omega^2}\right]\cos\left(\mathbf{q}\Delta\mathbf{r}-2\Omega z\right)\right)$$
$$\langle\theta(\mathbf{r},z)\theta(\mathbf{r}+\Delta\mathbf{r},z)\rangle = \frac{\epsilon^2}{4}\int\frac{d^2\mathbf{q}}{(2\pi)^2}\gamma(\mathbf{q})\left(\left[1+\frac{\Omega^2}{K_{kin}^2}\right]\cos\left(\mathbf{q}\Delta\mathbf{r}\right)+\left[1-\frac{\Omega^2}{K_{kin}^2}\right]\cos\left(\mathbf{q}\Delta\mathbf{r}-2\Omega z\right)\right)$$

The term depending on the relative position difference can be factorized. This is revealed by using the trigonometric identity: $\cos(\mathbf{q}\Delta\mathbf{r}-2\Omega z) = \cos(\mathbf{q}\Delta\mathbf{r})\cos(2\Omega z)+\sin(\mathbf{q}\Delta\mathbf{r})\sin(2\Omega z)$, and noticing that the sin term vanishes upon integration since it gives an odd integrand. We therefore end up with:

$$\frac{\langle\delta\rho(\mathbf{r},z)\delta\rho(\mathbf{r}+\Delta\mathbf{r},z)\rangle}{\rho_0^2} = \epsilon^2\int\frac{d^2\mathbf{q}}{(2\pi)^2}\gamma(\mathbf{q})\left(\left[1+\frac{K_{kin}^2}{\Omega^2}\right]+\left[1-\frac{K_{kin}^2}{\Omega^2}\right]\cos\left(2\Omega z\right)\right)\cos\left(\mathbf{q}\Delta\mathbf{r}\right)$$
$$\langle\theta(\mathbf{r},z)\theta(\mathbf{r}+\Delta\mathbf{r},z)\rangle = \frac{\epsilon^2}{4}\int\frac{d^2\mathbf{q}}{(2\pi)^2}\gamma(\mathbf{q})\left(\left[1+\frac{\Omega^2}{K_{kin}^2}\right]+\left[1-\frac{\Omega^2}{K_{kin}^2}\right]\cos\left(2\Omega z\right)\right)\cos\left(\mathbf{q}\Delta\mathbf{r}\right)$$

Rearranging the terms in the brackets one finally gets the final result:

$$\frac{\langle\delta\rho(\mathbf{r},z)\delta\rho(\mathbf{r}+\Delta\mathbf{r},z)\rangle}{\rho_0^2} = 2\epsilon^2\int\frac{d^2\mathbf{q}}{(2\pi)^2}\gamma(\mathbf{q})\left(1+\left[\frac{K_{kin}^2}{\Omega^2}-1\right]\sin^2\left(\Omega z\right)\right)\cos\left(\mathbf{q}\Delta\mathbf{r}\right) \tag{C.1}$$
$$\langle\theta(\mathbf{r},z)\theta(\mathbf{r}+\Delta\mathbf{r},z)\rangle = \frac{\epsilon^2}{2}\int\frac{d^2\mathbf{q}}{(2\pi)^2}\gamma(\mathbf{q})\left(1+\left[\frac{\Omega^2}{K_{kin}^2}-1\right]\sin^2\left(\Omega z\right)\right)\cos\left(\mathbf{q}\Delta\mathbf{r}\right) \tag{C.2}$$

This is exactly the result shown in the eqn 6.34.

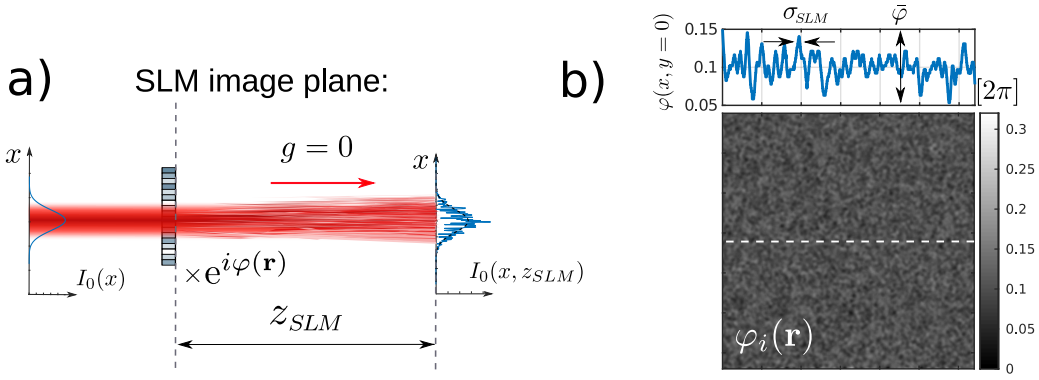

Figure C.1: SLM produced speckle: figure a) shows the experimental configuration, in which an initially collimated Gaussian beam is phase modulated by an SLM with an example of phase a mask shown in b) (note that in real experiment the SLM was used in reflection), and propagates by a distance z_{SLM} after the SLM plane. Diffraction of the SLM induced phase fluctuations enables mixing of the phase and intensity fluctuations.

C.2 Statistics of the SLM generated speckle

C.2.1 Theoretical description: SLM shaped input state

Based on the experimental configuration shown on fig. C.1, I first assume the total field just after the reflection by the SLM to be given by:

$$\mathcal{E}(\mathbf{r}, z = 0) = \mathcal{E}_0.\exp\left(-\frac{\mathbf{r}^2}{\omega_0^2}\right).e^{i\varphi(\mathbf{r})} \tag{C.3}$$

and want to calculate the field $\mathcal{E}$ after a certain distance z of free space propagation after the SLM plane (which I set as the $z = 0$ plane), in order to deduce its statistical characteristics at this new plane. Assuming the paraxial approximation, the propagation is governed by the eqn:

$$\left[i\partial_z + \frac{\Delta_{\mathbf{r}}}{2k}\right]\mathcal{E}(\mathbf{r}, z) = 0 \tag{C.4}$$

This equation being linear and invariant wrt translation in the transverse plane, one can define the associated Green function:

$$\left[i\partial_z + \frac{\Delta_{\mathbf{r}}}{2k}\right]G(\mathbf{r} - \mathbf{r}', z) = \delta(\mathbf{r} - \mathbf{r}', z) \tag{C.5}$$

Where $\Delta_{\mathbf{r}}$ means that the Laplacian only acts on the $\mathbf{r}$ variable. It is a useful tool because knowing the initial field distribution and the Green fcn, one can calculate the field at any space position as:

$$\mathcal{E}(\mathbf{r}, z) = \int d^2\mathbf{r}' G(\mathbf{r} - \mathbf{r}', z)\mathcal{E}(\mathbf{r}', 0) \tag{C.6}$$

The Green fcn calculation is straightforward in Fourier space, I therefore need to define the direct and inverse Fourier transformations:

$$G(\mathbf{q},q_z)\mathrm{e}^{-i\mathbf{q}\mathbf{r}'}=\int d^2\mathbf{r}\int dz G(\mathbf{r}-\mathbf{r}',z)\mathrm{e}^{-i\mathbf{q}\mathbf{r}+iq_z z} \tag{C.7}$$

$$G(\mathbf{r}-\mathbf{r}',z)=\int d^2\mathbf{q}\int dq_z G(\mathbf{q},q_z)\mathrm{e}^{i\mathbf{q}(\mathbf{r}-\mathbf{r}')-iq_z z} \tag{C.8}$$

Inserting the eqn C.8 into C.5, one gets:

$$G(\mathbf{q},q_z)=\frac{1}{q_z-\frac{\mathbf{q}^2}{2k}} \tag{C.9}$$

The corresponding Green fcn in real space can be calculated using the eqn C.8:

$$\begin{aligned} G(\mathbf{r}-\mathbf{r}',z)&=\lim_{\zeta\to 0}\int d^2\mathbf{q}\int\frac{dq_z\mathrm{e}^{i\mathbf{q}(\mathbf{r}-\mathbf{r}')-iq_z z}}{q_z-\frac{\mathbf{q}^2}{2k}+i\zeta}=\int d^2\mathbf{q}\mathrm{e}^{i\mathbf{q}(\mathbf{r}-\mathbf{r}')-i\frac{\mathbf{q}^2}{2k}z}\\ G(\mathbf{r}-\mathbf{r}',z)&=-\frac{ik}{2\pi z}\mathrm{e}^{\frac{ik}{2z}(\mathbf{r}-\mathbf{r}')^2}\end{aligned} \tag{C.10}$$

Inserting this result into the eqn C.6 one gets the Fresnel diffraction formula that will be used to calculate the field at plane z knowing it at $z=0$:

$$\mathcal{E}(\mathbf{r},z)=\frac{-ik\mathrm{e}^{\frac{ik\mathbf{r}^2}{2z}}}{2\pi z}\int d^2\mathbf{r}'\exp\left(\frac{ik}{2z}(\mathbf{r}'^2-2\mathbf{r}.\mathbf{r}')\right)\mathcal{E}(\mathbf{r}',0) \tag{C.11}$$

To be completed

The field at the cell entrance reads:

$$\mathcal{E}(\mathbf{r},z=0)=\mathcal{E}_0\left(\exp\left(-\frac{\mathbf{r}^2}{\omega_0^2}\right)+\epsilon^2\delta\mathcal{E}(\mathbf{r})\right) \tag{C.12}$$

$$\epsilon^2=\frac{\pi^2\sigma^2\overline{\delta\varphi}^2\omega_0^2}{(\lambda z)^2},\quad \sigma=\frac{2z}{k\omega_0} \tag{C.13}$$

$$\langle\delta\mathcal{E}^*(\mathbf{r})\delta\mathcal{E}(\mathbf{r}')\rangle=\exp\left[-\frac{1}{2}\frac{z_R^2}{z^2}(\mathbf{r}-\mathbf{r}')^2+\frac{ik}{2z}(\mathbf{r}^2-\mathbf{r}'^2)\right] \tag{C.14}$$

Which gives the following coherence at the cell input:

$$g(\mathbf{r},-\mathbf{r},0)=\left[\exp\left(-\frac{\Delta\mathbf{r}^2}{2\omega_0^2}\right)+\epsilon^2\exp\left(-\frac{1}{2}\left(\frac{k\omega_0}{2z}\right)^2\Delta\mathbf{r}^2\right)\right] \tag{C.15}$$

C.2.2 Numerical simulation of the SLM generated speckle

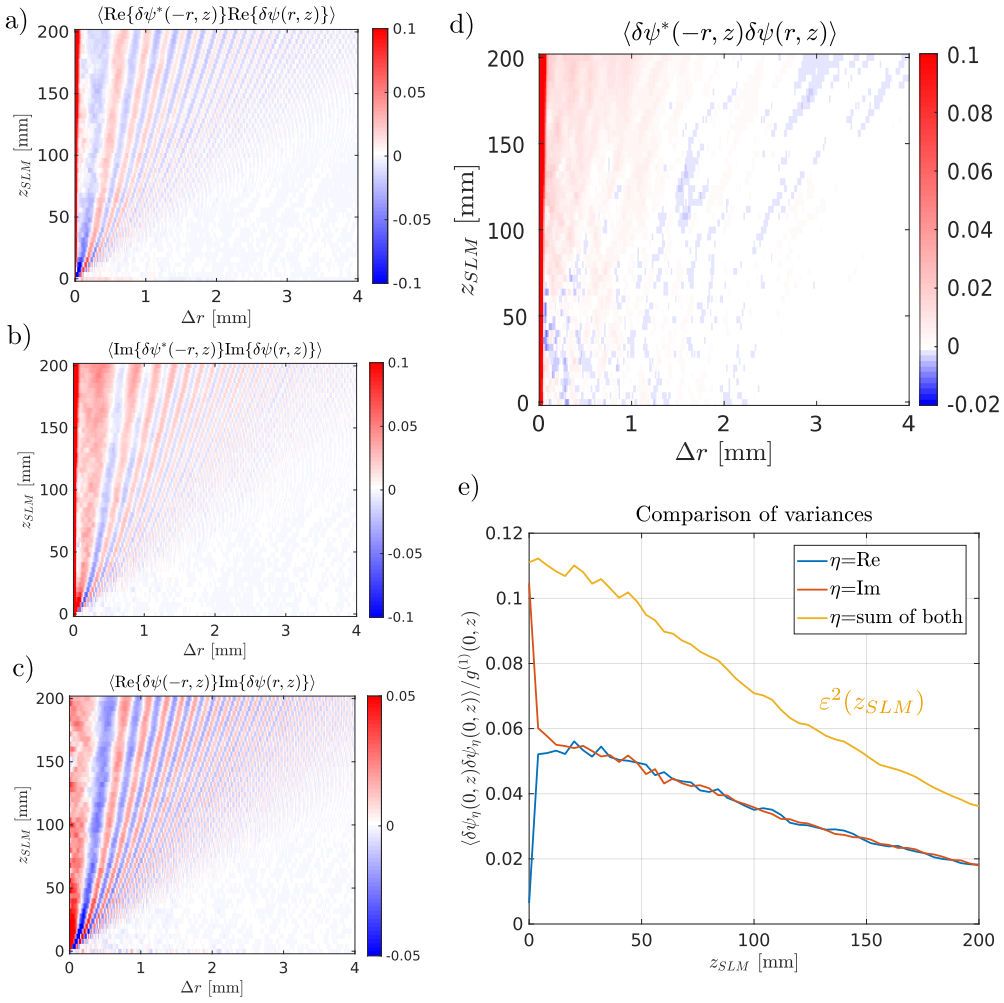

Figure C.2: SLM produced speckle statistics explored with numerical experiments. Dynamics in the transverse and propagation direction z of the a) autocorrelation of the field's real part, b) autocorrelation of the field's imaginary part, c) cross-correlation of the field's real and imaginary parts, all normalized by the total field's variance. d) The field fluctuation's auto-correlation versus space and the "time" z. e) Comparison of the variances of the fluctuation field's real part, imaginary part and their sum normalized by the total field's variance. Ensemble averaging over 5000 realizations.

Appendix D

$g^{(1)}$ with scatterer produced speckle fluctuations

Rotating diffuser configuration .
Results with Gaussian/Lorentzian speckle correlation

Bibliography

[1] Dmitry A. Abanin, Ehud Altman, Immanuel Bloch, and Maksym Serbyn. Colloquium: Many-body localization, thermalization, and entanglement. *Rev. Mod. Phys.*, 91:021001, May 2019.

[2] Murad Abuzarli, Tom Bienaimé, Elisabeth Giacobino, Alberto Bramati, and Quentin Glorieux. Blast waves in a paraxial fluid of light (a). *EPL (Europhysics Letters)*, 134(2):24001, 2021.

[3] Imad H Agha, Christina Giarmatzi, Quentin Glorieux, Thomas Coudreau, Philippe Grangier, and Gaétan Messin. Time-resolved detection of relative-intensity squeezed nanosecond pulses in an 87rb vapor. *New Journal of Physics*, 13:043030, 2011.

[4] Alberto Amo, Jérôme Lefrère, Simon Pigeon, Claire Adrados, Cristiano Ciuti, Iacopo Carusotto, Romuald Houdré, Elisabeth Giacobino, and Alberto Bramati. Superfluidity of polaritons in semiconductor microcavities. *Nature Phys*, 5(11):805–810, November 2009. Number: 11 Publisher: Nature Publishing Group.

[5] P. W. Anderson. More Is Different. *Science*, 177(4047):393–396, August 1972. Publisher: American Association for the Advancement of Science.

[6] Francesco Andreoli, Michael J. Gullans, Alexander A. High, Antoine Browaeys, and Darrick E. Chang. Maximum refractive index of an atomic medium. *Phys. Rev. X*, 11:011026, Feb 2021.

[7] Michelle O. Araújo, Hugo L. D. de S.Cavalcante, Marcos Oriá, Martine Chevrollier, Thierry Passerat de Silans, Romeu Castro, and Danieverton Moretti. Measurement of the Kerr nonlinear refractive index of Cs vapor. *Physical Review A*, 88(6):063818, December 2013.

[8] Alain Aspect, Jean Dalibard, and Gérard Roger. Experimental test of bell's inequalities using time-varying analyzers. *Phys. Rev. Lett.*, 49:1804–1807, Dec 1982.

[9] Pierre Azam, Adrien Fusaro, Quentin Fontaine, Josselin Garnier, Alberto Bramati, Antonio Picozzi, Robin Kaiser, Quentin Glorieux, and Tom Bienaimé. Dissipation-enhanced collapse singularity of a nonlocal fluid of light in a hot atomic vapor. *Phys. Rev. A*, 104(1):013515, July 2021.

[10] F. Baboux, L. Ge, T. Jacqmin, M. Biondi, E. Galopin, A. Lemaître, L. Le Gratiet, I. Sagnes, S. Schmidt, H. E. Türeci, A. Amo, and J. Bloch. Bosonic condensation and disorder-induced localization in a flat band. *Phys. Rev. Lett.*, 116:066402, Feb 2016.

[11] Carlos Barceló, S. Liberati, and Matt Visser. Probing semiclassical analog gravity in bose-einstein condensates with widely tunable interactions. *Phys. Rev. A*, 68:053613, Nov 2003.

[12] Tamara Bardon-Brun. *Propagation de la lumière en milieu complexe : effet Hall de spin optique en présence de désordre et force de Casimir en milieu Kerr.* Theses, Sorbonne Université, January 2021.

[13] Tamara Bardon-brun, Simon Pigeon, and Nicolas Cherroret. Classical casimir force from a quasi-condensate of light. *Phys. Rev. Research*, 2:013297, Mar 2020.

[14] Christopher Barsi, Wenjie Wan, Can Sun, and Jason W. Fleischer. Dispersive shock waves with nonlocal nonlinearity. *Opt. Lett.*, 32(20):2930, October 2007.

[15] C Becker, P Soltan-Panahi, J Kronjäger, S Dörscher, K Bongs, and K Sengstock. Ultracold quantum gases in triangular optical lattices. *New J. Phys.*, 12(6):065025, June 2010.

[16] Abdelkrim Bendahmane, Gang Xu, Matteo Conforti, Alexandre Kudlinski, Arnaud Mussot, and Sefano Trillo. Optical fiber analogous of the piston shock problem. In *Advanced Photonics 2018*, page JTu6G.2. Optica Publishing Group, 2018.

[17] J. Berges, Sz. Borsányi, and C. Wetterich. Prethermalization. *Phys. Rev. Lett.*, 93:142002, Sep 2004.

[18] T Bienaimé, M Isoard, Q Fontaine, A Bramati, AM Kamchatnov, Q Glorieux, and N Pavloff. Controlled shock wave dynamics in a fluid of light. *arXiv:2101.00720*, 2021.

[19] Erwan Bimbard. *Production and interaction of photons using atomic polaritons and Rydberg interactions.* phdthesis, Institut d'Optique Graduate School, December 2014.

[20] Eric D. Black. An introduction to Pound–Drever–Hall laser frequency stabilization. *American Journal of Physics*, 69(1):79–87, December 2000. Publisher: American Association of Physics Teachers.

[21] G. Boudebs, M. Chis, and X. Nguyen Phu. Third-order susceptibility measurement by a new Mach–Zehnder interferometry technique. *Journal of the Optical Society of America B*, 18(5):623, May 2001.

[22] Omar Boughdad, Omar Boughdad, Aurélien Eloy, Aurélien Eloy, Fabrice Mortessagne, Matthieu Bellec, Matthieu Bellec, Claire Michel, and Claire Michel. Anisotropic nonlinear

refractive index measurement of a photorefractive crystal via spatial self-phase modulation. *Optics Express*, 27(21):30360–30370, October 2019. Publisher: Optical Society of America.

[23] Robert W. Boyd. *Nonlinear Optics*. Elsevier, May 2008.

[24] Maria Chiara Braidotti, Radivoje Prizia, Calum Maitland, Francesco Marino, Angus Prain, Ilya Starshynov, Niclas Westerberg, Ewan M. Wright, and Daniele Faccio. Measurement of penrose superradiance in a photon superfluid. *Phys. Rev. Lett.*, 128:013901, Jan 2022.

[25] Guillaume Brochier. Optical control upon quantum fluids of light, 2021.

[26] Mark Buchanan. Past the Schwinger limit. *Nature Phys*, 2(11):721–721, November 2006. Number: 11 Publisher: Nature Publishing Group.

[27] David Campo and Renaud Parentani. Inflationary spectra and partially decohered distributions. *Phys. Rev. D*, 72:045015, Aug 2005.

[28] Iacopo Carusotto. Superfluid light in bulk nonlinear media. *Proc. Royal Soc. A: Mathematical, Physical and Engineering Sciences*, 470(2169):20140320, 2014.

[29] Iacopo Carusotto and Cristiano Ciuti. Quantum fluids of light. *Rev. Mod. Phys.*, 85(1):299–366, February 2013. Publisher: American Physical Society.

[30] Nicolas Cherroret, Thibault Scoquart, and Dominique Delande. Coherent multiple scattering of out-of-equilibrium interacting Bose gases. *Annals of Physics*, 435:168543, 2021.

[31] Raymond Y. Chiao. Bogoliubov dispersion relation for a 'photon fluid': Is this a superfluid? *Optics Communications*, 179(1):157–166, 2000.

[32] Raymond Y. Chiao and Jack Boyce. Bogoliubov dispersion relation and the possibility of superfluidity for weakly interacting photons in a two-dimensional photon fluid. *Phys. Rev. A*, 60:4114–4121, Nov 1999.

[33] P. Cladé, C. Ryu, A. Ramanathan, K. Helmerson, and W. D. Phillips. Observation of a 2d bose gas: From thermal to quasicondensate to superfluid. *Phys. Rev. Lett.*, 102:170401, Apr 2009.

[34] Ferdinand Claude, Maxime J. Jacquet, Romain Usciati, Iacopo Carusotto, Elisabeth Giacobino, Alberto Bramati, and Quentin Glorieux. High-resolution coherent probe spectroscopy of a polariton quantum fluid. *arXiv:2112.09903 [cond-mat]*, December 2021. arXiv: 2112.09903.

[35] Claude Cohen-Tannoudji and Cécile Robilliard. Wave functions, relative phase and interference for atomic Bose–Einstein condensates. *Comptes Rendus de l'Académie des Sciences - Series IV - Physics*, 2(3):445–477, April 2001.

[36] Claudio Conti, Andrea Fratalocchi, Marco Peccianti, Giancarlo Ruocco, and Stefano Trillo. Observation of a gradient catastrophe generating solitons. *Phys. Rev. Lett.*, 102(8):083902, 2009.

[37] Steck D.A. Rubidium 85 d line data. https://steck.us/alkalidata/rubidium85numbers.pdf.

[38] Steck D.A. Rubidium 87 d line data. https://steck.us/alkalidata/rubidium87numbers.pdf.

[39] Ioan Dancus, Silviu T. Popescu, and Adrian Petris. Single shot interferometric method for measuring the nonlinear refractive index. *Optics Express*, 21(25):31303, December 2013.

[40] Hui Deng, Hartmut Haug, and Yoshihisa Yamamoto. Exciton-polariton bose-einstein condensation. *Rev. Mod. Phys.*, 82:1489–1537, May 2010.

[41] Ivan H. Deutsch, Raymond Y. Chiao, and John C. Garrison. Diphotons in a nonlinear fabry-pérot resonator: Bound states of interacting photons in an optical "quantum wire". *Phys. Rev. Lett.*, 69:3627–3630, Dec 1992.

[42] Louisiane Devaud, Bernhard Rauer, Jakob Melchard, Matthias Kühmayer, Stefan Rotter, and Sylvain Gigan. Speckle engineering through singular value decomposition of the transmission matrix. *Phys. Rev. Lett.*, 127:093903, Aug 2021.

[43] John M. Dewey. *Measurement of the Physical Properties of Blast Waves*, pages 53–86. Springer, 2016.

[44] A. Dousse, L. Lanco, J. Suffczyński, E. Semenova, A. Miard, A. Lemaître, I. Sagnes, C. Roblin, J. Bloch, and P. Senellart. Controlled light-matter coupling for a single quantum dot embedded in a pillar microcavity using far-field optical lithography. *Phys. Rev. Lett.*, 101:267404, Dec 2008.

[45] S. D. Durbin, S. M. Arakelian, and Y. R. Shen. Laser-induced diffraction rings from a nematic-liquid-crystal film. *Optics Letters*, 6(9):411–413, September 1981.

[46] Stephan Dürr and Gerhard Rempe. Can wave–particle duality be based on the uncertainty relation? *American Journal of Physics*, 68(11):1021–1024, November 2000. Publisher: American Association of Physics Teachers.

[47] Christoph Eigen, Jake A. P. Glidden, Raphael Lopes, Eric A. Cornell, Robert P. Smith, and Zoran Hadzibabic. Universal prethermal dynamics of Bose gases quenched to unitarity. *Nature*, 563(7730):221–224, November 2018. Number: 7730 Publisher: Nature Publishing Group.

[48] A. Eloy, O. Boughdad, M. Albert, P.-É. Larré, F. Mortessagne, M. Bellec, and C. Michel. Experimental observation of turbulent coherent structures in a superfluid of light (a). *Europhysics Letters*, 134(2):26001, apr 2021.

[49] Sebastian Erne, Robert Bücker, Thomas Gasenzer, Jürgen Berges, and Jörg Schmiedmayer. Universal dynamics in an isolated one-dimensional Bose gas far from equilibrium. *Nature*, 563(7730):225–229, November 2018. Number: 7730 Publisher: Nature Publishing Group.

[50] J. Fatome, C. Finot, G. Millot, A. Armaroli, and S. Trillo. Observation of Optical Undular Bores in Multiple Four-Wave Mixing. *Phys. Rev. X*, 4(2):021022, May 2014.

[51] Petr O. Fedichev and Uwe R. Fischer. "cosmological" quasiparticle production in harmonically trapped superfluid gases. *Phys. Rev. A*, 69:033602, Mar 2004.

[52] Faye Flam. Making Waves With Interfering Atoms. *Science*, 252(5008):921–922, May 1991. Publisher: American Association for the Advancement of Science.

[53] V. Fleurov and R. Schilling. Regularization of fluctuations near the sonic horizon due to the quantum potential and its influence on Hawking radiation. *Phys. Rev. A*, 85(4):045602, April 2012.

[54] Q. Fontaine, T. Bienaimé, S. Pigeon, E. Giacobino, A. Bramati, and Q. Glorieux. Observation of the bogoliubov dispersion in a fluid of light. *Phys. Rev. Lett.*, 121:183604, Oct 2018.

[55] Quentin Fontaine. *Paraxial fluid of light in hot atomic vapors*. Theses, Sorbonne Université, January 2020.

[56] Quentin Fontaine, Pierre-Élie Larré, Giovanni Lerario, Tom Bienaimé, Simon Pigeon, Daniele Faccio, Iacopo Carusotto, Élisabeth Giacobino, Alberto Bramati, and Quentin Glorieux. Interferences between bogoliubov excitations in superfluids of light. *Physical Review Research*, 2(4):043297, 2020.

[57] Quentin Fontaine, Davide Squizzato, Florent Baboux, Ivan Amelio, Aristide Lemaître, Marina Morassi, Isabelle Sagnes, Luc Le Gratiet, Abdelmounaim Harouri, Michiel Wouters, Iacopo Carusotto, Alberto Amo, Maxime Richard, Anna Minguzzi, Léonie Canet, Sylvain Ravets, and Jacqueline Bloch. Observation of KPZ universal scaling in a one-dimensional polariton condensate. *arXiv:2112.09550 [cond-mat, physics:physics]*, December 2021. arXiv: 2112.09550.

[58] T. Frisch, Y. Pomeau, and S. Rica. Transition to dissipation in a model of superflow. *Phys. Rev. Lett.*, 69(11):1644–1647, September 1992.

[59] Dennis C. Ghiglia and Louis A. Romero. Robust two-dimensional weighted and unweighted phase unwrapping that uses fast transforms and iterative methods. *J. Opt. Soc. Am. A*, 11(1):107–117, Jan 1994. Link for the used MATLAB function: https://fr.mathworks.com/matlabcentral/fileexchange/60345-2d-weighted-phase-unwrapping.

[60] Jake A. P. Glidden, Christoph Eigen, Lena H. Dogra, Timon A. Hilker, Robert P. Smith, and Zoran Hadzibabic. Bidirectional dynamic scaling in an isolated Bose gas far from equilibrium. *Nat. Phys.*, 17(4):457–461, April 2021. Number: 4 Publisher: Nature Publishing Group.

[61] V. Goblot, A. Štrkalj, N. Pernet, J. L. Lado, C. Dorow, A. Lemaître, L. Le Gratiet, A. Harouri, I. Sagnes, S. Ravets, A. Amo, J. Bloch, and O. Zilberberg. Emergence of criticality through a cascade of delocalization transitions in quasiperiodic chains. *Nat. Phys.*, 16(8):832–836, August 2020. Number: 8 Publisher: Nature Publishing Group.

[62] Christian Gogolin and Jens Eisert. Equilibration, thermalisation, and the emergence of statistical mechanics in closed quantum systems. *Reports on Progress in Physics*, 79(5):056001, apr 2016.

[63] Markus Greiner, Olaf Mandel, Tilman Esslinger, Theodor W. Hänsch, and Immanuel Bloch. Quantum phase transition from a superfluid to a Mott insulator in a gas of ultracold atoms. *Nature*, 415(6867):39–44, January 2002. Number: 6867 Publisher: Nature Publishing Group.

[64] Markus Greiner, Olaf Mandel, Theodor W. Hänsch, and Immanuel Bloch. Collapse and revival of the matter wave field of a Bose–Einstein condensate. *Nature*, 419(6902):51–54, September 2002. Number: 6902 Publisher: Nature Publishing Group.

[65] Rudolf Grimm and Jürgen Mlynek. Light-pressure-induced nonlinear dispersion of a laser field interacting with an atomic gas. *Phys. Rev. A*, 42:2890–2905, Sep 1990.

[66] M. Gring, M. Kuhnert, T. Langen, T. Kitagawa, B. Rauer, M. Schreitl, I. Mazets, D. Adu Smith, E. Demler, and J. Schmiedmayer. Relaxation and Prethermalization in an Isolated Quantum System. *Science*, 337(6100):1318–1322, September 2012. Publisher: American Association for the Advancement of Science.

[67] L. P. Grishchuk and Y. V. Sidorov. Squeezed quantum states of relic gravitons and primordial density fluctuations. *Phys. Rev. D*, 42:3413–3421, Nov 1990.

[68] Christian Gross and Immanuel Bloch. Quantum simulations with ultracold atoms in optical lattices. *Science*, 357(6355):995–1001, September 2017. Publisher: American Association for the Advancement of Science.

[69] Zoran Hadzibabic, Peter Krüger, Marc Cheneau, Baptiste Battelier, and Jean Dalibard. Berezinskii–Kosterlitz–Thouless crossover in a trapped atomic gas. *Nature*, 441(7097):1118–1121, June 2006. Number: 7097 Publisher: Nature Publishing Group.

[70] Lene Vestergaard Hau, S. E. Harris, Zachary Dutton, and Cyrus H. Behroozi. Light speed reduction to 17 metres per second in an ultracold atomic gas. *Nature*, 397(6720):594–598, February 1999. Number: 6720 Publisher: Nature Publishing Group.

[71] M. Himsworth and T. Freegarde. Rubidium pump-probe spectroscopy: Comparison between *ab initio* theory and experiment. *Physical Review A*, 81(2):023423, February 2010.

[72] M. A. Hoefer, M. J. Ablowitz, I. Coddington, E. A. Cornell, P. Engels, and V. Schweikhard. Dispersive and classical shock waves in Bose-Einstein condensates and gas dynamics. *Phys. Rev. A*, 74(2):023623, August 2006.

[73] J. J. Hopfield. Theory of the contribution of excitons to the complex dielectric constant of crystals. *Phys. Rev.*, 112:1555–1567, Dec 1958.

[74] Wayne Hu and Scott Dodelson. Cosmic microwave background anisotropies. *Annual Review of Astronomy and Astrophysics*, 40(1):171–216, 2002.

[75] Chen-Lung Hung, Victor Gurarie, and Cheng Chin. From Cosmology to Cold Atoms: Observation of Sakharov Oscillations in Quenched Atomic Superfluids. *Science*, 341(6151):1213–1215, September 2013.

[76] M. Isoard, A. M. Kamchatnov, and N. Pavloff. Wave breaking and formation of dispersive shock waves in a defocusing nonlinear optical material. *Phys. Rev. A*, 99:053819, May 2019.

[77] Sergey K. Ivanov, Jules-Elémir Suchorski, Anatoly M. Kamchatnov, Mathieu Isoard, and Nicolas Pavloff. Formation of dispersive shock waves in a saturable nonlinear medium. *Phys. Rev. E*, 102(3):032215, September 2020.

[78] T. Jacqmin, I. Carusotto, I. Sagnes, M. Abbarchi, D. D. Solnyshkov, G. Malpuech, E. Galopin, A. Lemaître, J. Bloch, and A. Amo. Direct observation of dirac cones and a flatband in a honeycomb lattice for polaritons. *Phys. Rev. Lett.*, 112:116402, Mar 2014.

[79] D. Jaksch, C. Bruder, J. I. Cirac, C. W. Gardiner, and P. Zoller. Cold bosonic atoms in optical lattices. *Phys. Rev. Lett.*, 81:3108–3111, Oct 1998.

[80] Shu Jia, Mikko Haataja, and Jason W. Fleischer. Rayleigh–Taylor instability in nonlinear Schrödinger flow. *New Journal of Physics*, 14(7):075009, July 2012. Publisher: IOP Publishing.

[81] Gyu-Boong Jo, Jennie Guzman, Claire K. Thomas, Pavan Hosur, Ashvin Vishwanath, and Dan M. Stamper-Kurn. Ultracold atoms in a tunable optical kagome lattice. *Phys. Rev. Lett.*, 108:045305, Jan 2012.

[82] D. E. Jones, J. D. Franson, and T. B. Pittman. Saturation of atomic transitions using subwavelength diameter tapered optical fibers in rubidium vapor. *Journal of the Optical Society of America B*, 31(8):1997, August 2014.

[83] J. Kasprzak, M. Richard, S. Kundermann, A. Baas, P. Jeambrun, J. M. J. Keeling, F. M. Marchetti, M. H. Szymańska, R. André, J. L. Staehli, V. Savona, P. B. Littlewood, B. Deveaud, and Le Si Dang. Bose–Einstein condensation of exciton polaritons. *Nature*, 443(7110):409–414, September 2006. Number: 7110 Publisher: Nature Publishing Group.

[84] J. Keaveney, I. G. Hughes, A. Sargsyan, D. Sarkisyan, and C. S. Adams. Maximal refraction and superluminal propagation in a gaseous nanolayer. *Phys. Rev. Lett.*, 109:233001, Dec 2012.

[85] Bongjune Kim, Ko-Tang Chen, Shih-Si Hsiao, Sheng-Yang Wang, Kai-Bo Li, Julius Ruseckas, Gediminas Juzeliūnas, Teodora Kirova, Marcis Auzinsh, Ying-Cheng Chen, Yong-Fan Chen, and Ite A. Yu. A weakly-interacting many-body system of Rydberg polaritons based on electromagnetically induced transparency. *Commun Phys*, 4(1):101, December 2021.

[86] Toshiya Kinoshita, Trevor Wenger, and David S. Weiss. A quantum Newton's cradle. *Nature*, 440(7086):900–903, April 2006. Number: 7086 Publisher: Nature Publishing Group.

[87] Jan Klaers, Julian Schmitt, Tobias Damm, Frank Vewinger, and Martin Weitz. Statistical physics of bose-einstein-condensed light in a dye microcavity. *Phys. Rev. Lett.*, 108:160403, Apr 2012.

[88] Martin J. Klein. Max planck and the beginnings of the quantum theory. *Archive for History of Exact Sciences*, 1(5):459–479, 1962.

[89] Marcus Kollar, F. Alexander Wolf, and Martin Eckstein. Generalized gibbs ensemble prediction of prethermalization plateaus and their relation to nonthermal steady states in integrable systems. *Phys. Rev. B*, 84:054304, Aug 2011.

[90] Wiesław Królikowski and Ole Bang. Solitons in nonlocal nonlinear media: Exact solutions. *Phys. Rev. E*, 63:016610, Dec 2000.

[91] C. C. Kwong, D. Wilkowski, D. Delande, and R. Pierrat. Coherent light propagation through cold atomic clouds beyond the independent scattering approximation. *Physical Review A*, 99(4):043806, April 2019.

[92] T. Langen, R. Geiger, M. Kuhnert, B. Rauer, and J. Schmiedmayer. Local emergence of thermal correlations in an isolated quantum many-body system. *Nature Phys*, 9(10):640–643, October 2013.

[93] Tim Langen, Sebastian Erne, Remi Geiger, Bernhard Rauer, Thomas Schweigler, Maximilian Kuhnert, Wolfgang Rohringer, Igor E. Mazets, Thomas Gasenzer, and Jörg Schmiedmayer. Experimental observation of a generalized Gibbs ensemble. *Science*, 348(6231):207–211, April 2015. Publisher: American Association for the Advancement of Science.

[94] Tim Langen, Remi Geiger, and Jörg Schmiedmayer. Ultracold atoms out of equilibrium. *Annual Review of Condensed Matter Physics*, 6(1):201–217, 2015.

[95] Pierre-Élie Larré, Stefano Biasi, Fernando Ramiro-Manzano, Lorenzo Pavesi, and Iacopo Carusotto. Pump-and-probe optical transmission phase shift as a quantitative probe of the Bogoliubov dispersion relation in a nonlinear channel waveguide. *Eur. Phys. J. D*, 71(6):146, June 2017.

[96] Pierre-Élie Larré and Iacopo Carusotto. Propagation of a quantum fluid of light in a cavityless nonlinear optical medium: General theory and response to quantum quenches. *Phys. Rev. A*, 92(4):043802, 2015. Publisher: American Physical Society.

[97] Pierre-Élie Larré and Iacopo Carusotto. Prethermalization in a quenched one-dimensional quantum fluid of light. *Eur. Phys. J. D*, 70(3):45, March 2016.

[98] T. Lindvall and I. Tittonen. Effect of optical pumping on alkali-atom Doppler-limited spectra. *Journal of Modern Optics*, 54(18):2779–2793, December 2007.

[99] E. Madelung. Quantentheorie in hydrodynamischer Form. *Z. Physik*, 40(3):322–326, March 1927.

[100] Krishnanand Mallayya, Marcos Rigol, and Wojciech De Roeck. Prethermalization and thermalization in isolated quantum systems. *Phys. Rev. X*, 9:021027, May 2019.

[101] Sandra McConville, David Laurent, Alessio Guarino, and Stefania Residori. Measurement of the giant nonlinear response of dye-doped liquid crystals. *American Journal of Physics*, 73(5):425–432, May 2005.

[102] C. F. McCormick, D. R. Solli, R. Y. Chiao, and J. M. Hickmann. Saturable nonlinear refraction in hot atomic vapor. *Physical Review A*, 69(2):023804, February 2004.

[103] Claire Michel, Omar Boughdad, Mathias Albert, Pierre-Élie Larré, and Matthieu Bellec. Superfluid motion and drag-force cancellation in a fluid of light. *Nature Communications*, 9(1):2108, May 2018.

[104] Christophe Mora and Yvan Castin. Extension of bogoliubov theory to quasicondensates. *Phys. Rev. A*, 67:053615, May 2003.

[105] Sebabrata Mukherjee, Harikumar K. Chandrasekharan, Patrik Öhberg, Nathan Goldman, and Robert R. Thomson. State-recycling and time-resolved imaging in topological photonic lattices. *Nat Commun*, 9(1):4209, December 2018.

[106] Sergey S. Nalegaev, Andrey V. Belashov, and Nikolay V. Petrov. Application of Photothermal Digital Interferometry for Nonlinear Refractive Index Measurements within a Kerr Approximation. *Optical Materials*, 69:437–443, 2017.

[107] G. Natale, R. M. W. van Bijnen, A. Patscheider, D. Petter, M. J. Mark, L. Chomaz, and F. Ferlaino. Excitation spectrum of a trapped dipolar supersolid and its experimental evidence. *Phys. Rev. Lett.*, 123:050402, 2019.

[108] L. Neuhaus, R. Metzdorff, S. Chua, T. Jacqmin, T. Briant, A. Heidmann, P.-F. Cohadon, and S. Deléglise. Pyrpl - an open-source software package for fpga-controlled quantum optics experiments. Optical Society of America, 2017.

[109] J. Nuño, C. Finot, G. Xu, G. Millot, M. Erkintalo, and J. Fatome. Vectorial dispersive shock waves in optical fibers. *Commun Phys*, 2(1):138, December 2019.

[110] P. G. Pappas, M. M. Burns, D. D. Hinshelwood, M. S. Feld, and D. E. Murnick. Saturation spectroscopy with laser optical pumping in atomic barium. *Physical Review A*, 21(6):1955–1968, June 1980.

[111] L. Parker. Particle creation in expanding universes. *Phys. Rev. Lett.*, 21:562–564, Aug 1968.

[112] A. Parriaux, M. Conforti, A. Bendahmane, J. Fatome, C. Finot, S. Trillo, N. Picqué, and G. Millot. Spectral broadening of picosecond pulses forming dispersive shock waves in optical fibers. *Opt. Lett., OL*, 42(15):3044–3047, August 2017. Publisher: Optical Society of America.

[113] Dr Rüdiger Paschotta. Tunable Lasers, www.rp-photonics.com/tunable_lasers.html.

[114] Nicolas Pavloff. Optical hydrodynamics and nonlinear diffraction. In *Waves Côte d'Azur*, 2019.

[115] P. J. E. Peebles and J. T. Yu. Primeval Adiabatic Perturbation in an Expanding Universe. , 162:815, December 1970.

[116] Abhijit Pendse and A Bhattacharyay. Probing non-locality of interactions in a bose–einstein condensate using solitons. *Journal of Physics: Condensed Matter*, 30(45):455602, oct 2018.

[117] D. S. Petrov, M. Holzmann, and G. V. Shlyapnikov. Bose-einstein condensation in quasi-2d trapped gases. *Phys. Rev. Lett.*, 84:2551–2555, Mar 2000.

[118] William D. Phillips. Nobel lecture: Laser cooling and trapping of neutral atoms. *Rev. Mod. Phys.*, 70:721–741, Jul 1998.

[119] Clara Piekarski, Wei Liu, Jeff Steinhauer, Elisabeth Giacobino, Alberto Bramati, and Quentin Glorieux. Measurement of the static structure factor in a paraxial fluid of light using bragg-like spectroscopy. *Phys. Rev. Lett.*, 127:023401, Jul 2021.

[120] Clara Piekarski, Wei Liu, Jeff Steinhauer, Elisabeth Giacobino, Alberto Bramati, and Quentin Glorieux. Measurement of the static structure factor in a paraxial fluid of light using bragg-like spectroscopy. *Phys. Rev. Lett.*, 127:023401, Jul 2021.

[121] Lev P. Pitaevskij and Sandro Stringari. *Bose-Einstein condensation and superfluidity*. Number 164 in International series of monographs on physics. Oxford University Press, Oxford, reprinted (with corrections) edition, 2016.

[122] Anatoli Polkovnikov, Krishnendu Sengupta, Alessandro Silva, and Mukund Vengalattore. Colloquium: Nonequilibrium dynamics of closed interacting quantum systems. *Rev. Mod. Phys.*, 83:863–883, Aug 2011.

[123] Angus Prain, Serena Fagnocchi, and Stefano Liberati. Analogue cosmological particle creation: Quantum correlations in expanding bose-einstein condensates. *Phys. Rev. D*, 82:105018, Nov 2010.

[124] Maximilian Prüfer, Philipp Kunkel, Helmut Strobel, Stefan Lannig, Daniel Linnemann, Christian-Marcel Schmied, Jürgen Berges, Thomas Gasenzer, and Markus K. Oberthaler. Observation of universal dynamics in a spinor Bose gas far from equilibrium. *Nature*, 563(7730):217–220, November 2018. Number: 7730 Publisher: Nature Publishing Group.

[125] G. T. Purves, G. Jundt, C. S. Adams, and I. G. Hughes. Refractive index measurements by probe-beam deflection. *The European Physical Journal D - Atomic, Molecular and Optical Physics*, 29(3):433–436, June 2004.

[126] Saifollah Rasouli and Mahnaz Ghorbani. Nonlinear refractive index measuring using a double-grating interferometer in pump–probe configuration and Fourier transform analysis. *Journal of Optics*, 14(3):035203, March 2012.

[127] João D Rodrigues, José T Mendonça, and Hugo Terças. Turbulence excitation in counterstreaming paraxial superfluids of light. *Physical Review A*, 101(4):043810, 2020.

[128] L. Rodriguez, C. Simos, M. Sylla, A. Marcano O., and X. Nguyen Phu. New holographic technique for third-order optical properties measurement. *Optics Communications*, 247(4):453–460, 2005.

[129] Joshua E. Rothenberg and D. Grischkowsky. Observation of the formation of an optical intensity shock and wave breaking in the nonlinear propagation of pulses in optical fibers. *Phys. Rev. Lett.*, 62:531–534, Jan 1989.

[130] R Z Sagdeev. Cooperative phenomena and shock waves in collisionless plasmas. *Rev. Plasma Phys. (USSR)(Engl. Transl.)*.

[131] J Sagle, R K Namiotka, and J Huennekens. Measurement and modelling of intensity dependent absorption and transit relaxation on the cesium line. *Journal of Physics B: Atomic, Molecular and Optical Physics*, 29(12):2629–2643, June 1996.

[132] Abrarov Sanjar. The voigt/complex error function (second version), 2022. https://www.mathworks.com/matlabcentral/fileexchange/47801-the-voigt-complex-error-function-second-version.

[133] F. C. Dias dos Santos, J. C. de Aquino Carvalho, G. T. Moura, and T. Passerat de Silans. Measurement of the nonlinear refractive index of Cs D_1 line using z-scan. *JOSA B*, 36(9):2468–2472, September 2019. Publisher: Optical Society of America.

[134] Michael Schreiber, Sean S. Hodgman, Pranjal Bordia, Henrik P. Lüschen, Mark H. Fischer, Ronen Vosk, Ehud Altman, Ulrich Schneider, and Immanuel Bloch. Observation of many-body localization of interacting fermions in a quasirandom optical lattice. *Science*, 349(6250):842–845, August 2015. Publisher: American Association for the Advancement of Science.

[135] E. Schrodinger. The proper vibrations of the expanding universe. *Physica*, 6(7-12):899–912, July 1939.

[136] Florian Schäfer, Takeshi Fukuhara, Seiji Sugawa, Yosuke Takasu, and Yoshiro Takahashi. Tools for quantum simulation with ultracold atoms in optical lattices. *Nat Rev Phys*, 2(8):411–425, August 2020. Number: 8 Publisher: Nature Publishing Group.

[137] T. Scoquart, P.-É. Larré, D. Delande, and N. Cherroret. Weakly interacting disordered bose gases out of equilibrium: From multiple scattering to superfluidity (a). *Europhysics Letters*, 132(6):66001, dec 2020.

[138] I. Shammass, S. Rinott, A. Berkovitz, R. Schley, and J. Steinhauer. Phonon dispersion relation of an atomic bose-einstein condensate. *Phys. Rev. Lett.*, 109:195301, Nov 2012.

[139] M. Sheik-bahae, A. A. Said, and E. W. Van Stryland. High-sensitivity, single-beam n_2 measurements. *Optics Letters*, 14(17):955, September 1989.

[140] Paul Siddons, Charles S. Adams, Chang Ge, and Ifan G. Hughes. Absolute absorption on rubidium D lines: comparison between theory and experiment. *Journal of Physics B: Atomic, Molecular and Optical Physics*, 41(15):155004, July 2008.

[141] Paul Siddons, Charles S Adams, and Ifan G Hughes. Off-resonance absorption and dispersion in vapours of hot alkali-metal atoms. *Journal of Physics B: Atomic, Molecular and Optical Physics*, 42(17):175004, 2009.

[142] S. Skupin, M. Saffman, and W. Królikowski. Nonlocal Stabilization of Nonlinear Beams in a Self-Focusing Atomic Vapor. *Physical Review Letters*, 98(26), June 2007.

[143] David A. Smith and Ifan G. Hughes. The role of hyperfine pumping in multilevel systems exhibiting saturated absorption. *American Journal of Physics*, 72(5):631–637, May 2004.

[144] J. Steinhauer, N. Katz, R. Ozeri, N. Davidson, C. Tozzo, and F. Dalfovo. Bragg spectroscopy of the multibranch bogoliubov spectrum of elongated bose-einstein condensates. *Phys. Rev. Lett.*, 90:060404, Feb 2003.

[145] Jeff Steinhauer. Observation of quantum hawking radiation and its entanglement in an analogue black hole. *Nature Physics*, 12(10):959–965, 2016. Number: 10 Publisher: Nature Publishing Group.

[146] Jeff Steinhauer, Murad Abuzarli, Tangui Aladjidi, Tom Bienaimé, Clara Piekarski, Wei Liu, Elisabeth Giacobino, Alberto Bramati, and Quentin Glorieux. Analogue cosmological particle creation in an ultracold quantum fluid of light. *Nature Communications*, 13(1):2890, 2022.

[147] Can Sun, Shu Jia, Christopher Barsi, Sergio Rica, Antonio Picozzi, and Jason W. Fleischer. Observation of the kinetic condensation of classical waves. *Nature Physics*, 8(6):470–474, 2012.

[148] D. Tanese, H. Flayac, D. Solnyshkov, A. Amo, A. Lemaître, E. Galopin, R. Braive, P. Senellart, I. Sagnes, G. Malpuech, and J. Bloch. Polariton condensation in solitonic gap states in a one-dimensional periodic potential. *Nature Communications*, 4(1):1749, April 2013. Number: 1 Publisher: Nature Publishing Group.

[149] Andreas Trabesinger. Quantum simulation. *Nature Phys*, 8(4):263–263, April 2012. Number: 4 Publisher: Nature Publishing Group.

[150] S. Trotzky, Y.-A. Chen, A. Flesch, I. P. McCulloch, U. Schollwöck, J. Eisert, and I. Bloch. Probing the relaxation towards equilibrium in an isolated strongly correlated one-dimensional Bose gas. *Nature Phys*, 8(4):325–330, April 2012. Number: 4 Publisher: Nature Publishing Group.

[151] A J van Lange, P van der Straten, and D van Oosten. Combined effect of non-linear optical and collisional processes on absorption saturation in a dense rubidium vapour. *Journal of Physics B: Atomic, Molecular and Optical Physics*, 53(12):125402, may 2020.

[152] Konrad Viebahn, Matteo Sbroscia, Edward Carter, Jr-Chiun Yu, and Ulrich Schneider. Matter-wave diffraction from a quasicrystalline optical lattice. *Phys. Rev. Lett.*, 122:110404, Mar 2019.

[153] David Vocke, Kali Wilson, Francesco Marino, Iacopo Carusotto, Ewan M. Wright, Thomas Roger, Brian P. Anderson, Patrik Öhberg, and Daniele Faccio. Role of geometry in the superfluid flow of nonlocal photon fluids. *Phys. Rev. A*, 94:013849, Jul 2016.

[154] BB Voronov, AI Korobov, and Oleg V Rudenko. Nonlinear acoustic waves in media with absorption and dispersion. *Soviet Physics Uspekhi*, 35(9):796, 1992.

[155] Wenjie Wan, Shu Jia, and Jason W Fleischer. Dispersive superfluid-like shock waves in nonlinear optics. *Nat. Phys.*, 3(1):46–51, 2007.

[156] Hai Wang, David Goorskey, and Min Xiao. Dependence of enhanced Kerr nonlinearity on coupling power in a three-level atomic system. *Opt. Lett., OL*, 27(4):258–260, February 2002. Publisher: Optical Society of America.

[157] Hendrik Weimer, Markus Müller, Igor Lesanovsky, Peter Zoller, and Hans Peter Büchler. A Rydberg quantum simulator. *Nature Phys*, 6(5):382–388, May 2010. Number: 5 Publisher: Nature Publishing Group.

[158] Christof Weitenberg and Juliette Simonet. Tailoring quantum gases by Floquet engineering. *Nature Physics*, 17(12):1342–1348, December 2021. Number: 12 Publisher: Nature Publishing Group.

[159] L. Weller, R. J. Bettles, C. L. Vaillant, M. A. Zentile, R. M. Potvliege, C. S. Adams, and I. G. Hughes. Cooperative enhancement of energy transfer in a high-density thermal vapor, 2013.

[160] Lee Weller, Robert J Bettles, Paul Siddons, Charles S Adams, and Ifan G Hughes. Absolute absorption on the rubidium d1line including resonant dipole–dipole interactions. *Journal of Physics B: Atomic, Molecular and Optical Physics*, 44(19):195006, 2011.

[161] Benjamin Wetzel, Domenico Bongiovanni, Michael Kues, Yi Hu, Zhigang Chen, Stefano Trillo, John M Dudley, Stefano Wabnitz, and Roberto Morandotti. Experimental generation of riemann waves in optics: a route to shock wave control. *Phys. Rev. Lett.*, 117(7):073902, 2016.

[162] William K. Wootters and Wojciech H. Zurek. Complementarity in the double-slit experiment: Quantum nonseparability and a quantitative statement of bohr's principle. *Phys. Rev. D*, 19:473–484, Jan 1979.

[163] G. Xu, D. Vocke, D. Faccio, J. Garnier, T. Roger, S. Trillo, and A. Picozzi. From coherent shocklets to giant collective incoherent shock waves in nonlocal turbulent flows. *Nat Commun*, 6(1):8131, November 2015.

[164] Gang Xu, Matteo Conforti, Alexandre Kudlinski, Arnaud Mussot, and Stefano Trillo. Dispersive dam-break flow of a photon fluid. *Phys. Rev. Lett.*, 118(25):254101, 2017.

[165] Neven Šantić, Adrien Fusaro, Sabeur Salem, Josselin Garnier, Antonio Picozzi, and Robin Kaiser. Nonequilibrium Precondensation of Classical Waves in Two Dimensions Propagating through Atomic Vapors. *Physical Review Letters*, 120(5):055301, February 2018.

[166] Nikola Šibalić and Charles S Adams. *Rydberg Physics*. 2399-2891. IOP Publishing, 2018.

Murad Abuzarli **21 4 2022**

Sujet : Dynamique hors équilibre dans un fluide de lumière paraxial

Résumé : Les fluides quantiques produits avec des condensats de Bose-Einstein des gas d'atomes ultra-froids sont utilisés pour l'éxploration de l'évolution hors équilibre des systems quantiques à plusieurs corps. D'un autre coté, la propagation paraxiale de la lumière dans un milieu non-linéaire Kerr confère des interactions et une masse effective aux photons, et transforme la lumière en un fluide analogue dont la coordonnée temporelle est la direction de propagation du faisceau. Dans ce travail un tel fluide de lumière est produit dans les vapeurs atomiques de Rubidium. Trois aspects de sa dynamique hors équilibre ont été mis en évidence. D'abord, la perturbation du fluide avec une forte surdensité a permis d'observer son comportement hydrodynamique non-linéaire avec les ondes de choc. Ensuite, en perturbant un état initial Gaussien avec des faibles fluctuations, la pré-thermalisation du fluide a été observée à l'aide de sa cohérence spatiale. Enfin, la réponse du fluide à des trempes d'intéractions photoniques survenant à des interfaces de la cellule de vapeur atomique, a été sondée avec ses fluctuations intrinsèques venant du bruit de grenaille du faiseau laser. La mesure du spectre de bruit de densité du fluide a revelé la suppression des fluctuations de densité à faibles impulsions et l'emergence des pics acoustiques à des temps ultérieurs.

Mots clés : Superfluid,Fluid of light,Kerr medium,Blast waves,Pre-thermalization,interaction quench, spatial correlations

Subject : Nonequilibrium dynamics in a paraxial fluid of light

Abstract: Quantum fluids produced with Bose-Einstein Condensates of ultracold atoms are commonly used for exploring the out-of-equilibrium evolution of many-body quantum systems. On the other hand, paraxial propagation of light in a non-linear Kerr medium confers to photons interactions and an effective mass, and transforms the light into an analogue fluid, whose time coordinate is the beam's propagation direction. In this work, hot Rb vapors were used to produce such a fluid of light. Three different aspects of its out-of-equilibrium dynamics were evidenced. First, disturbing the fluid with a strong density perturbation led to the observation of its non-linear hydrodynamics in form of blast waves. Second, disturbing a Gaussian initial state with small random fluctuations the fluid's pre-thermalization was observed with its spatial coherence. Finally, the fluid's response to interaction quenches, occurring at the vapor cell's interfaces, was probed with its intrinsic fluctuations stemming from the shot noise of the laser beam. The measurement of the fluid's spatial density power spectrum revealed the suppression of density fluctuations at low momenta and emergence of the acoustic peaks at later times.

Keywords : Fluid of light,Kerr index,Blast waves,Pre-thermalization,interaction quench, spatial correlations